

LOAN DOCUMENT

PHOTOGRAPH THIS SHEET

AD-A239 095



DTIC ACCESSION NUMBER

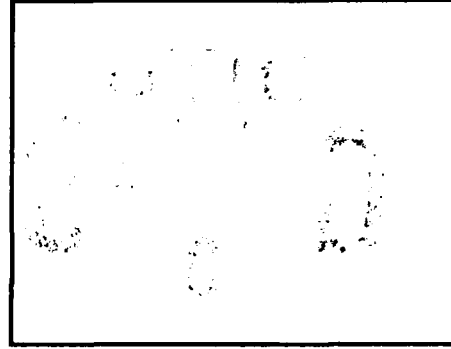
LEVEL

INVENTORY

Performance of Digital Communication Systems ... et.
DOCUMENT IDENTIFICATION
Aug 1986

DISTRIBUTION STATEMENT

ACCESSION FOR	
NTIS	GRA&I
DTIC	TRAC
UNANNOUNCED	
JUSTIFICATION	
BY <i>Pac AD34095</i>	
DISTRIBUTION/	
AVAILABILITY CODES	
DISTRIBUTION	AVAILABILITY AND/OR SPECIAL
<i>A-1</i>	



DATE ACCESSIONED

DISTRIBUTION STAMP

DATE RETURNED

26 91 7 30 026
91-06533



DATE RECEIVED IN DTIC

REGISTERED OR CERTIFIED NUMBER

PHOTOGRAPH THIS SHEET AND RETURN TO DTIC-FDAC

H
A
N
D
L
E

W
I
T
H

C
A
R
E

AD-A239 095



OSU

The Ohio State University

**PERFORMANCE OF DIGITAL COMMUNICATION SYSTEMS
WITH ADAPTIVE ARRAYS**

Matthew W. Ganz

The Ohio State University

ElectroScience Laboratory

Department of Electrical Engineering
Columbus, Ohio 43212

Technical Report 717253-4
Contract No. N00019-85-C-0119
August 1986

Department of the Navy
Naval Air Systems Command
Washington, DC 20461

NOTICES

When Government drawings, specifications, or other data are used for any purpose other than in connection with a definitely related Government procurement operation, the United States Government thereby incurs no responsibility nor any obligation whatsoever, and the fact that the Government may have formulated, furnished, or in any way supplied the said drawings, specifications, or other data, is not to be regarded by implication or otherwise as in any manner licensing the holder or any other person or corporation, or conveying any rights or permission to manufacture, use, or sell any patented invention that may in any way be related thereto.

REPORT DOCUMENTATION PAGE	1. REPORT NO.	2.	3. Recipient's Accession No.
4. Title and Subtitle Performance of Digital Communication Systems with Adaptive Arrays		5. Report Date August 1986	
7. Author(s) Matthew W. Ganz		6.	
9. Performing Organization Name and Address The Ohio State University ElectroScience Laboratory 1320 Kinnear Road Columbus, Ohio 43212		8. Performing Organization Rept. No. 717253-4	
12. Sponsoring Organization Name and Address Department of the Navy Naval Air Systems Command Washington, DC 20461		10. Project/Task/Work Unit No.	
		11. Contract(C) or Grant(G) No (C) N00019-85-C-0119 (G)	
		13. Type of Report & Period Covered Technical	
15. Supplementary Notes		14.	
16. Abstract (Limit: 200 words) <p>This report examines the protection offered to digital communication systems by the LMS adaptive array. The performances of systems that use binary phase-shift-keyed (BPSK), quadrature phase-shift-keyed (QPSK), binary differential phase-shift-keyed (DPSK), and noncoherent frequency-shift-keyed (FSK) modulation are calculated when the desired signal is corrupted by continuous wave (CW) interference. The probability of a symbol error at the system output is used as the measure of system performance.</p> <p>It is shown that the LMS array provides a significant degree of interference protection to each of these systems. The most protection is offered when the desired and interfering signals are spatially well separated. It is also shown that the performance generally improves as the array input bandwidth is reduced; however, for the modulation types listed above, the array input bandwidth must be several times larger than the data bandwidth if intersymbol interference is to be avoided.</p> <p>A narrowband BPSK system is described that allows relatively small array input bandwidths to be used. The performance of this narrowband system is examined for both CW and Gaussian noise interference. It is shown that this system is most vulnerable to noise interference when the interference bandwidth is equal to the desired signal bandwidth.</p> <p>The performance of an adaptive array with tapped delay line weights is also examined. It is shown that, with a single noise interferer, a communication system using this array performs better than one using a conventional LMS array.</p>			
17. Document Analysis a. Descriptors			
b. Identifiers/Open-Ended Terms			
c. COSATI Field/Group			
18. Availability Statement A. Approved for public release; distribution is unlimited.		19. Security Class (This Report) Unclassified	21. No of Pages 230
		20. Security Class (This Page) Unclassified	22. Price

TABLE OF CONTENTS

CHAPTER	PAGE
LIST OF FIGURES	v
I INTRODUCTION	1
II THE LMS ADAPTIVE ARRAY	6
A. INTRODUCTION	6
B. THE COMPLEX LMS ARRAY	6
III PERFORMANCE OF A BPSK SYSTEM WITH CW JAMMING	17
A. INTRODUCTION	17
B. ARRAY PERFORMANCE	18
C. BPSK DETECTOR PERFORMANCE WITH CW AND NOISE INTERFERENCE	24
D. PERFORMANCE CALCULATIONS FOR COMBINED LMS ARRAY/BPSK DETECTOR	41
III PERFORMANCE OF A QPSK SYSTEM WITH CW INTERFERENCE	64
A. INTRODUCTION	64
B. ARRAY PERFORMANCE	65
C. QPSK DETECTOR PERFORMANCE WITH CW AND AWGN INTERFERENCE	66
D. PERFORMANCE OF THE COMBINED LMS ARRAY/QPSK DETECTOR	77
V PERFORMANCE OF A DPSK SYSTEM WITH CW INTERFERENCE	93
A. INTRODUCTION	93
B. ADAPTIVE ARRAY PERFORMANCE	94
C. DPSK DETECTOR PERFORMANCE WITH CW AND AWGN INTERFERENCE	95
D. PERFORMANCE OF COMBINED LMS ARRAY/DPSK DETECTOR	106
VI PERFORMANCE OF AN FSK COMMUNICATION SYSTEM WITH CW INTERFERENCE	130
A. INTRODUCTION	130
B. ARRAY PERFORMANCE	132
C. FSK DETECTOR PERFORMANCE WITH CW INTERFERENCE AND AWGN	136
D. PERFORMANCE OF THE COMBINED LMS ARRAY/FSK DETECTOR	144

CHAPTER	PAGE
VII PERFORMANCE OF A NARROWBAND ADAPTIVE ARRAY WITH BPSK SIGNALLING AND CW INTERFERENCE	151
A. INTRODUCTION	151
B. BPSK SIGNALLING OVER A NARROWBAND CHANNEL	152
C. BPSK SYSTEM PERFORMANCE WITH AN LMS ARRAY AND CW INTERFERENCE	161
VIII PROTECTION OF A BPSK SYSTEM FROM WIDEBAND INTERFERENCE	178
A. INTRODUCTION	178
B. SYSTEM MODEL	179
C. RESULTS OF PERFORMANCE CALCULATIONS	189
D. PERFORMANCE OF A TAPPED DELAY LINE LMS ARRAY WITH WIDEBAND INTERFERENCE	202
IX SUMMARY AND CONCLUSIONS	214
REFERENCES	217

LIST OF FIGURES

Figure	Page
2.1. The complex LMS array.	7
3.1. BPSK signal and spectrum.	19
3.2. Noise spectrum and transfer function for ideal integrator.	26
3.3. The ideal BPSK detector.	28
3.4. Performance of ideal BPSK detector with CW interference ($\Delta\omega T = 0$).	37
3.5. Performance of ideal BPSK detector with CW interference ($\Delta\omega T = 0$).	39
3.6. Performance of ideal BPSK detector vs. SINR for 2 SNR values ($\Delta\omega T = 5$, noise bandwidth = $10/T$, INR varying).	40
3.7. Ideal integrator and BPF transfer functions (only positive frequencies shown).	44
3.8. BPSK $P(e)$ vs. SNR for 3-element array ($\theta_i=10^\circ$, $k=5$, $\Delta\omega T=0$).	47
3.9. BPSK $P(e)$ vs. INR for 3-element array ($\theta_i=10^\circ$, $k=5$, $\Delta\omega T=0$).	48
3.10. BPSK $P(e)$ vs. SNR for 3-element array ($\theta_i=20^\circ$, $k=5$, $\Delta\omega T=0$).	51
3.11. BPSK $P(e)$ vs. INR for 3-element array ($\theta_i=20^\circ$, $k=5$, $\Delta\omega T=0$).	52
3.12. BPSK $P(e)$ vs. SNR for 3-element array ($\theta_i=80^\circ$, $k=5$, $\Delta\omega T=0$).	53
3.13. BPSK $P(e)$ vs. INR for 3-element array ($\theta_i=80^\circ$, $k=5$, $\Delta\omega T=0$).	54
3.14. BPSK $P(e)$ vs. SNR for 3-element array ($\theta_i=10^\circ$, $k=10$, $\Delta\omega T=0$).	55
3.15. BPSK $P(e)$ vs. INR for 3-element array ($\theta_i=10^\circ$, $k=10$, $\Delta\omega T=0$).	56

Figure	Page
3.16. BPSK $P(e)$ vs. SNR for 3-element array ($\theta_i=20^\circ$, $k=10$, $\Delta\omega T=0$).	57
3.17. BPSK $P(e)$ vs. INR for 3-element array ($\theta_i=20^\circ$, $k=10$, $\Delta\omega T=0$).	58
3.18. BPSK $P(e)$ vs. SNR for 3-element array ($\theta_i=80^\circ$, $k=10$, $\Delta\omega T=0$).	59
3.19. BPSK $P(e)$ vs. INR for 3-element array ($\theta_i=80^\circ$, $k=10$, $\Delta\omega T=0$).	60
3.20. BPSK $P(e)$ vs. SNR for 3-element array ($\theta_i=10^\circ$, $k=10$, $\Delta\omega T=2\pi$).	61
3.21. BPSK $P(e)$ vs. INR for 3-element array ($\theta_i=10^\circ$, $k=10$, $\Delta\omega T=2\pi$).	62
4.1. A typical QPSK waveform with bit-pair assignments.	65
4.2. The ideal QPSK detector.	67
4.3. QPSK decision space.	67
4.4. Normalized decision space showing composite received signal.	72
4.5. Performance of ideal QPSK detector with CW interference ($\Delta\omega T=0$).	75
4.6. Performance of ideal QPSK detector with CW interference ($\Delta\omega T=0$).	76
4.7. QPSK $P(e)$ vs. SNR for 3-element array ($\theta_i=10^\circ$, $k=5$, $\Delta\omega T=0$).	78
4.8. QPSK $P(e)$ vs. INR for 3-element array ($\theta_i=10^\circ$, $k=5$, $\Delta\omega T=0$).	79
4.9. QPSK $P(e)$ vs. SNR for 3-element array ($\theta_i=20^\circ$, $k=5$, $\Delta\omega T=0$).	80
4.10. QPSK $P(e)$ vs. INR for 3-element array ($\theta_i=20^\circ$, $k=5$, $\Delta\omega T=0$).	81
4.11. QPSK $P(e)$ vs. SNR for 3-element array ($\theta_i=80^\circ$, $k=5$, $\Delta\omega T=0$).	82
4.12. QPSK $P(e)$ vs. INR for 3-element array ($\theta_i=80^\circ$, $k=5$, $\Delta\omega T=0$).	83

Figure	Page
4.13. QPSK $P(e)$ vs. SNR for 3-element array ($\theta_i=10^\circ$, $k=10$, $\Delta\omega T=0$).	85
4.14. QPSK $P(e)$ vs. INR for 3-element array ($\theta_i=10^\circ$, $k=10$, $\Delta\omega T=0$).	86
4.15. QPSK $P(e)$ vs. SNR for 3-element array ($\theta_i=20^\circ$, $k=10$, $\Delta\omega T=0$).	87
4.16. QPSK $P(e)$ vs. INR for 3-element array ($\theta_i=20^\circ$, $k=10$, $\Delta\omega T=0$).	88
4.17. QPSK $P(e)$ vs. SNR for 3-element array ($\theta_i=80^\circ$, $k=10$, $\Delta\omega T=0$).	89
4.18. QPSK $P(e)$ vs. INR for 3-element array ($\theta_i=80^\circ$, $k=10$, $\Delta\omega T=0$).	90
4.19. QPSK $P(e)$ vs. SNR for 3-element array ($\theta_i=10^\circ$, $k=10$, $\Delta\omega T=2\pi$).	91
4.20. QPSK $P(e)$ vs. INR for 3-element array ($\theta_i=10^\circ$, $k=10$, $\Delta\omega T=2$).	92
5.1. Ideal DPSK Detector.	96
5.2. DPSK decision space.	97
5.3. DPSK composite signal.	98
5.4. Performance of ideal DPSK detector with CW interference ($\Delta\omega T=0$).	108
5.5. Performance of ideal DPSK detector with CW interference ($\Delta\omega T=0$).	109
5.6. Performance of ideal DPSK detector with CW interference ($\Delta\omega T=\pi/2$).	110
5.7. Performance of ideal DPSK detector with CW interference ($\Delta\omega T=\pi/2$).	111
5.8. Performance of an ideal DPSK detector as a function of $\Delta\omega T$ (SNR=10 dB).	112
5.9. Performance of an ideal DPSK detector as a function of $\Delta\omega T$ (SNR=13 dB).	113

Figure	Page
5.10. DPSK $P(e)$ vs. SNR for 3-element array ($\theta_i=10^\circ$, $k=5$, $\Delta\omega T=0$).	114
5.11. DPSK $P(e)$ vs. INR for 3-element array ($\theta_i=10^\circ$, $k=5$, $\Delta\omega T=0$).	115
5.12. DPSK $P(e)$ vs. SNR for 3-element array ($\theta_i=20^\circ$, $k=5$, $\Delta\omega T=0$).	116
5.13. DPSK $P(e)$ vs. INR for 3-element array ($\theta_i=20^\circ$, $k=5$, $\Delta\omega T=0$).	117
5.14. DPSK $P(e)$ vs. SNR for 3-element array ($\theta_i=80^\circ$, $k=5$, $\Delta\omega T=0$).	118
5.15. DPSK $P(e)$ vs. INR for 3-element array ($\theta_i=80^\circ$, $k=5$, $\Delta\omega T=0$).	119
5.16. DPSK $P(e)$ vs. SNR for 3-element array ($\theta_i=10^\circ$, $k=10$, $\Delta\omega T=0$).	120
5.17. DPSK $P(e)$ vs. INR for 3-element array ($\theta_i=10^\circ$, $k=10$, $\Delta\omega T=0$).	121
5.18. DPSK $P(e)$ vs. SNR for 3-element array ($\theta_i=20^\circ$, $k=10$, $\Delta\omega T=0$).	122
5.19. DPSK $P(e)$ vs. INR for 3-element array ($\theta_i=20^\circ$, $k=10$, $\Delta\omega T=0$).	123
5.20. DPSK $P(e)$ vs. SNR for 3-element array ($\theta_i=80^\circ$, $k=10$, $\Delta\omega T=0$).	124
5.21. DPSK $P(e)$ vs. INR for 3-element array ($\theta_i=80^\circ$, $k=10$, $\Delta\omega T=0$).	125
5.22. DPSK $P(e)$ vs. SNR for 3-element array ($\theta_i=10^\circ$, $k=10$, $\Delta\omega T=\pi/2$).	126
5.23. DPSK $P(e)$ vs. INR for 3-element array ($\theta_i=10^\circ$, $k=10$, $\Delta\omega T=\pi/2$).	127
5.24. DPSK $P(e)$ vs. SNR for 3-element array ($\theta_i=10^\circ$, $k=10$, $\Delta\omega T=2\pi$).	128
5.25. DPSK $P(e)$ vs. INR for 3-element array ($\theta_i=10^\circ$, $k=10$, $\Delta\omega T=2\pi$).	129
6.1. A typical FSK waveform.	131

Figure	Page
6.2. FSK detector.	134
6.3. Performance of ideal FSK detector with CW interference.	142
6.4. Performance of ideal FSK detector with CW interference.	143
6.5. FSK $P(e)$ vs. SNR for 3-element array ($\theta_i=10^\circ$, $k=5$).	145
6.6. FSK $P(e)$ vs. INR for 3-element array ($\theta_i=10^\circ$, $k=5$).	146
6.7. FSK $P(e)$ vs. SNR for 3-element array ($\theta_i=20^\circ$, $k=5$).	147
6.8. FSK $P(e)$ vs. INR for 3-element array ($\theta_i=20^\circ$, $k=5$).	148
6.9. FSK $P(e)$ vs. SNR for 3-element array ($\theta_i=80^\circ$, $k=5$).	149
6.10. FSK $P(e)$ vs. INR for 3-element array ($\theta_i=90^\circ$, $k=5$).	150
7.1. Narrowband BPSK communication system.	153
7.2. Transmitter processing of baseband pulse.	155
7.3. Baseband signal for simple binary sequence.	159
7.4. Narrowband BPSK receiver using an adaptive array.	163
7.5. Desired signal PSD.	164
7.6. $P(e)$ vs. SNR for 3-element narrowband array ($\theta_d=0^\circ$, $\theta_i=10^\circ$, $k=1/2$).	167
7.7. $P(e)$ vs. INR for 3-element narrowband array ($\theta_d=0^\circ$, $\theta_i=10^\circ$, $k=1/2$).	168
7.8. $P(e)$ vs. SNR for 3-element narrowband array ($\theta_d=0^\circ$, $\theta_i=20^\circ$, $k=1/2$).	169
7.9. $P(e)$ vs. INR for 3-element narrowband array ($\theta_d=0^\circ$, $\theta_i=20^\circ$, $k=1/2$).	170
7.10. $P(e)$ vs. SNR for 3-element narrowband array ($\theta_d=0^\circ$, $\theta_i=80^\circ$, $k=1/2$).	171
7.11. $P(e)$ vs. INR for 3-element narrowband array ($\theta_d=0^\circ$, $\theta_i=80^\circ$, $k=1/2$).	172
7.12. $P(e)$ vs. INR for SNR=12 dB for two different k values ($\theta_d=0^\circ$, $\theta_i=10^\circ$).	173

Figure	Page
7.13. Adapted antenna patterns for two k values. SNR=12 dB, $\theta_d=0^\circ$, $\theta_i=10^\circ$.	174
7.14. $P(e)$ vs. INR for three k values. SNR=12 dB, $\theta_d=0^\circ$, $\theta_i=10^\circ$.	177
8.1. Interference PSD at element BPF inputs.	179
8.2. Transversal filter with two delay elements and three weights.	183
8.3. Frequency response of LMS array in the desired signal direction ($\theta_d=0^\circ$, $\theta_i=10^\circ$, SNR = 12 dB, INR = 20 dB, $k = 1/2$, $B_d = B_i = 0.1$).	186
8.4. Frequency response of LMS array in the interference signal direction ($\theta_d=0^\circ$, $\theta_i=10^\circ$, SNR = 12 dB, INR = 20 dB, $k = 1/2$, $B_d = B_i = 0.1$).	188
8.5. Three-element array performance with noise interference ($\theta_d=0^\circ$, $\theta_i=10^\circ$, $k = 1/2$, $B_d = 0.1$).	191
8.6. Performance of a 3-element array with noise interference for various SIR values ($\theta_d=0^\circ$, $k=1/2$, $B_d=0.1$). B_i values and scales are the same as those of Figure 8.5.	192
8.7. Performance of a 3-element array with noise interference for various SIR values ($r_d=90^\circ$, $k=1/2$, $B_d=0.1$). B_i values and scales are the same as those of Figure 8.5.	194
8.8. 3-element array performance - Case (A).	196
8.9. 3-element array performance - case (B).	197
8.10. 3-element array performance - case (C).	199
8.11. 3-element array performance - case (D).	200
8.12. Sample interference waveform with $B_i \approx 0$.	203
8.13. 2-tap transversal filter.	205
8.14. 3-element tapped delay line LMS array.	206
8.15. Performance of the 3-element TDL LMS array for the same cases shown in Figure 8.5.	213

CHAPTER I

INTRODUCTION

An adaptive array is an antenna that can change its pattern in response to the signals it receives [1,2]. By forming pattern nulls in the directions of undesired signals, an adaptive array can protect a communication system from interference. The Applebaum adaptive array [1] uses a steering vector to control the direction of its main beam. This array nulls signals that arrive from angles other than the direction specified by this vector. The LMS array [2] uses a reference signal to control the main beam direction. Both Applebaum and LMS arrays can be used in communication systems. When the desired signal arrival angle is known, the Applebaum array is the best choice. The LMS array is appropriate if we wish to track a desired signal whose arrival angle is unknown.

The LMS array requires a reference signal that is correlated with the desired signal and uncorrelated with any interfering signals [3]. Methods for deriving suitable reference signals have been developed for several modulation types including binary phase-shift-keying (BPSK) [3], quadrature phase-shift-keying (QPSK) [4], conventional amplitude modulation (AM) [5], and frequency-shift-keying (FSK) [6,7]. Experimental systems have been built that verify the feasibility of each of these systems [3,4,5,7].

The output of the LMS array is a weighted sum of the signals at its inputs. The LMS weights maximize the signal to interference-plus-noise ratio (SINR) at the array output [8]. Therefore, in much of the early work, the output SINR was used as a figure of merit for adaptive array performance [8-13]. However, a few recent studies have used the bit-error probability at the communication system output as a measure of performance. Al-Ruwais, Acar, and Compton [12,13,14] estimated $P(e)$ at the output of differential phase-shift-keyed (DPSK) communication systems that included LMS arrays. Their estimates were based on the assumption that the noise and interference at the array output contributed equally to the degradation in detector performance. Furthermore they assumed that the detector performance was not dependent on the spectral distribution of the noise or interference.

In this report we examine the performance of digital communication systems that use LMS adaptive arrays. We consider the performance with BPSK, QPSK, binary DPSK, and binary FSK modulation of the desired signal. We examine the effects of single tone (i.e., CW) interference and bandlimited Gaussian noise interference on these systems. We identify key operating parameters and calculate their effects on system performance. These parameters include the received signal powers, frequencies, arrival angles, and bandwidths. The results will be of interest to both the theoretician and the system designer.

We use $P(e)$, the probability of a symbol error at the receiver output, as the measure of system performance. For each combination of desired signal and interference, we calculate the signals at the array

output. We then calculate $P(e)$ of the detector when the array output signals appear at its input. In each case we assume that the system uses the ideal detector for the desired signal in the presence of white Gaussian noise.

Although a high SINR at the array output is generally desirable, we show that $P(e)$ at the detector output cannot generally be determined from the SINR alone. For example, the performance of most digital detectors with Gaussian noise and continuous wave (CW) interference depends on several factors including desired signal power, interference power, noise spectral density, and noise bandwidth. If we hold all but one of these parameters constant and let the remaining parameter vary, then we find that $P(e)$ does vary monotonically with SINR. However, if we allow more than one parameter to vary at a time, we find it impossible to predict $P(e)$ from the SINR alone. In fact, there are many cases where $P(e)$ becomes worse as the SINR increases. Therefore, we use $P(e)$ and not SINR as the measure of performance.

We find that the performance of a communication system that includes an LMS array is strongly dependent upon the bandwidth of the signals at the array input. Generally, we find the system performance improves as the array bandwidth decreases (as long as this bandwidth is large enough to pass the desired signal). However, many systems require an array bandwidth that is several times larger than the data bandwidth of the transmitted bit stream. There are many reasons why this might be the case. First, the spectrum of a signal modulated by any of the classical digital modulation techniques discussed above is not limited to the data bandwidth. Such a signal will be distorted if it is

filtered to occupy a narrow bandwidth. Second, it may be difficult to implement the filters required at the array input to limit the array bandwidth. Third, the system may be required to operate over a wide frequency range to accommodate several signal channels or unknown doppler shifts. Finally, the spectrum of the desired signal may be intentionally spread for data security or to permit the generation of a reference signal [3,4,13]. For these reasons we examine the system performance for several array bandwidths.

We first examine the performance of wideband BPSK, QPSK, DPSK, and FSK systems with CW interference. By wideband we mean that the array bandwidth in Hz is at least ten times as large as the transmitted bit rate in bits/sec. We find that the qualitative performance of the various systems are commensurate with the well-known performance characteristics of their respective modulation techniques. Therefore, for the remainder of the study, we use BPSK modulation with the understanding that similar results would be obtained using other modulation methods.

We examine several array bandwidths using the wideband models. In each case we find that the system performance improves as we reduce the array bandwidth. In order to determine the optimum array bandwidth we develop a narrowband BPSK modulation method. This method allows the desired signal to occupy a channel with a bandwidth equal to the desired signal data rate. We examine the system performance for a wide range of array input bandwidths. Under most interference scenarios, we find the best performance when the array bandwidth is as small as possible (i.e.,

when the array bandwidth is equal to the data bandwidth). However, for weak interference, this general rule does not always hold. We examine the reasons for this anomalous behavior.

In addition to CW interference, we also examine the effects of bandlimited noise interference on the BPSK system performance. We find that the LMS array with a single complex weight behind each element often has difficulty nulling strong broadband interference. This problem is overcome if we use tapped delay line filters to implement the weights [15]. We compare the performance of arrays using both of these weight implementations for various signal powers, bandwidths, and arrival angles.

Chapter II presents a description of the LMS array and the calculations required to predict the signal power levels at the array output. Chapters III through VI describe the performance of the BPSK, QPSK, DPSK, and FSK systems with CW interference. Chapter VII examines the performance of a narrowband BPSK system with CW interference for various input bandwidths. Chapter VIII describes the performance of a BPSK system with broadband interference for both the LMS and the tapped delay line LMS arrays. Finally, Chapter IX contains the conclusions.

CHAPTER II

THE LMS ADAPTIVE ARRAY

A. INTRODUCTION

In this chapter we will describe the basic operating principles of the LMS adaptive array. We present the mathematical models used in later sections to predict array performance.

The discussion of array operation presented in this chapter is abbreviated and is presented mainly to define the notation used in the following chapters. More detailed descriptions of the LMS array and its operation are given in [2] and [15]. The notation used in this section is generally consistent with that used in these references.

B. THE COMPLEX LMS ARRAY

Figure 2.1 shows a block diagram of an N-element adaptive array. The signal from each antenna element is fed through an ideal bandpass filter (BPF), which limits the thermal noise power and rejects out-of-band interference at the array input. We denote the analytic signal at the input to the i^{th} array input by $\tilde{x}_i(t)$. For the N-element array we define the signal vector X which is composed of the array input signals,

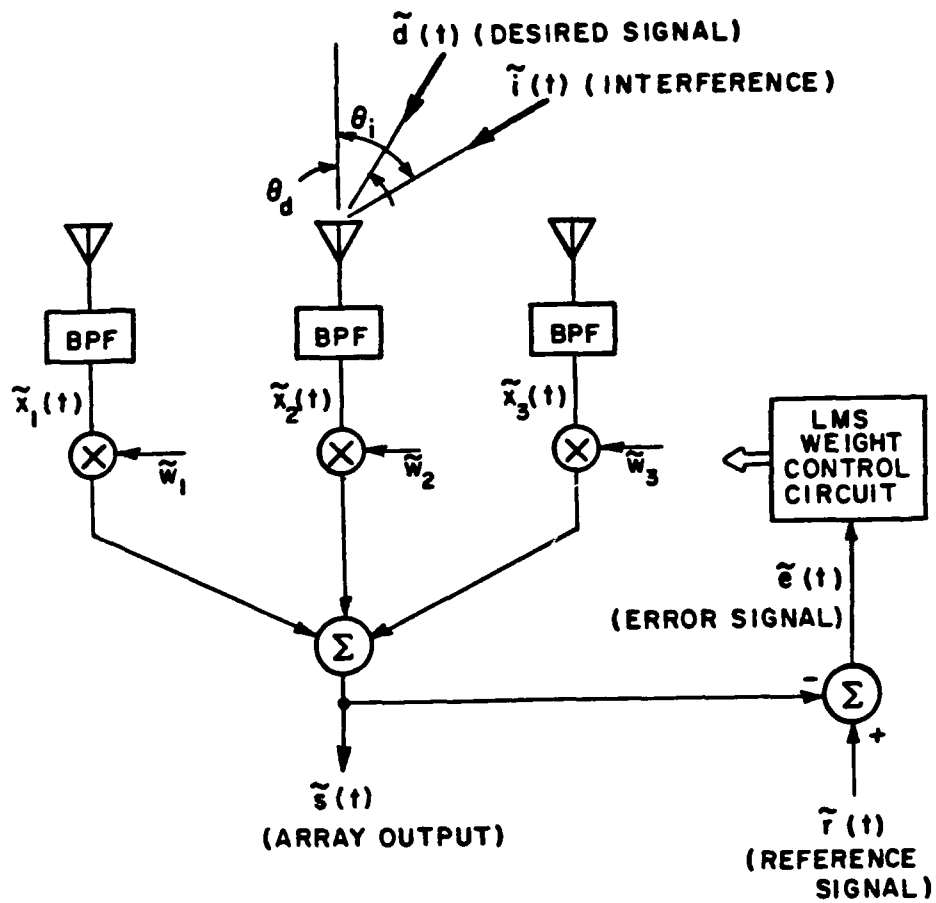


Figure 2.1. The complex LMS array.

$$X = \begin{bmatrix} \tilde{x}_1(t) \\ \tilde{x}_2(t) \\ \vdots \\ \tilde{x}_N(t) \end{bmatrix} . \quad (2.1)$$

Each element signal is multiplied by a complex weight and the weighted signals are summed to produce the array output $\tilde{s}(t)$. We define the complex weight vector,

$$W = \begin{bmatrix} \tilde{w}_1 \\ \tilde{w}_2 \\ \vdots \\ \tilde{w}_N \end{bmatrix} . \quad (2.2)$$

The array output is given by,

$$\tilde{s}(t) = W^T X . \quad (2.3)$$

The array output is subtracted from a reference signal, $\tilde{r}(t)$, to produce an error signal $\tilde{e}(t)$,

$$\tilde{e}(t) = \tilde{r}(t) - \tilde{s}(t) . \quad (2.4)$$

The LMS array adjusts the array weights to minimize the mean square value of this error signal [2]. A suitable reference signal for the array can often be extracted from the signals at the array output. The circuit that derives this reference signal typically uses known

properties of the desired signal (such as spread-spectrum sequence characteristics) to partially separate the desired and undesired components of the array output [3,4,5]. The signal at the circuit output should be well correlated with the desired signal and poorly correlated with the interference. The references cited in Chapter I discuss reference generation techniques for several types of desired signal modulation. In this report we do not address the problem of reference signal generation. We simply assume that the reference signal is a perfect replica of the desired signal at the output of BFP1.

In steady state the LMS weight vector is given by [1],

$$W = \phi^{-1}S , \quad (2.5)$$

where ϕ is the Covariance Matrix,

$$\phi = E[X^*X^T] , \quad (2.6)$$

and S is the reference correlation vector, which is given by,

$$S = E[X^* \tilde{r}(t)] . \quad (2.7)$$

where $E[\bullet]$ denotes the expected value. It can be shown [15] that the steady state weights given by (2.5) produce the maximum attainable Signal-to-Interference-plus-Noise-Ratio (SINR) at the array output.

It is often convenient to separate the desired, interfering, and thermal noise components of the incoming signal vector as,

$$X = X_d + X_i + X_n \quad (2.8)$$

If we assume that the desired, interfering, and thermal noise signals are uncorrelated (and zero mean), then we can separate the three related components of the covariance matrix

$$\begin{aligned}
 \Phi &= E[X^* X^T] \\
 &= E[X_d^* X_d^T] + E[X_i^* X_i^T] + E[X_n^* X_n^T] . \\
 &= \Phi_d + \Phi_i + \Phi_n
 \end{aligned}
 \tag{2.9}$$

where

$$\Phi_d = E[X_d^* X_d^T] ,
 \tag{2.10}$$

$$\Phi_i = E[X_i^* X_i^T] ,
 \tag{2.11}$$

and

$$\Phi_n = E[X_n^* X_n^T] .
 \tag{2.12}$$

Thus we have divided the covariance matrix into a sum of three separate matrices, each involving only one signal. This step simplifies subsequent derivations.

We assume in the derivations below that we have a three element linear array with one half wavelength spacing between elements. Figure 2.1 shows the array geometry. Of course, we can extend our results to cases where the array has more than three elements; however, the three element array calculations suitably illustrate the system operating principles and performance.

We assume in the derivations below that we have a 3-element linear array with one-half wavelength element spacing as shown in Figure 2.1.

A 3-element array has two degrees of freedom. The array can therefore steer a null on the interference and simultaneously maximize the desired signal response.*

We assume that the desired signal is incident from an angle of θ_d (measured from the broadside direction) and a single interfering signal is incident from an angle of θ_i .

The interelement time delay between the signals on adjacent elements are given by

$$T_d = (L/c)\sin\theta_d \quad (2.13)$$

and,

$$T_i = (L/c)\sin\theta_i \quad (2.14)$$

for the desired signal and interference respectively, where c is the propagation velocity and L is the element spacing. The interelement phase shifts for the desired and interfering signals are given by,

$$\phi_d = \pi\sin(\theta_d) \quad (2.15)$$

and,

$$\phi_i = \pi(\omega_i/\omega_d)\sin(\theta_i) \quad (2.16)$$

respectively, where ω_d & ω_i are the desired signal and interference frequencies. Slight variations in ω_i about ω_d have little effect on

*There are limits to the resolution capabilities of the 3-element array. We shall find in later chapters that the array cannot keep the desired signal at a pattern maximum when a very strong interfering signal is spatially close to the desired signal.

most performance calculations. From Equation (2.16) we see that a small change in ω_i produces a corresponding change in ϕ_i . Similarly a small change in θ_i has the same effect. Therefore, the change in the array performance caused by variations in ω_i are identical to those caused by a corresponding variation in θ_i . If these variations are small, then the array performance is negligibly affected. In the following chapters we usually assume that $\phi_i = \pi \sin \theta_i$. This assumption will allow us to calculate the system performance without specifying the operating frequency.

We denote the analytic signal representation of the desired, and interfering signals as received by element 1 by $\tilde{d}(t)$ and $\tilde{i}(t)$ respectively. We define the complex autocorrelation function (ACF) for the desired and interfering signals as,

$$R_{\tilde{d}}(\tau) = E[\tilde{d}^*(t)\tilde{d}(t+\tau)] \quad (2.17)$$

and,

$$R_{\tilde{i}}(\tau) = E[\tilde{i}^*(t)\tilde{i}(t+\tau)] . \quad (2.18)$$

We assume that white Gaussian noise is present at the input of each of the element BPF's. We assume that the noise signals at the various BPF outputs are mutually statistically independent. We denote these signals by $\tilde{n}_1(t)$, $\tilde{n}_2(t)$ and $\tilde{n}_3(t)$ with,

$$E[\tilde{n}_i(t)\tilde{n}_j(t)] = \sigma^2 \delta_{ij} , \quad (2.19)$$

where δ_{ij} is the Kronecker delta.

We now can write the desired signal, interference signal, and noise covariance matrices for the three-element array,

$$\Phi_d = \begin{bmatrix} \tilde{R}_d(0) & \tilde{R}_d(-T_d) & \tilde{R}_d(-2T_d) \\ \tilde{R}_d(T_d) & \tilde{R}_d(0) & \tilde{R}_d(-T_d) \\ \tilde{R}_d(2T_d) & \tilde{R}_d(T_d) & \tilde{R}_d(0) \end{bmatrix} \quad (2.20)$$

$$\Phi_i = \begin{bmatrix} \tilde{R}_i(0) & \tilde{R}_i(-T_i) & \tilde{R}_i(-2T_i) \\ \tilde{R}_i(T_i) & \tilde{R}_i(0) & \tilde{R}_i(-T_i) \\ \tilde{R}_i(2T_i) & \tilde{R}_i(T_i) & \tilde{R}_i(0) \end{bmatrix} \quad (2.21)$$

and,

$$\Phi_n = \sigma^2 I, \quad (2.22)$$

where I is the identity matrix.

The covariance matrix Φ can now be determined from (2.9), and (2.20) through (2.22).

We assume the reference signal for the array is of the form,

$$\tilde{r}(t) = R \tilde{d}(t) \quad (2.23)$$

We note that the SINR at the array output is independent of the magnitude of R (for non-zero R). An increase or decrease in R produces a proportionate increase or decrease in the level of each signal at the array output. We are therefore free to arbitrarily set R without affecting the relative values of the signals at the array output. Typically a reference generation system generates a reference signal which is highly correlated with the desired signal and has fixed

amplitude. We can model such a fixed-amplitude signal by letting

$R = 1/\sqrt{(P_d)_{in}}$ where $(P_d)_{in}$ is the power of the desired signal.

With the reference signal of the form given by (2.23) the reference correlation vector is given by,

$$\begin{aligned} S &= E[X^* \tilde{r}(t)] \\ &= R E[X^* \tilde{d}(t)] . \end{aligned} \quad (2.24)$$

Since $\tilde{d}(t)$, $\tilde{i}(t)$, and the noise signals are uncorrelated we can expand (2.24) into,

$$\begin{aligned} S &= R E[(X_d^* + X_i^* + X_n^*) \tilde{d}(t)] \\ &= R E[X_d^* \tilde{d}(t)] . \end{aligned} \quad (2.25)$$

Thus, for our three element array

$$S = R \begin{bmatrix} R_d(0) \\ R_d(T_d) \\ R_d(2T_d) \end{bmatrix} . \quad (2.26)$$

The complex weight vector is then determined from (2.5), (2.9), and (2.25).

We can now determine the desired, interfering and noise signals at the array output. From (2.3) and (2.8) we write the array output signal $\tilde{s}(t)$ as,

$$\tilde{s}(t) = s_d(t) + s_i(t) + s_n(t) \quad (2.27)$$

where,

$$S_d^{\sim}(t) = \sum_{j=1}^3 w_j \tilde{d}[t-(j-1)T_d] \quad (2.28)$$

$$S_i^{\sim}(t) = \sum_{j=1}^3 w_j \tilde{i}[t-(j-1)T_i] \quad (2.29)$$

and,

$$S_n^{\sim}(t) = w_1 \tilde{n}_1(t) + w_2 \tilde{n}_2(t) + w_3 \tilde{n}_3(t) . \quad (2.30)$$

The power of the desired signal at the array output is given by,

$$\begin{aligned} P_d^{\sim} &= 1/2 R_d^{\sim}(0) \\ &= 1/2 E\{[s_d^{\sim}(t)][s_d^{\sim}(t)]^*\} . \end{aligned} \quad (2.31)$$

From (2.28) and (2.31), we have

$$P_d = 1/2 \sum_{j=1}^3 \sum_{k=1}^3 w_j w_k^* R_d^{\sim}[(j-k)T_d] \quad (2.32)$$

Similarly we have,

$$P_i = 1/2 \sum_{j=1}^3 \sum_{k=1}^3 w_j w_k^* R_i^{\sim}[(j-k)T_i] \quad (2.33)$$

and,

$$P_n = 1/2 \sum_{j=1}^3 |w_j|^2 \sigma^2 . \quad (2.34)$$

The SINR at the array output is given by,

$$\text{SINR} = \frac{P_d}{P_i + P_n} \quad (2.35)$$

In many of the previous adaptive array studies, the SINR at the array output was used as a figure of merit. In the following sections we examine several different types of digital communication systems and determine their performance using the probability of error as a figure of merit. We show that, although SINR is often useful, it does not always give sufficient information to accurately predict the system performance.

CHAPTER III
PERFORMANCE OF A BPSK SYSTEM WITH CW JAMMING

A. INTRODUCTION

In this chapter we examine the performance of a BPSK communication system that includes an LMS array to suppress CW interference. Figure 3.1(a) shows a typical BPSK signal waveform. A "1" symbol is represented by a sinusoidal waveform of duration T seconds. A "0" symbol is represented by a similar sinusoid waveform which is 180° out of phase with the "1" waveform. The receiver estimates the phase of the received signal at the end of each symbol interval and decides whether a "1" or "0" was sent during the interval.

The model we develop in this chapter assumes that the bandwidths of the BPFs at the element inputs are several times larger than the data bandwidth of the transmitted bit stream. There are several reasons why this assumption accurately models many real systems. First, the spectrum of a BPSK signal is not limited to the data bandwidth. Such a signal will be distorted if it is filtered to occupy a narrow bandwidth. Second, it may be difficult to implement the filters required at the array input to limit the array bandwidth. Third, the system may be required to operate over a wide frequency range to accommodate several signal channels or unknown doppler shifts. Finally, the spectrum of the desired signal may be intentionally spread for data security [16] or to

permit the generation of a reference signal. In the last case the spectrum may be spread by either direct-sequence spreading [3,4] or frequency hopping [14]. We defer consideration of more narrowband systems (those with input bandwidths that are approximately equal to the data bandwidth) until Chapter VII.

In Section B we examine the performance of the LMS array with the desired and interfering signals as described above. In Section C we calculate $P(e)$ for the ideal BPSK detector when the desired signal is corrupted by both CW interference and Gaussian noise. In Section D we determine the performance of the combined LMS array and BPSK detector. We determine how this performance depends on the received signal power levels, frequencies, and the bit duration.

B. ARRAY PERFORMANCE

During the n^{th} symbol interval the BPSK desired signal at the output of BPF1 is given by,

$$\tilde{d}(t) = A_d \exp\{j[\omega_d t + \phi_n(t) + \psi_d]\} \quad (n-1)T < t < nT \quad (3.1)$$

where

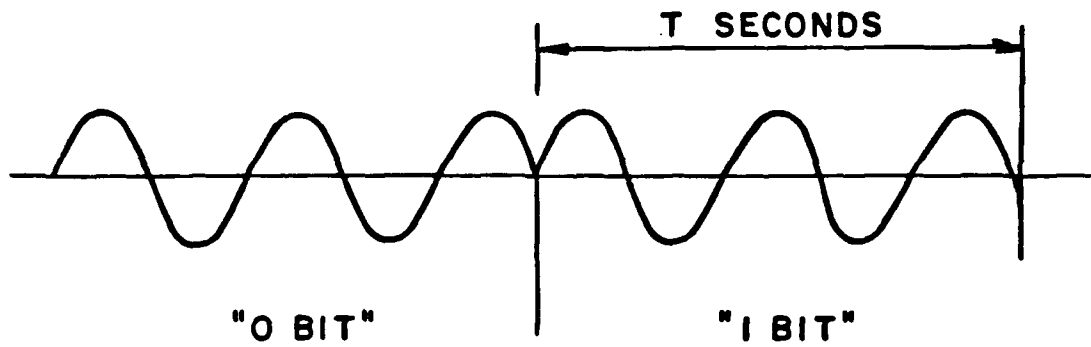
A_d = the desired signal amplitude at the array input,

ω_d = the desired signal carrier frequency,

ψ_d = a random phase angle uniformly distributed on $[0, 2\pi]$
(We denote this by saying U_d is $U[0, 2\pi]$.)

$\phi_n(t)$ = the data modulation during the n^{th} symbol interval where,

$$\phi_n(t) = \begin{cases} 0 & \text{with prob. } 1/2 \text{ (during "0" symbols)} \\ \pi & \text{with prob. } 1/2 \text{ (during "1" symbols)}. \end{cases}$$



(a) BPSK waveform.



(b) BPSK PSD.

Figure 3.1. BPSK signal and spectrum.

and T is the symbol duration.

We assume that the symbol stream is stationary. The complex autocorrelation function for the desired signal is given by,

$$\begin{aligned} R_{\tilde{d}}(\tau) &= E[\tilde{d}^*(\tau)\tilde{d}(t+\tau)] \\ &= \begin{cases} A_d^2 [1 - |\tau|/T] \exp[j\omega_d \tau] & |\tau| < T \\ 0 & |\tau| > 0. \end{cases} \end{aligned} \quad (3.2)$$

The Power Spectral Density (PSD) of the desired signal is shown in Figure 3.1(b).

$\tilde{i}(t)$, the CW interfering signal, is given by,

$$\tilde{i}(t) = A_i \exp[j\omega_i t + \psi_i] \quad (3.3)$$

where,

A_i = the interference amplitude,

ψ_i = the interference phase. ψ_i is $U[0, 2\pi]$ and independent of ψ_d .

and,

ω_i = the interference frequency.

The complex autocorrelation function of this signal is given by,

$$\begin{aligned} R_{\tilde{i}}(\tau) &= E[\tilde{i}^*(t)\tilde{i}(t+\tau)] \\ &= A_i^2 \exp[j\omega_i \tau]. \end{aligned} \quad (3.4)$$

We assume an independent thermal noise component with power σ^2 is present in each element signal. We therefore have

$$E[\tilde{n}_i^*(t)\tilde{n}_j(t)] = \sigma^2 \delta_{ij} . \quad (3.5)$$

We now calculate the array weights and the power levels of the various signals at the array output. Since $\tilde{d}(t)$, $\tilde{i}(t)$ and the thermal noise are uncorrelated we can determine the covariance matrix by summing its three components,

$$\Phi_d = A_d^2 \begin{bmatrix} 1 & (1-\frac{|T_d|}{T})e^{-j\phi_d} & (1-\frac{|2T_d|}{T})e^{-j2\phi_d} \\ (1-\frac{|T_d|}{T})e^{j\phi_d} & 1 & (1-\frac{|T_d|}{T})e^{-j\phi_d} \\ (1-\frac{|2T_d|}{T})e^{j2\phi_d} & (1-\frac{|T_d|}{T})e^{j\phi_d} & 1 \end{bmatrix} \quad (3.6)$$

$$\Phi_i = A_i^2 \begin{bmatrix} 1 & e^{-j\phi_i} & e^{-j2\phi_i} \\ e^{j\phi_i} & 1 & e^{-j\phi_i} \\ e^{j2\phi_i} & e^{j\phi_i} & 1 \end{bmatrix} \quad (3.7)$$

and,

$$\Phi_n = \sigma^2 I \quad (3.8)$$

where I is the identity matrix and it is assumed that $|2T_d| < T$.

We make the simplifying assumption that the symbol period is very long compared with the interelement time delay. This assumption is reasonable since the elements are one-half wavelength apart. Thus only a fraction of an RF carrier cycle occurs during a time interval of duration T_d . Many such cycles occur, however, during each bit interval of length T . With this assumption we can calculate the array performance without specifying the operating frequency or symbol rate. The desired signal covariance matrix becomes

$$\mathbf{\Sigma}_d \approx A_d^2 \begin{bmatrix} 1 & e^{-j\phi_d} & e^{-j2\phi_d} \\ e^{j\phi_d} & 1 & e^{-j\phi_d} \\ e^{j2\phi_d} & e^{j\phi_d} & 1 \end{bmatrix}. \quad (3.9)$$

The total covariance matrix then becomes,

$$\Phi = \Phi_d + \Phi_i + \Phi_n$$

$$= \begin{bmatrix} A_d^2 + A_i^2 + \sigma^2 & A_d^2 e^{-j\phi_d} + A_i^2 e^{-j\phi_i} & A_d^2 e^{-j2\phi_d} + A_i^2 e^{-j2\phi_i} \\ A_d^2 e^{j\phi_d} + A_i^2 e^{j\phi_i} & A_d^2 + A_i^2 + \sigma^2 & A_d^2 e^{-j\phi_d} + A_i^2 e^{-j\phi_i} \\ A_d^2 e^{j2\phi_d} + A_i^2 e^{j2\phi_i} & A_d^2 e^{j\phi_d} + A_i^2 e^{j\phi_i} & A_d^2 + A_i^2 + \sigma^2 \end{bmatrix} \quad (3.10)$$

The reference correlation vector (2.26) is given by,

$$S = A_d \begin{bmatrix} 1 \\ \exp[j\phi_d] \\ \exp[j2\phi_d] \end{bmatrix} \quad (3.11)$$

We can now calculate the weight vector from (2.5) and P_d , P_i , and P_n from (2.32), (2.33) and (2.34).

In the next section we derive the performance of the ideal BPSK detector when the desired signal is corrupted by thermal noise and CW interference. In order to determine the detector performance we must know the composite signal at the detector input. To determine this signal we switch to the real representation of the signals at the array output.

At the array output the desired signal is a BPSK signal with power P_d . This (real) signal during the n^{th} bit interval is given by,

$$s_d(t) = \sqrt{2P_d} \cos[\omega_d t + \phi_n(t) + \gamma_d], \quad (3.12)$$

where P_d , ω_d , and $\phi_n(t)$ are as defined above and γ_d is the desired signal phase angle at the array output. Since the covariance matrix and the reference correlation vector are both independent of ψ_d (the phase angle of the desired signal at the array input), the steady state weights are also independent of ψ_d . Therefore, γ_d is given by $(\gamma_d)_0 + \psi_d$ where $(\gamma_d)_0$ is some fixed phase angle. Thus, since ψ_d is $U[0, 2\pi]$, the (modulo- 2π) value of γ_d is also $U[0, 2\pi]$. This is a property of the modulo- M sum of two variables, one of which is $U[0, M]$. This property is proven in [17] by Scire.

We now determine the amplitude and phase of the CW interfering signal at the array output. This signal, which has power P_i , is given by,

$$s_i(t) = \sqrt{2P_i} \cos[\omega_i(t) + \gamma_i] , \quad (3.13)$$

where γ_i is the phase angle of the interference at the array output. We can show that γ_i is $U[0, 2\pi]$ using arguments analogous to those used above to show that γ_d is $U[0, 2\pi]$.

Finally, the noise signal at the array output is a zero-mean Gaussian random process, $s_n(t)$, with variance P_n . This noise is bandlimited Gaussian noise with a flat PSD in the passband of the ideal BPFs at the element inputs. The value of the two-sided PSD in this passband, which we denote by $n/2$ is given by,

$$n/2 = \frac{N_0}{4} \sum_{m=1}^3 |w_m|^2 \quad (3.14)$$

where $N_0/2$ is the two-sided thermal noise PSD at the element inputs. The PSD of the noise signal at the array output is shown in Figure 3.2(a).

C. BPSK DETECTOR PERFORMANCE WITH CW AND NOISE INTERFERENCE

In this section we derive the performance of an ideal BPSK detector when the BPSK desired signal is corrupted by additive white Gaussian noise (AWGN) and CW interference. Rosenbaum [18] and Prabhu [19] have examined similar problems; however, these early works were typically rather vague in their description of the "ideal" receiver. The receiver

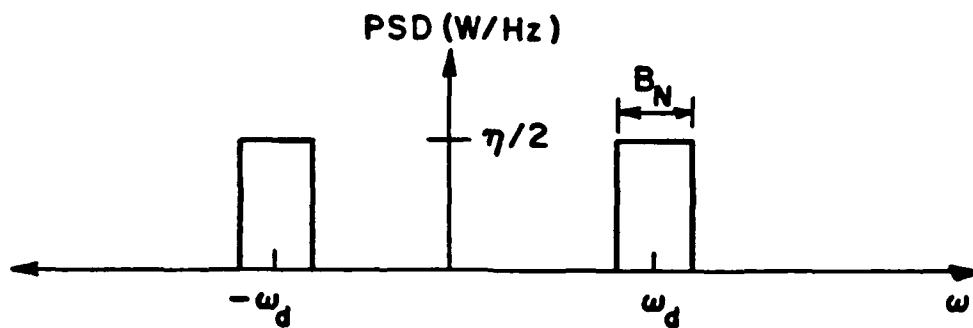
model in these papers assumes that, in addition to a desired and interfering signals, there is Gaussian noise with power σ^2 at the detector input. However, the importance of the noise PSD and the signal energy-per-bit are generally not discussed in detail. The dependence of performance on the frequency of the interfering signal is also not discussed.

To thoroughly understand the effects of the various signal energies, the noise PSD, and the interference frequency on the detector performance we shall carefully derive $P(e)$ of the ideal BPSK detector. The BPSK detector shown in Figure 3.3 is ideal if the only undesired signal is additive white Gaussian noise (AWGN) [20]. The incoming signal, $s(t)$, is multiplied by $\cos(\omega_d t + \gamma_d)$. The output of the multiplier is integrated over the bit interval and a bit decision is made based upon the sign of the integrator output at the end of the bit interval. A positive output indicates a "0" bit and a negative output indicates a "1" bit.

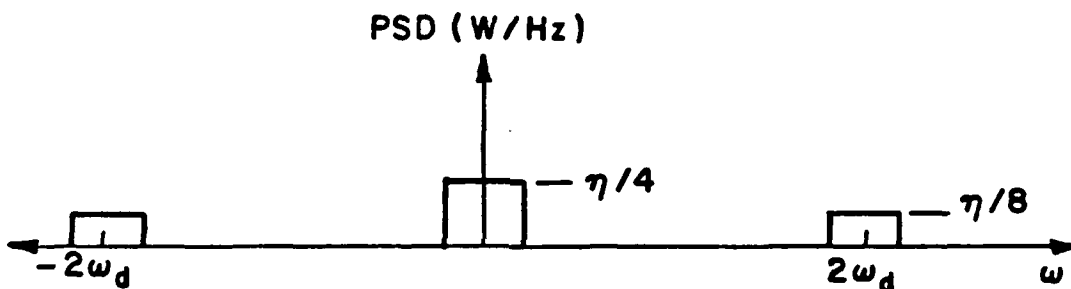
Note that this ideal detector requires a coherent reference signal to operate. A method for deriving such a signal from the received signal is discussed in [3]. We assume that a suitable reference signal is available and that this signal is free of amplitude and phase noise.

Summarizing the results of the previous sections, the composite signal at the detector input is

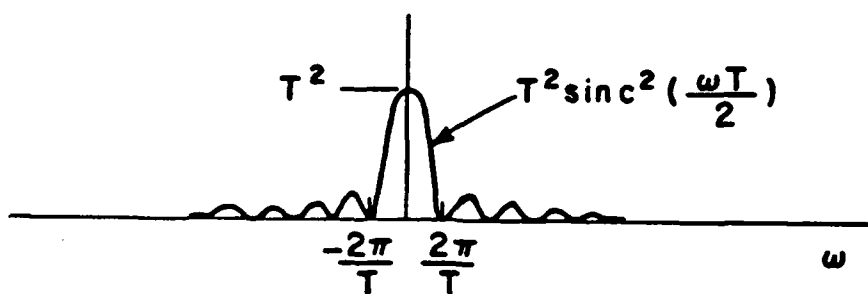
$$s(t) = s_d(t) + s_i(t) + s_n(t) \quad (3.15)$$



(a) Noise spectrum at detector input.



(b) Noise spectrum at integrator input.



(c) $|H(\omega)|^2$ for ideal integrator.

Figure 3.2. Noise spectrum and transfer function for ideal integrator.

where $s_d(t)$ and $s_i(t)$ are given by (3.12) and (3.13), and $s_n(t)$ is a narrowband Gaussian random process which has a flat (two-sided) PSD with magnitude $n/2$ in the passband.

The signal at the input to the integrator is given by

$$s(t)\cos(\omega_d t + \gamma_d) = [s_d(t) + s_i(t) + s_n(t)] \cos(\omega_d t + \gamma_d) \quad (3.16)$$

We can substitute $s_d(t)$ and $s_i(t)$ into this expression and integrate between $(n-1)T$ and nT to determine the signal at the integrator output at the end of the bit interval

$$S(n) = X_d(n) + X_i(n) + X_n(n) \quad (3.17)$$

where,

$$X_d(n) = \int_{(n-1)T}^{nT} \sqrt{2P_d} \cos[\omega_d t + \phi_n(t) + \gamma_d] \cos[\omega_d t + \gamma_d] dt \quad (3.18)$$

$$X_i(n) = \int_{(n-1)T}^{nT} \sqrt{2P_i} \cos[\omega_i t + \gamma_i] \cos[\omega_d t + \gamma_d] dt \quad (3.19)$$

and,

$$X_n(n) = \int_{(n-1)T}^{nT} s_n(t) \cos[\omega_d t + \gamma_d] dt \quad (3.20)$$

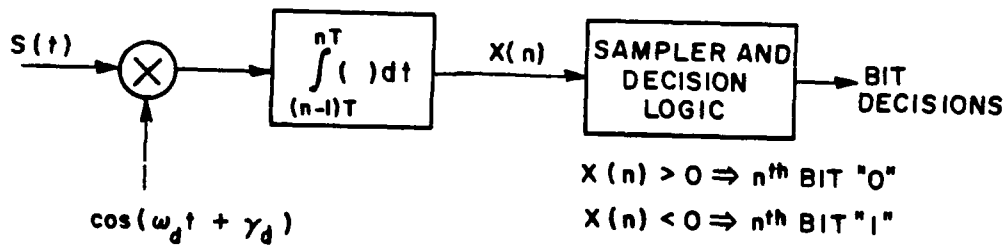


Figure 3.3. The ideal BPSK detector.

We now evaluate $X_d(n)$, $X_i(n)$ and $X_n(n)^*$ and then combine the results to determine $X(n)$. Application of a standard trigonometric identity to the integrand in Equation (3.18) yields,

$$X_d(n) = \sqrt{P_d/2} \int_{(n-1)T}^{nT} \cos[2\omega_d t + \phi_n(t) + 2\gamma_d] + \cos[\phi_n(t)] dt \quad (3.21)$$

* Note that $X_d(n)$, $X_i(n)$ and $X_n(n)$ are not the signal vectors X_d , X_i and X_n defined in Chapter 2. Although the similar notation might be somewhat confusing at first, the intended variable should be clear from the context.

We ignore the double frequency term since its contribution to the value of the integral is negligible due to our assumption that many carrier cycles occur during each bit interval. Therefore, we have,

$$\begin{aligned} X_d(n) &= \sqrt{P_d/2} \int_{(n-1)T}^{nT} \cos[\phi_n(t)] dt \\ &= \sqrt{(P_d/2)T} \cos[\phi_n(t)] , \end{aligned} \quad (3.22)$$

since $\phi_n(t)$ is constant during the bit interval.

We now calculate $X_i(n)$. We first expand the integrand in Equation (3.19),

$$\begin{aligned} X_i(n) &= \sqrt{P_i/2} \int_{(n-1)T}^{nT} \{ \cos[(\omega_d + \omega_i)t + \gamma_d + \gamma_i] \\ &\quad + \cos[(\omega_d - \omega_i)t + \gamma_d - \gamma_i] \} dt . \end{aligned} \quad (3.23)$$

We let

$$\gamma_{rel} = \gamma_d - \gamma_i , \quad (3.24)$$

and,

$$\Delta\omega = \omega_d - \omega_i . \quad (3.25)$$

Substitution of these new variables into (3.23) yields,

$$X_i(n) = \sqrt{P_i/2} \int_{(n-1)T}^{nT} \cos(\Delta\omega t + \gamma_{rel}) dt. \quad (3.26)$$

after we drop the second harmonic terms. We evaluate the integral to give us,

$$X_i(n) = \sqrt{P_i/2} \frac{1}{\Delta\omega} [\sin(n\Delta\omega T + \gamma_{rel}) - \sin((n-1)\Delta\omega T + \gamma_{rel})] \quad (3.27)$$

Simplification of this expression with standard trigonometric identities yields,

$$X_i(n) = \sqrt{P_i/2T} \operatorname{sinc}\left(\frac{\Delta\omega T}{2}\right) \cos\left(\gamma_{rel} + \frac{2n-1}{2} \Delta\omega T\right), \quad (3.28)$$

where the sinc function is given by,

$$\operatorname{sinc}(x) = [\sin(x)]/x, \quad (3.29)$$

with

$$\operatorname{sinc}(0) = 1. \quad (3.30)$$

From (3.28) we see that, for a given interference power level, the amplitude of the interference at the integrator output is directly proportional to $\operatorname{sinc}(\Delta\omega T/2)$. At the points where the sinc function is zero (i.e. for $\Delta\omega T/2 = n\pi$) the interference does not disrupt the

detector. At these values of $\Delta\omega T$, the baseband interference product at the multiplier output is a sinusoid with an integral number of cycles occurring during the integration period. Therefore the contribution of the interference to the integrator output is zero. The third integral, $\chi_n(n)$, is the integral of the product $s_n(t)\cos(\omega_d t + \gamma_d)$. $\chi_n(n)$ is most easily evaluated in the frequency domain. If the input noise signal has the PSD shown in Figure 3.2(a) then the signal at the integrator input has the PSD $N(\omega)$ shown in Figure 3.2(b).

In the frequency domain the integrator is equivalent to a linear filter with a transfer function of

$$H(\omega) = \frac{1 - \exp(j\omega T)}{j\omega} \quad (3.31)$$

At the end of the integration period the noise produces an additive Gaussian random variable at the integrator output. This zero mean random variable has a variance N' , which is given by,

$$\begin{aligned} N' &= \left(\frac{1}{2\pi}\right) \int_{-\infty}^{\infty} N(\omega) |H(\omega)|^2 d\omega \\ &= \left(\frac{1}{2\pi}\right) T^2 \int_{-\infty}^{\infty} N(\omega) \text{sinc}^2\left(\frac{\omega T}{2}\right) d\omega. \end{aligned} \quad (3.32)$$

We can make some simplifying assumptions which make evaluation of (3.32) more straightforward with only negligible effects on the results. In Figure 3.2(c) we show $\text{sinc}^2\left(\frac{\omega T}{2}\right)$. The integrand in (3.32) is the

product of the two curves shown in Figure 3.2(b) and 3.2(c). From these figures it is apparent that the contribution of $N(\omega)\text{sinc}^2\left(\frac{\omega T}{2}\right)$ to the value of the integral quickly diminishes as ω becomes large (due to the fast roll-off of the sinc^2 term). Since we have assumed that the input BPFs are much larger than the data bandwidth of the desired signal, we can make the approximation that the noise at the integrator input is white, with PSD $\frac{n}{4}$ at all frequencies. With this approximation we can easily evaluate (3.32)

$$N' = \left(\frac{1}{2\pi}\right)^2 T^2 \left(\frac{n}{4}\right) \int_{-\infty}^{\infty} \text{sinc}^2\left(\frac{\omega T}{2}\right) d\omega. \quad (3.33)$$

If we now make the substitution,

$$x = \frac{\omega T}{2}, \quad (3.34)$$

then (3.33) becomes,

$$N' = \left(\frac{1}{\pi}\right)\left(\frac{n}{4}\right)T \int_{-\infty}^{\infty} \text{sinc}^2(x) dx. \quad (3.35)$$

The integral in (3.35) is found to be equal to π using Parseval's theorem [21]. Thus N' , the variance of the noise random variable at the integrator output, is given by

$$N' = Tn/4. \quad (3.36)$$

The error in N' due to our assumption that the noise at the detector input is white is less than 2% if the actual noise bandwidth at this input is greater than approximately $10/T$ Hz. The effects of noise bandwidth are discussed further in the next section.

We now combine (3.22), (3.28), and (3.36) to form the expression for the composite random variable at the integrator output at the sampling instant. This random variable, $X(n)$, is given by,

$$X(n) = \sqrt{(P_d/2)}T \cos[\phi_n(t)] + \sqrt{(P_i/2)}T \text{sinc}(\Delta\omega T/2) \cos(\gamma_{rel} + \frac{2n-1}{2} \Delta\omega T) + X_n(n), \quad (3.37)$$

where $\phi_n(t)$ is either 0 or π depending on the data bit and $X_n(n)$ is normally distributed with zero mean and variance $nT/4$.

We now can determine the probability of error for the ideal BPSK receiver. If both bits are equally likely the conditional probability of error given γ_{rel} is given by,

$$P(e|\gamma_{rel}) = 0.5P(e|\gamma_{rel}, \text{"0" sent}) + 0.5P(e|\gamma_{rel}, \text{"1" sent}) \\ = 0.5P\{X(n) < 0 | \gamma_{rel}, \phi_n(t)=0\} + 0.5P\{X(n) > 0 | \gamma_{rel}, \phi_n(t)=\pi\}$$

$$P(e|\gamma_{rel}) = 0.5P\{\sqrt{(P_d/2)}T + \sqrt{(P_i/2)}T \text{sinc}(\Delta\omega T/2) \cos(\gamma_{rel} + \frac{2n-1}{2} \Delta\omega T) + X_n(n) < 0\} \\ + 0.5P\{-\sqrt{(P_d/2)}T + \sqrt{(P_i/2)}T \text{sinc}(\Delta\omega T/2) \cos(\gamma_{rel} + \frac{2n-1}{2} \Delta\omega T) + X_n(n) > 0\}.$$

$$P(e|\gamma_{rel}) = 0.5P\{X_n(n) < -\sqrt{(P_d/2)}T - \sqrt{(P_i/2)}T \text{sinc}(\Delta\omega T/2) \cos(\gamma_{rel} + \frac{2n-1}{2} \Delta\omega T)\} \\ + 0.5P\{X_n(n) > \sqrt{(P_d/2)}T - \sqrt{(P_i/2)}T \text{sinc}(\Delta\omega T/2) \cos(\gamma_{rel} + \frac{2n-1}{2} \Delta\omega T)\}$$

$$\begin{aligned}
P(e|\gamma_{rel}) = & 0.5 \operatorname{erfc} \left[\sqrt{\frac{2P_d T}{n}} - \sqrt{\frac{2P_i T}{n}} \operatorname{sinc}\left(\frac{\Delta\omega T}{2}\right) \cos\left(\gamma_{rel} + \frac{2n-1}{2}\Delta\omega T\right) \right] \\
& + 0.5 \operatorname{erfc} \left[\sqrt{\frac{2P_d T}{n}} + \sqrt{\frac{2P_i T}{n}} \operatorname{sinc}(\Delta\omega T) \cos\left(\gamma_{rel} + \frac{2n-1}{2}\Delta\omega T\right) \right]
\end{aligned} \tag{3.38}$$

where erfc is the complementary error function defined by,

$$\operatorname{erfc}(x) = \sqrt{\frac{1}{2\pi}} \int_x^\infty \exp(-z^2/2) dz. \tag{3.39}$$

We now define the desired signal and interference energy-per-bit-interval by,

$$E_d = P_d T, \tag{3.40}$$

and

$$E_i = P_i T, \tag{3.41}$$

respectively. Equation (3.38) can then be rewritten as,

$$\begin{aligned}
P(e|\gamma_{rel}) = & 0.5 \operatorname{erfc} \left[\sqrt{(2E_d/n)} \right. \\
& \left. - \sqrt{2E_i/n} \operatorname{sinc} \left[\frac{\Delta\omega T}{2} \right] \cos \left[\gamma_{rel} + \frac{2n-1}{2} \Delta\omega T \right] \right] \\
& + 0.5 \operatorname{erfc} \left[\sqrt{(2E_d/n)} \right. \\
& \left. + \sqrt{\frac{2E_i}{n}} \operatorname{sinc}(\Delta\omega T/2) \cos \left[\gamma_{rel} + \frac{2n-1}{2} \Delta\omega T \right] \right]. \tag{3.42}
\end{aligned}$$

Since γ_{rel} is uniformly distributed on $[0, 2\pi]$ (due to (3.24) and the theorem proven by Scire in [17]) we can determine the probability of error by evaluating

$$P(e) = \left[\frac{1}{2\pi} \right] \int_0^{2\pi} P(e|\gamma_{rel}) d\gamma_{rel} \quad (3.43)$$

where $P(e|\gamma_{rel})$ is given by (3.42) above.

Several simplifications can be made before evaluating (3.43). Since the integrand, $P(e|\gamma_{rel})$, is periodic in γ_{rel} with period 2π and the integral is over a full period of γ_{rel} , both of the two error functions which compose the integrand contribute equally to the value of the integral. The fact that the integration is over a whole period of γ_{rel} allows us to remove the factor of $\Delta\omega T/2$ from the argument of the cosine in the integrand without affecting the result. With the above simplifications and (3.42) and (3.43), the expression for $P(e)$ becomes,

$$P(e) = \left(\frac{1}{2\pi} \right) \int_0^{2\pi} \text{erfc} \left\{ \sqrt{\frac{2E_d}{n}} + \sqrt{\frac{2E_i}{n}} \text{sinc} \left(\frac{\Delta\omega T}{2} \cos(\gamma_{rel}) \right) \right\} d\gamma_{rel} \cdot \quad (3.44)$$

We define the signal energy-to-noise density ratio at the detector input by

$$\text{SNR} = E_d/n, \quad (3.45)$$

and similarly define the INR at the detector input by

$$\text{INR} = E_i/n. \quad (3.46)$$

These definitions can be used together with (3.44) to calculate $P(e)$ for various values of SNR and INR by numerically evaluating the required integral.

Figure 3.4 contains several curves which illustrate the detector performance when the interference frequency offset is zero (i.e. $\Delta\omega T=0$). Each curve is a plot of $P(e)$ vs. SNR for a fixed value of signal-to-interference ratio, SIR ($SIR=E_d/E_i$)^{*}. Note that, although this figure is very similar to that shown by Rosenbaum [10], the approach taken in the derivation is different here as discussed previously. From this figure we see that, for a fixed SIR, $P(e)$ decreases as SNR increases. Similarly, for a fixed SNR value, $P(e)$ increases as SIR decreases. We find very poor performance for SIR values of 0 dB and less.

Figure 3.5 shows the same data which are plotted in Figure 3.4; however, in Figure 3.5 the parameterization has been changed. In Figure 3.5 $P(e)$ is plotted vs. INR for several fixed values of SNR. Although Figures 3.4 and 3.5 show the same data, one or the other is often more useful when trying to understand a particular facet of the system performance. In the remainder of this report we shall often present results in similar pairs of plots, one showing $P(e)$ vs. SNR (for several fixed SIRs) and one showing $P(e)$ vs. INR (for several fixed SNRs).

*The value of SIR is constant for each curve in Figure 3.4. Therefore, it is assumed that, as we move along a curve by varying the SNR, the interference power simultaneously varies in order to keep the SIR fixed.

P (E) VS. SNR

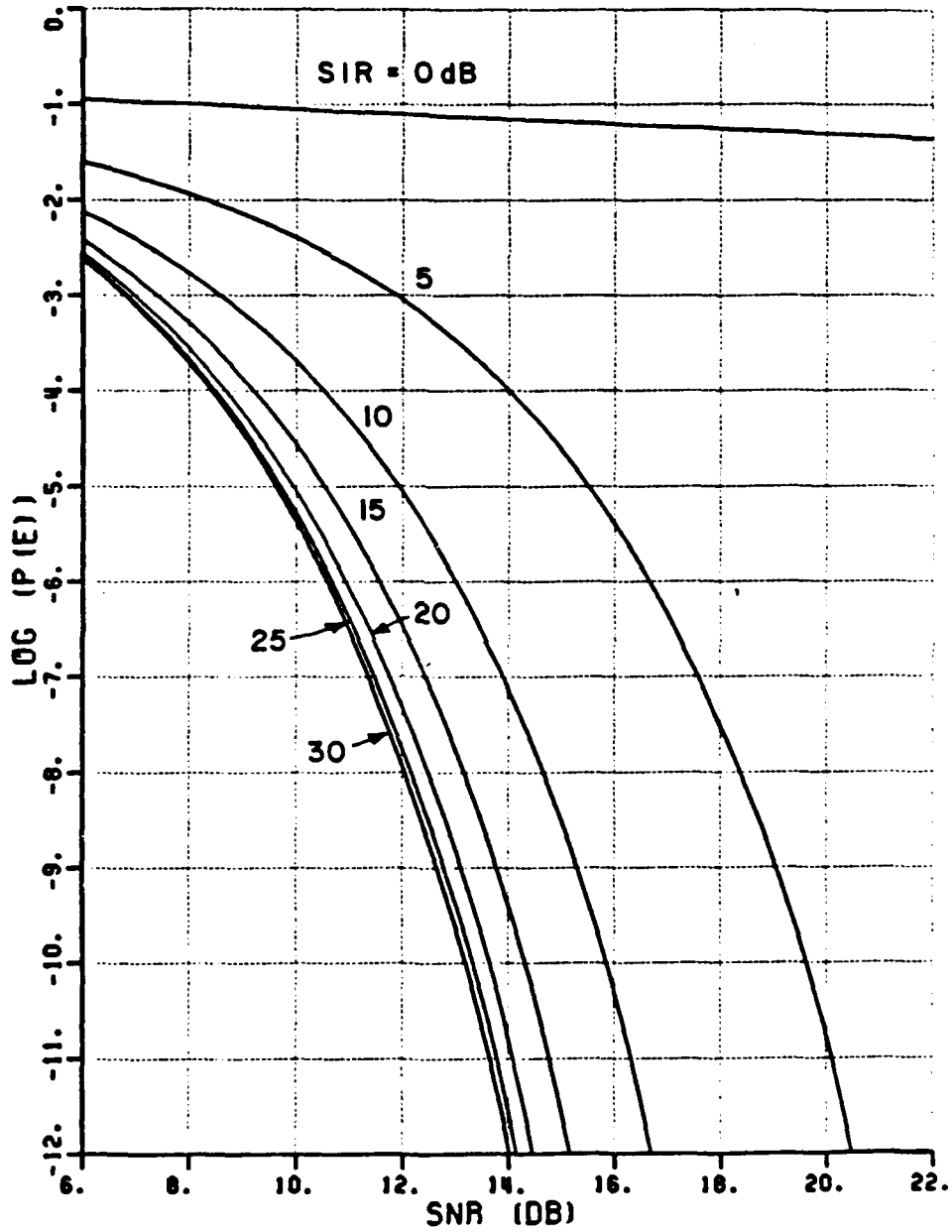


Figure 3.4. Performance of ideal BPSK detector with CW interference ($\Delta\omega T = 0$).

It is interesting to examine $P(e)$ for the ideal BPSK detector as a function of SINR as defined by (2.31). Since the denominator in this expression for SINR contains two terms, it is clear that different combinations of interference and noise power can lead to the same value of SINR. However, from (3.44) we see that the ideal detector is not equally susceptible to interference power and total input noise power. From this equation we see that the detector performance is dependent upon the noise PSD, the interference energy-per-bit-interval, and the interference frequency. Therefore we might suspect that two different combinations of the input signals which have equal SINR values might produce different $P(e)$ values. Figure 3.6 shows that this can indeed happen. This figure shows how $P(e)$ varies with SINR for two different SNR values. The interference power was allowed to vary for each curve but the noise bandwidth, noise PSD level, and the interference frequency were held fixed for each curve. From this figure we see that vastly different error rates can occur for the same SINR value. For example, for a SINR value of -7 dB, there is a difference of 7 orders of magnitude between the two $P(e)$ curves.

In general we find that $P(e)$ is a function of desired signal power, interference power, interference frequency, noise PSD, and noise bandwidth. If all but one of these parameters is held constant and the remaining parameter is allowed to vary, we find that $P(e)$ does decrease monotonically as SINR increases. However, in the general case, we must calculate $P(e)$ for a given scenario using (3.44). The inability to accurately predict system performance using SINR alone was the prime motivation for this study.

P (E) VS. INR

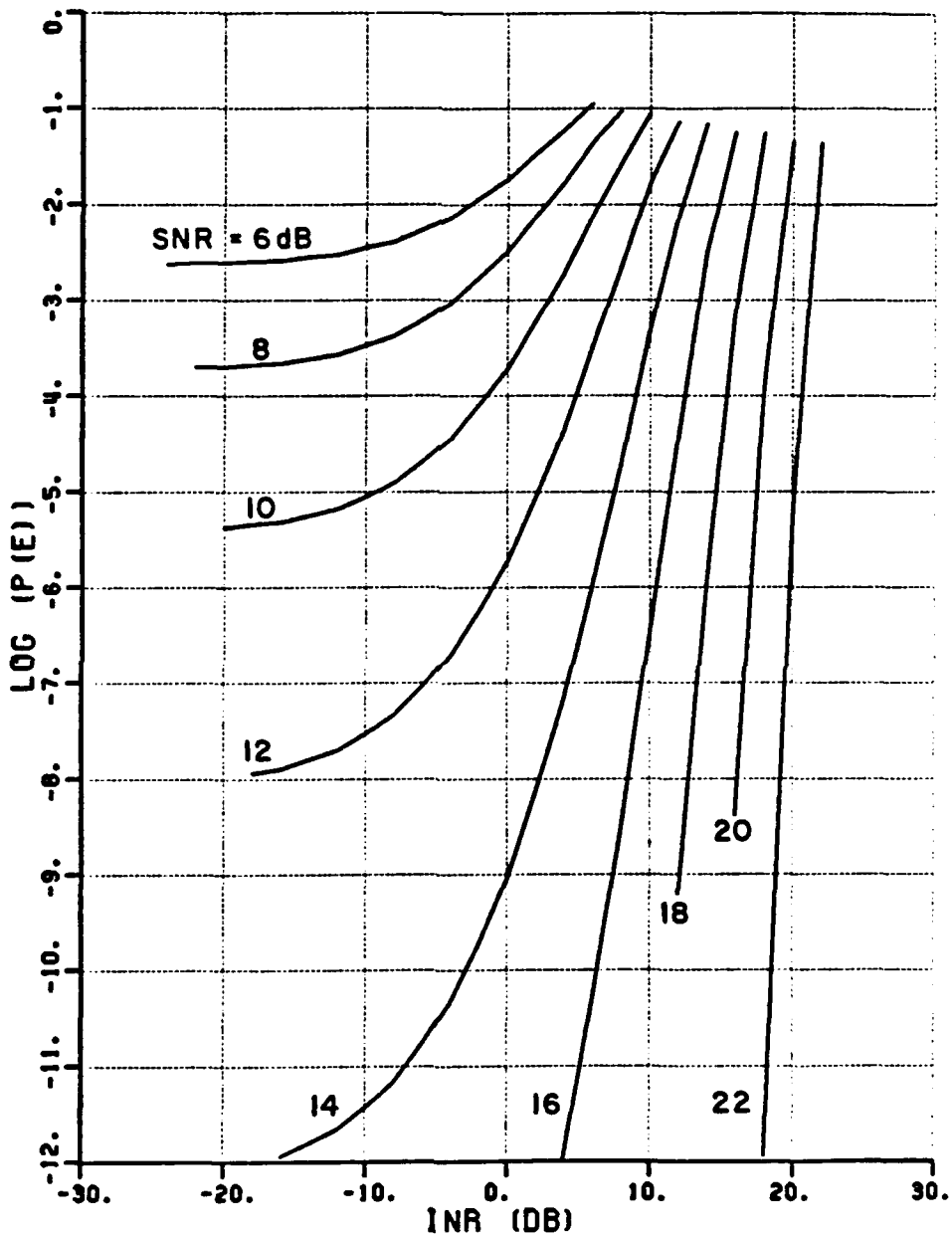


Figure 3.5. Performance of ideal BPSK detector with CW interference ($\Delta\omega T = 0$).

P (E) VS. SINR

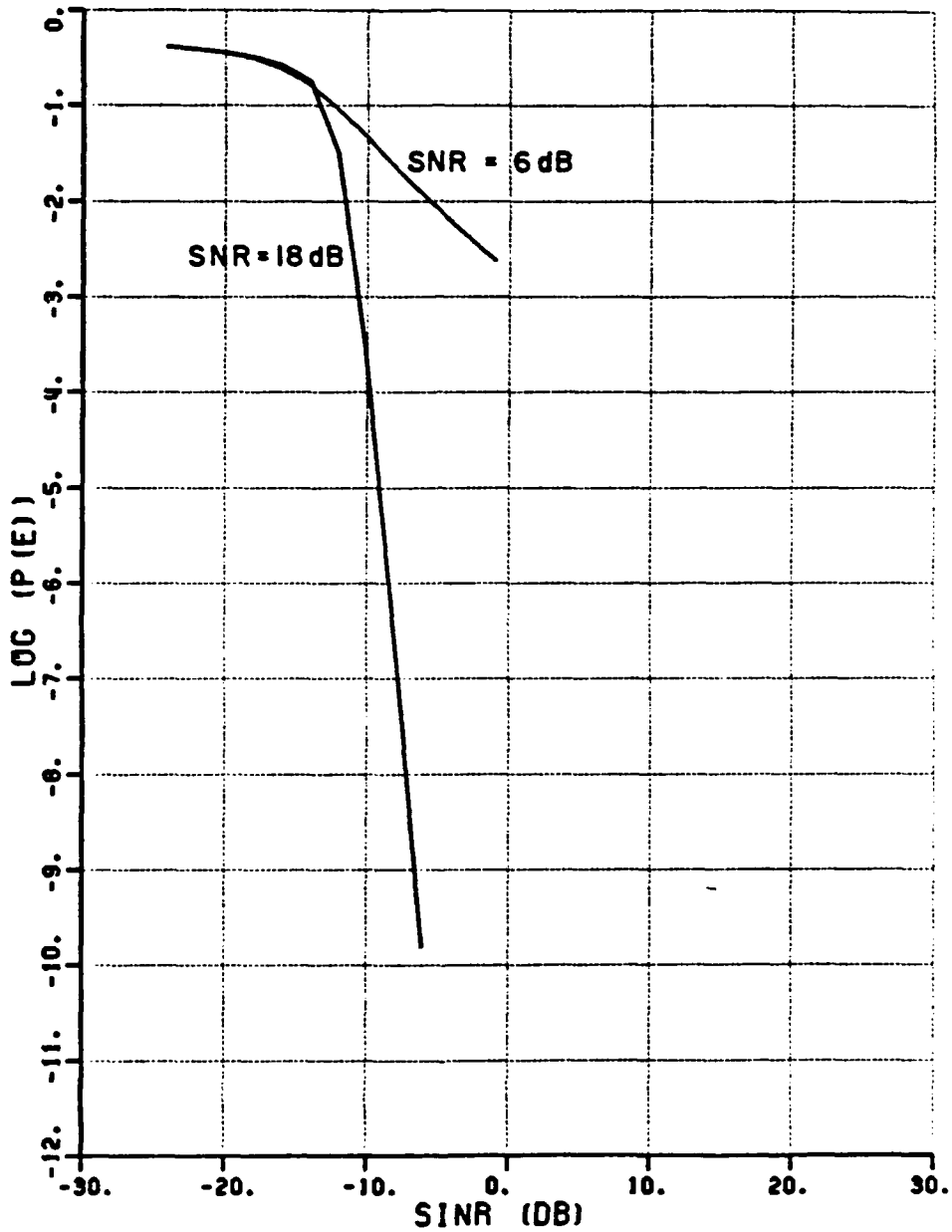


Figure 3.6. Performance of ideal BPSK detector vs. SINR for 2 SNR values ($\Delta\omega T = 5$, noise bandwidth = $10/T$, INR varying).

D. PERFORMANCE CALCULATIONS FOR COMBINED LMS ARRAY/BPSK DETECTOR

In this section we combine the results of the previous two sections to determine the overall performance of the BPSK communication system which uses the LMS array. We first present a set of variables (such as SNR, signal arrival angles, etc.) which completely specify the problem. We then calculate the adaptive array performance using the derivations in part B of this chapter. Once we have determined the power of each signal at the array output (or PSD in the case of the noise) we calculate $P(e)$ of the system using the results of the previous section. Several scenarios are then examined in order to obtain both a qualitative and quantitative understanding of the system performance.

We first present a set of six variables which specify the problem. These variables are:

$(E_d)_{in}/N_0$ = the SNR* at each element input.
 E_d is the desired signal energy-per-bit at each element input and $N_0/2$ is the 2-sided noise PSD (in W/Hz).

$(E_i)_{in}/N_0$ = the INR at each element input.
 E_i is the interference signal energy-per-bit-interval at each element input and $N_0/2$ is as defined above.

θ_d = the desired signal arrival angle as defined in Section 2.

θ_i = the interference arrival angle as defined in Section 2.

*In this report we define the SNR and INR as $(E_d)_{in}/N_0$ and $(E_i)_{in}/N_0$, respectively. These ratios are actually energy-per-bit-interval to noise PSD ratios. In most previous adaptive array work SNR and INR are defined as A_d^2/σ^2 and A_i^2/σ^2 . We use the former definition since these are the forms that SNR and INR typically appear in the expressions for the detector $P(e)$.

k = the array bandwidth factor.

$k = B_A / (2/T)$ where B_A is the input BPF bandwidth (in Hz.) and T is the bit duration. Thus k is the ratio of the input noise bandwidth of the array to the width of the main peak in the desired signal PSD. Figure 3.7 illustrates this definition.

$\Delta\omega T$ = the change in phase of the interference signal with respect to the desired signal during each bit interval (see section C of this chapter).

To calculate the array weights we only need to specify the ratios $\frac{A_d^2}{\sigma^2}$ and $\frac{A_i^2}{\sigma^2}$. These ratios can be calculated given the first five of the variables listed above. We first note that the noise power at each BPF output is given by

$$\sigma^2 = kN_0(2/T). \quad (3.47)$$

We solve this expression for N_0 ,

$$N_0 = \frac{\sigma^2 T}{2k} \quad (3.48)$$

We now write the desired signal energy at each element input as,

$$(E_d)_{in} = N_0(E_d)_{in}/N_0. \quad (3.49)$$

Substitution of (3.48) into (3.49) yields

$$(E_d)_{in} = \left(\frac{\sigma^2 T}{2k}\right) (E_d)_{in}/N_0 \quad (3.50)$$

which we can rearrange as

$$\frac{(E_d)_{in}}{T\sigma^2} = \frac{1}{2k} \frac{(E_d)_{in}}{N_0} \quad (3.51)$$

Since the desired signal power (P_d) at each BPF output is equal to $(E_d)_{in}/T$, (3.51) becomes

$$\frac{(P_d)_{in}}{\sigma^2} = \frac{1}{2k} \frac{(E_d)_{in}}{N_0}, \quad (3.52)$$

or equivalently,

$$\frac{A_d^2}{\sigma^2} = \frac{1}{2k} \frac{(E_d)_{in}}{N_0}. \quad (3.53)$$

A similar derivation shows that,

$$\frac{A_i^2}{\sigma^2} = \frac{1}{2k} \frac{(E_i)_{in}}{N_0} \quad (3.54)$$

Having determined $\frac{A_d^2}{\sigma^2}$ and $\frac{A_i^2}{\sigma^2}$, we can apply the methods discussed in section B of this chapter to determine the desired signal and interference powers at the array output. The noise PSD at the array output is given by (3.14).

Once we have determined the signals at the array output we can use the results of the previous section to determine $P(e)$ for the BPSK detector which follows the adaptive array.

The procedure outlined above was performed for several different scenarios. Figures 3.8 and 3.9 show typical results. These figures show how $P(e)$ varies with SNR and INR for the 3-element array when the desired signal arrives from the broadside direction (i.e., $\theta_d=0^\circ$) and the interference arrival angle θ_i , is 10° . The array bandwidth factor

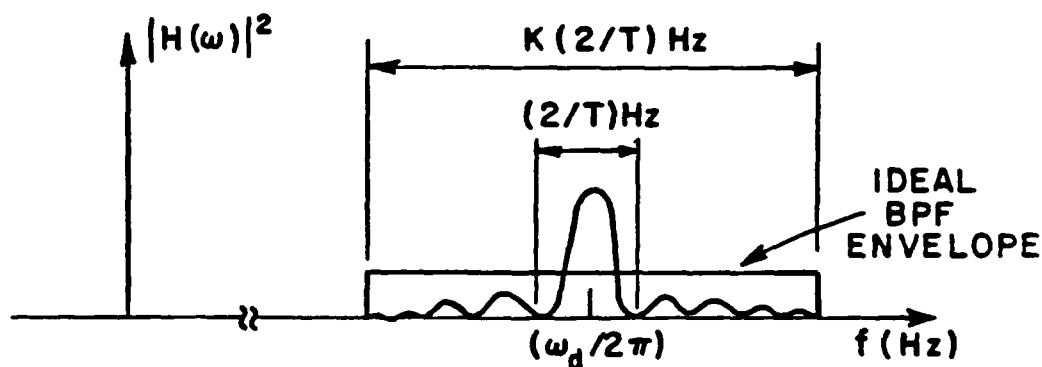


Figure 3.7. Ideal integrator and BPF transfer functions (only positive frequencies shown).

k , was set equal to 5 in each of the cases shown in these figures and $\Delta\omega T$ was set equal to zero.

The array behavior is most easily explained by examination of Figure 3.9. For each given SNR curve we see that, as INR increases, $P(e)$ first increases and then decreases. The maximum in the $P(e)$ curve occurs typically at INR values between 10 and 20 dB. It is in this INR range where the interference and noise powers are roughly equal at the element inputs. At INR values below approximately 10 dB the thermal noise is dominant at the array input and the array pattern is relatively unaffected by the interference. Thus as INR increases, the interference power at the array output and $P(e)$ both increase. As the INR increases

above approximately 10 dB the array begins to null the jammer. As the INR is increased further this null becomes deeper and a point is reached where any additional increase in input interference power produces a corresponding decrease in the interference power at the array output. Therefore, at very high INR values, a very deep null is formed in the interfering signal direction. At these high INR values the interference power becomes negligible at the array output (when compared with the thermal noise) and the $P(e)$ curves each asymptotically approach a constant value.

It is interesting to note that the $P(e)$ value which a particular curve approaches at high INR values is larger than the value which this curve has at very low INR values. This phenomenon is easily explained. At very low INR values the array is not affected by the interference and it can adjust its weights in order to maximize gain in the desired signal direction. At very high INR values the array behavior is constrained so that it must keep a deep null in the direction of the interference.

Since the desired and interfering signals are spatially close, the desired signal lies very close to the null. The 3-element array does not have sufficient resolution to simultaneously steer a null and a pattern maximum only a few degrees apart. Therefore, at high INR values, even though the interference power at the array output is reduced to a negligible level, the desired signal power is also slightly reduced. The resulting decrease in the SNR in the array output produces the larger value of $P(e)$ at very high INR values compared to $P(e)$ at low INR levels.

The performance at high INR values can generally be improved by adding elements (and thus degrees of freedom) to the array or by increasing the spatial separation between the desired and interfering signals. To determine the effects of signal arrival angle on performance we have calculated the expected system $P(e)$ for interference arrival angles of 20° and 80° . The results for these cases are shown in Figures 3.10 through 3.13. As in the previous cases the array bandwidth factor k , was set equal to at 5. Figures 3.10 and 3.11 show the results for $\theta_i=20^\circ$ and Figures 3.12 and 3.13 show the results for $\theta_i=80^\circ$.

Several interesting results can be seen from these figures. From a comparison of Figures 3.9, 3.11, and 3.13, we observe the effects of θ_i on system performance. First we see that, at very low INR values, the system performance is not very sensitive to changes in θ_i . In these cases the effects of the interference are negligible and the array can easily form a pattern maximum in the desired signal direction. At moderate and high INR values the performance improves (as expected) as θ_i increases.

From Figures 3.8 through 3.13 we see that the interference is most effective when $|\theta_i-\theta_d|$ is small and when the INR is in the 10-20 dB range.

In order to illustrate the effects of the noise bandwidth at the element inputs, the calculations described above were repeated with k increased from 5 to 10. The results of these calculations are shown in Figures 3.14 through 3.19. The results in these plots correspond

P (E) VS. SNR

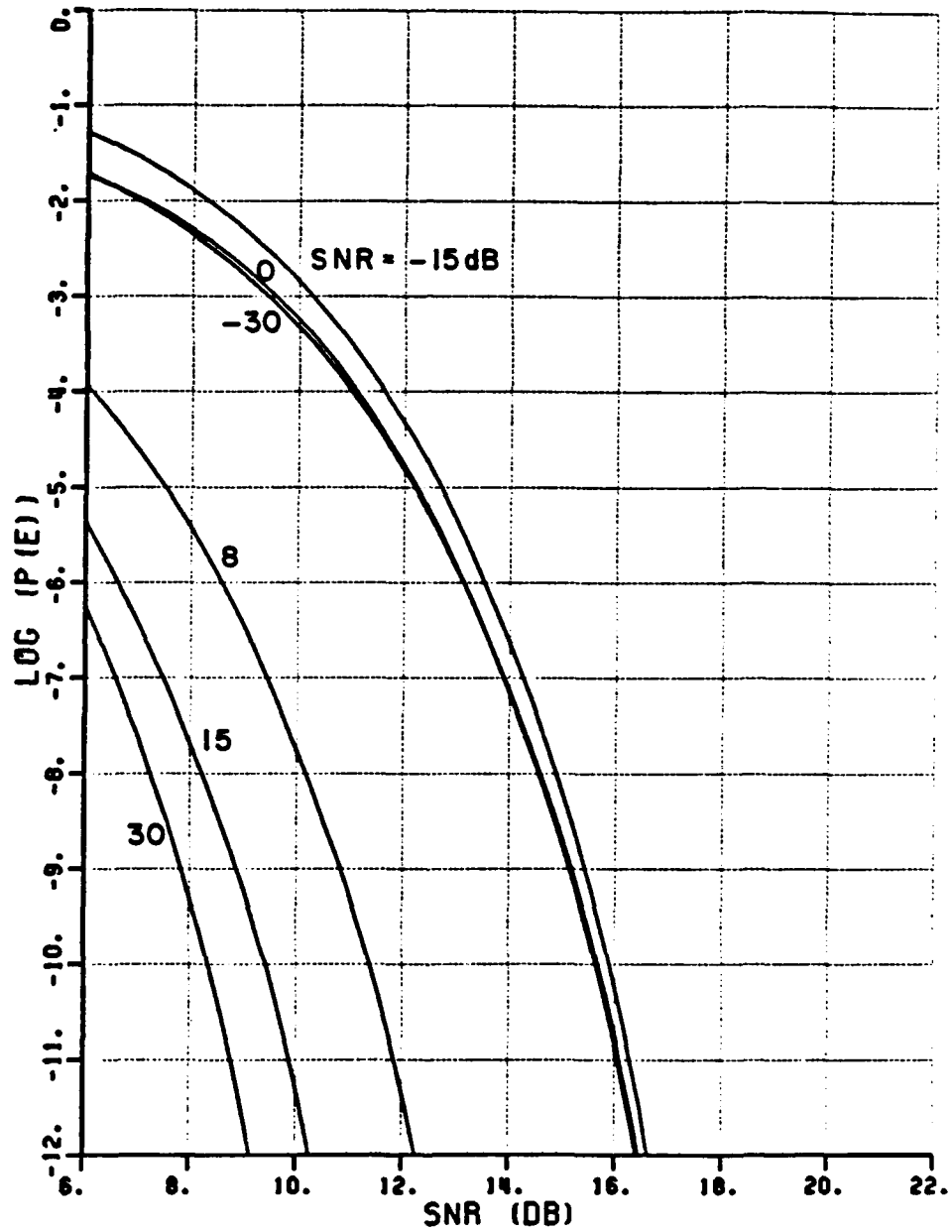


Figure 3.8. BPSK P(e) vs. SNR for 3-element array ($\theta_i=10^\circ$, $k=5$, $\Delta\omega T=0$).

P (E) VS. INR

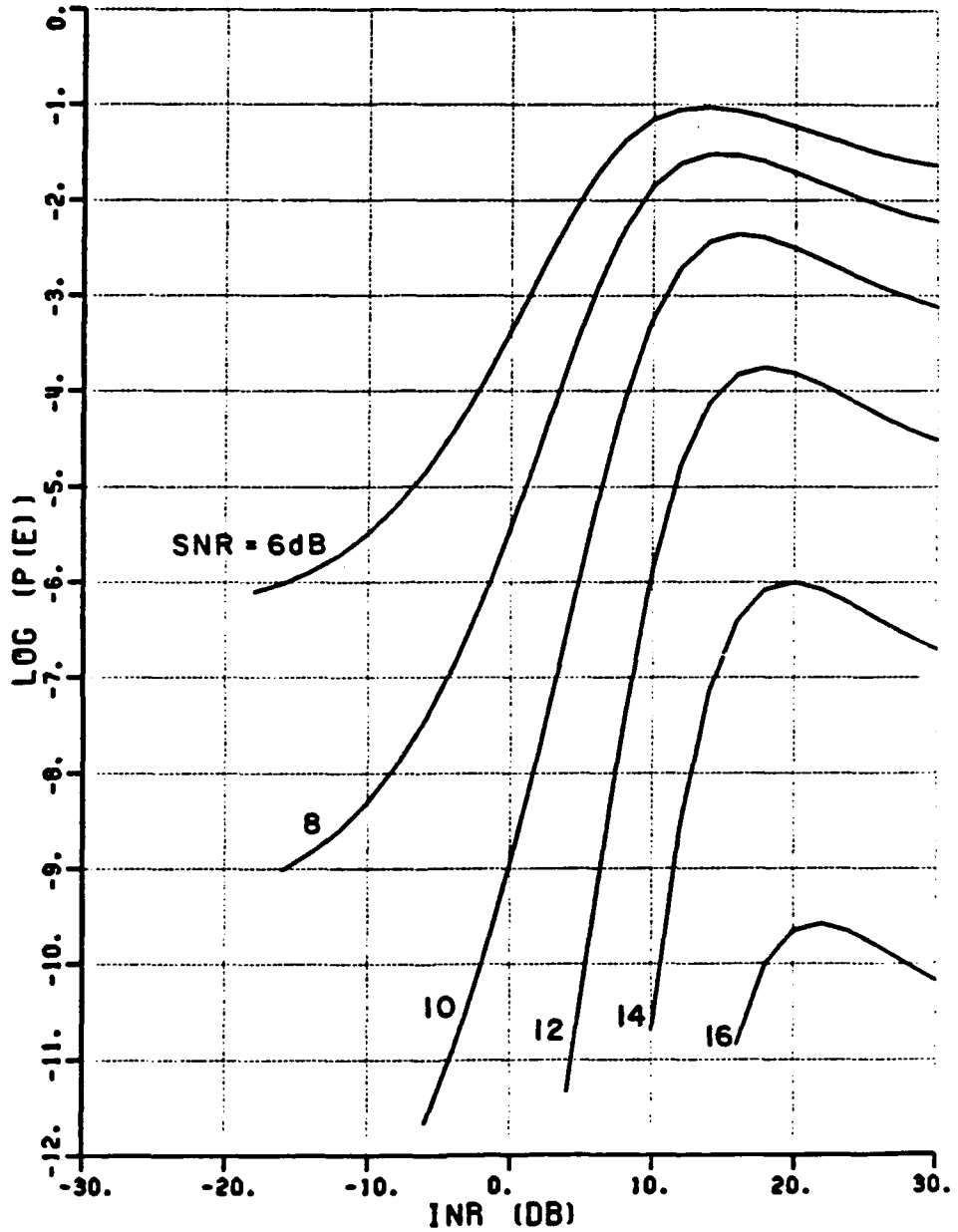


Figure 3.9. BPSK P(e) vs. INR for 3-element array ($\theta_i=10^\circ$, $k=5$, $\Delta\omega T=0$).

directly to the data shown in Figures 3.8 through 3.13 (the only exception being the increase in k from 5 to 10).

From these new plots we see that the array behaves similarly to the previous cases. However, when the input bandwidth is increased, the height of the peak in the $P(e)$ vs. INR curves is increased and this peak is shifted slightly to the right. This behavior can be explained as follows. With the doubling of the input bandwidth twice as much thermal noise is present at each element input. As described above, the array does not begin to null the interference effectively until $(P_i)_{in}$ is roughly equal to the input thermal noise power. Since the increased bandwidth results in more noise power at the array input, a higher INR is required before the array begins to reject the interference. Hence the slight rightward shift in the curves. Since the maximum output interference power level is higher in the wider bandwidth case, the maximum $P(e)$ is also higher in this case. In light of these results we conclude that the system performance is significantly degraded when we doubled the input bandwidth.

We have now shown how the BPSK/LMS array system is affected by SNR, INR, signal arrival angles, and array bandwidth. Next we examine how the interference frequency affects the system. The contribution of the interference to the integrator output (i.e. $X_i(n)$) is given by Equation (3.28). From this equation we see that $X_i(n)$ will be zero for those frequencies at which $\text{sinc}(\Delta\omega T/2)$ is zero. At these points (i.e., when $\Delta\omega T = 2n\pi$ where n is any non-zero integer) the detector performance will not be degraded by the interference.

Figures 3.20 and 3.21 show the system performance when $\Delta\omega T=2\pi$. In these figures the array bandwidth factor k was set equal to 10 and the interference arrival angle θ_i was set equal to 10° . Since we established in section C of this chapter that the detector is not affected by the interference with $\Delta\omega T=2\pi$ we might be surprised to see that Figures 3.20 and 3.21 show that the system performance becomes worse as the interference power increases. This behavior should not be surprising, however, since the adaptive array which precedes the detector must change its pattern to null the interference at high INR levels. As the array nulls this interference, the SNR at the array output decreases due to the constraints placed on the array by the nulling requirement (this phenomenon is discussed above). The decreased performance at high INR levels is caused by this decrease in SNR at the array output.

It is interesting to note, however, that there are no relative maxima in the $P(e)$ curves in Figure 3.21. These peaks, which we observed in previous $P(e)$ vs. INR curves, were caused by the interference signal at the detector input (i.e., the array output) at moderate INR levels. For the case shown in Figure 3.21 the detector is not affected by the interference and therefore there are no peaks in the curves. In these special cases (where $\Delta\omega T=2n\pi$) SNR and not SINR is the most meaningful measure of system performance (since the detector is immune to the interference). We also find that, for array bandwidths of interest, the SNR as defined by Equation (3.51) is not significantly dependent on the array input bandwidth.

P (E) VS. SNR

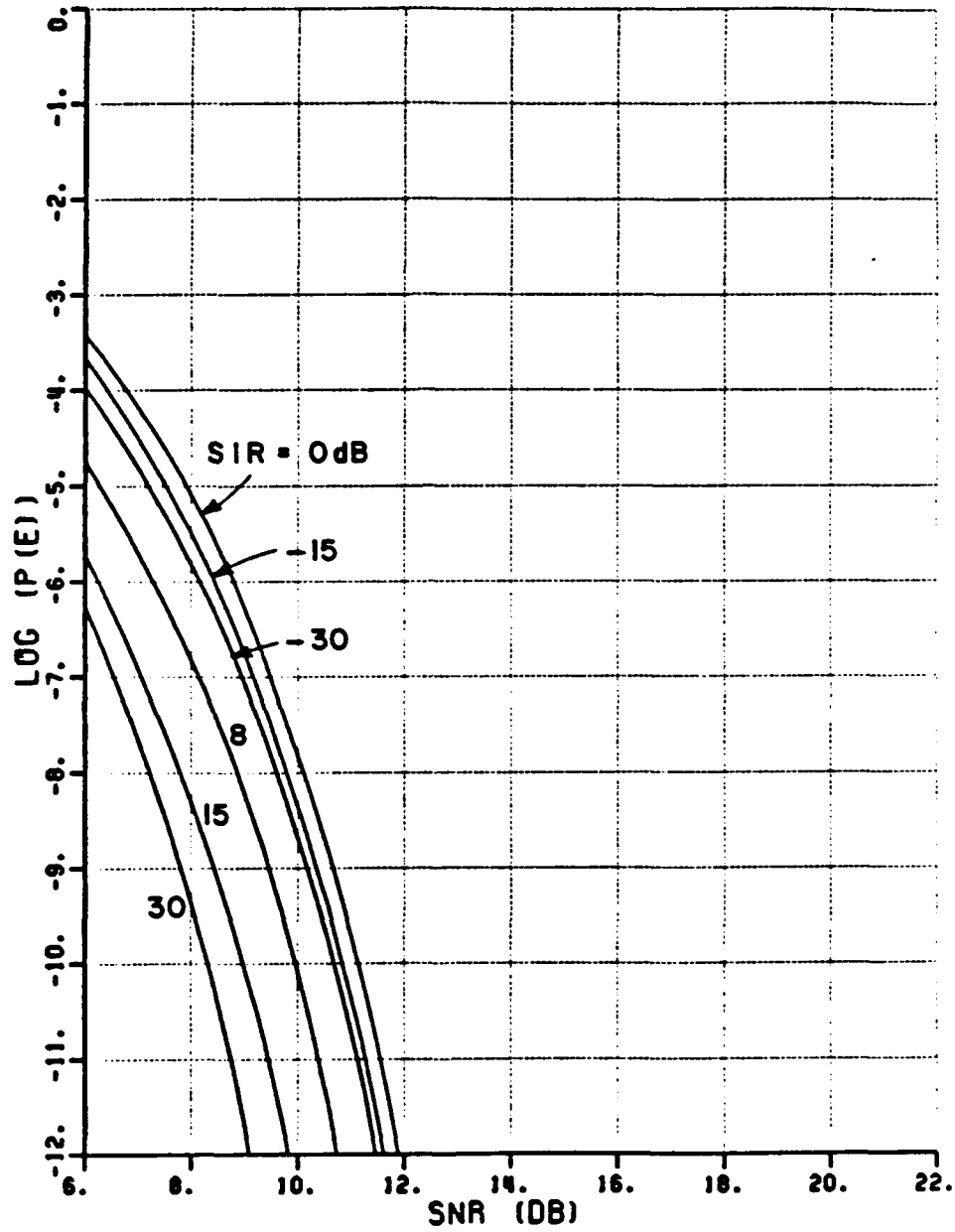


Figure 3.10. BPSK P(e) vs. SNR for 3-element array ($\theta_i=20^\circ$, $k=5$, $\Delta\omega T=0$).

P (E) VS. INR

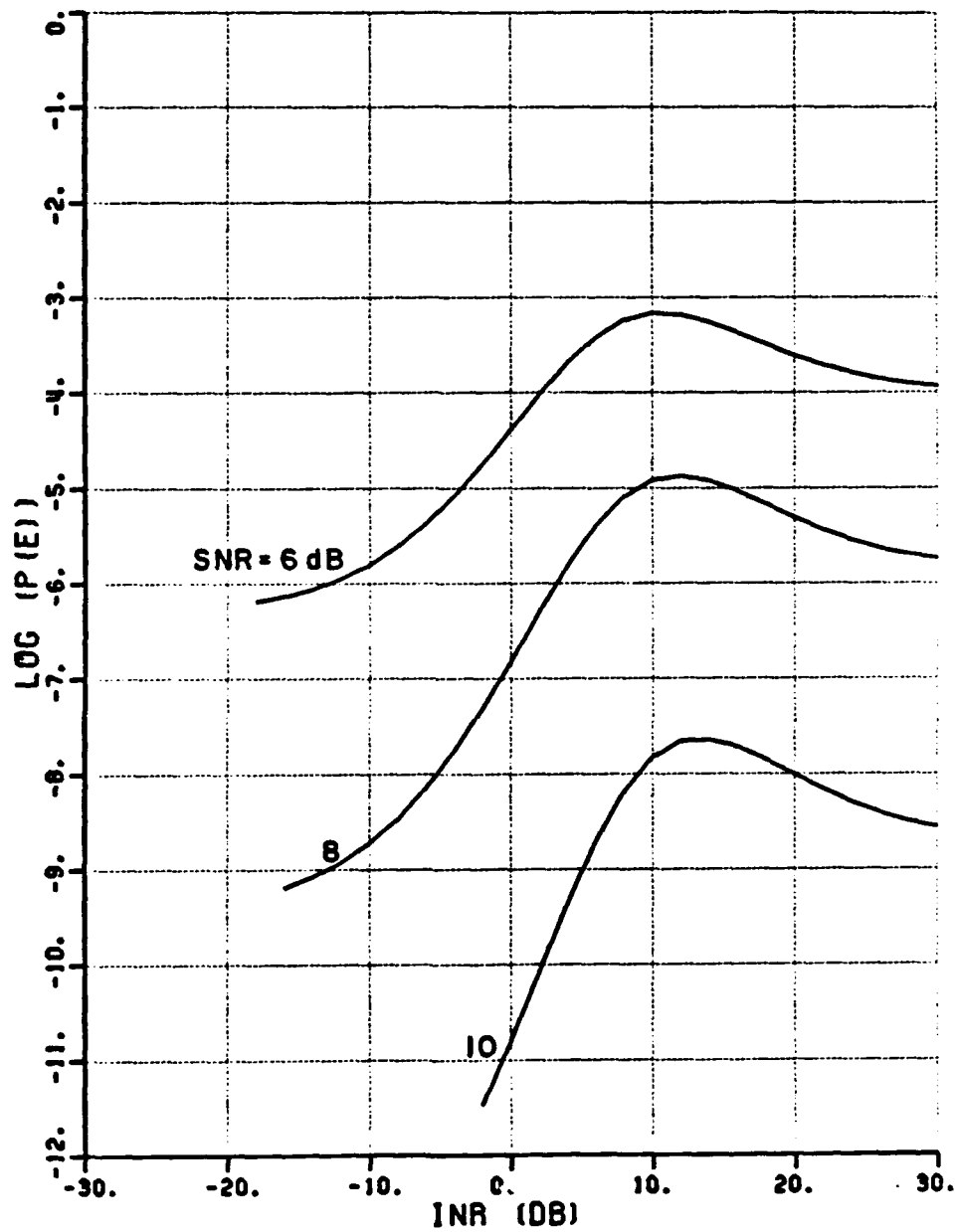


Figure 3.11. BPSK $P(e)$ vs. INR for 3-element array ($\theta_1=20^\circ$, $k=5$, $\Delta\omega T=0$).

P (E) VS. SNR

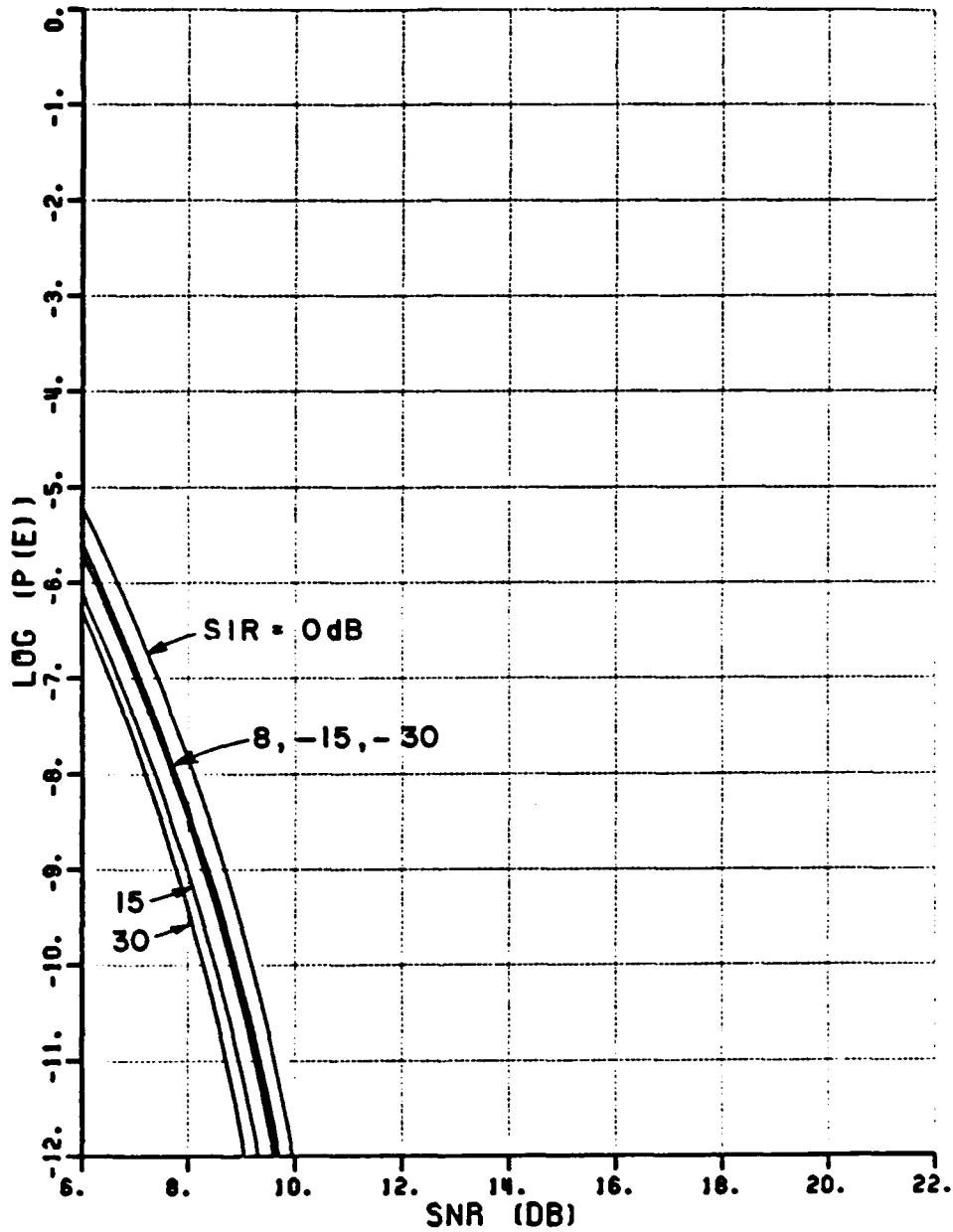


Figure 3.12. BPSK $P(e)$ vs. SNR for 3-element array ($\theta_i=80^\circ$, $k=5$, $\Delta\omega T=0$).

P (E) VS. INR

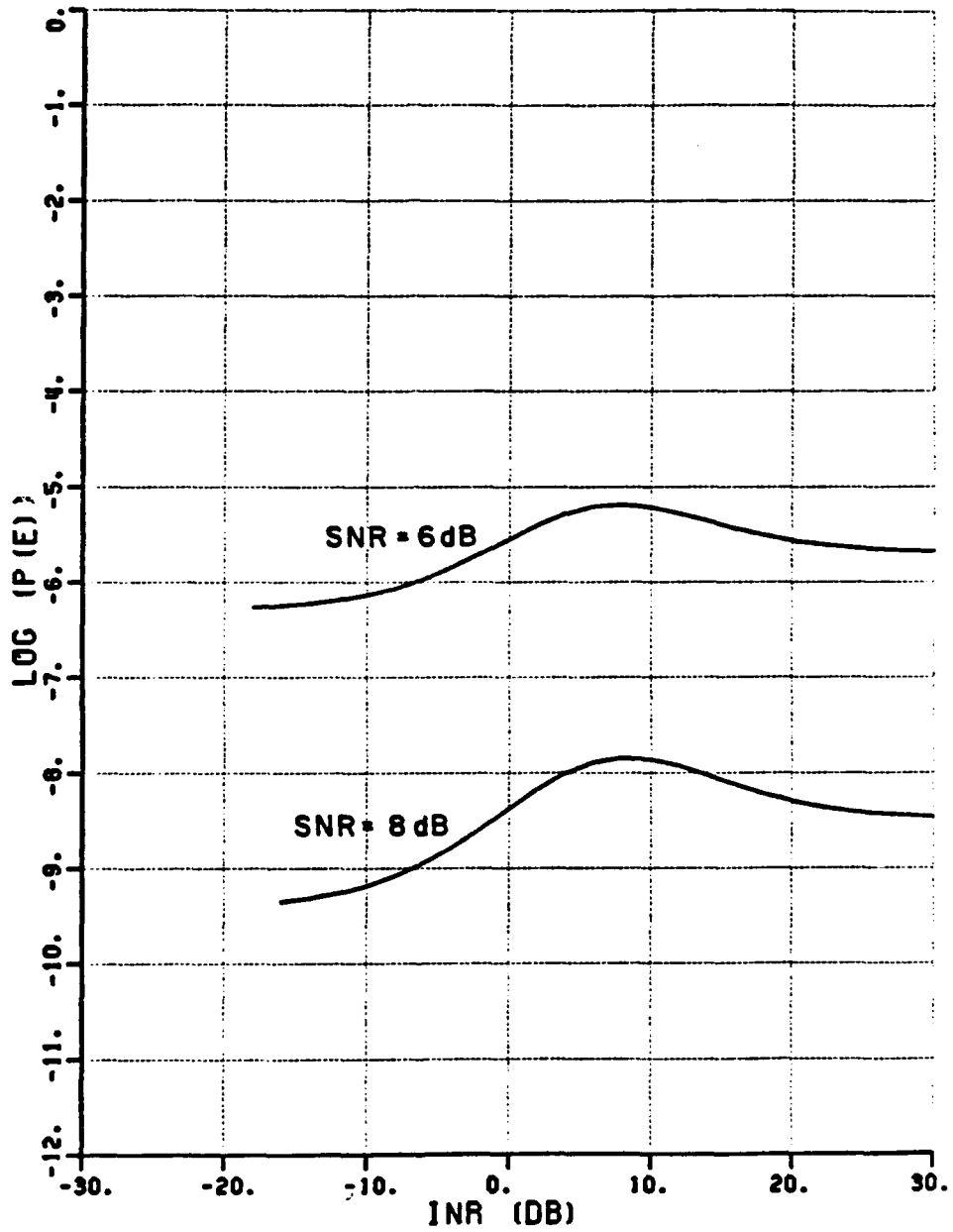


Figure 3.13. BPSK $P(e)$ vs. INR for 3-element array ($\theta_j=80^\circ$, $k=5$, $\Delta\omega T=0$).

P (E) VS. SNR

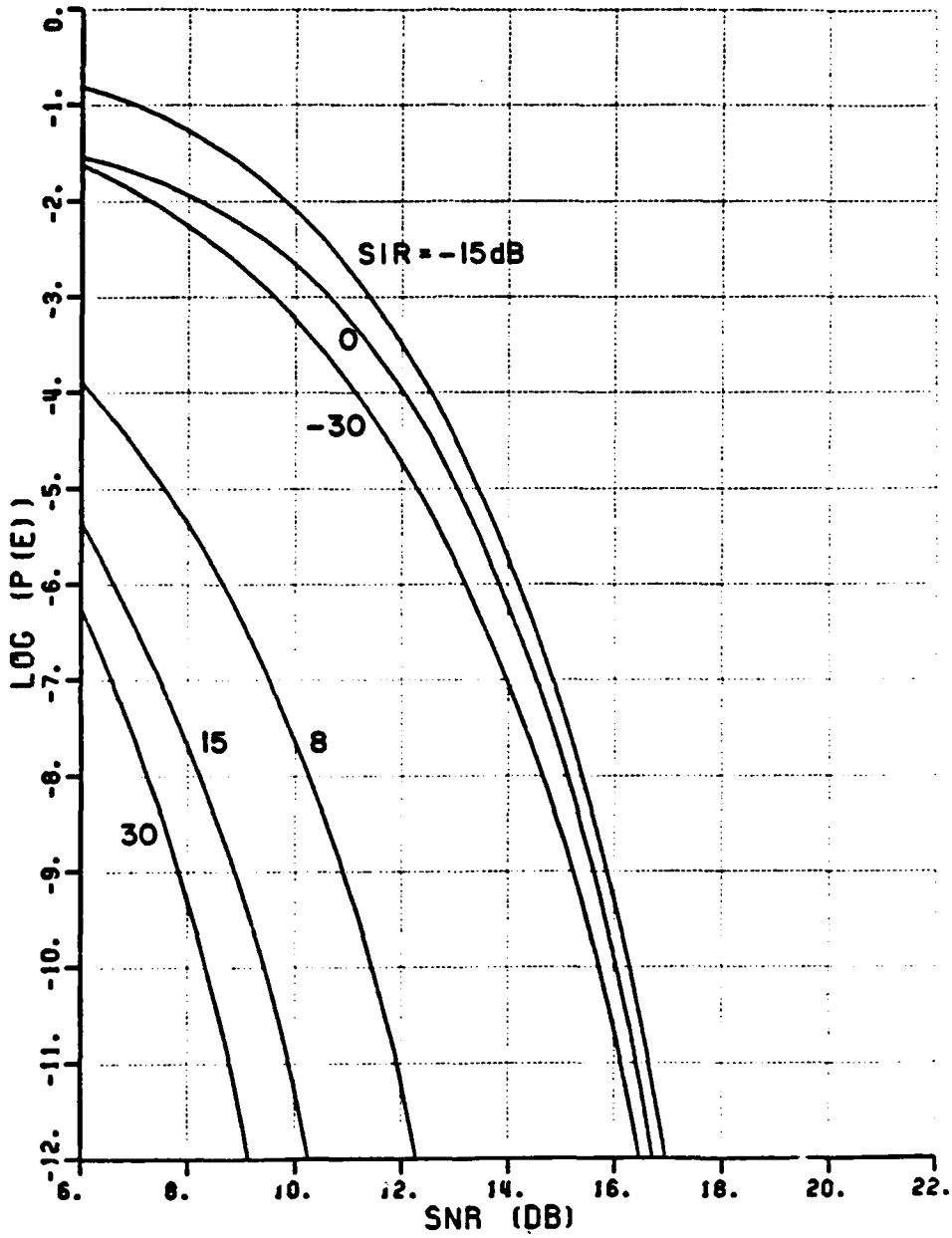


Figure 3.14. BPSK $P(e)$ vs. SNR for 3-element array ($\theta_1=10^\circ$, $k=10$, $\Delta\omega T=0$).

P (E) VS. INR

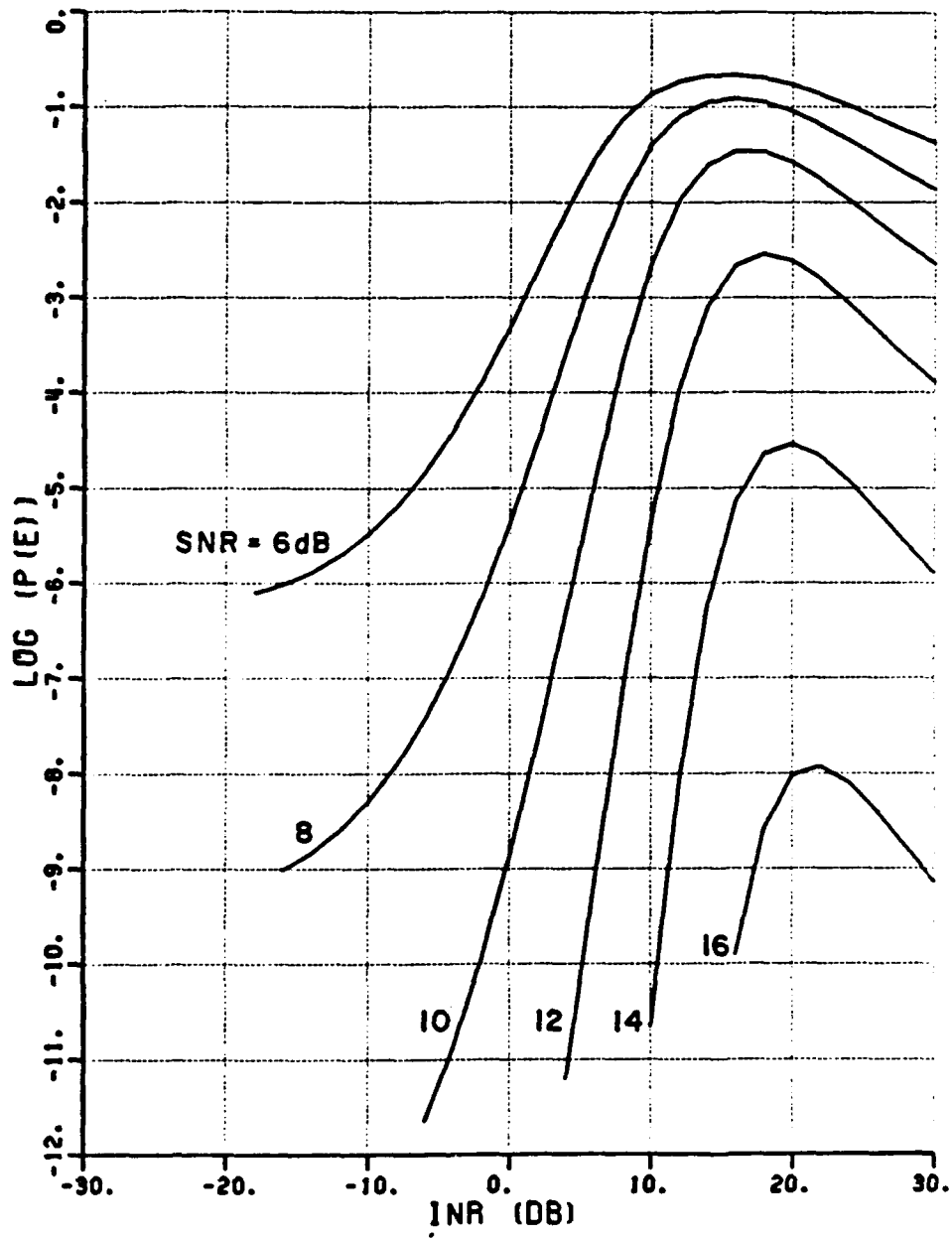


Figure 3.15. BPSK $P(e)$ vs. INR for 3-element array ($\theta_j=10^\circ$, $k=10$, $\Delta\omega T=0$).

P (E) VS. SNR

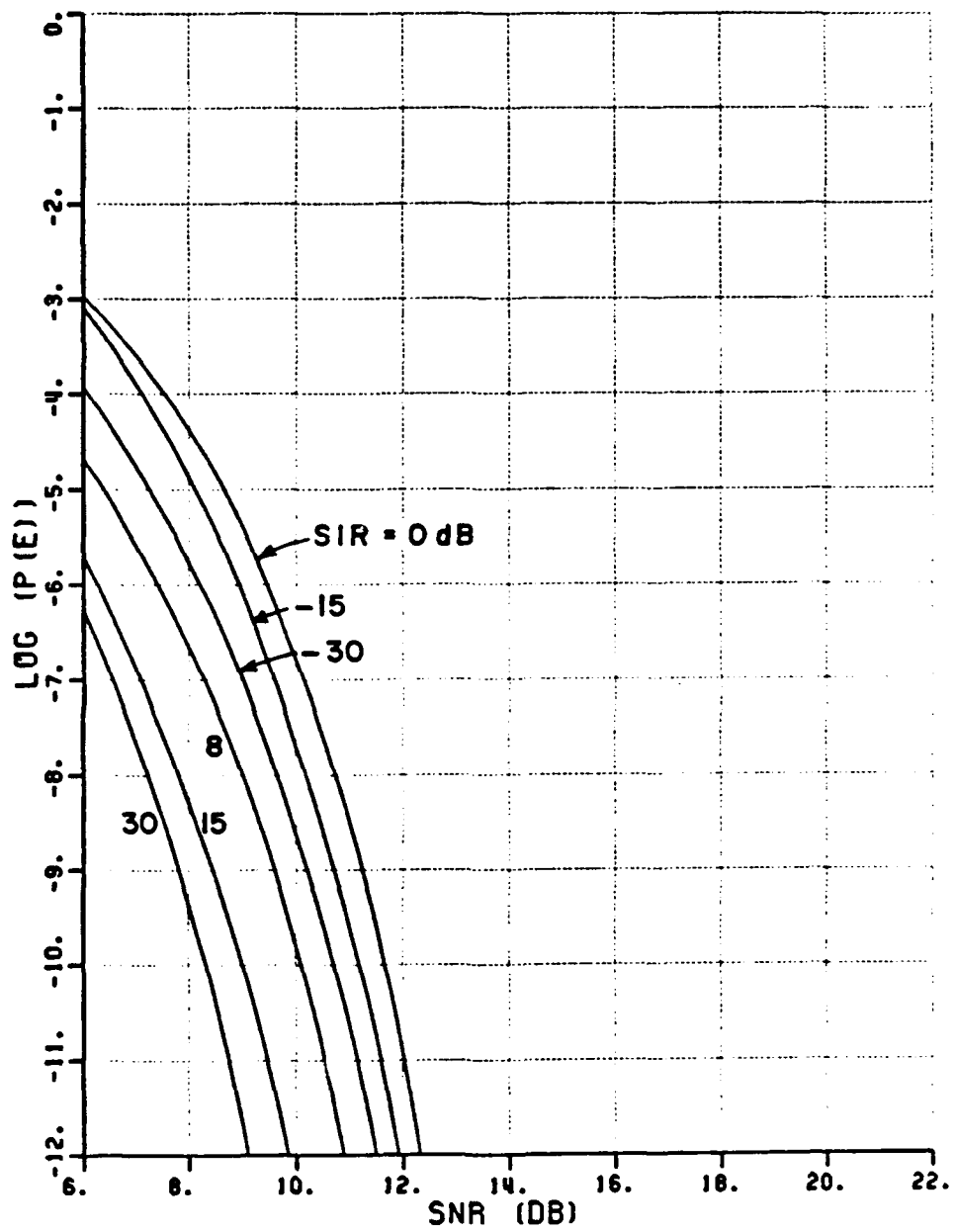


Figure 3.16. BPSK $P(e)$ vs. SNR for 3-element array ($\theta_i=20^\circ$, $k=10$, $\Delta\omega T=0$).

P (E) VS. INR

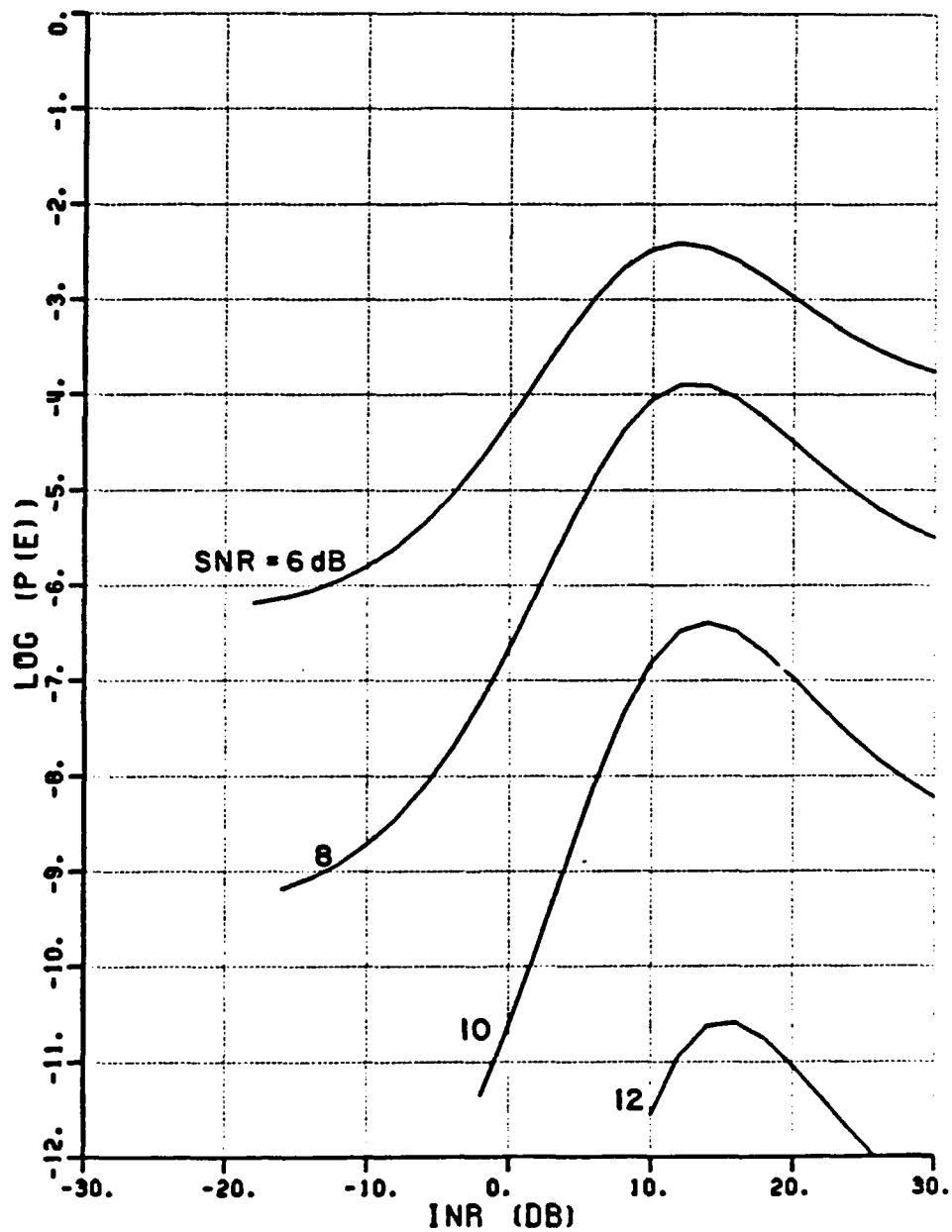


Figure 3.17. BPSK P(e) vs. INR for 3-element array ($\theta_i=20^\circ$, $k=10$, $\Delta\omega T=0$).

P (E) VS. SNR

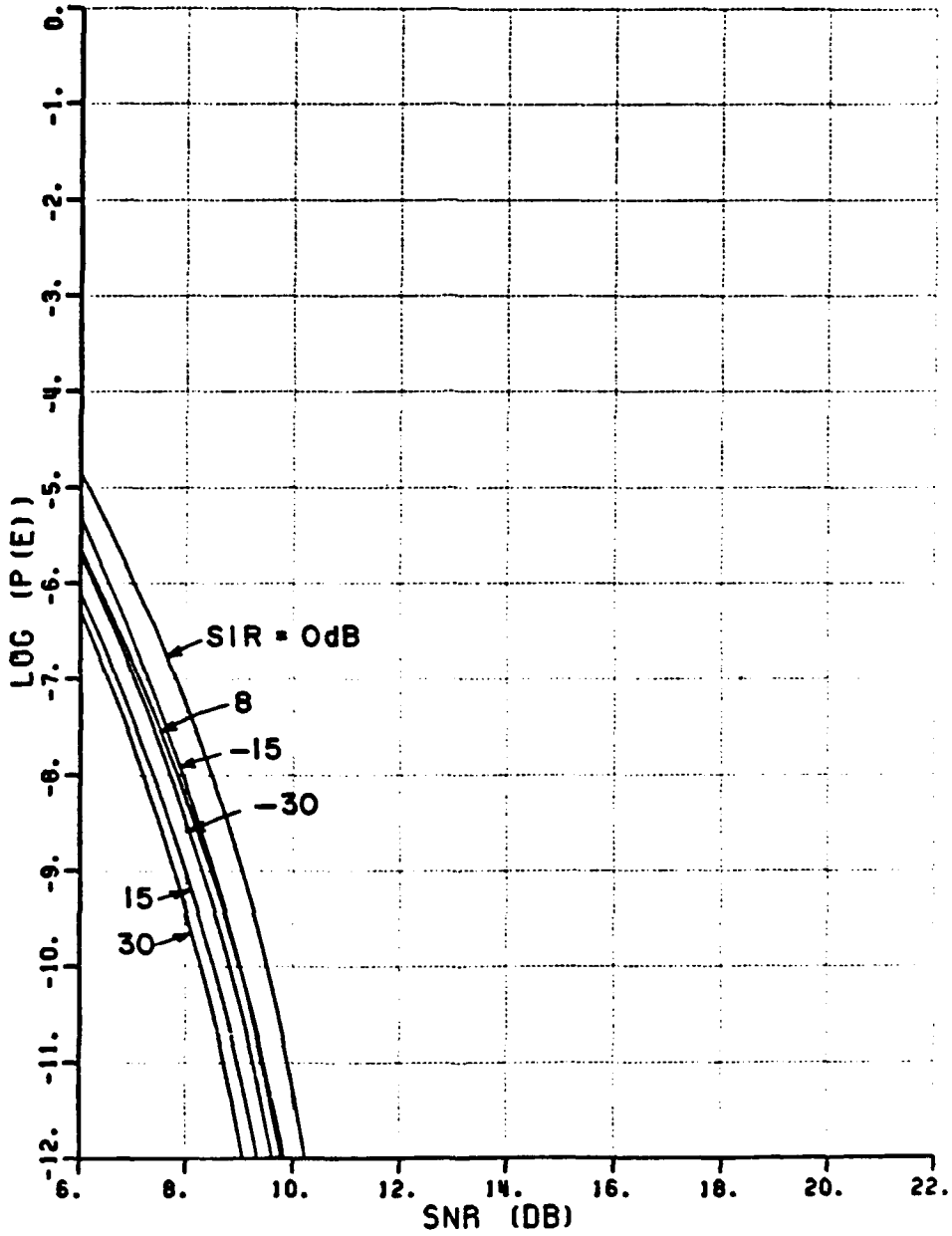


Figure 3.18. BPSK $P(e)$ vs. SNR for 3-element array ($\theta_i=80^\circ$, $k=10$, $\Delta\omega T=0$).

P (E) VS. INR

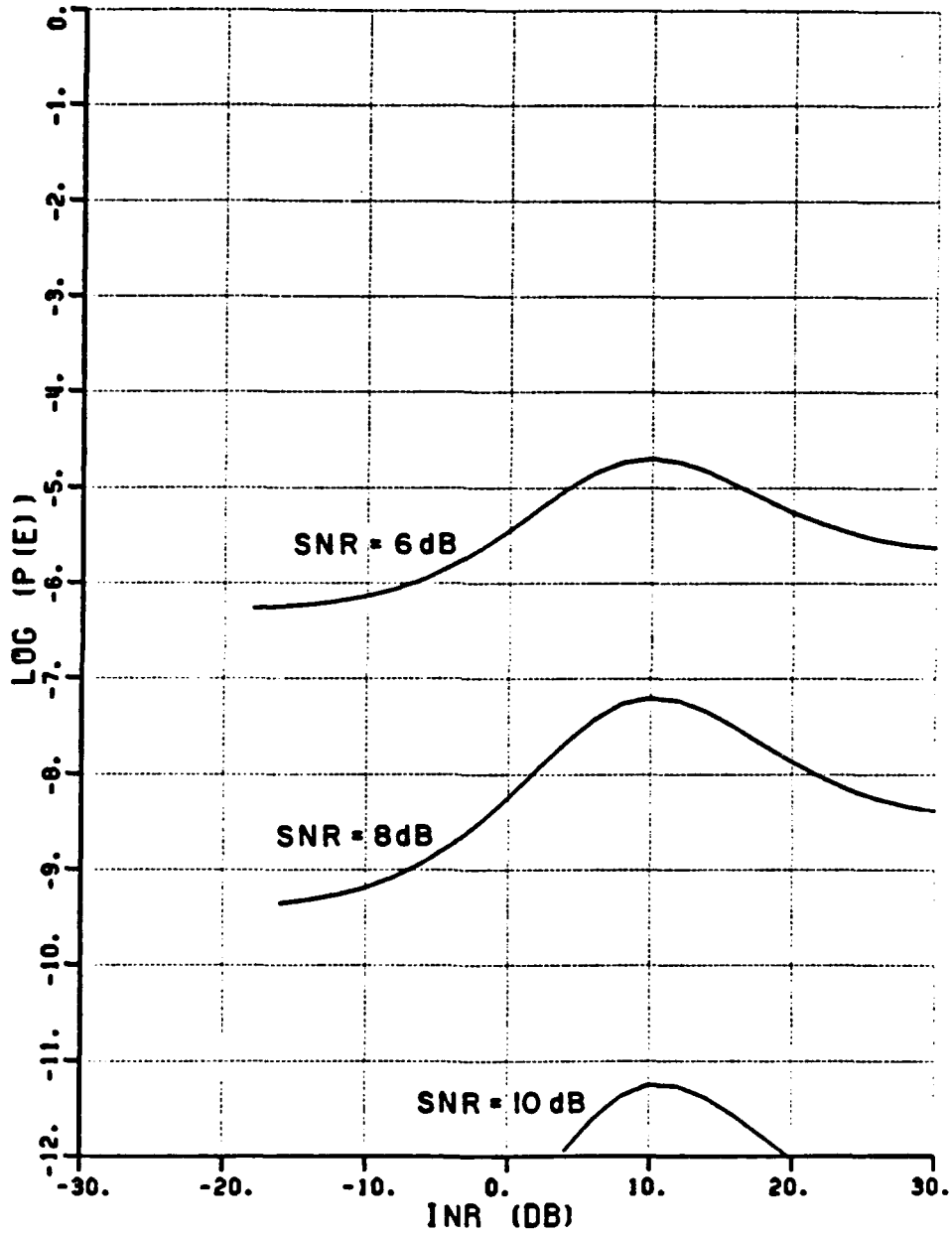


Figure 3.19. BPSK $P(e)$ vs. INR for 3-element array ($\theta_i=80^\circ$, $k=10$, $\Delta\omega T=0$).

P (E) VS. SNR

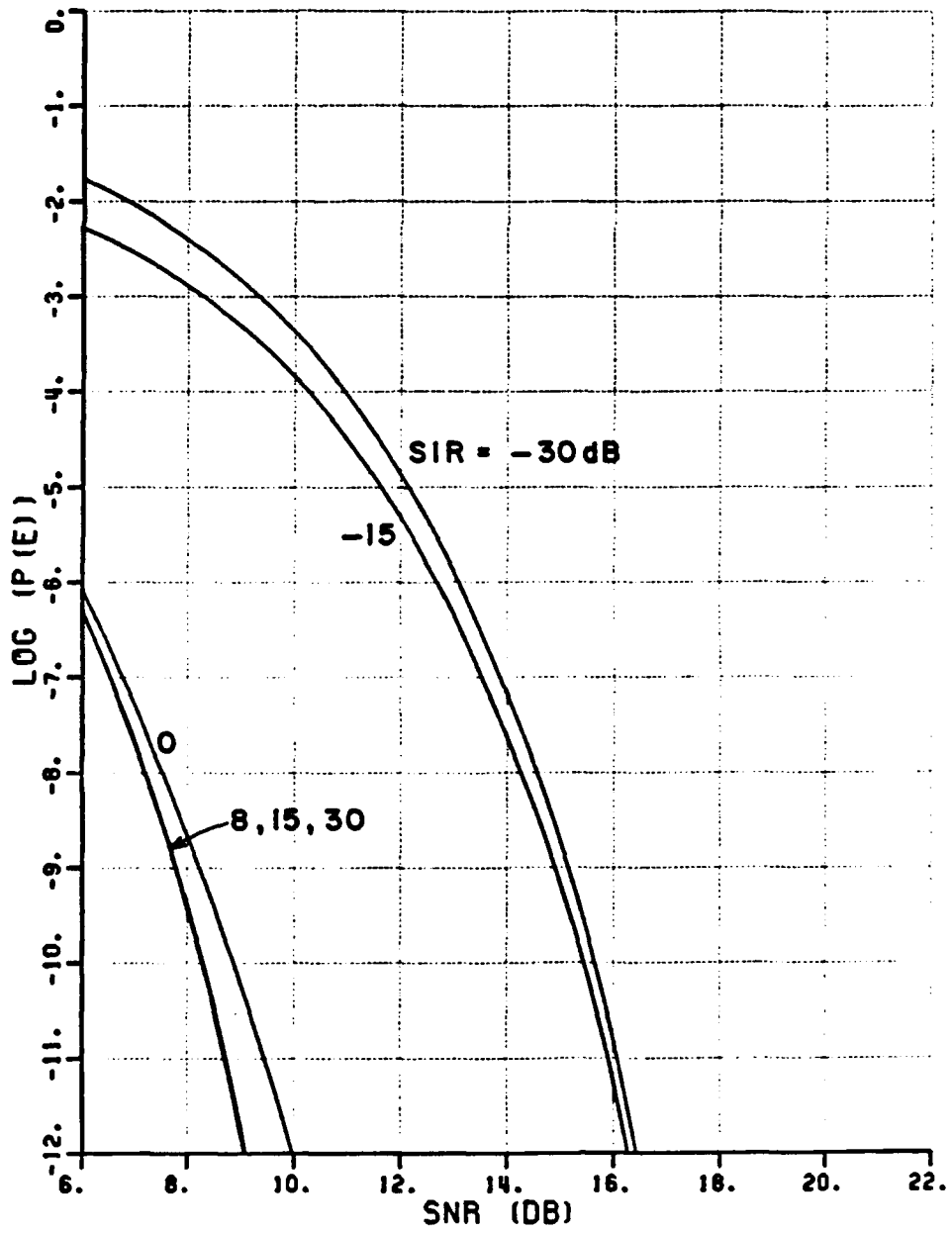


Figure 3.20. BPSK $P(e)$ vs. SNR for 3-element array ($\theta_1=10^\circ$, $k=10$, $\Delta\omega T=2\pi$).

P (E) VS. INR

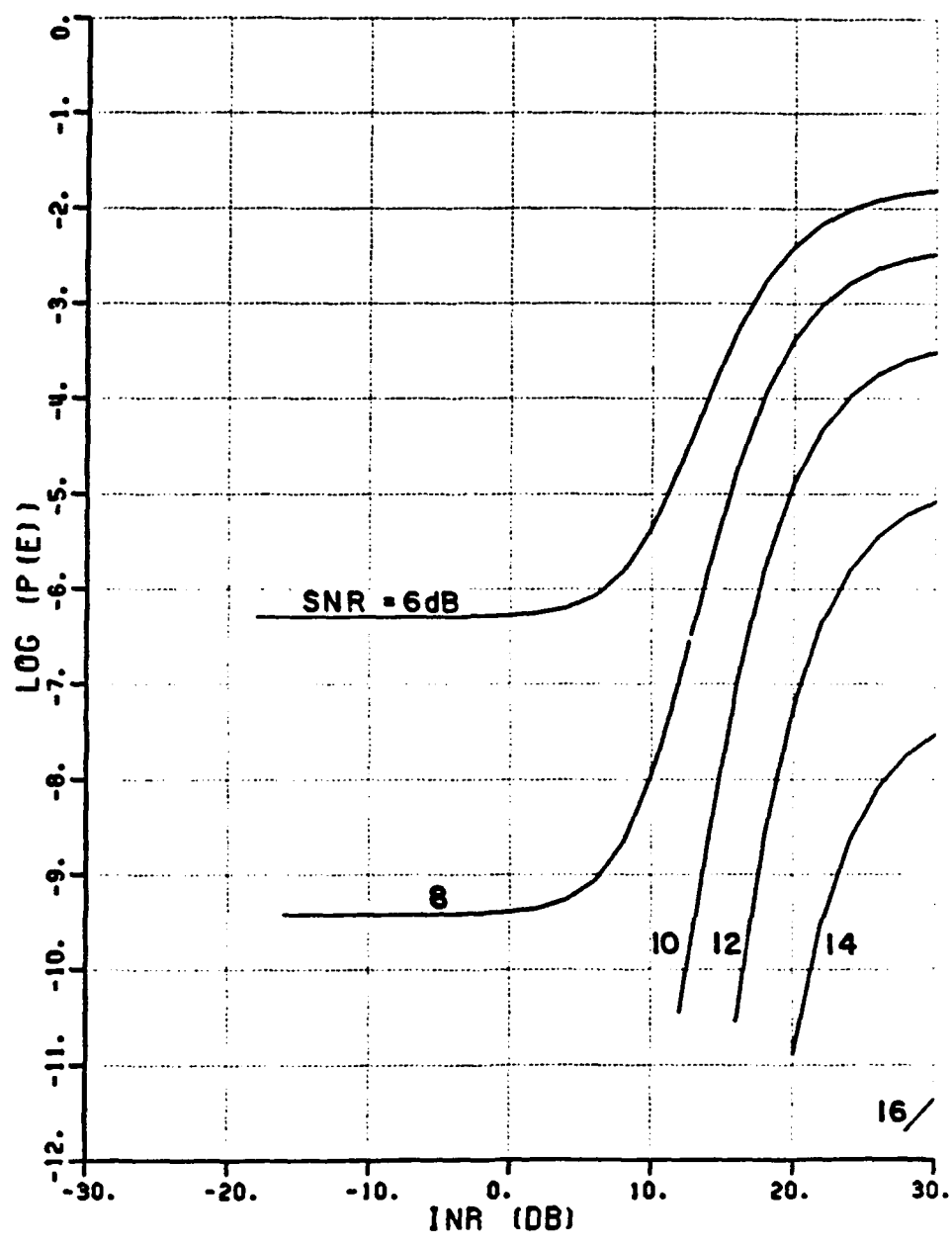


Figure 3.21. BPSK (P(e) vs. INR for 3-element array ($\theta_i=10^\circ$, $k=10$, $\Delta\omega T=2\pi$).

If $\Delta\omega T/2 \gg 0$ the sinc function in the expression for the detector $P(e)$ will be very close to zero even if $\Delta\omega T \neq 2n\pi$. Therefore, for this case, the detector performance is not degraded by the interference. However, the SNR at the array output is still reduced at high INR levels. Therefore, even though the interference is outside of the detector bandwidth, the overall system performance is still adversely affected by the interference. The system designer can limit this susceptibility to out-of-band interference by keeping the array input bandwidth as small as possible.

CHAPTER IV

PERFORMANCE OF A QPSK SYSTEM WITH CW INTERFERENCE

A. INTRODUCTION

In this chapter we examine the effects of CW interference on a quadrature phase shift keyed (QPSK) communication system that uses an LMS array. The organization and analytical techniques of this chapter are very similar to those of the previous chapter. The equations describing the QPSK and BPSK systems are so similar that we shall often use the results from derivations in Chapter III with only minor modifications.

Figure 4.1 shows a typical QPSK waveform. Each of the four possible QPSK symbols represents two bits of information. We shall be careful to use the word "symbol" and not "bit" to describe a burst of energy at one of the signalling phases. In Chapter III we could use the terms "bit" and "symbol" interchangeably since, for BPSK signalling, each symbol represents only one bit of information.

A method for generating a reference signal for an LMS array using QPSK signalling is described by Winters in [3]. This reference-generation technique, like that discussed in Chapter III for BPSK, relies on spread-spectrum coding of the desired signal in order to derive a reference signal from the array output. We assume that a perfect reference signal (one which is identical to the incoming desired signal) is available to the array.

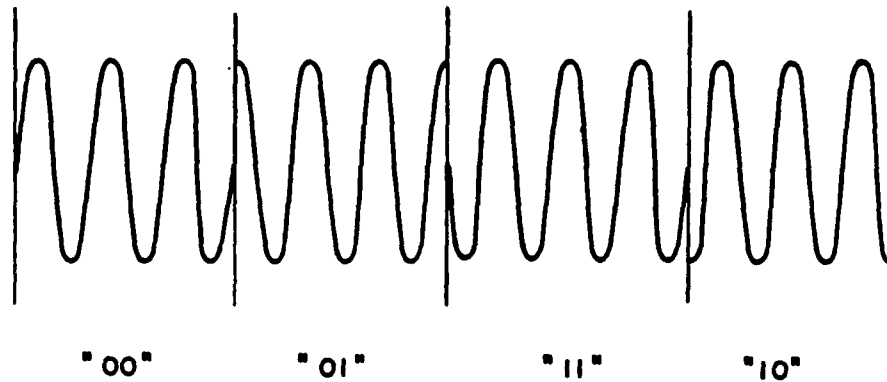


Figure 4.1. A typical QPSK waveform with bit-pair assignments.

B. ARRAY PERFORMANCE

The array performance with QPSK signalling is very similar to that for the BPSK case. The desired signal at the input to the first array element during the n^{th} symbol interval is given by,

$$\tilde{d}(t) = A_d \exp[j\omega_d t + \phi_n(t) + \psi_d], \quad (4.1)$$

where each variable is identical to the corresponding variable in Equation (3.1) except that, for QPSK, $\phi_n(t)$ is equally likely to be any member of the set $\{0, \frac{\pi}{2}, \pi, \frac{3\pi}{2}\}$ during each symbol interval.

It is straightforward to show that the autocorrelation function (and thus the PSD) of the QPSK signal is the same as that for BPSK. We use the same interference and noise models that were used for the BPSK system in Chapter III. Therefore the covariance matrix $\mathbf{\Sigma}$, the

reference correlation vector S , and thus the array weights, are identical to those derived for BPSK in Chapter III. The desired signal, interfering signal and the noise PSD at the array output are given by (3.12), (3.13), and (3.14) respectively, the only exception being that $\phi_n(t)$ can assume four values in the QPSK case.

Since the array calculations for the BPSK and QPSK systems are the same, the only difference in performance for these two systems is due to the difference in detector performance. In the next section we determine the performance of the QPSK detector.

C. QPSK DETECTOR PERFORMANCE WITH CW AND AWGN INTERFERENCE

In this section we derive the performance of an ideal QPSK detector when the QPSK desired signal is corrupted by CW interference and AWGN. The QPSK detector shown in Figure 4.2 [20] is ideal if the only undesired signal is AWGN. This detector is essentially two BPSK detectors in which the reference signals at the two multipliers are in phase quadrature. At the end of the n^{th} symbol interval the integrator outputs, $X(n)$ and $Y(n)$, are examined and a symbol decision is made based upon the values at these outputs. The decision regions for the different symbols are shown in Figure 4.3.

In order to determine the probability of a symbol error we must first calculate the joint statistics of the integrator outputs, $X(n)$ and $Y(n)$. We note that the process by which $X(n)$ is derived is identical to the process by which $X(n)$ was derived for the ideal BPSK detector of Figure 3.3. Therefore, from (4.1) and (3.37) the expression for $X(n)$ is

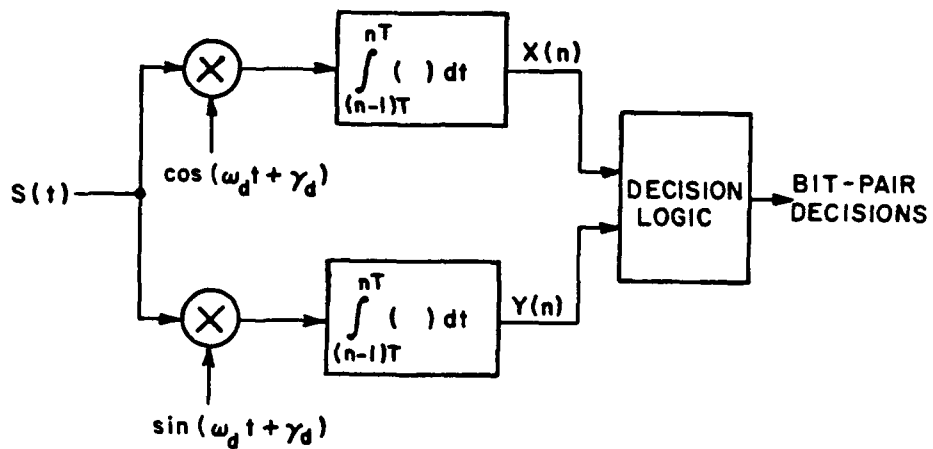


Figure 4.2. The ideal QPSK detector.

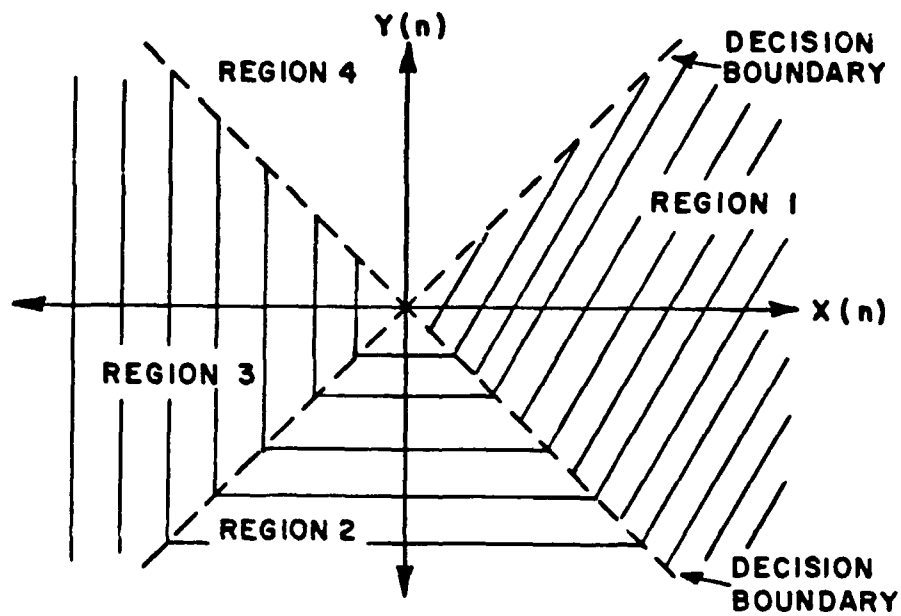


Figure 4.3. QPSK decision space.

immediately found to be

$$\begin{aligned}
 x(n) = & \sqrt{\frac{P_d}{2}} T \cos[\phi_n(t)] \\
 & + \sqrt{\frac{P_i}{2}} T \operatorname{sinc}\left(\frac{\Delta\omega T}{2}\right) \cos\left(\gamma_{rel} + \frac{2n-1}{2} \Delta\omega T\right) + X_n(n)
 \end{aligned} \quad (4.2)$$

where $\phi_n(t)$ is equally likely to be any member of the set $\{0, \frac{\pi}{2}, \pi, \frac{3\pi}{2}\}$ during any symbol interval. The noise term $X_n(n)$ is normally distributed with zero mean and variance $\frac{nT}{4}$ where $\frac{n}{2}$ is the noise PSD at the array output.

We next examine $Y(n)$ which is given by,

$$Y(n) = Y_d(n) + Y_i(n) + Y_n(n) \quad (4.3)$$

where,

$$Y_d(n) = \int_{(n-1)T}^{nT} \sqrt{2P_d} \sin(\omega_d t + \gamma_d) \cos[\omega_d t + \phi_n(t) + \gamma_d] dt, \quad (4.4)$$

$$Y_i(n) = \int_{(n-1)T}^{nT} \sqrt{2P_i} \sin[\omega_d t + \gamma_d] \cos[\omega_i t + \gamma_i] dt, \quad (4.5)$$

and,

$$Y_n(n) = \int_{(n-1)T}^{nT} s_n(t) \sin[\omega_d t + \gamma_d] dt. \quad (4.6)$$

As in Chapter III we evaluate each of these three integrals and then combine the results to determine $Y(n)$.

It is easily shown using techniques very similar to those used to derive (3.22) that $Y_d(n)$ reduces to,

$$Y_d(n) = -\sqrt{\frac{P_d}{2}} T \sin[\phi_n(t)]. \quad (4.7)$$

The second integral to be evaluated, $Y_i(n)$, is given by,

$$Y_i(n) = \sqrt{\frac{P_i}{2}} \int_{(n-1)T}^{nT} \sin[(\omega_d + \omega_i)t + \gamma_d + \gamma_i] \\ + \sin[(\omega_d - \omega_i)t + \gamma_d - \gamma_i] dt. \quad (4.8)$$

After we drop the double frequency term we have,

$$Y_i(n) = \sqrt{\frac{P_i}{2}} \int_{(n-1)T}^{nT} \sin(\Delta\omega t + \gamma_{rel}) dt, \quad (4.9)$$

where $\Delta\omega$, γ_{rel} , and T are defined as in Chapter III. Evaluating this integral we have

$$Y_i(n) = \sqrt{\frac{P_i}{2}} \left(\frac{1}{\Delta\omega}\right) [\cos(n\Delta\omega T + \gamma_{rel}) - \cos((n-1)\Delta\omega T + \gamma_{rel})]. \quad (4.10)$$

Standard trigonometric identities can be used to simplify this equation to,

$$Y_i(n) = \sqrt{\frac{P_i}{2}} T \text{sinc}\left(\frac{\Delta\omega T}{2}\right) \sin\left(\gamma_{rel} + \frac{2n-1}{2} \Delta\omega T\right). \quad (4.11)$$

We denote the noise signal at the integrator output at the end of the n^{th} symbol interval by $Y_n(n)$. Using an analysis nearly identical to that used to derive the statistics of $X_n(n)$ as in Chapter III it is straightforward to show that $Y_n(n)$ is a zero mean Gaussian random variable with variance $\frac{\eta T}{4}$.

Furthermore, if we assume that the PSD of the noise at the detector input is symmetric about ω_d , then $X_n(n)$ and $Y_n(n)$ will be independent of

each other at the end of each symbol interval. This property is easily shown using the standard decomposition of narrowband noise into quadrature components [22]. The values of $X_n(n)$, $Y_n(n)$, $X(m)$, and $Y(m)$ will be uncorrelated (and thus independent) for $m \neq n$.

The desired, interfering, and noise signals at the integrator output can now be combined using (4.3), (4.7) and (4.11) yielding,

$$Y(n) = -\gamma \sqrt{\frac{P_d}{2}} T \sin[\phi_n(t)] + \gamma \sqrt{\frac{P_i}{2}} T \operatorname{sinc}\left(\frac{\Delta\omega T}{2}\right) \sin(\gamma_{\text{rel}} + \frac{2n-1}{2} \Delta\omega T) + Y_n(n), \quad (4.13)$$

where $Y_n(n)$ is a zero mean normal random variable with variance $\frac{\eta T}{4}$.

The probability of a symbol error can be calculated using the expressions for $X(n)$ and $Y(n)$ given by (4.2) and (4.13), and the decision regions shown in Figure 4.3. If we assume equally likely symbols, then $P(e)$ is given by

$$P(e) = \frac{1}{4} [P[e|\phi_n(t)=0] + P[e|\phi_n(t) = \frac{\pi}{2}] + P[e|\phi_n(t)=\pi] + P[e|\phi_n(t) = \frac{3\pi}{2}]] \quad (4.14)$$

The symmetry of the decision regions and the distribution of $X(n)$ and $Y(n)$ insure that the probability of a symbol error is independent of which symbol is transmitted (for equally likely symbols). Therefore the probability of error is,

$$P(e) = P[e|\phi_n(t) = 0] \quad (4.15)$$

If $\phi_n(t) = 0$ then $X(n)$ and $Y(n)$ become,

$$X(n) = \sqrt{\frac{P_d}{2}} T + \sqrt{\frac{P_i}{2}} T \text{sinc}\left(\frac{\Delta\omega T}{2}\right) \cos\left(\gamma_{rel} + \frac{2n-1}{2} \Delta\omega T\right) + X_n(n), \quad (4.16)$$

and,

$$Y(n) = \sqrt{\frac{P_i}{2}} T \text{sinc}\left(\frac{\Delta\omega T}{2}\right) \sin\left(\gamma_{rel} + \frac{2n-1}{2} \Delta\omega T\right) + Y_n(n). \quad (4.17)$$

The problem of calculating $P(e)$ for QPSK given $X(n)$ and $Y(n)$ is very similar to a problem addressed by Rosenbaum [18] and we shall use similar notation and procedures for ease of comparison. We first normalize $X(n)$ and $Y(n)$ by dividing each by $\sqrt{\frac{P_d}{2}} T$ yielding

$$X' = 1 + b \cos\left(\gamma_{rel} + \frac{2n-1}{2} \Delta\omega T\right) + n_x, \quad (4.18)$$

and,

$$Y' = b \sin\left(\gamma_{rel} + \frac{2n-1}{2} \Delta\omega T\right) + n_y, \quad (4.19)$$

where,

$$b = \sqrt{\frac{P_i}{P_d}} \text{sinc}\left(\frac{\Delta\omega T}{2}\right), \quad (4.20)$$

and n_x and n_y are independent and identically distributed normal random variables with zero mean and variance,

$$\begin{aligned} \sigma_{xy}^2 &= \frac{(nT/4)}{(P_d T^2/2)} \\ &= \frac{1}{(2E_d/n)}. \end{aligned} \quad (4.20)$$

The normalized variables X' and Y' are shown on the decision space diagram in Figure 4.4.

Since X' and Y' are independent jointly Gaussian random variables, their joint probability density function (PDF) conditioned on γ_{rel} is,

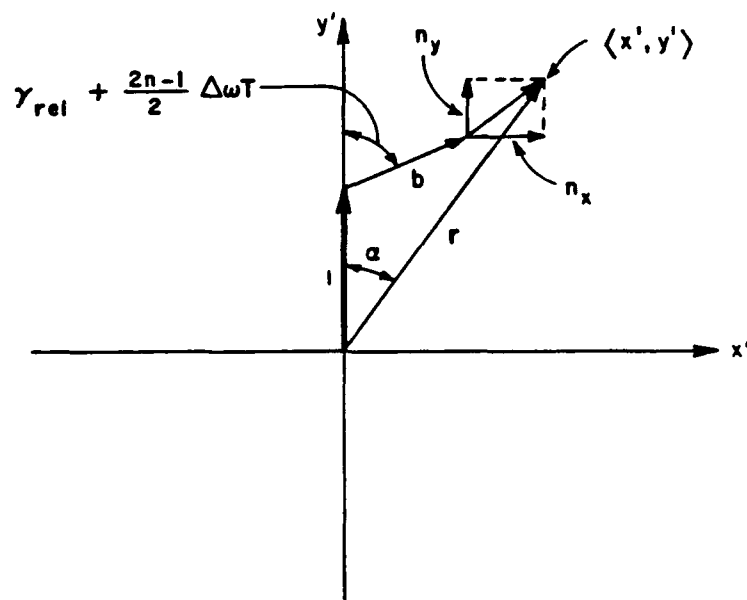


Figure 4.4. Normalized decision space showing composite received signal.

$$f_{xy}(X', Y' | \gamma_{rel}) = \frac{1}{2\pi\sigma_{xy}^2} \exp \left[\frac{-1}{2\sigma_{xy}^2} [(X' - b \sin \gamma)^2 + (Y' - 1 - b \cos \gamma)^2] \right] \quad (4.21)$$

where,

$$\gamma = \gamma_{rel} + \left(\frac{\Delta\omega T}{2} \right). \quad (4.22)$$

After eliminating the dependence of this PDF on γ by integrating the product of $f_{xy}(X', Y' | \gamma_{rel})$ and $\frac{1}{2\pi}$ (the PDF of the uniformly distributed variable γ) we have,

$$f_{xy}(X', Y') = \left(\frac{1}{2\pi\sigma_{xy}}\right)^2 \exp\left[\frac{-1}{2\sigma_{xy}^2} [(X'^2 + (Y'-1)^2 + b^2)]\right] \\ \cdot \int_0^{2\pi} \exp\left[\frac{b}{\sigma_{xy}^2} [\sqrt{X'^2 + (Y'-1)^2} \cos(\gamma+\Gamma)]\right] d\gamma, \quad (4.23)$$

where $\Gamma = -\cot^{-1} \frac{(Y'-1)}{X'}$ is not a function of γ .

This expression can be simplified after we recognize the integral to give us

$$f_{xy}(X', Y') = \left(\frac{1}{2\pi\sigma_{xy}}\right)^2 \exp\left[\frac{-1}{2\sigma_{xy}^2} [(X'^2 + (Y'-1)^2 + b^2)]\right] \\ \cdot I_0\left\{\frac{b}{2\sigma_{xy}^2} \sqrt{X'^2 + (Y'-1)^2}\right\}, \quad (4.24)$$

where I_0 is the modified Bessel function of the first kind of order zero.

We can now change from rectangular to polar coordinates using the transformation,

$$X = r \sin(\alpha), \quad (4.25)$$

and,

$$Y = r \cos(\alpha). \quad (4.26)$$

The geometrical interpretation of r and α is shown in Figure 4.4. To implement the transformation we perform the indicated change of variables, and multiply the resulting function by the Jacobian of the transformation, r . We can then eliminate the dependency on r by integrating the density over all possible values of r . The resulting expression will be the probability density function of the angle α . This PDF is given by,

$$f_{\alpha}(\alpha) = \frac{1}{2\pi\sigma_{xy}^2} \int_0^{\infty} \exp \left[\frac{-1}{2\sigma_{xy}^2} [r^2 + b^2 + 1 - 2rcos\alpha] \right] \cdot I_0 \left\{ \frac{b}{\sigma_{xy}^2} \sqrt{r^2 + 1 - 2rcos\alpha} \right\} r dr. \quad (4.27)$$

The probability of error, $P(e)$ will be given by the probability that α does not lie between $\frac{-\pi}{4}$ and $\frac{\pi}{4}$ when $\phi_n(t) = 0$. Thus $P(e)$ is given by,

$$P(e) = \int_{-\pi}^{-\pi/4} f_{\alpha}(\alpha) d\alpha + \int_{\pi/4}^{\pi} f_{\alpha}(\alpha) d\alpha \quad (4.28)$$

From the symmetry of the integrand it is seen that (4.28) can be rewritten,

$$P(e) = 2 \int_{\pi/4}^{\pi} f_{\alpha}(\alpha) d\alpha \quad (4.29)$$

Equation (4.29) was evaluated numerically for several SNR and INR values. Figures 4.5 and 4.6 show results of these calculations for $\Delta\omega T = 0$. Simpson's rule was used to evaluate the integral where the Bessel function was evaluated by a combination of polynomial and asymptotic approximations. From Figures 4.5 and 4.6 we see that these curves are similar to the curves shown in Chapter III for BPSK. However, $P(e)$, the probability of a symbol error is higher for QPSK. We should remember that each symbol in the QPSK symbol stream represents two bits of information. Thus, for QPSK, it is possible for one symbol error to produce two bit errors.*

* The probability of two bits being in error for a given symbol is very small if the bit pair assignments for the decision regions are chosen properly. If they are chosen so that only one bit differs for any two adjacent regions then both $X(n)$ and $Y(n)$ must be simultaneously large to produce a double bit error.

P (E) VS. SNR

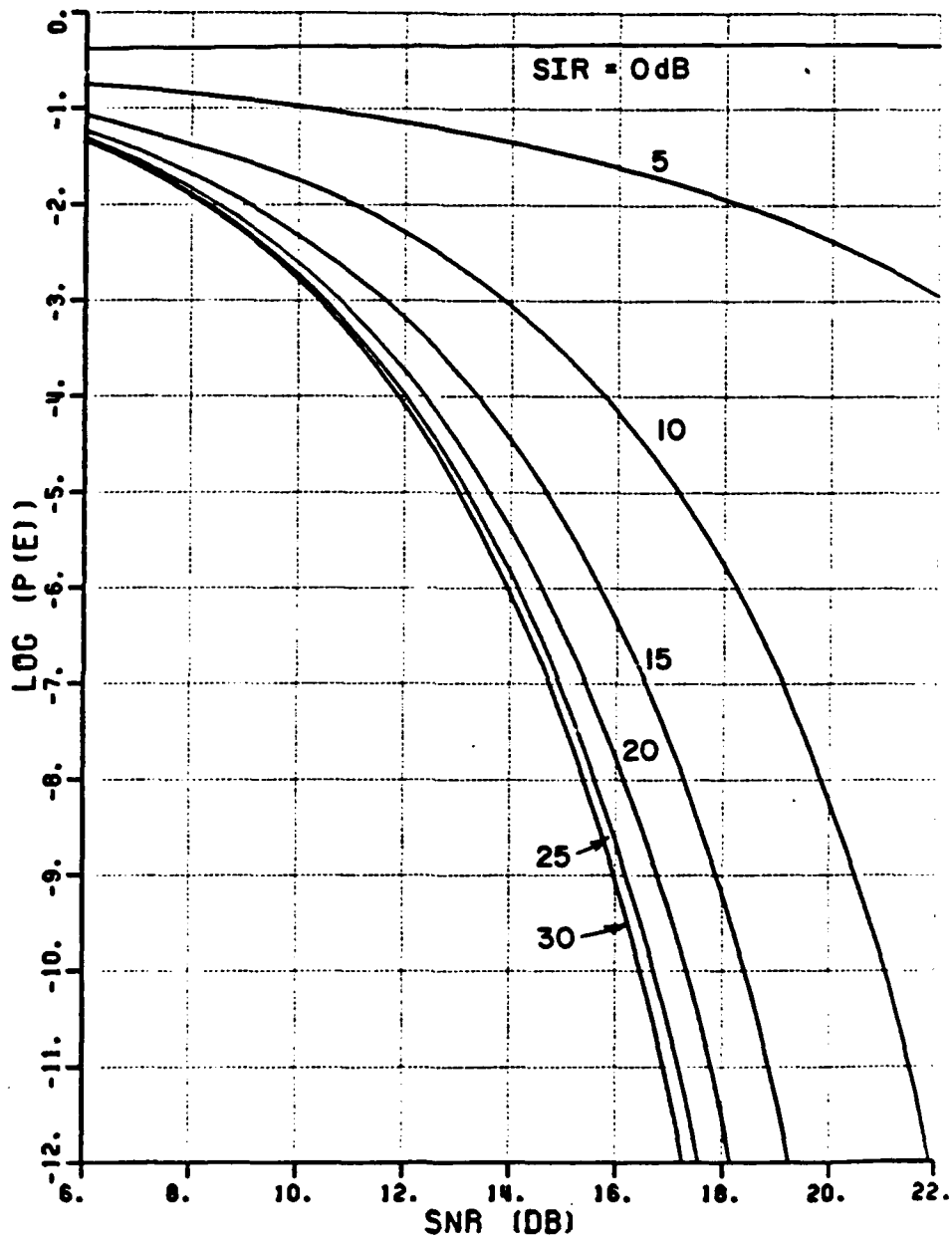


Figure 4.5. Performance of ideal QPSK detector with CW interference ($\Delta\omega T=0$).

P (E) VS. INR

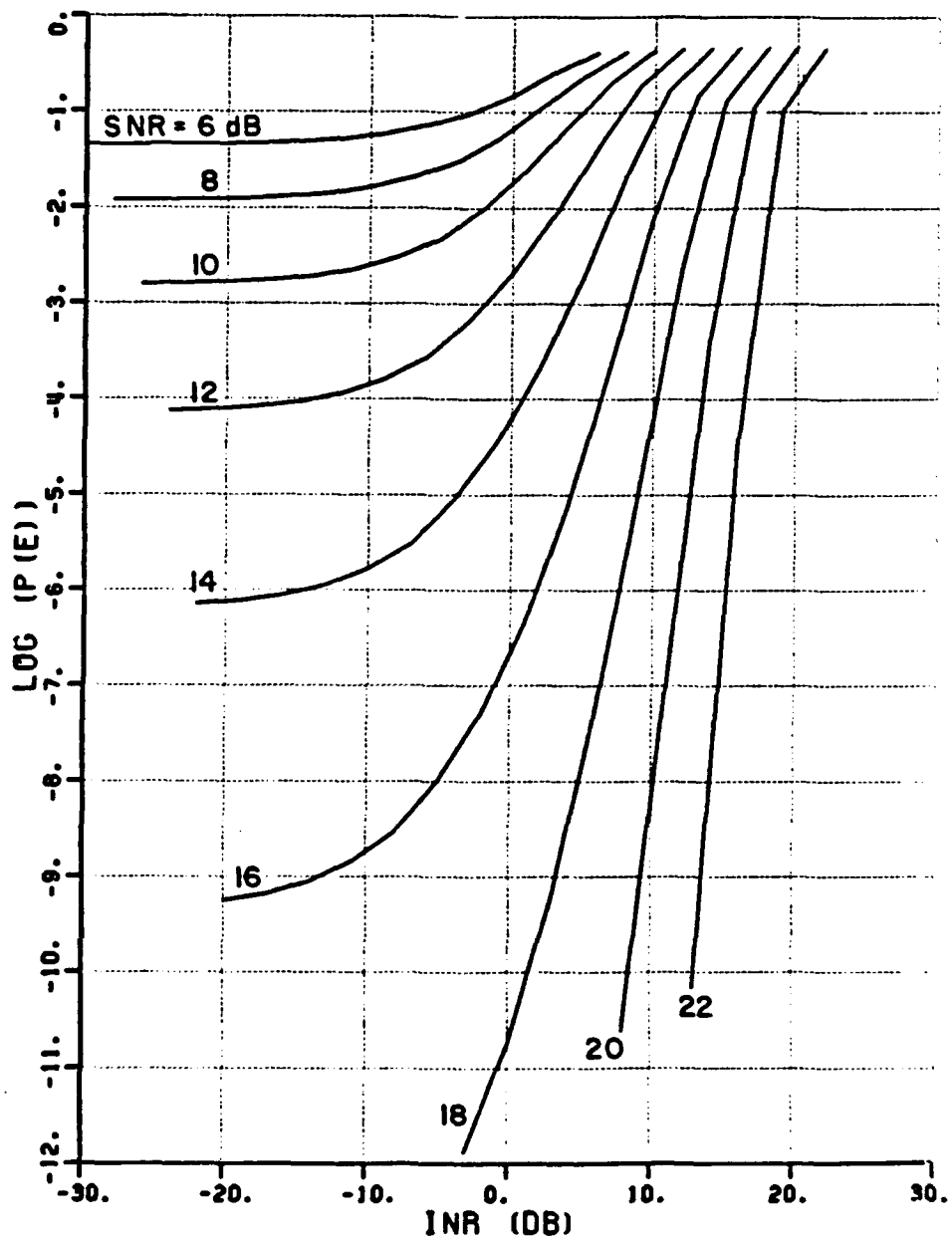


Figure 4.6. Performance of ideal QPSK detector with CW interference ($\Delta\omega T=0$).

It should be noted that the detector shown in Figure 4.2 is the ideal detector for M-ary PSK with AWGN. The only change required is the division of the decision space into M regions. The probability of error for M-ary PSK is given by (4.29) with the lower limit of integration changed to $\frac{\pi}{M}$.

D. PERFORMANCE OF THE COMBINED LMS ARRAY/QPSK DETECTOR

In this section we combine the results of the previous two sections in order to determine the overall performance of a QPSK detector that is preceded by an LMS adaptive array. Again in this section we find that the required derivations closely parallel those of the corresponding Section in Chapter III. In fact, the results from the beginning of section D of Chapter III apply exactly through Equation (3.56). Thus the adaptive array calculations are identical for BPSK and QPSK signalling. The only difference in the performance of the two systems is caused by the differences in the BPSK and QPSK detectors.

The performance of the LMS array/QPSK detector was calculated for several scenarios. Results are shown in Figure 4.7 through 4.20. The scenarios examined correspond one-to-one with the curves shown in Figures 3.7 through 3.20. Figures 4.7 and 4.8 show the system performance with $\theta_d = 0^\circ$, $\theta_i = 10^\circ$, the array bandwidth factor $k = 5$, and the interference phase-offset-per-symbol ($\Delta\omega T$) equal to zero.

Figures 4.9 through 4.12 show similar results for θ_i values of 20 and 80 degrees. From these figures we see that the QPSK performance curves are shaped similarly to those for BPSK. However, the QPSK symbol error probability is higher in each case.

P (E) VS. SNR

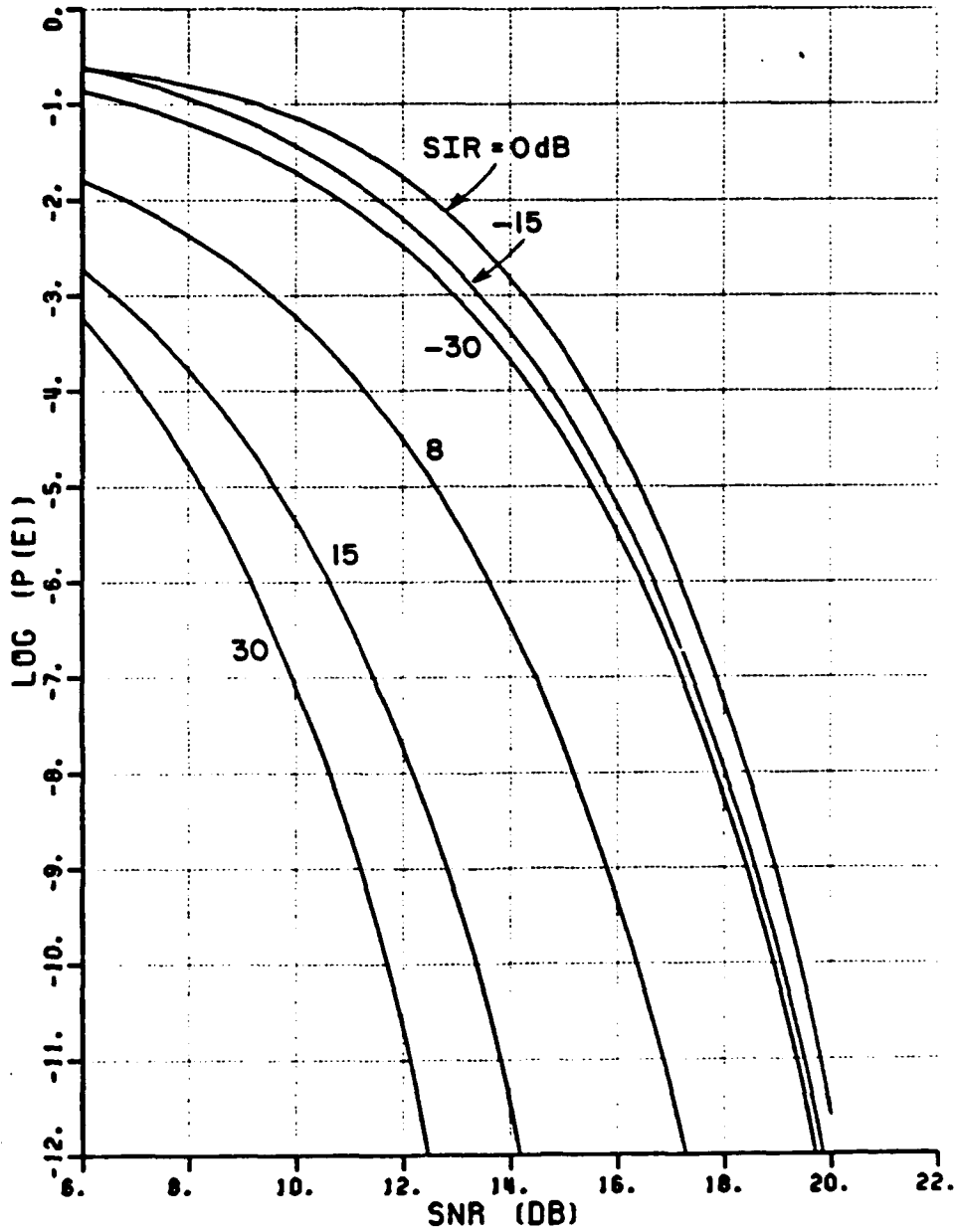


Figure 4.7. QPSK $P(e)$ vs. SNR for 3-element array ($\theta_i=10^\circ$, $k=5$, $\Delta\omega T=0$).

P (E) VS. INR

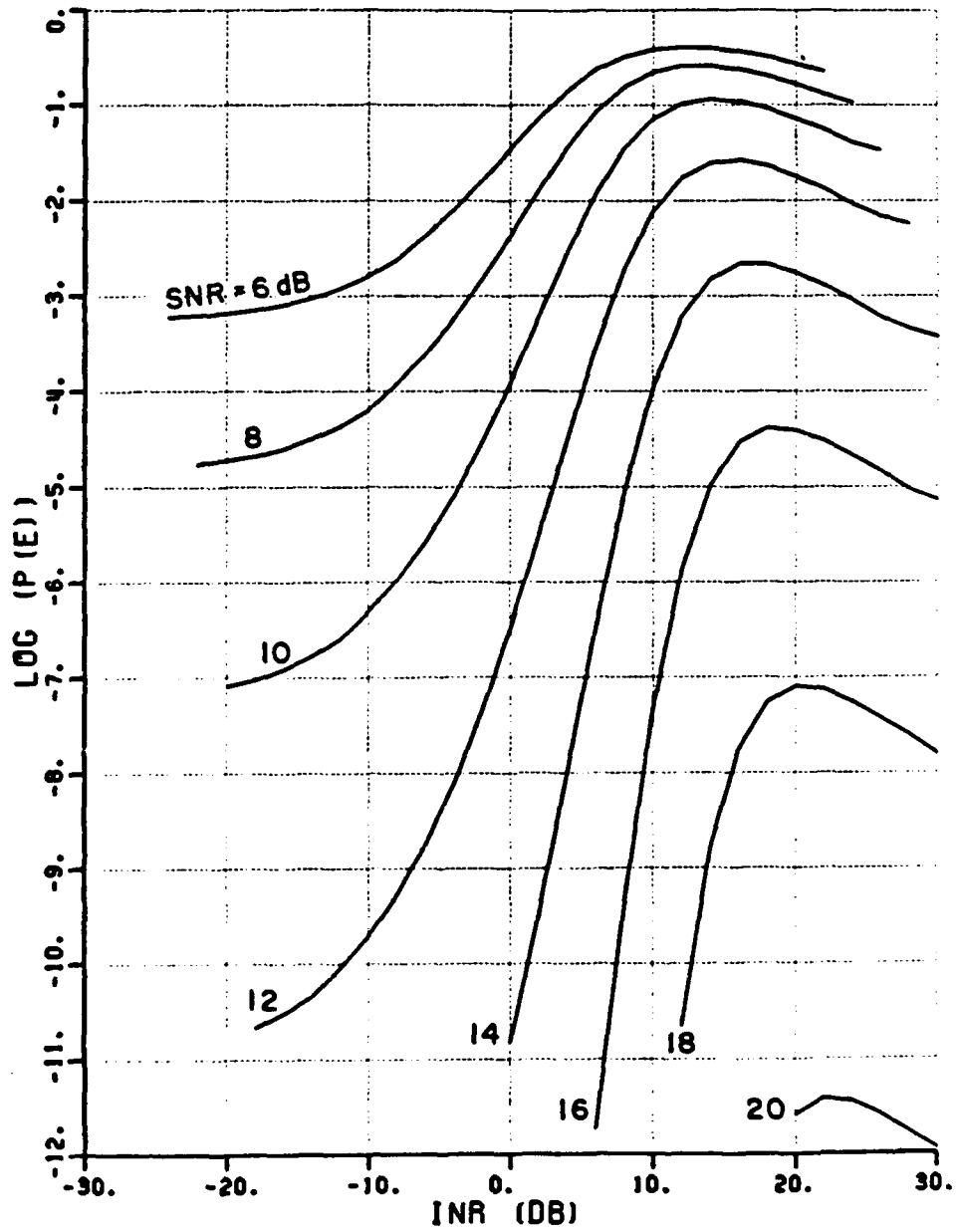


Figure 4.8. QPSK $P(e)$ vs. INR for 3-element array ($\theta_i=10^\circ$, $k=5$, $\Delta\omega T=0$).

P (E) VS. SNR

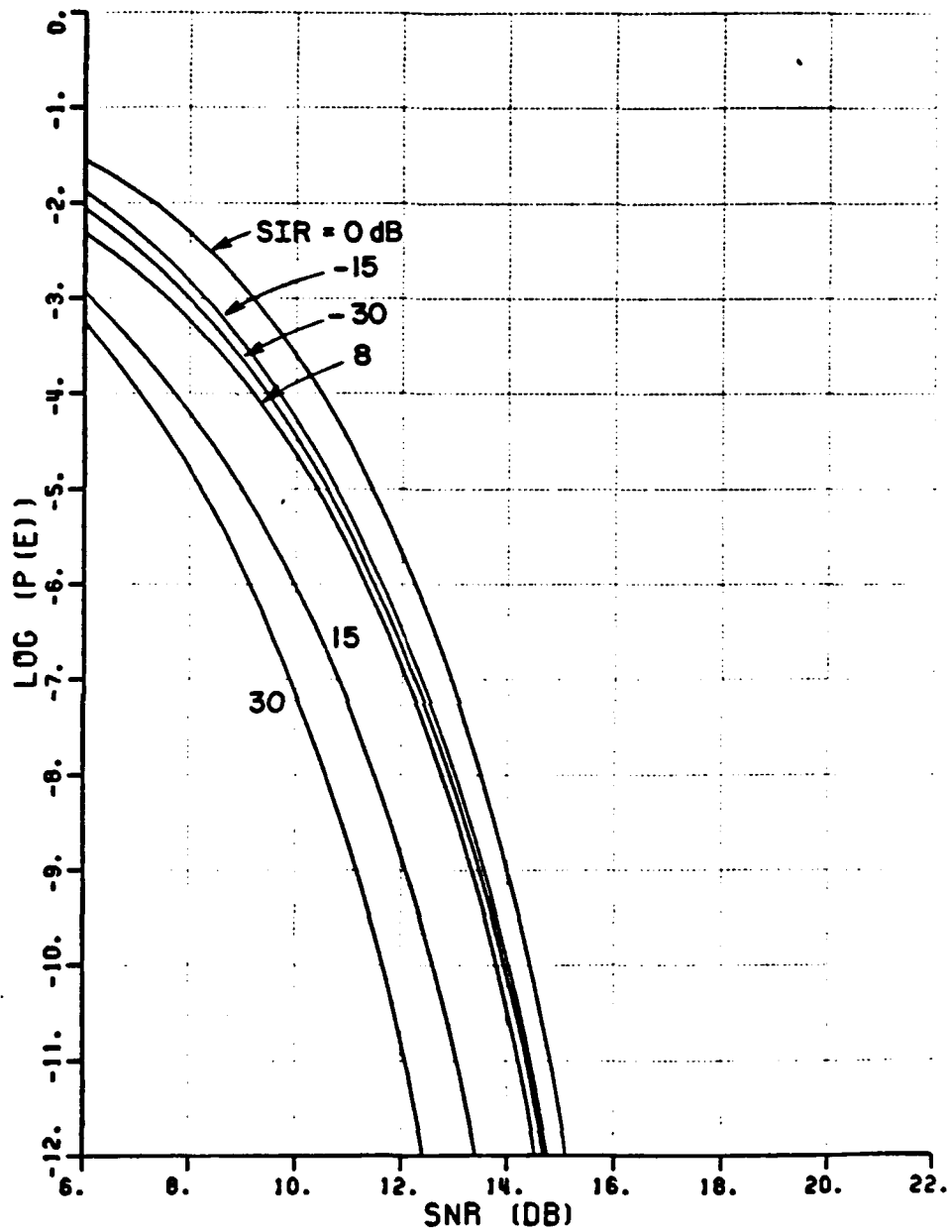


Figure 4.9. QPSK P(e) vs. SNR for 3-element array ($\theta_i=20^\circ$, $k=5$, $\Delta\omega T=0$).

P (E) VS. INR

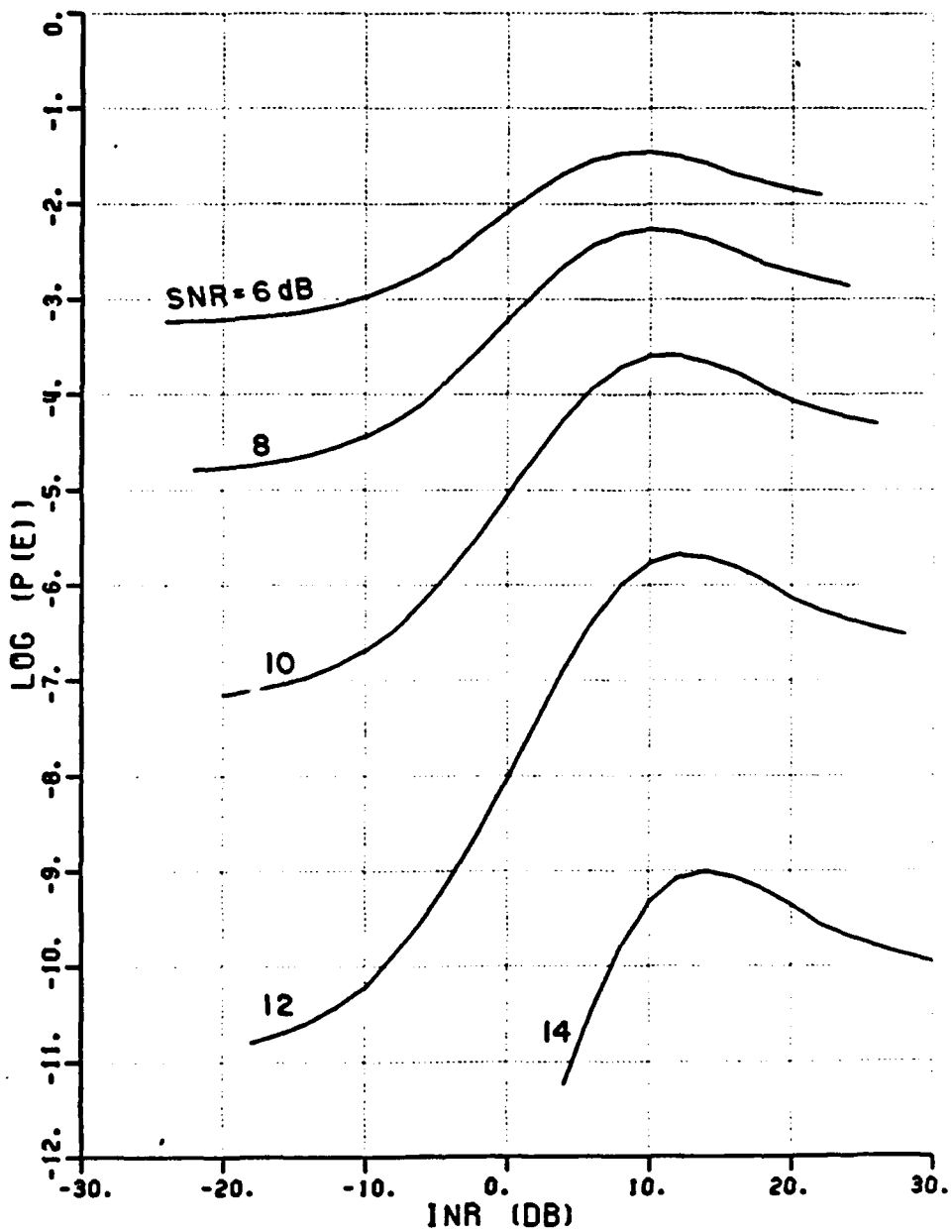


Figure 4.10. QPSK $P(e)$ vs. INR for 3-element array ($\theta_i=20^\circ$, $k=5$, $\Delta\omega T=0$).

P (E) VS. SNR

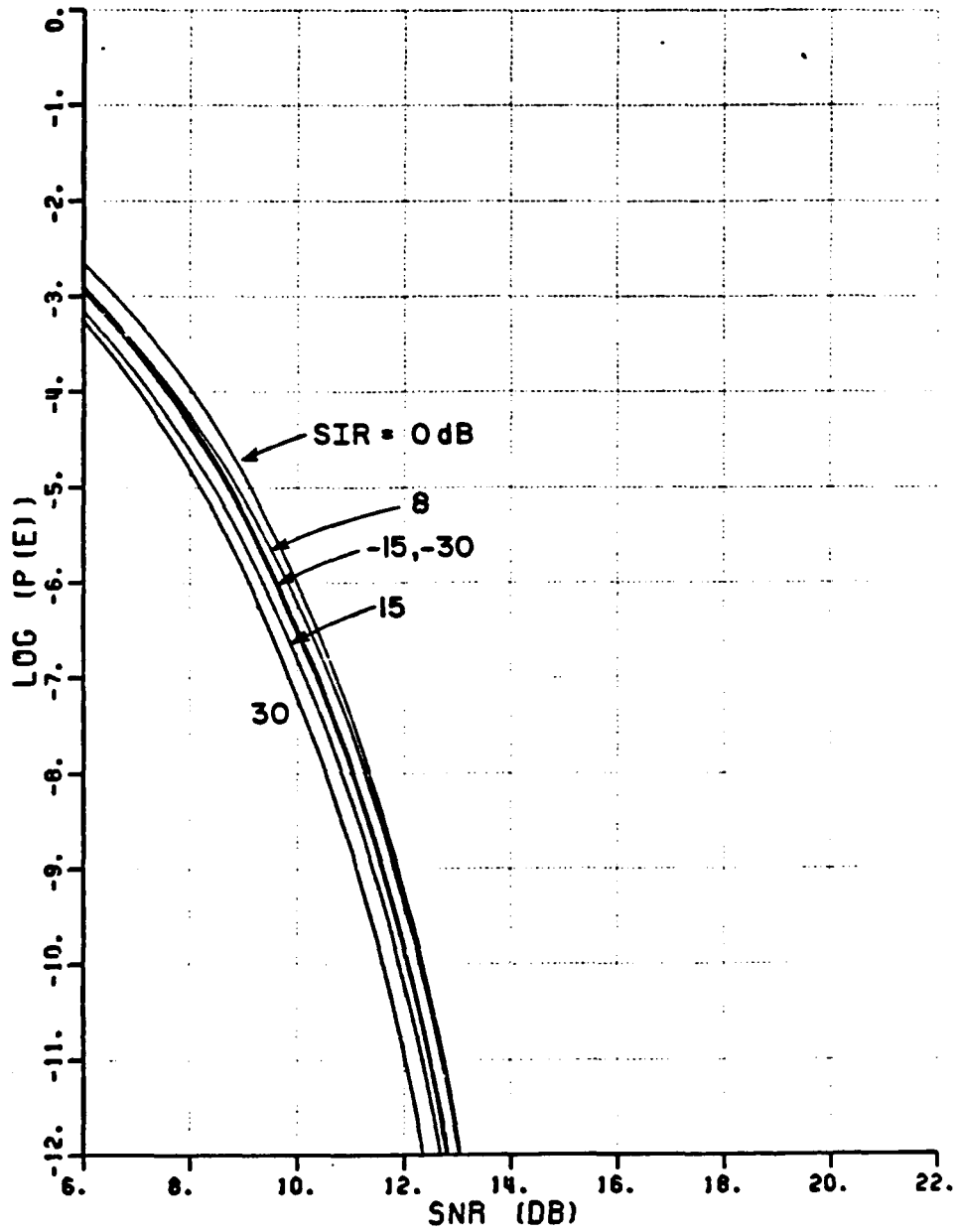


Figure 4.11. QPSK P(e) vs. SNR for 3-element array ($\psi_1=80^\circ$, $\kappa=5$, $\Delta\omega T=0$).

P (E) VS. INR

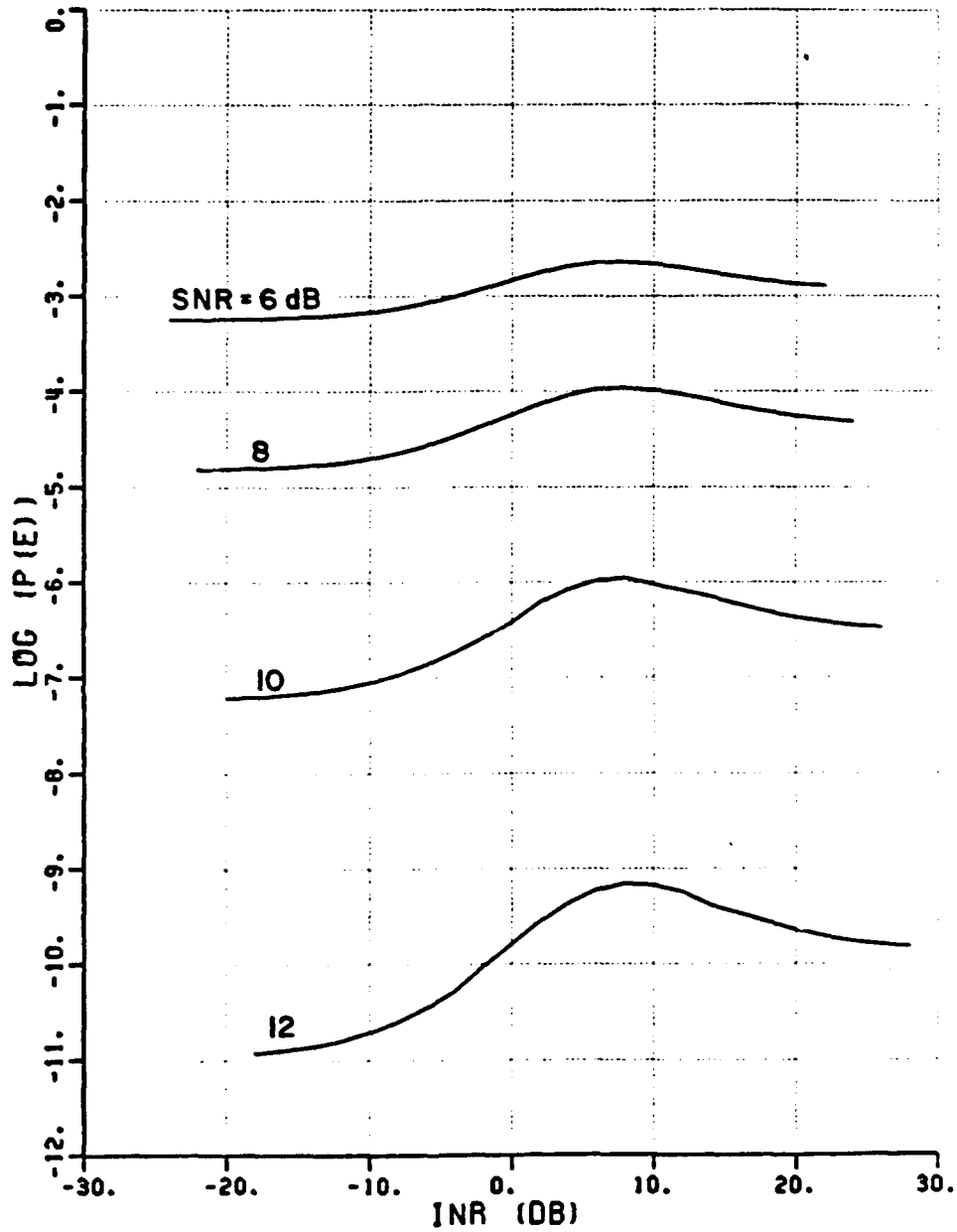


Figure 4.12. QPSK $P(e)$ vs. INR for 3-element array ($\theta_i=80^\circ$, $k=5$, $\Delta\omega T=0$).

Figures 4.13 through 4.18 show the system performance with the array bandwidth factor k , increased to 10 with all other variables the same as in Figures 4.7 through 4.12. Figures 4.19 and 4.20 show the performance with the interference phase-shift-per-symbol $\Delta\omega T$ set equal to π . Again in these cases we see that the system performance is similar to, but slightly worse than, the BPSK system of Chapter III.

The qualitative descriptions of the system behavior are identical for the BPSK and QPSK cases and the discussion at the end of Chapter III applies directly to the QPSK case. The only difference in the two cases is the uniformly poorer performance of the QPSK case. In return for this performance degradation, QPSK offers a bit rate double that of BPSK for a fixed signal bandwidth.

P (E) VS. SNR

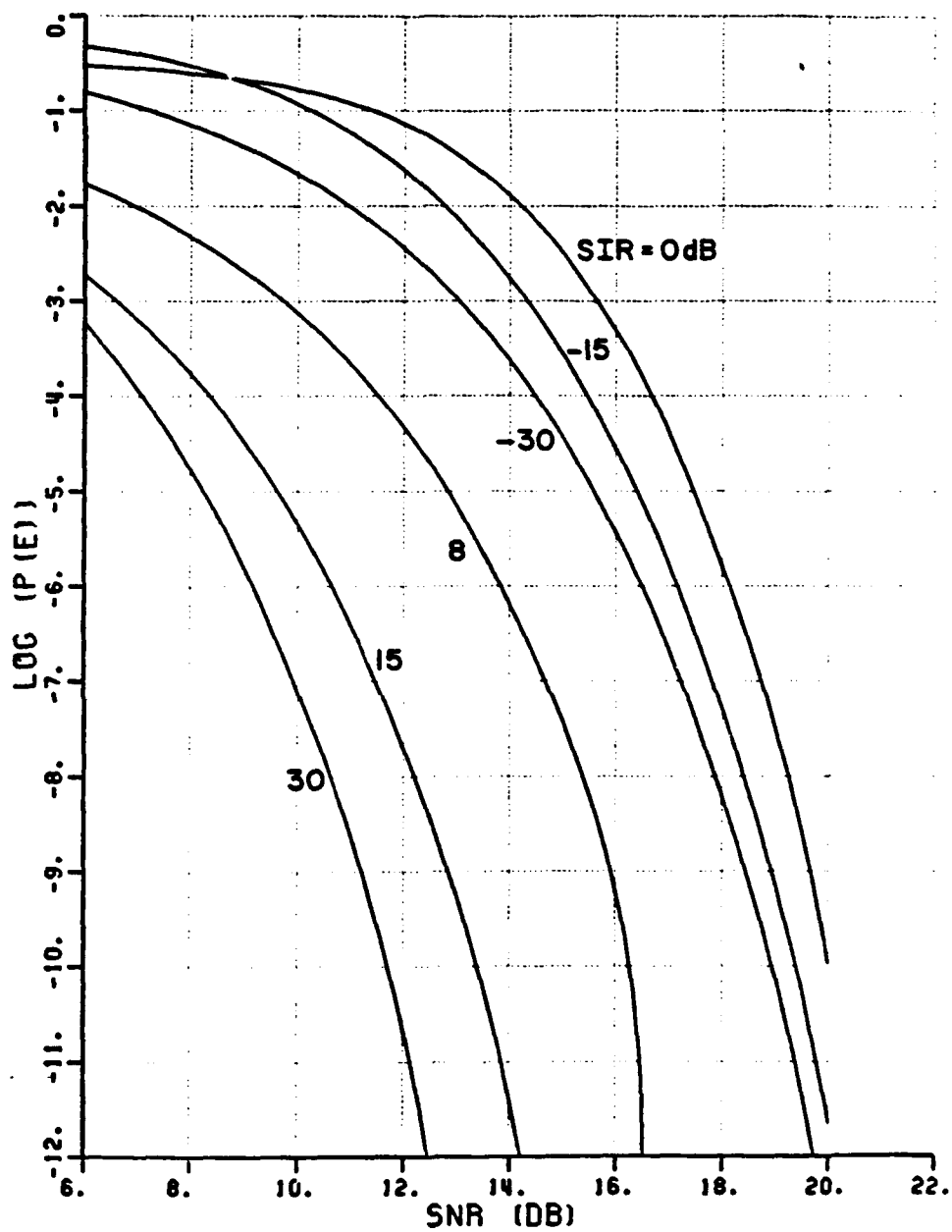


Figure 4.13. QPSK $P(e)$ vs. SNR for 3-element array ($\theta_i=10^\circ$, $k=10$, $\Delta\omega T=0$).

P (E) VS. INR

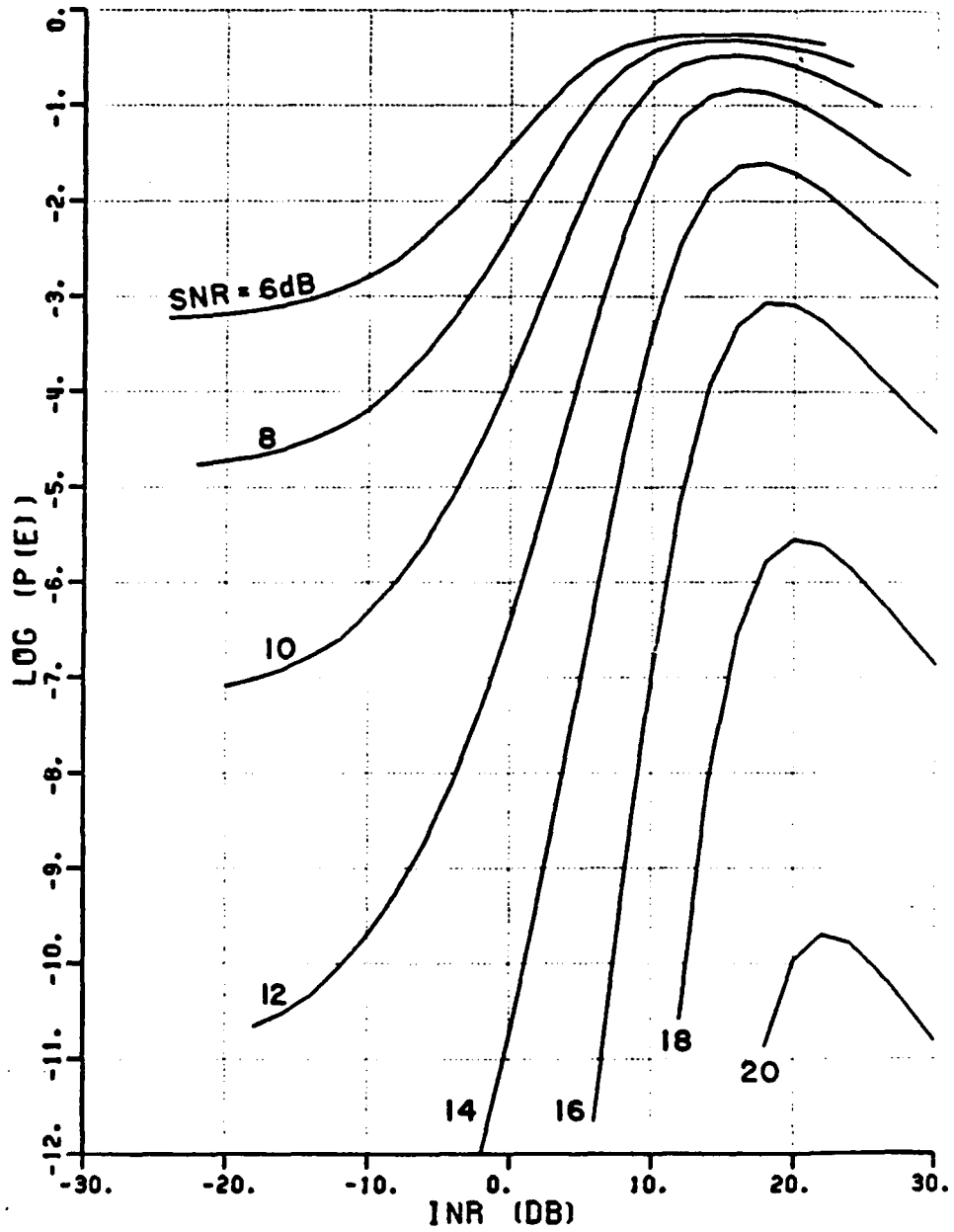


Figure 4.14. γ PSK $P(e)$ vs. INR for 3-element array ($\theta_i=10^\circ$, $k=10$, $\Delta\omega T=0$).

P (E) VS. SNR

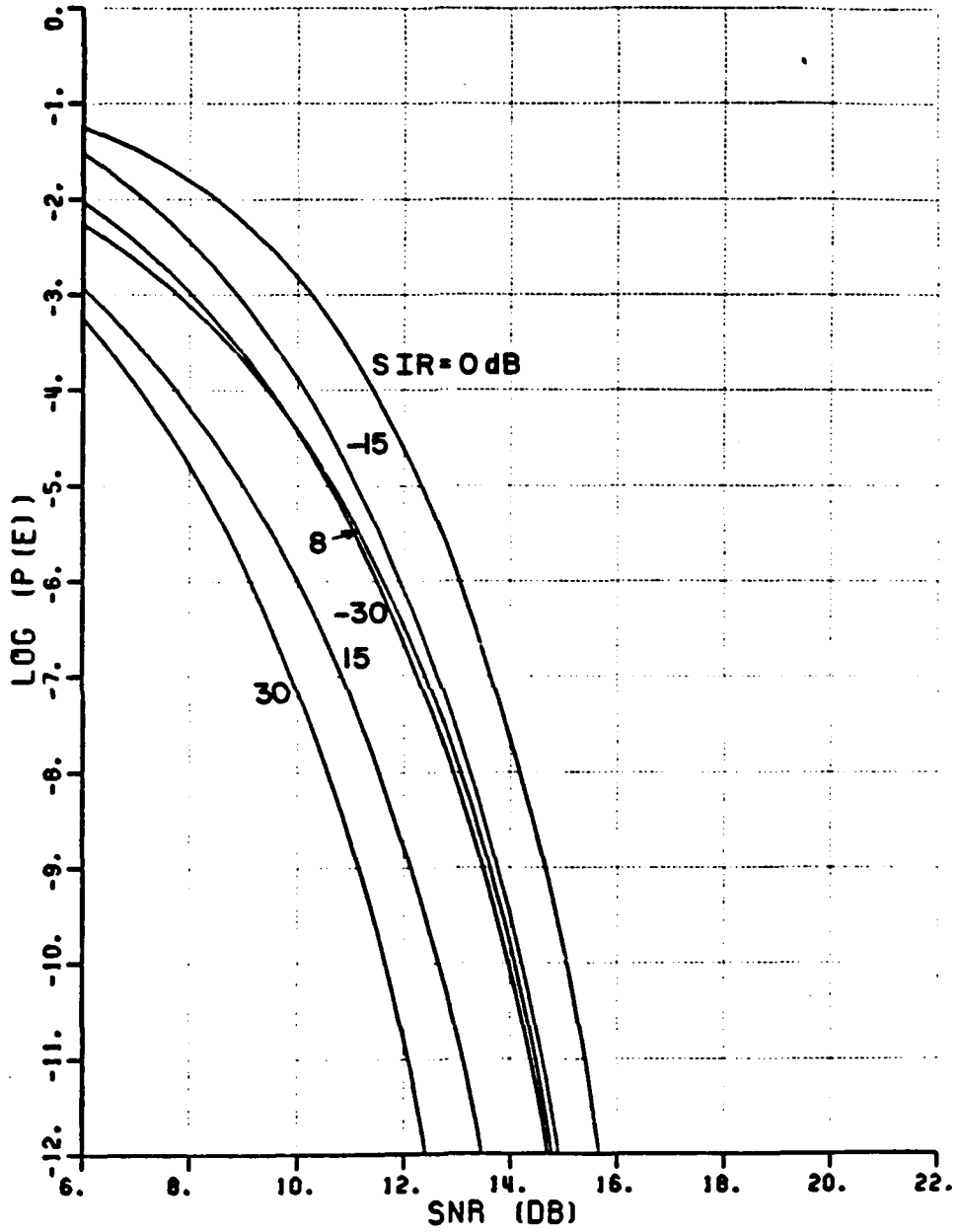


Figure 4.15. QPSK P(e) vs. SNR for 3-element array ($\theta_i=20^\circ$, $k=10$, $\Delta\omega T=0$).

P (E) VS. INR

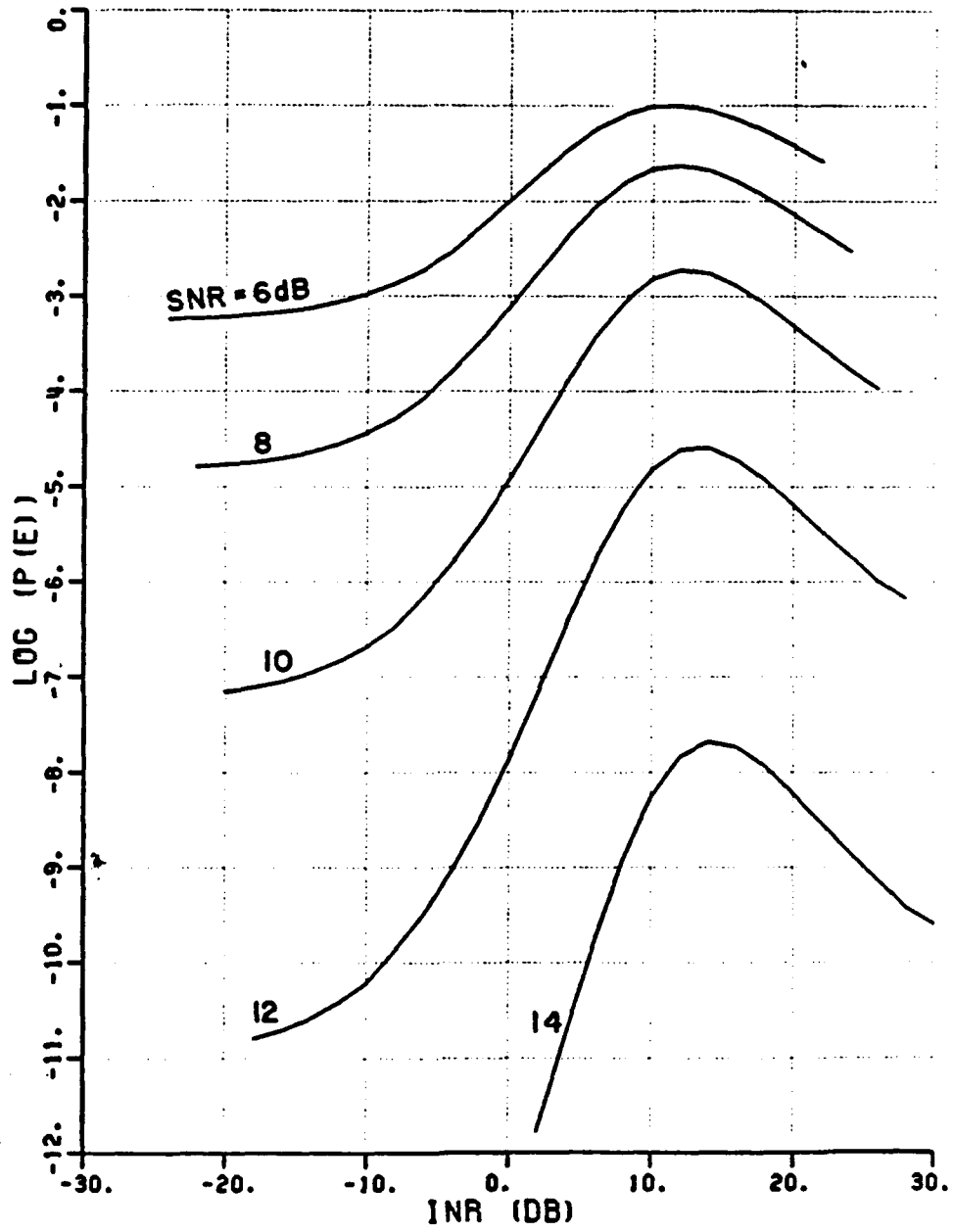


Figure 4.16. QPSK $P(e)$ vs. INR for 3-element array ($\theta_i=20^\circ$, $k=10$, $\Delta\omega T=0$).

P (E) VS. SNR

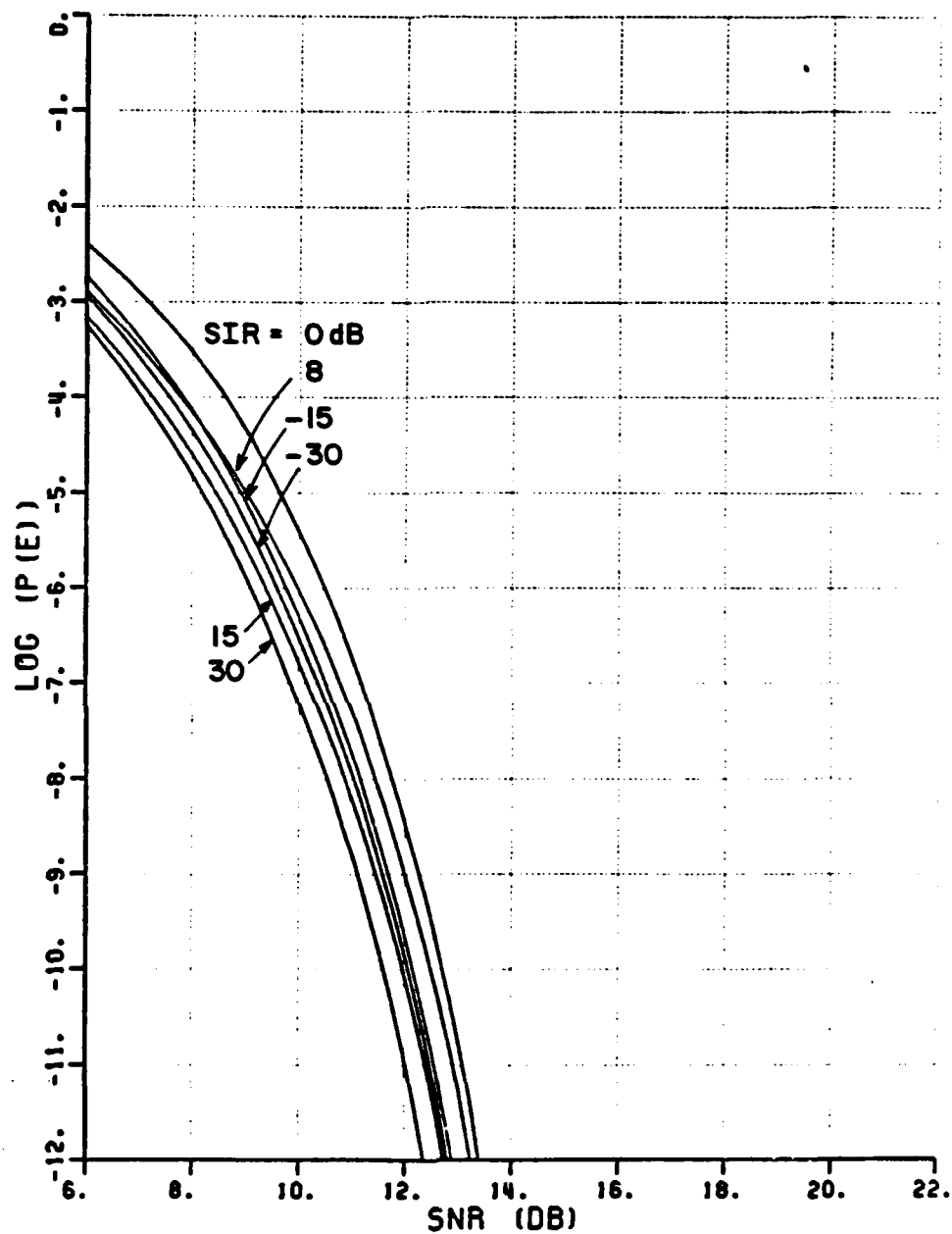


Figure 4.17. QPSK P(e) vs. SNR for 3-element array ($\theta_i=80^\circ$, $k=10$, $\Delta\omega T=0$).

P (E) VS. INR

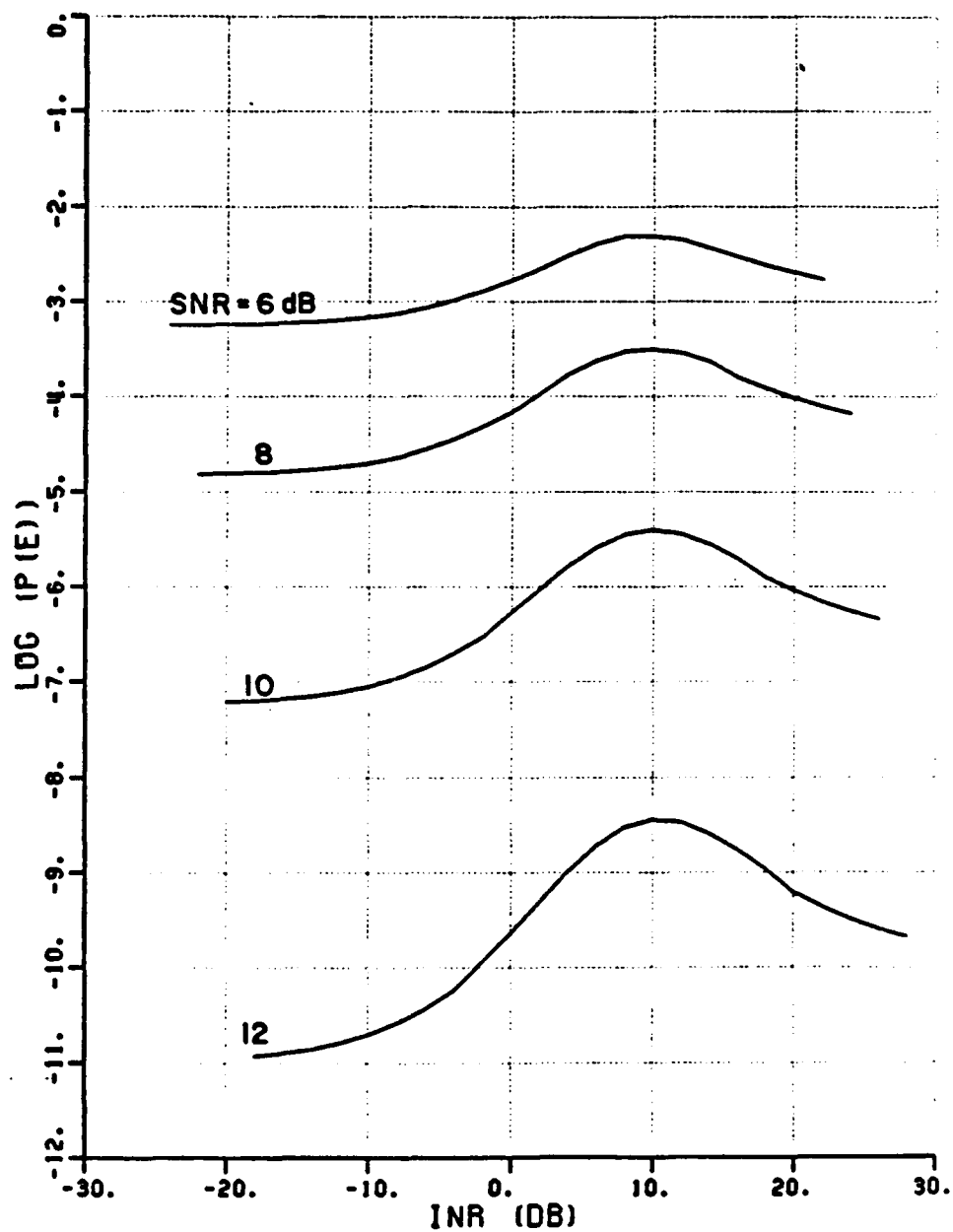


Figure 4.18. QPSK $P(e)$ vs. INR for 3-element array ($\theta_i=80^\circ$, $k=10$, $\Delta\omega T=0$).

P (E) VS. SNR

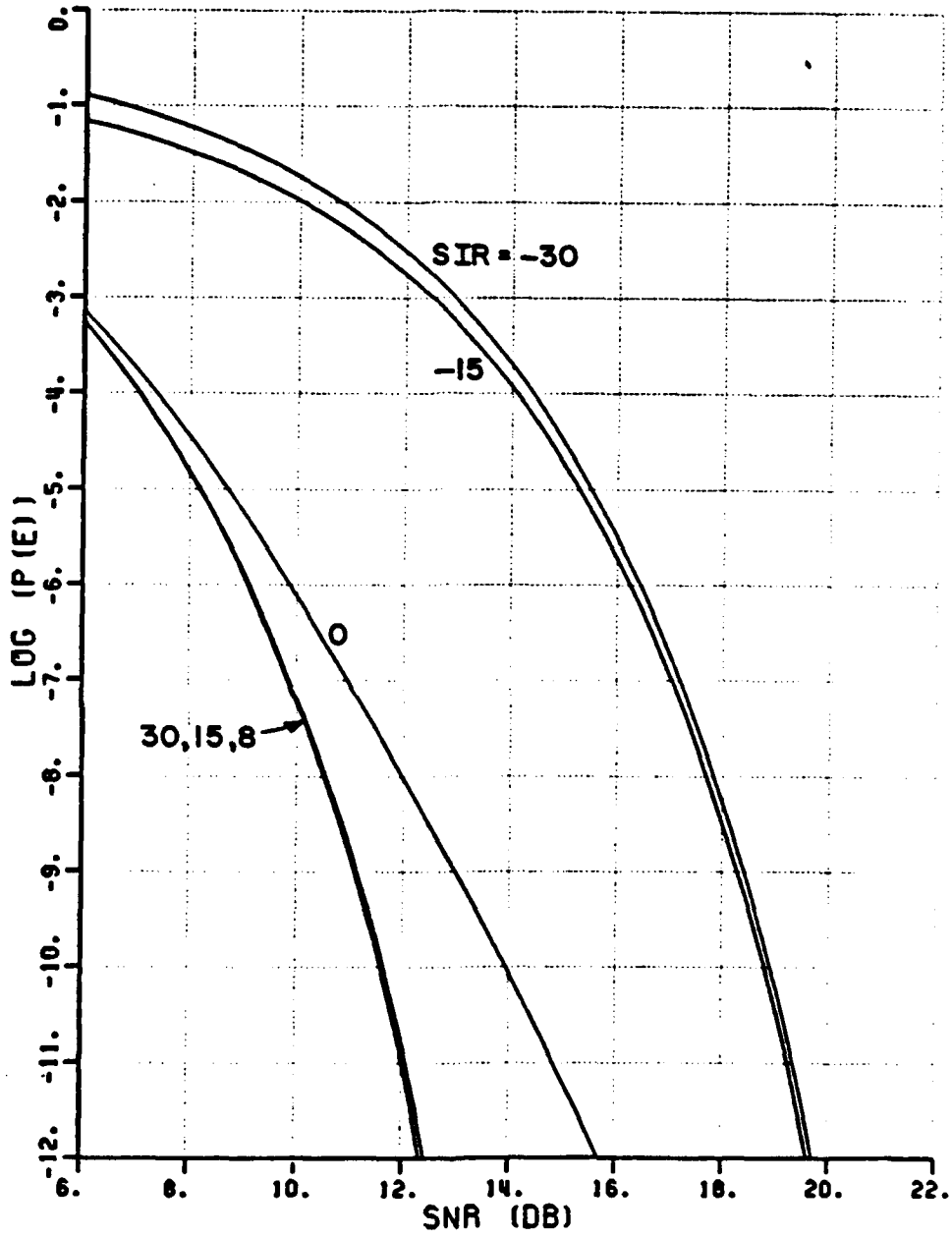


Figure 4.19. QPSK $P(e)$ vs. SNR for 3-element array ($\theta_1=10^\circ$, $k=10$, $\Delta\omega T=2\pi$).

P (E) VS. INR

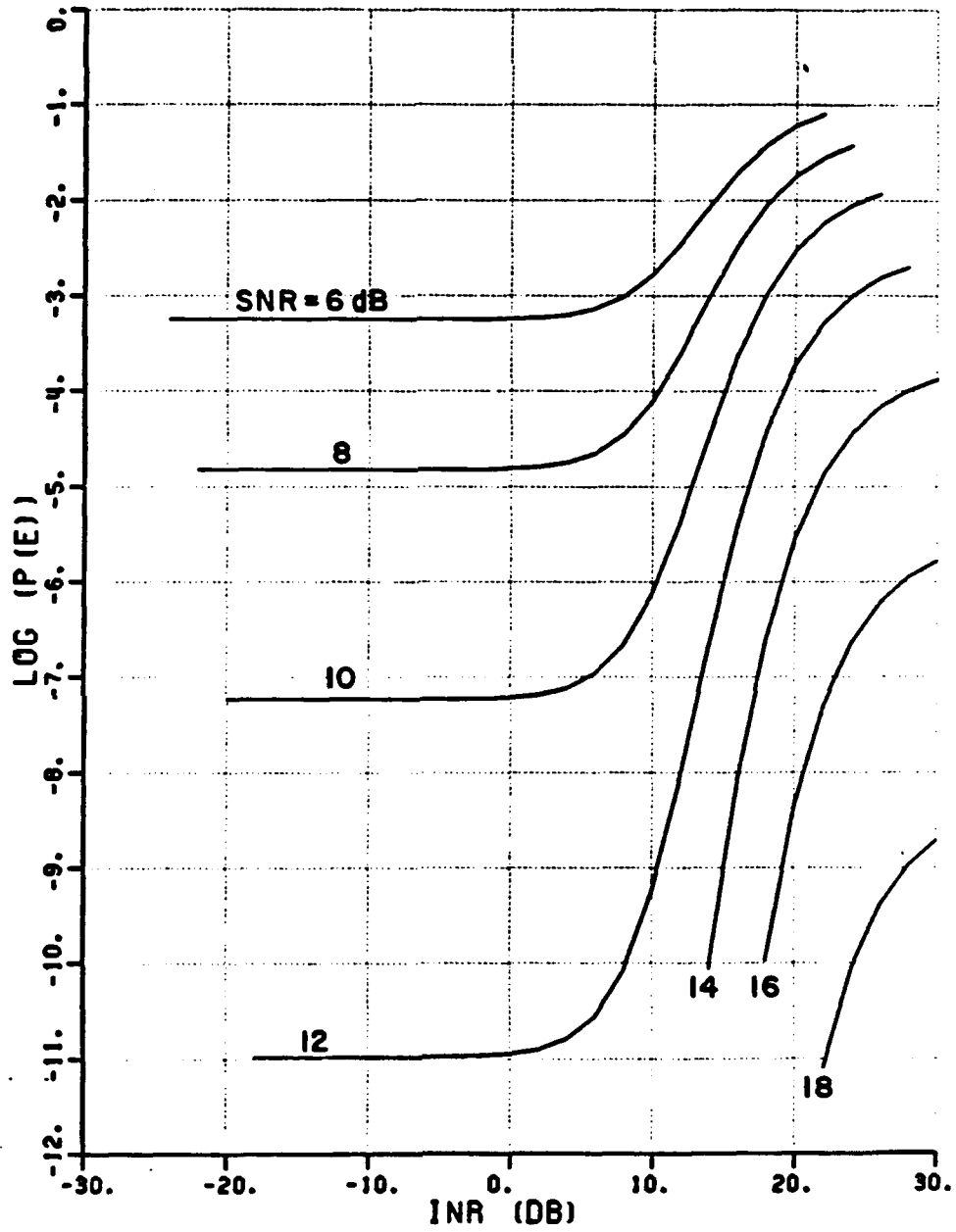


Figure 4.20. QPSK $P(e)$ vs. INR for 3-element array ($\theta_i=10^\circ$, $k=10$, $\Delta\omega T=2.$).

CHAPTER V

PERFORMANCE OF A DPSK SYSTEM WITH CW INTERFERENCE

A. INTRODUCTION

In this chapter we examine the effects of CW interference on a (binary) differential phase-shift-keyed (DPSK) communication system that uses an LMS array. DPSK and BPSK systems are very similar; however, DPSK systems do not require a phase-coherent reference signal at the detector. Although the transmitted DPSK signal and PSD look identical to those of BPSK (see Figure 3.1) the method of modulating the carrier with the data bits is different for the two systems. In BPSK systems, the phase of the transmitted waveform during each symbol interval is determined directly by the bit to be transmitted, one phase value for a "0" bit and another for a "1" bit. In DPSK systems the data is encoded differentially. That is, a "1" is transmitted by the introduction of a phase reversal between two successive symbols and a "0" is transmitted by the absence of a phase change between the two symbols.

The DPSK detector compares the phase of each received symbol with the phase of the previous symbol. If the two phases are nearly the same the detector decides that a "0" was transmitted. If the two phases differ by more than 90° , the detector decides that a "1" was transmitted. Of course the DPSK detector can be used with more than two signalling phases by appropriately partitioning the detector decision space.

We first examine the array performance with a DPSK desired signal. We then calculate the detector performance and the overall system performance.

B. ADAPTIVE ARRAY PERFORMANCE

The binary DPSK desired signal at the output of BPF1 is given by,

$$d(t) = A_d \exp[\omega_d t + \phi_n(t) + \psi_d] \quad (n-1)T < t < nT \quad (5.1)$$

where all variables except $\phi_n(t)$ are defined as in Equation (3.1).

During the n^{th} bit interval $\phi_n(t)$ is given by,

$$\phi_n(t) = \begin{cases} \phi_{(n-1)}(t) & \text{during "0" symbols} \\ \phi_{(n-1)}(t) + \pi & \text{during "1" symbols.} \end{cases} \quad (5.2)$$

Note that for DPSK, as for BPSK, the (modulo 2π) value of $\phi_n(t)$ is equally likely to be 0 or π during each symbol interval. To the LMS array, the BPSK and DPSK signals are indistinguishable. Therefore the results of Section B of Chapter III apply directly to the DPSK case. These results can be used to calculate the signal powers at the array output.

The difference in performance for the DPSK and BPSK systems is due only to the difference in detector performance. In the next section we calculate the performance of the ideal DPSK detector.

C. DPSK DETECTOR PERFORMANCE WITH CW AND AWGN INTERFERENCE

In this section we determined the performance of a DPSK detector when the desired signal is corrupted by both AWGN and CW interference. We examine the effects of signal powers, arrival angles, and the interference frequency.

Figure 5.1 shows an ideal DPSK detector [23]. The incoming signal is split and the two resulting signals are multiplied by $\sin(\omega_d t)$ and $\cos(\omega_d t)$. These locally generated reference signals are not phase-coherent with the incoming desired signal (due to the random phase angle γ_d of the desired signal). The multiplier outputs are integrated over the symbol interval to produce two random variables, $X(n)$ and $Y(n)$. At the end of the n^{th} symbol interval, $X(n)$ and $Y(n)$ are compared with $X(n-1)$ and $Y(n-1)$ and a symbol decision is made based upon the value of $X(n)X(n-1) + Y(n)Y(n-1)$. The decision rule is,

$$X(n)X(n-1) + Y(n)Y(n-1) > 0 \Rightarrow \text{decide } n^{\text{th}} \text{ symbol was "0"},$$

$$X(n)X(n-1) + Y(n)Y(n-1) < 0 \Rightarrow \text{decide } n^{\text{th}} \text{ symbol was "1"}.$$

Figure 5.2 shows the DPSK decision space and typical values of $X(n-1)$, $Y(n-1)$, $X(n)$, and $Y(n)$. From this figure we see that the decision boundary produces a useful geometric interpretation. If the absolute value of the angle (δ) between the vectors drawn from the origin to the points $\langle X(n-1), Y(n-1) \rangle$ and $\langle X(n), Y(n) \rangle$ is less than 90° a "0" decision is made. If $|\delta|$ is greater than 90° a "1" decision is made.

We now calculate the performance of the DPSK detector when the detector input is of the form,

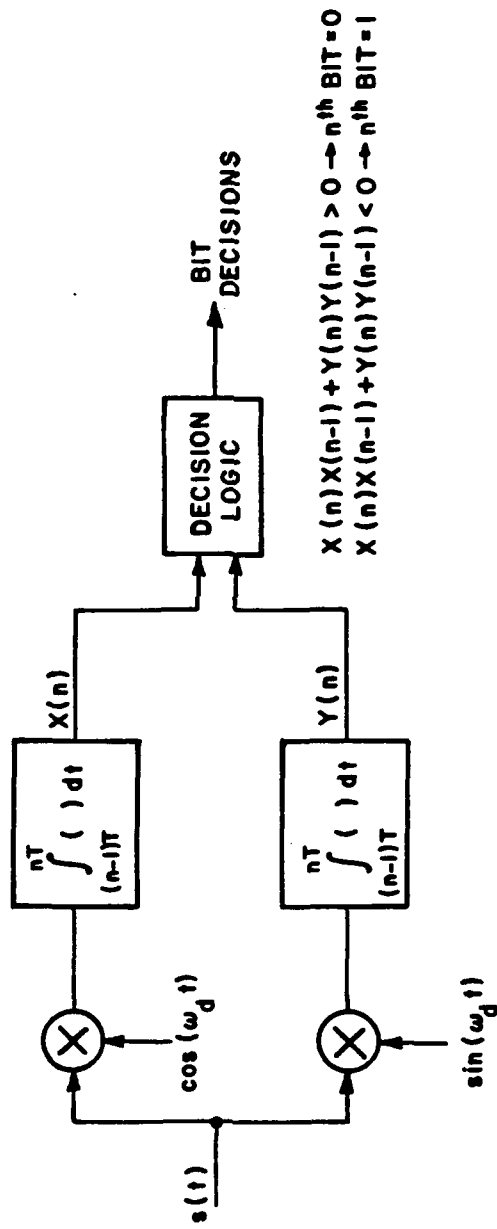


Figure 5.1. Ideal DPSK Detector.

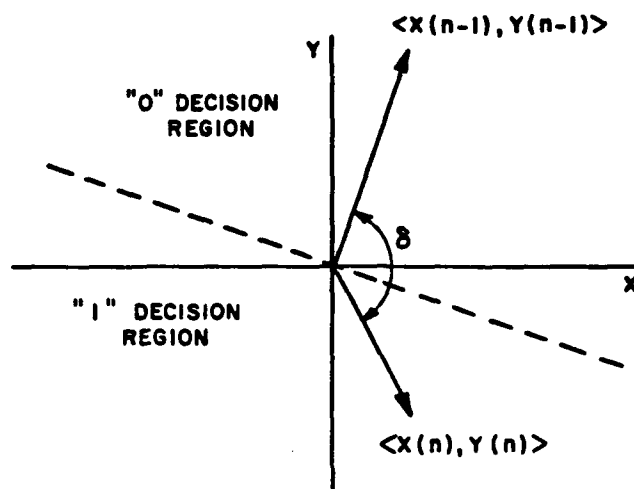


Figure 5.2. DPSK decision space.

$$s(t) = \sqrt{2P_d} \cos(\omega_d t + \phi_n(t) + \gamma_d) + \sqrt{2P_i} \cos(\omega_i + \gamma_i) + n(t). \quad (5.3)$$

where all terms are as defined in Chapter III except for $\phi_n(t)$ which is defined in (5.2).

The signal at the output of the upper integrator in Figure 5.1 at the end of the n^{th} symbol interval is given by,

$$\begin{aligned} X(n) &= \int_{(n-1)T}^{nT} s(t) \cos(\omega_d t) dt \\ &= X_d(n) + X_i(n) + X_n(n), \end{aligned} \quad (5.4)$$

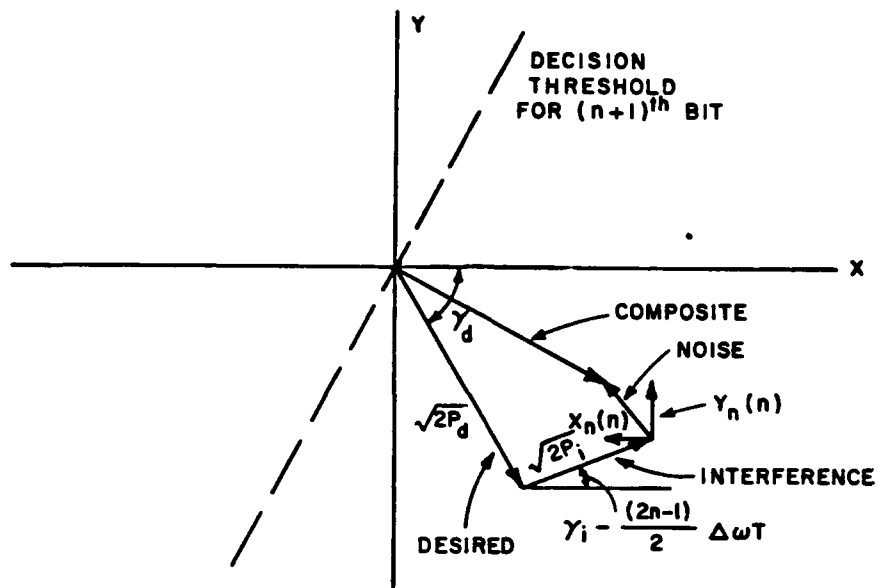


Figure 5.3. DPSK composite signal.

where

$$X_d(n) = \int_{(n-1)T}^{nT} \sqrt{2P_d} \cos(\omega_d t + \phi_n(t) + \gamma_d) \cos(\omega_d t) dt \quad (5.5)$$

$$X_i(n) = \int_{(n-1)T}^{nT} \sqrt{2P_i} \cos(\omega_i t + \gamma_i) \cos(\omega_d t) dt \quad (5.6)$$

and,

$$X_n(n) = \int_{(n-1)T}^{nT} n(t) \cos(\omega_d t) dt \quad (5.7)$$

Similarly the output of the lower integrator at the end of the n^{th} symbol interval is

$$\begin{aligned} Y(n) &= \int_{(n-1)T}^{nT} s(t) \sin(\omega_d t) dt \\ &= Y_d(n) + Y_i(n) + Y_n(n), \end{aligned} \quad (5.8)$$

where,

$$Y_d(n) = \int_{(n-1)T}^{nT} \sqrt{2P_d} \cos(\omega_d t + \phi_n(t) + \gamma_d) \sin(\omega_d t) dt \quad (5.9)$$

$$Y_i(n) = \int_{(n-1)T}^{nT} \sqrt{2P_i} \cos(\omega_i t + \gamma_i) \sin(\omega_d t) dt \quad (5.10)$$

and,

$$Y_n(n) = \int_{(n-1)T}^{nT} n(t) \sin(\omega_d t) dt \quad (5.11)$$

We now determine $X_d(n)$, $Y_d(n)$, $X_i(n)$, and the distribution of the random variables $X_n(n)$ and $Y_n(n)$. We simplify $X_d(n)$ by first expanding the integrand in Equation (5.5). We then drop the double frequency term and obtain the expression,

$$\begin{aligned} X_d(n) &= \sqrt{P_d/2} \int_{(n-1)T}^{nT} \cos(2\omega_d t + \phi_n(t) + \gamma_d) + \cos(\phi_n(t) + \gamma_d) dt \\ &= \sqrt{P_d/2} T \cos(\phi_n(t) + \gamma_d). \end{aligned} \quad (5.12)$$

Similarly $Y_d(n)$ is simplified from (5.9),

$$\begin{aligned} Y_d(n) &= \sqrt{P_d/2} \int_{(n-1)T}^{nT} \sin(2\omega_d t + \phi_n(t) + \gamma_d) - \sin(\phi_n(t) + \gamma_d) dt \\ &= -\sqrt{P_d/2} T \sin(\phi_n(t) + \gamma_d). \end{aligned} \quad (5.13)$$

The first of the interference terms, $X_i(n)$ is simplified from (5.6) in the same manner,

$$\begin{aligned}
X_i(n) &= \sqrt{P_i/2} \int_{(n-1)T}^{nT} \cos[(\omega_d + \omega_i)t + \gamma_i] \\
&\quad + \cos[(\omega_d - \omega_i)t - \gamma_i] dt \\
&= \sqrt{P_i/2} (1/\Delta\omega) \{ \sin[\Delta\omega nT - \gamma_i] - \sin(\Delta\omega(n-1)T - \gamma_i) \} \quad (5.14)
\end{aligned}$$

where $\Delta\omega$ is as defined in the previous chapters. We simplify this expression further using standard trigonometric identities,

$$X_i(n) = \sqrt{P_i/2} T \text{sinc}(\Delta\omega T/2) \cos[(2n-1)(\Delta\omega T/2) - \gamma_i]. \quad (5.15)$$

A similar procedure shows that Y_i is given by,

$$Y_i(n) = \sqrt{P_i/2} T \text{sinc}(\Delta\omega T/2) \sin[(2n-1)(\Delta\omega T/2) - \gamma_i]. \quad (5.16)$$

We next determine the distribution of $X_n(n)$ and $Y_n(n)$, the noise terms. These variables are the result of processing that is identical to that used to obtain $X_n(n)$ and $Y_n(n)$ for QPSK in Chapter IV. Using the results from Chapter IV we can immediately determine that $X_n(n)$ and $Y_n(n)$ are independent zero-mean Gaussian random variables each with variance $nT/4$ (where $n/2$ is the 2-sided noise PSD at the detector input.) $X_n(n)$ and $Y_n(n)$ will each be independent of $X_n(n+c)$ and $Y_n(n+c)$ for all non-zero integer values of c .

Figure 5.3 shows each of the components of $X(n)$ and $Y(n)$ as well as the composite signals. This figure shows the decision regions, which are separated by the line at $|\delta| = 90^\circ$.

In order to determine the probability of error we must determine the probability that $|\delta| > 90^\circ$ when "0" is transmitted and the probability that $|\delta| < 90^\circ$ when "1" is transmitted. Rosenbaum [18] addressed a

similar problem; however, as in the BPSK and QPSK cases, Rosenbaum's receiver model differs from ours and his expressions for $P(e)$ must be slightly modified for the integrate-and-dump type detector. The model discussed in [18] leads to a signal vector diagram very similar to that shown in Figure 5.3. The only difference is that Rosenbaum omits the factor of $\text{sinc}(\Delta\omega T/2)$ for the length of the interference vector. We outline Rosenbaum's derivation of $P(e)$ with the appropriate modifications of the vector lengths.

In order to determine the $P(e)$ we first define the complex variable $Z(n)$,

$$Z(n) = X(n) + jY(n). \quad (5.17)$$

We assume that the n^{th} symbol is a "0". We then note that

$$\cos\delta = \frac{\text{Re}[Z(n)Z^*(n-1)]}{|Z(n)||Z(n-1)|}. \quad (5.18)$$

Since the denominator is nonnegative, the conditional probability of error, given $\Delta\omega T$, γ_d , and γ_i , is,

$$P(e|\Delta\omega T, "0", \gamma_d, \gamma_i) = P(\text{Re}[Z(n)Z^*(n-1)] < 0) \quad (5.19)$$

Since

$$\text{Re}[Z(n)Z^*(n-1)] = \left| \frac{Z(n) + Z(n-1)}{2} \right|^2 - \left| \frac{Z(n) - Z(n-1)}{2} \right|^2, \quad (5.20)$$

we have,

$$P(e|\Delta\omega T, "0", \gamma_d, \gamma_i) = P(|Z(n) + Z(n-1)| < |Z(n) - Z(n-1)|), \quad (5.21)$$

We now define the variables,

$$\begin{aligned}\Sigma &= Z(n) + Z(n-1) \\ &= C_0(\Sigma) + X_n(n) + X_n(n-1) + j[Y_n(n) + Y_n(n-1)]\end{aligned}\quad (5.22)$$

and

$$\begin{aligned}\beta &= Z(n) - Z(n-1) \\ &= C_0(\beta) + X_n(n) - X_n(n-1) + j[Y_n(n) - Y_n(n-1)]\end{aligned}\quad (5.23)$$

where $C_0(\Sigma)$ and $C_0(\beta)$ are the components of Σ and β not due to the Gaussian noise,

$$\begin{aligned}C_0(\Sigma) &= X_d(n) + X_d(n-1) + X_i(n) + X_i(n-1) \\ &\quad + j[Y_d(n) + Y_d(n-1) + Y_i(n) + Y_i(n-1)]\end{aligned}\quad (5.24)$$

$$\begin{aligned}C_0(\beta) &= X_d(n) - X_d(n-1) + X_i(n) - X_i(n-1) \\ &\quad + j[Y_d(n) - Y_d(n-1) + Y_i(n) - Y_i(n-1)]\end{aligned}\quad (5.25)$$

where the subscript "0" indicates that we are assuming the n^{th} symbol is a zero. Evaluating $C_0(\Sigma)$ and $C_0(\beta)$ we find,

$$\begin{aligned}C_0(\Sigma) &= \sqrt{2P_d}T \cos(\phi_n) \\ &\quad + \sqrt{2P_i}T \operatorname{sinc}\left(\frac{\Delta\omega T}{2}\right) \cos[\gamma_d - \gamma_i + \Delta\omega T(n-1)] \cos\left(\frac{\Delta\omega T}{2}\right) \\ &\quad + k[-\sqrt{2P_d}T \sin(\phi_n) \\ &\quad + \sqrt{2P_i}T \operatorname{sinc}\left(\frac{\Delta\omega T}{2}\right) \sin[\gamma_d - \gamma_i + \Delta\omega T(n-1)] \cos\left(\frac{\Delta\omega T}{2}\right)]\end{aligned}\quad (5.26)$$

and

$$C_0(\beta) = \sqrt{2P_i T} \operatorname{sinc}\left(\frac{\Delta\omega T}{2}\right) \sin\left(\frac{\Delta\omega T}{2}\right) \quad (5.27)$$

We can show that $|\Sigma|$ and $|\beta|$ are independent Rician random variables. Therefore, the probability given in (5.21) is the probability that one Rician random variable exceeds another. This probability is given by [18],

$$P(e|\Delta\omega T, "0", \gamma_d, \gamma_i) = \frac{1}{2} \left[1 - Q\left(\frac{|C_0(\Sigma)|}{2\sigma}, \frac{|C_0(\beta)|}{2\sigma}\right) + Q\left(\frac{|C_0(\beta)|}{2\sigma}, \frac{|C_0(\Sigma)|}{2\sigma}\right) \right] \quad (5.28)$$

where $\sigma = \sqrt{\frac{\eta T}{4}}$, and $Q(A, B)$ is Marcum's Q function,

$$Q(A, B) = \int_B^\infty \tau \exp[-(A^2 + \tau^2)/2] I_0(A\tau) d\tau, \quad (5.29)$$

From (5.26) and (5.27) we find that $|C_0(\Sigma)|$ and $|C_0(\beta)|$ can be written,

$$\begin{aligned} |C_0(\Sigma)| = & \sqrt{2T} [P_d + \sqrt{P_d P_i} \operatorname{sinc}\left(\frac{\Delta\omega T}{2}\right) \cos\left(\frac{\Delta\omega T}{2}\right) \cos(\xi_0) + \\ & P_i \operatorname{sinc}^2\left(\frac{\Delta\omega T}{2}\right) \cos^2\left(\frac{\Delta\omega T}{2}\right)]^{1/2} \end{aligned} \quad (5.30)$$

and,

$$|C_0(\beta)| = \sqrt{2P_i T} \operatorname{sinc}\left(\frac{\Delta\omega T}{2}\right) \sin\left(\frac{\Delta\omega T}{2}\right) \quad (5.31)$$

where $\xi_0 = [\phi_n - \gamma_d + \gamma_i - (n-1)\Delta\omega T]$. Since γ_d and γ_i are $U[0, 2\pi]$, ξ_0 is also $U[0, 2\pi]$ (as shown in [17]).

We now average the expression for $P(e)$, given by Equation (5.28), over the uniformly distributed random variable ξ_0 to determine $P(e|\Delta\omega T, "0")$,

$$P(e|\Delta\omega T, "0") = \frac{1}{4\pi} \left[1 - Q\left(\frac{|C_0(\Sigma)|}{2\sigma}, \frac{|C_0(\beta)|}{2\sigma}\right) + Q\left(\frac{|C_0(\beta)|}{2\sigma}, \frac{|C_0(\Sigma)|}{2\sigma}\right) \right] d\xi_0, \quad (5.32)$$

A similar analysis performed under the assumption that a "1" symbol was transmitted yields,

$$P(e|\Delta\omega T, "1") = \frac{1}{4\pi} \int_0^{2\pi} \left[1 - Q\left(\frac{|C_1(\Sigma)|}{2\sigma}, \frac{|C_1(\beta)|}{2\sigma}\right) + Q\left(\frac{|C_1(\beta)|}{2\sigma}, \frac{|C_1(\Sigma)|}{2\sigma}\right) \right] d\xi_1, \quad (5.33)$$

where,

$$|C_1(\Sigma)| = \sqrt{2T} \left[P_d + \sqrt{P_d P_i} \operatorname{sinc}\left(\frac{\Delta\omega T}{2}\right) \cos\left(\frac{\pi - \Delta\omega T}{2}\right) \cos(\xi_1) + P_i \operatorname{sinc}^2\left(\frac{\Delta\omega T}{2}\right) \cos^2\left(\frac{\pi - \Delta\omega T}{2}\right) \right]^{1/2} \quad (5.34)$$

and,

$$|C_1(\beta)| = \sqrt{2P_i T} \operatorname{sinc}\left(\frac{\Delta\omega T}{2}\right) \sin\left(\frac{\pi - \Delta\omega T}{2}\right) \quad (5.35)$$

and ξ_1 is $U[0, 2\pi]$.

Finally, the expression for $P(e)$ is given by,

$$P(e|\Delta\omega T) = \frac{1}{2} P(e|\Delta\omega T, "0") + \frac{1}{2} P(e|\Delta\omega T, "1"). \quad (5.36)$$

We evaluated $P(e)$ for several values of SNR and INR (defined by (3.45) and (3.46)) numerically. Figures 5.4 and 5.5 show typical results for $\Delta\omega T=0$. These results are very similar to those shown for $\Delta\omega T=0$ in [18]. Figures 5.6 and 5.7 show similar results for $\Delta\omega T=\pi/2$. From Figures 5.6 and 5.7 we see that the system performance decreases slightly as $\Delta\omega T$ increases.

The curves shown in Figure 5.6 depict significantly better performance than that predicted by the results of [18] for $\Delta\omega T=\pi/2$. There is a simple explanation for this discrepancy. For a given interference signal vector length (in Figure 5.3) the DPSK detector is most prone to errors when $\Delta\omega T=\pi/2$ ($\pm n\pi$). However, the length of this vector is proportional to $\text{sinc}(\Delta\omega T/2)$, the factor which is not included in the analysis of [18]. Therefore, as $\Delta\omega T$ increases from zero to $\pi/2$, two processes occur. First, the detector sensitivity to the interference decreases due to the $\text{sinc}(\Delta\omega T/2)$ term. Second, the detector becomes more sensitive to the interference as $\Delta\omega T$ approaches $\pi/2$ due to the geometry of the signal vectors.

In order to determine how these two (often conflicting) processes interact, we examine how $P(e)$ varies as a function of $\Delta\omega T$ for few representative SNR and INR levels. Figures 5.8 and 5.9 show typical results. Figure 5.8 shows $P(e)$ vs. $\Delta\omega T$ for several INR values when the SNR is 10 dB. Figure 5.9 shows similar data for the same INR values with an SNR of 13 dB. From these curves we can see that the highest $P(e)$ values typically occur when $\Delta\omega T$ is approximately $\pi/2$.

D. PERFORMANCE OF COMBINED LMB ARRAY/DPSK DETECTOR

We now combine the results from the previous two sections in order to calculate the performance of the DPSK system. Figures 5.10 through 5.25 show typical results. Figures 5.10 through 5.15 show how $P(e)$ varies with SNR and INR with the array bandwidth factor, k , set equal to 5. As in the previous chapters, the figures show the performance for three different interference arrival angles, 10, 20 and 80°. Figures 5.16 through 5.21 show similar results when the array bandwidth factor is increased to 10. From these figures we see that the DPSK system performance is significantly poorer than that of the BPSK system discussed in Chapter III.

Figures 5.22 and 5.23 show how the performance varies when the interference and the desired signal frequencies are different. For each of these figures k is 10, $\theta_i = 10^\circ$, and $\Delta\omega T$ is $\pi/2$. From the previous section we expect this value of $\Delta\omega T$ to produce the worst performance.

Figures 5.24 and 5.25 show the performance for $\Delta\omega T = 2\pi$ (with $k = 10$ and $\theta_i = 10^\circ$). For this value of $\Delta\omega T$, the detector is not affected by the interference. Therefore, as we would expect, we observe the best performance for this value of $\Delta\omega T$.

We find that the system behavior with DPSK signalling is similar to that with BPSK or QPSK signalling. We find that, in general, the symbol error probability for DPSK is between that of BPSK and QPSK. The shapes of the curves for each of the different types of PSK signalling are very similar. We find that, for each type of PSK modulation, it is desirable to have a narrow array input bandwidth.

In Chapters III, IV, and V we have examined the performance of PSK communication systems. We found qualitatively similar performance for each of these systems. In the next chapter we examine the performance of an FSK system and compare its performance with that observed for the PSK systems.

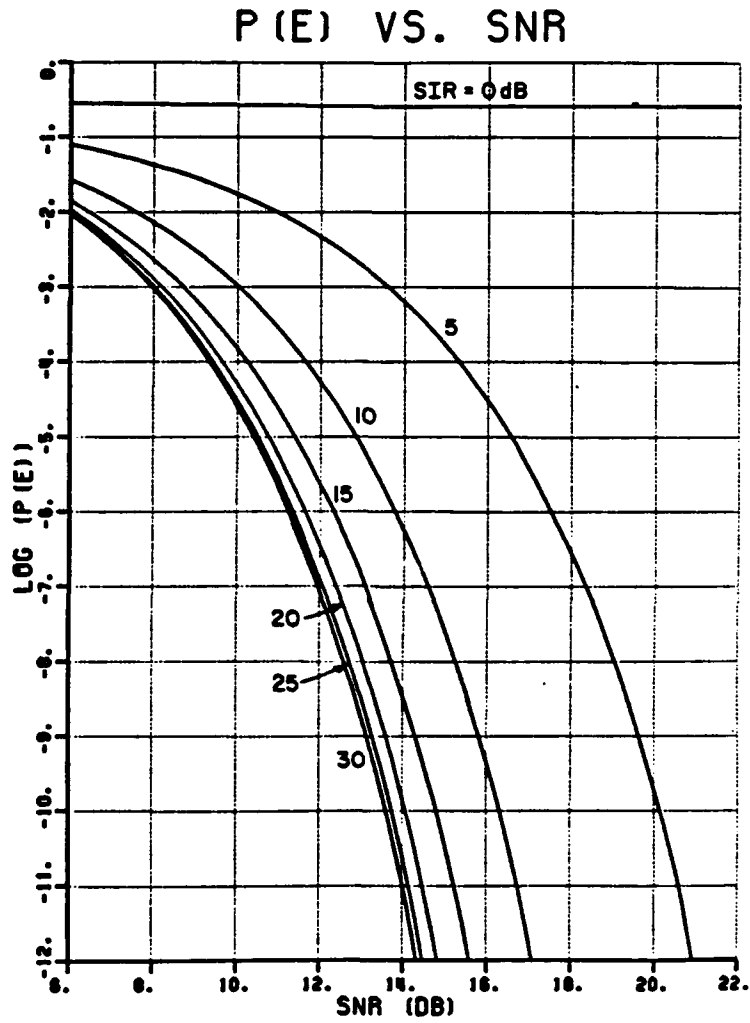


Figure 5.4. Performance of ideal DPSK detector with CW interference ($\Delta\omega T=0$).

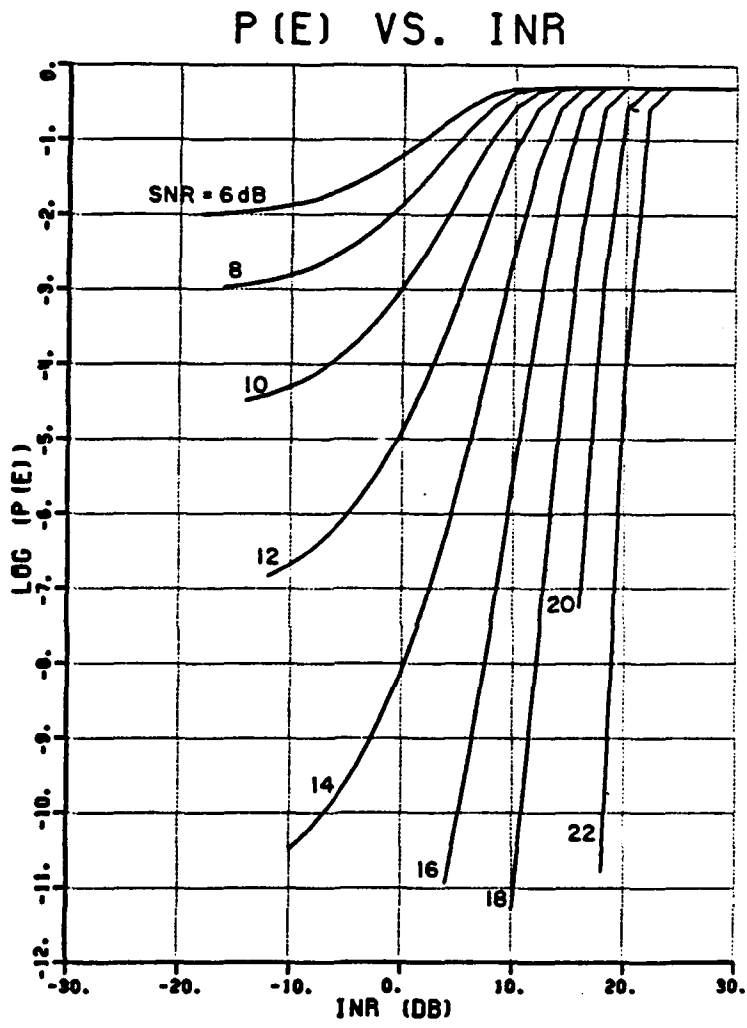


Figure 5.5. Performance of ideal DPSK detector with CW interference ($\Delta\omega T=0$).

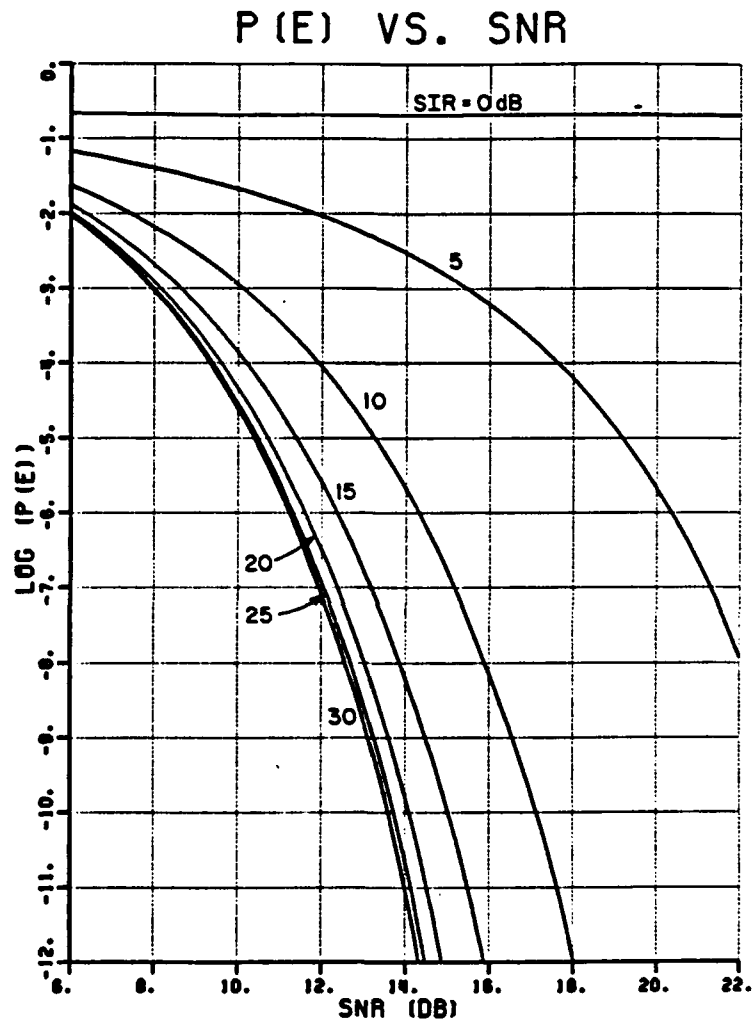


Figure 5.6. Performance of ideal DPSK detector with CW interference ($\Delta\omega T = \pi/2$).

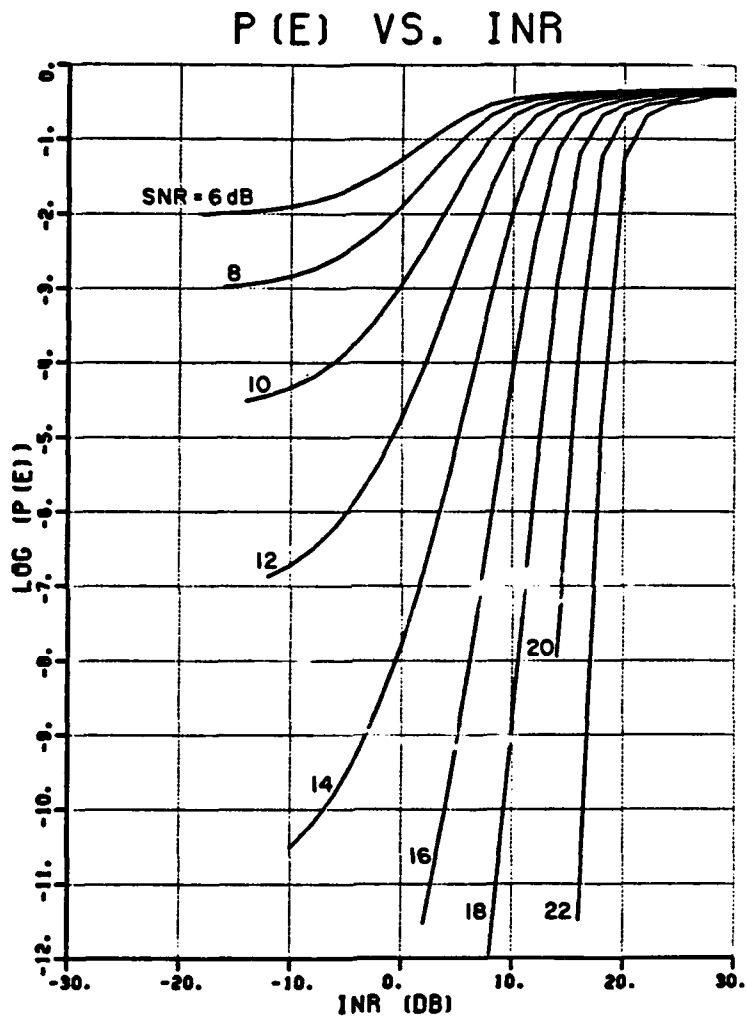


Figure 5.7. Performance of ideal DPSK detector with CW interference ($\Delta\omega T = \pi/2$).

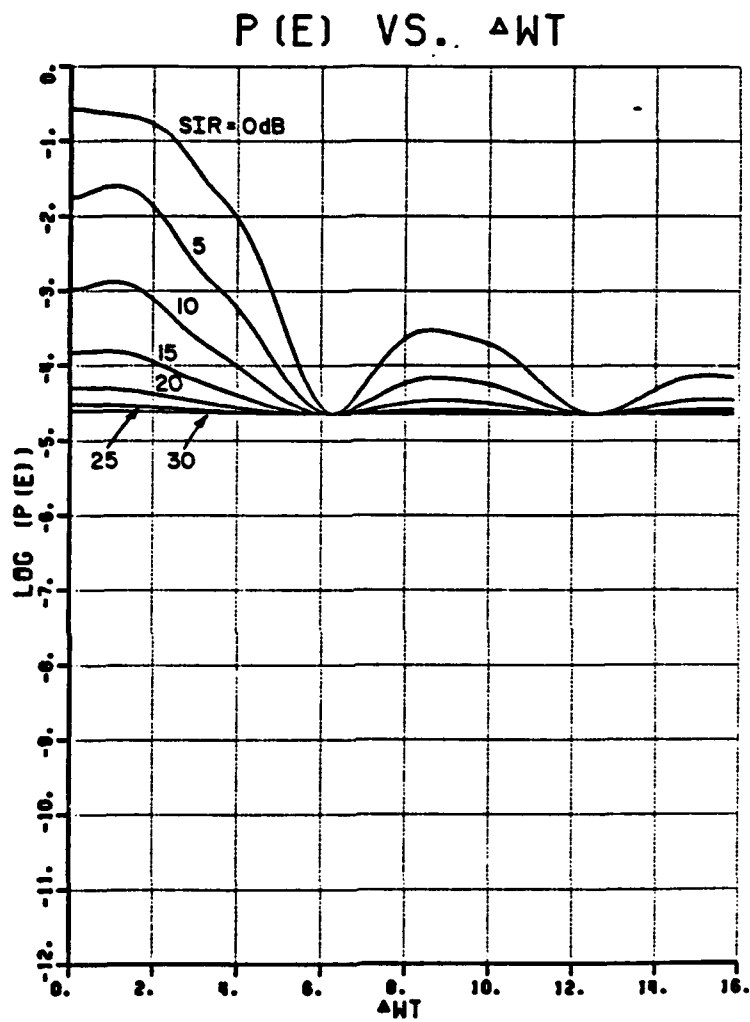


Figure 5.8. Performance of an ideal DPSK detector as a function of $\Delta\omega T$ (SNR=10 dB).

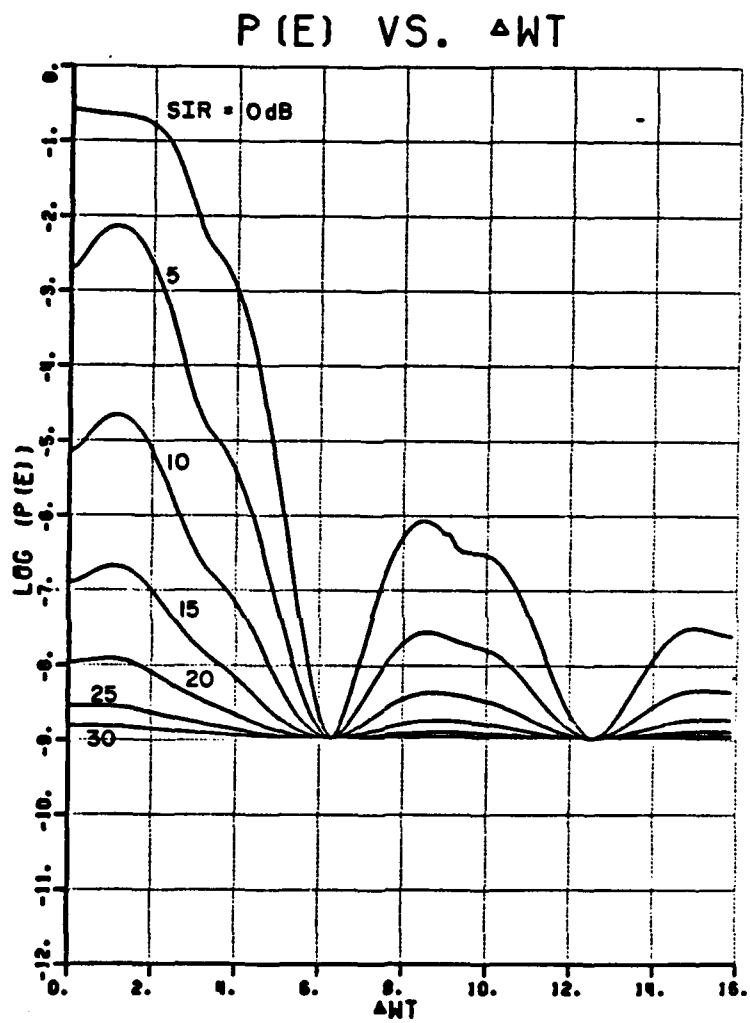


Figure 5.9. Performance of an ideal DPSK detector as a function of $\Delta\omega T$ (SNR=13 dB).

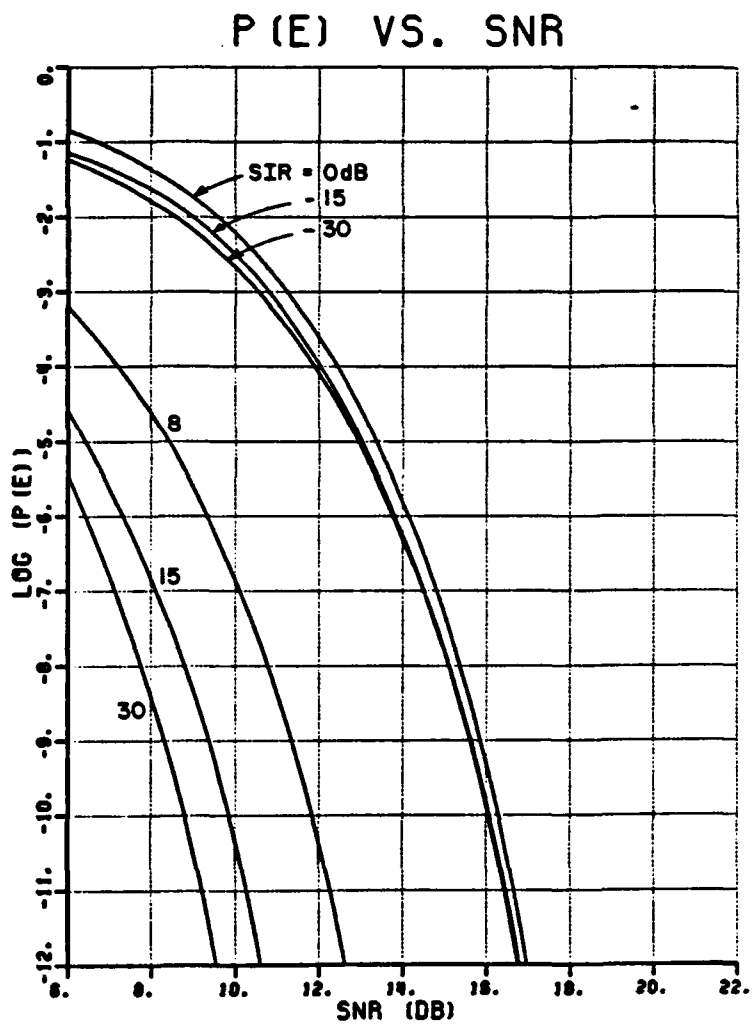


Figure 5.10. DPSK $P(e)$ vs. SNR for 3-element array ($\theta_i=10^\circ$, $k=5$, $\Delta\omega T=0$).

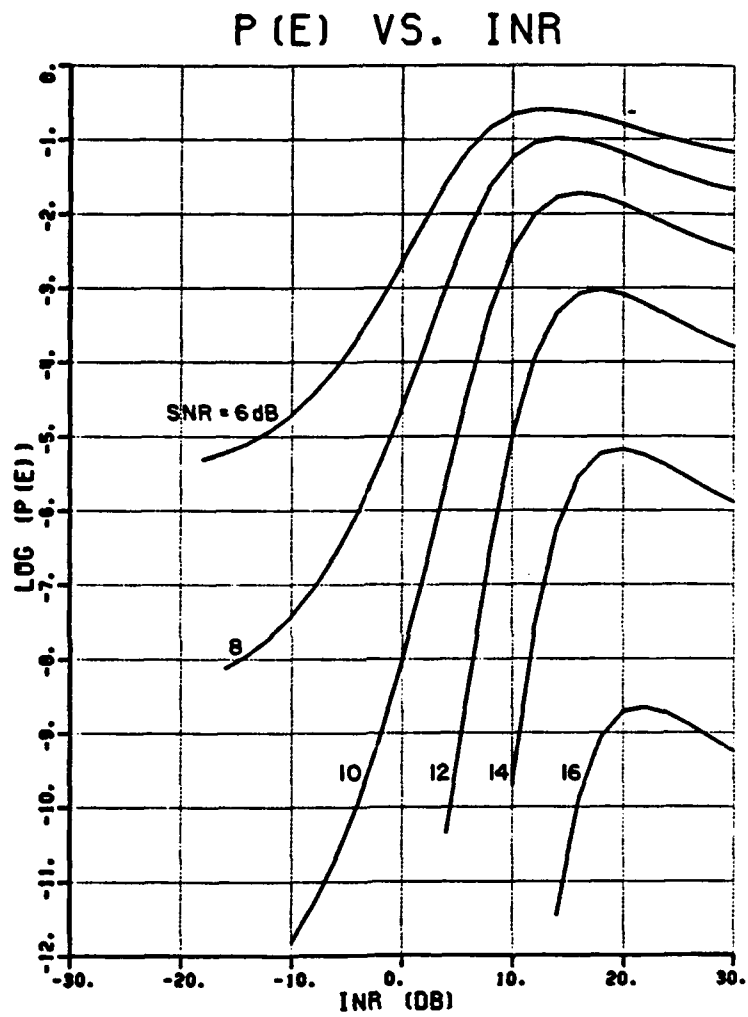


Figure 5.11. DPSK $P(e)$ vs. INR for 3-element array ($\theta_i=10^\circ$, $k=5$, $\Delta\omega T=0$).

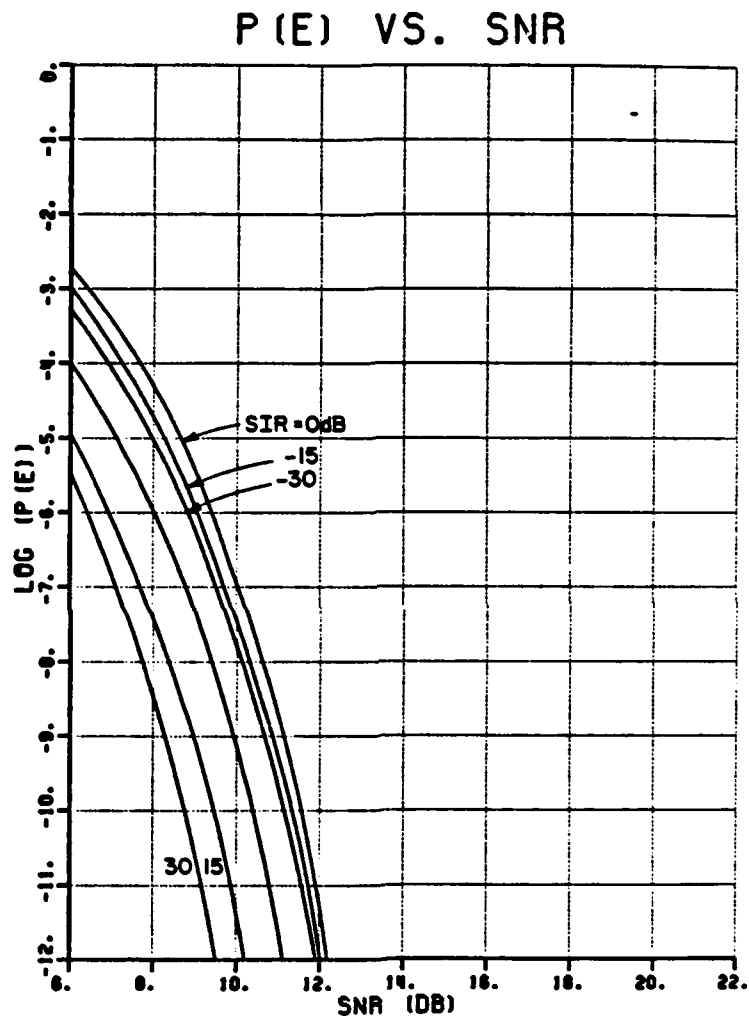


Figure 5.12. DPSK $P(e)$ vs. SNR for 3-element array ($\theta_j=20^\circ$, $k=5$, $\Delta\omega T=0$).

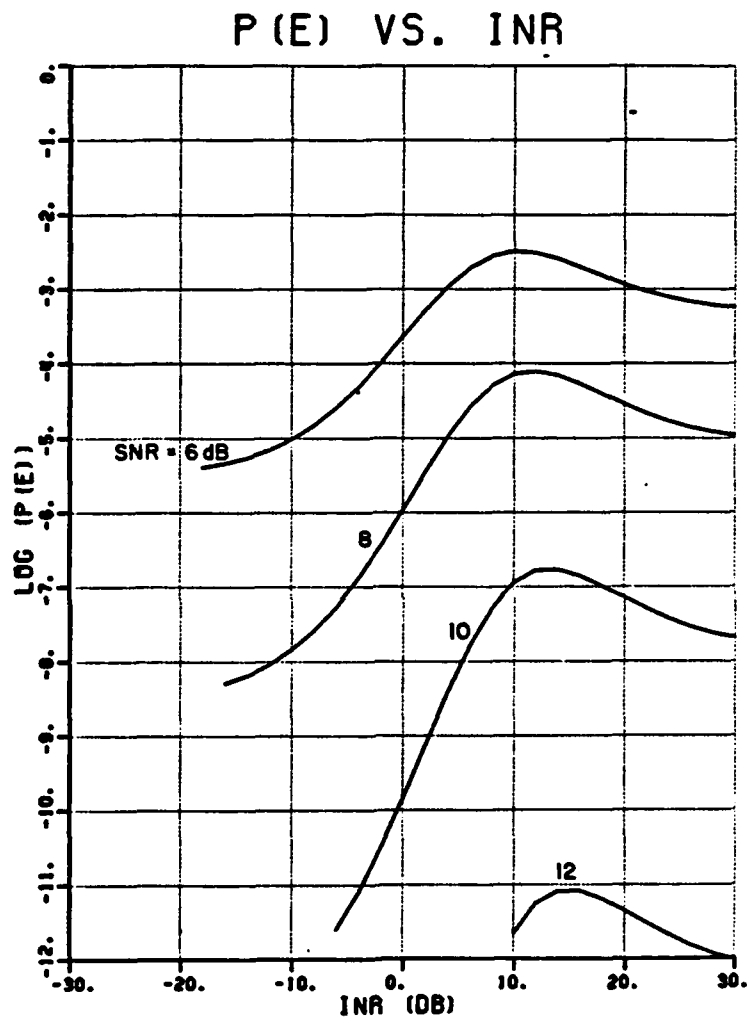


Figure 5.13. DPSK $P(e)$ vs. INR for 3-element array ($\theta_i=20^\circ$, $k=5$, $\Delta\omega T=0$).

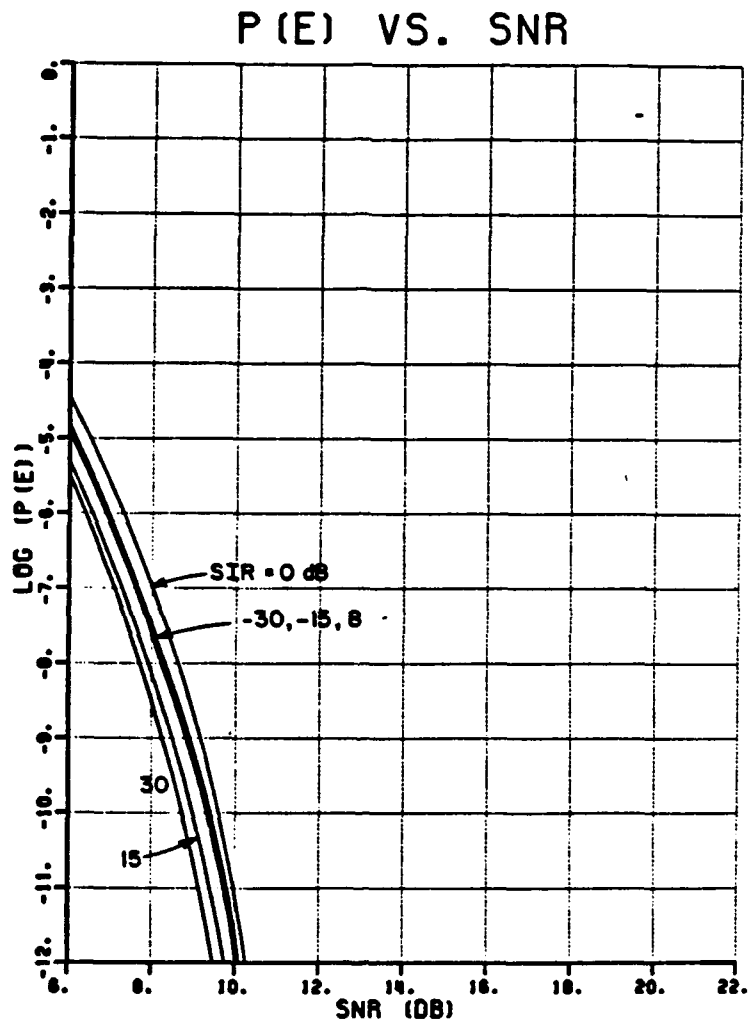


Figure 5.14. DPSK $P(e)$ vs. SNR for 3-element array ($\theta_i=80^\circ$, $k=5$, $\Delta\omega T=0$).

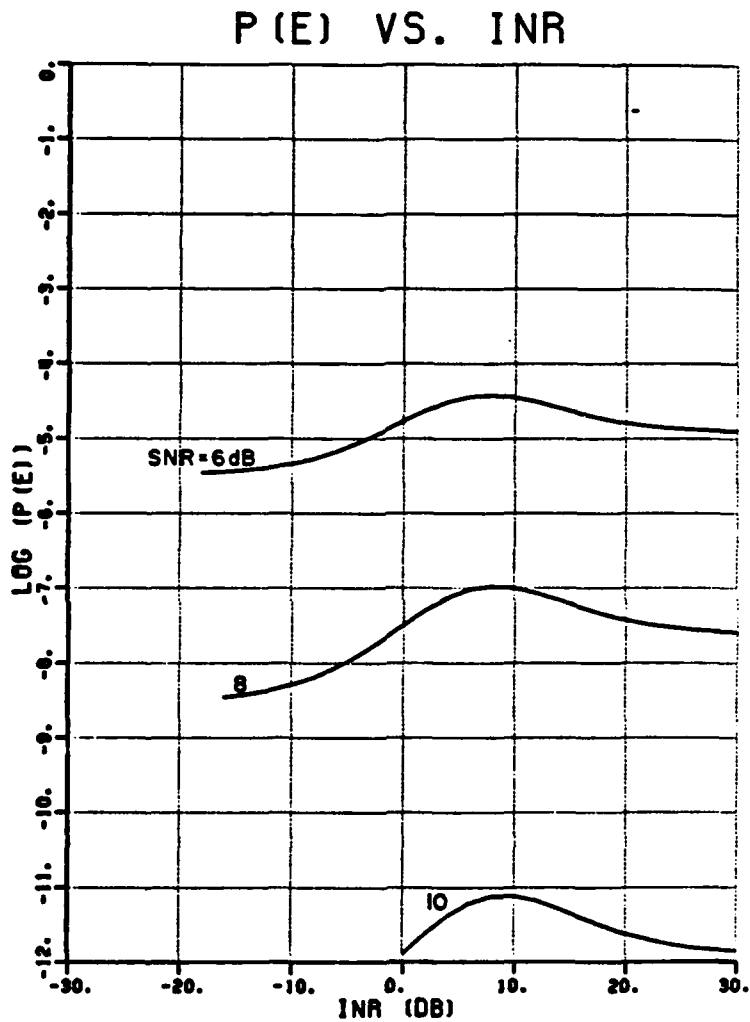


Figure 5.15. DPSK $P(e)$ vs. INR for 3-element array ($\theta_i=80^\circ$, $k=5$, $\Delta\omega T=0$).

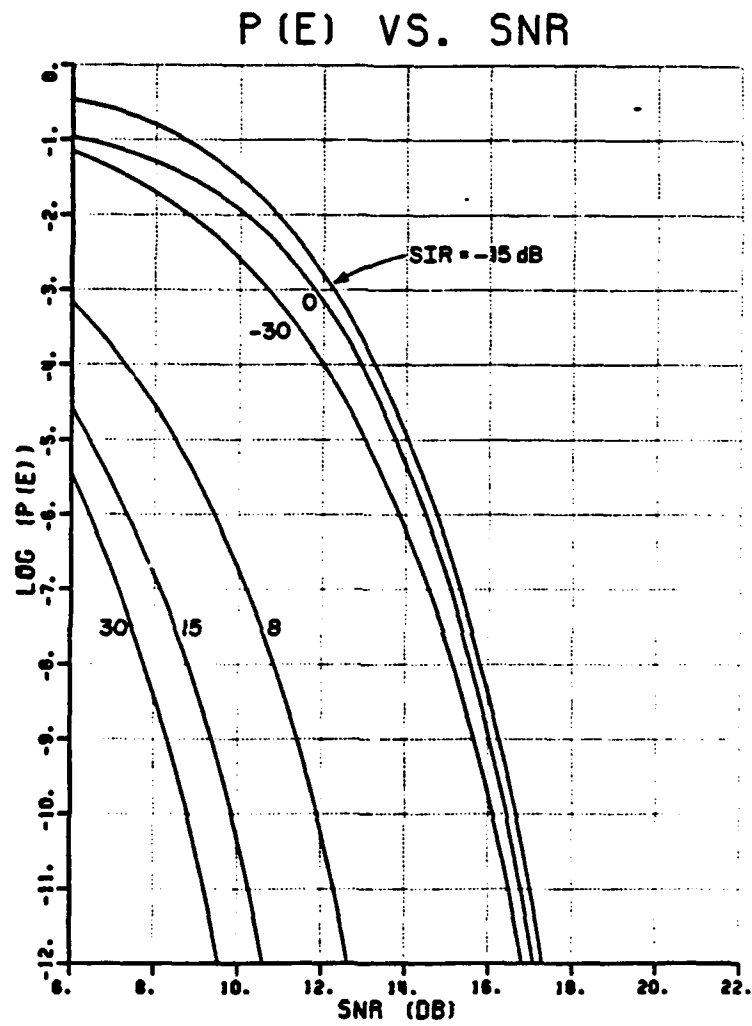


Figure 5.16. DPSK $P(e)$ vs. SNR for 3-element array ($\theta_i=10^\circ$, $k=10$, $\Delta\omega T=0$).

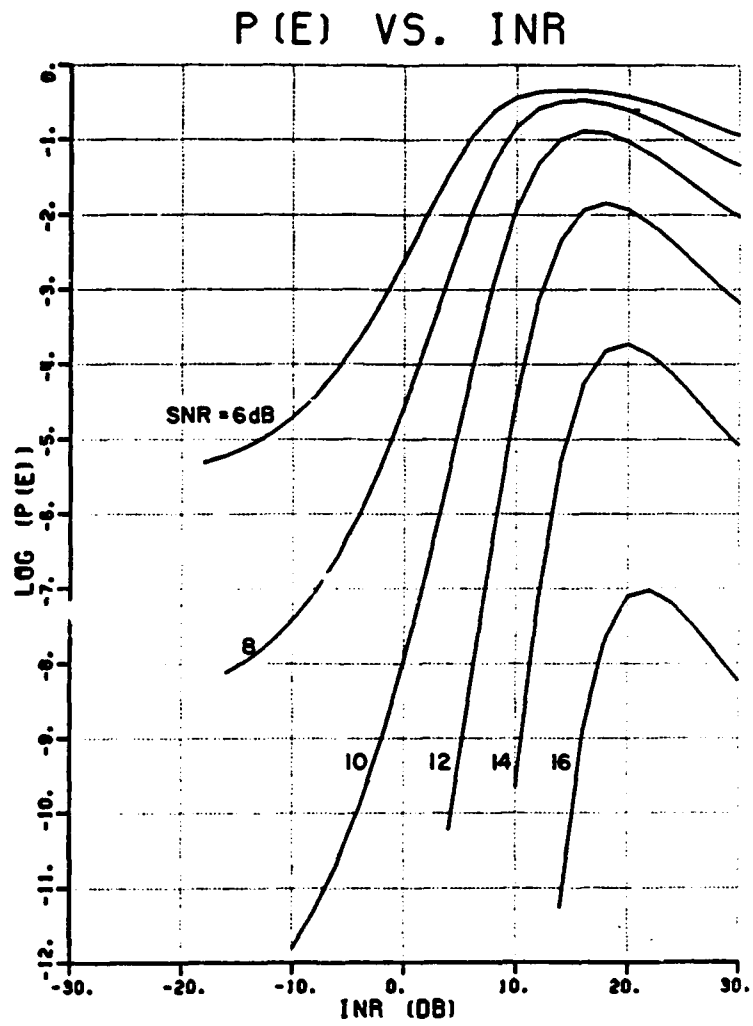


Figure 5.17. DPSK $P(e)$ vs. INR for 3-element array ($\theta_j=10^\circ$, $k=10$, $\Delta\omega T=0$).

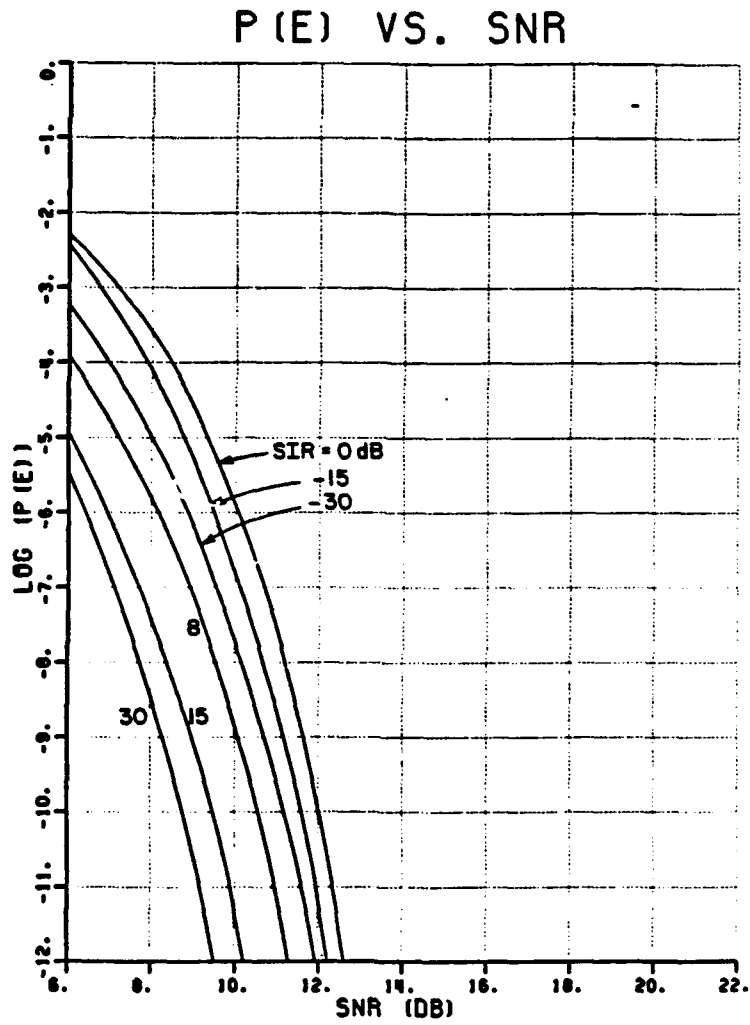


Figure 5.18. DPSK $P(e)$ vs. SNR for 3-element array ($\theta_j=20^\circ$, $k=10$, $\Delta\omega T=0$).

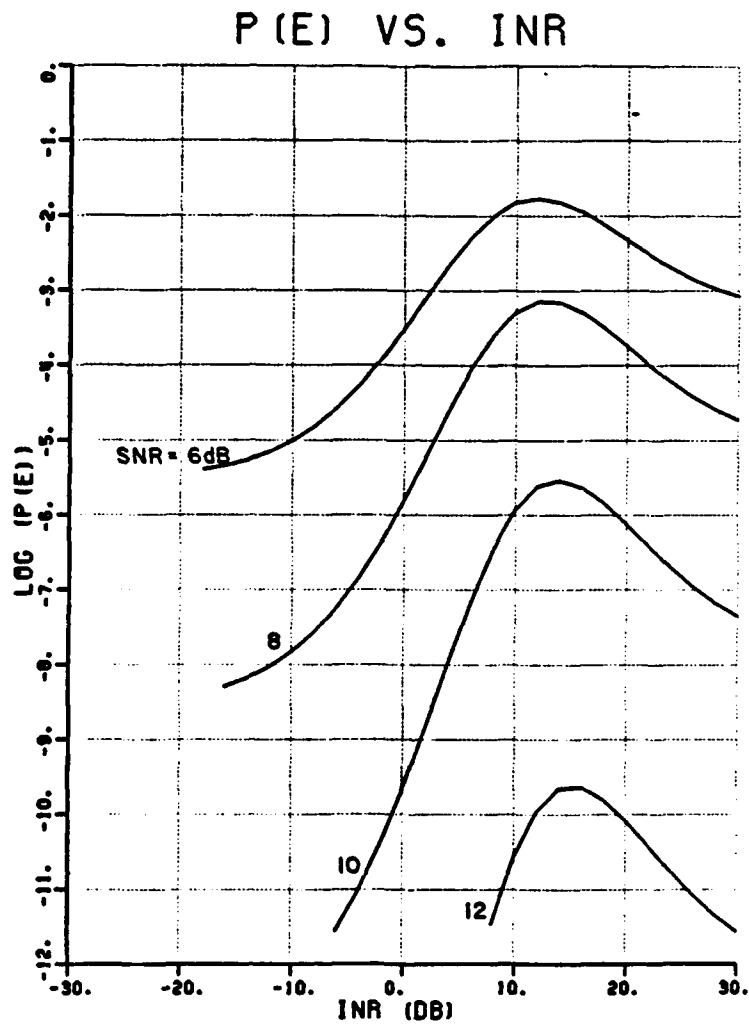


Figure 5.19. DPSK $P(e)$ vs. INR for 3-element array ($\theta_i=20^\circ$, $k=10$, $\Delta\omega T=0$).

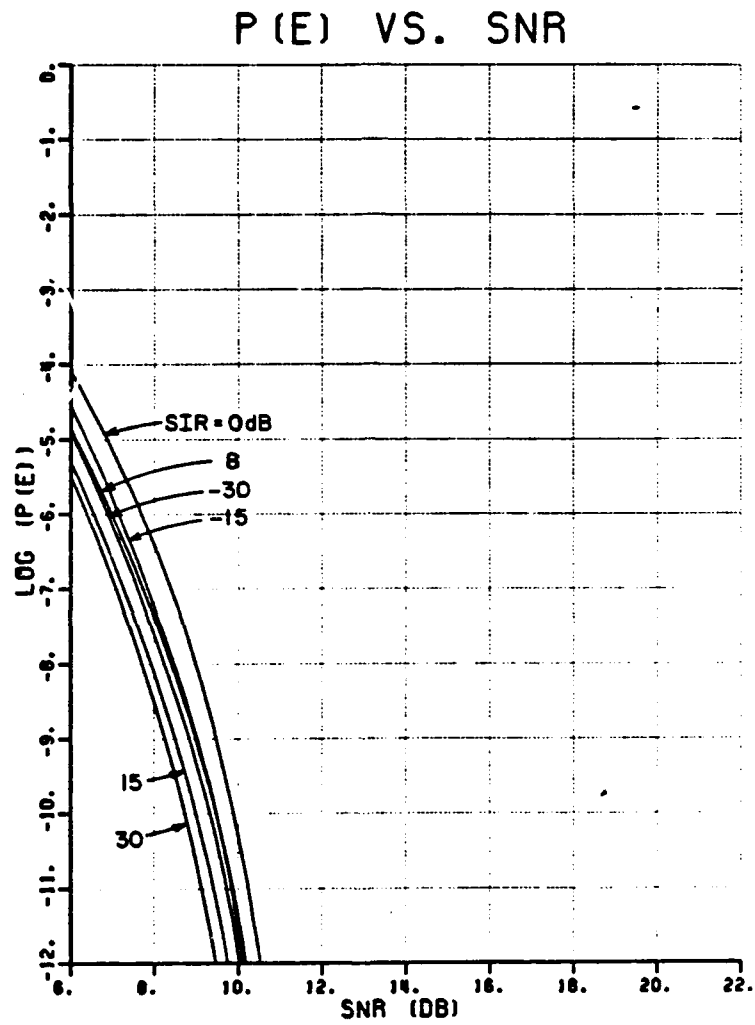


Figure 5.20. DPSK $P(e)$ vs. SNR for 3-element array ($\theta_j=80^\circ$, $k=10$, $\Delta\omega T=0$).

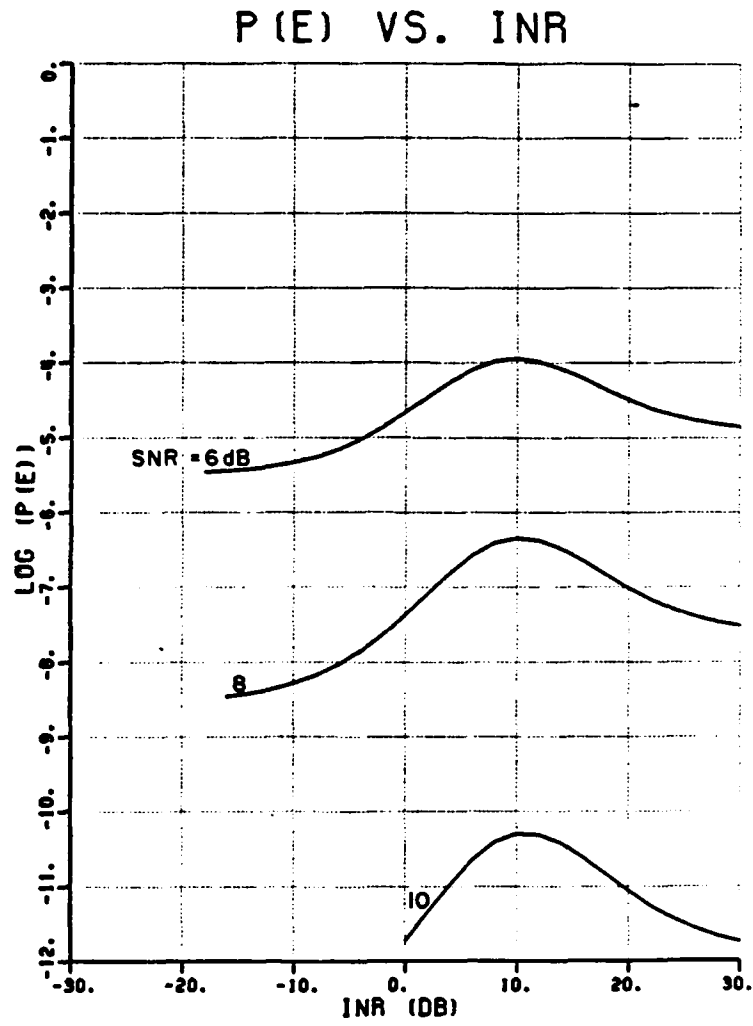


Figure 5.21. DPSK $P(e)$ vs. INR for 3-element array ($\theta_i=80^\circ$, $k=10$, $\Delta\omega T=0$).

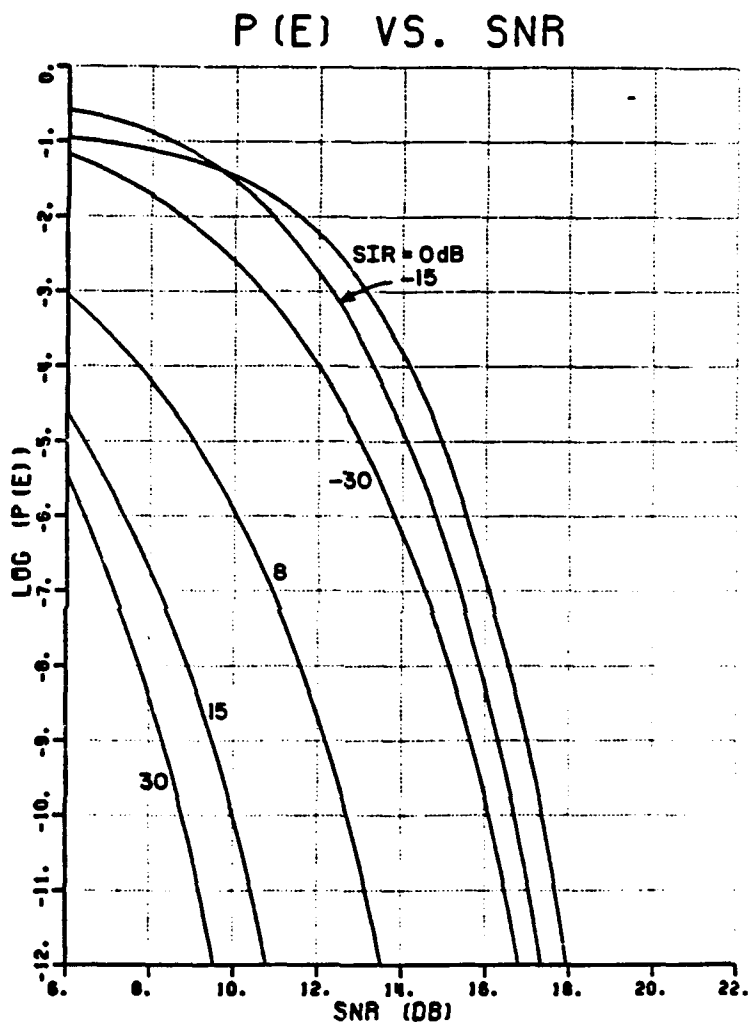


Figure 5.22. DPSK $P(e)$ vs. SNR for 3-element array ($\theta_i=10^\circ$, $k=10$, $\Delta\omega T=\pi/2$).

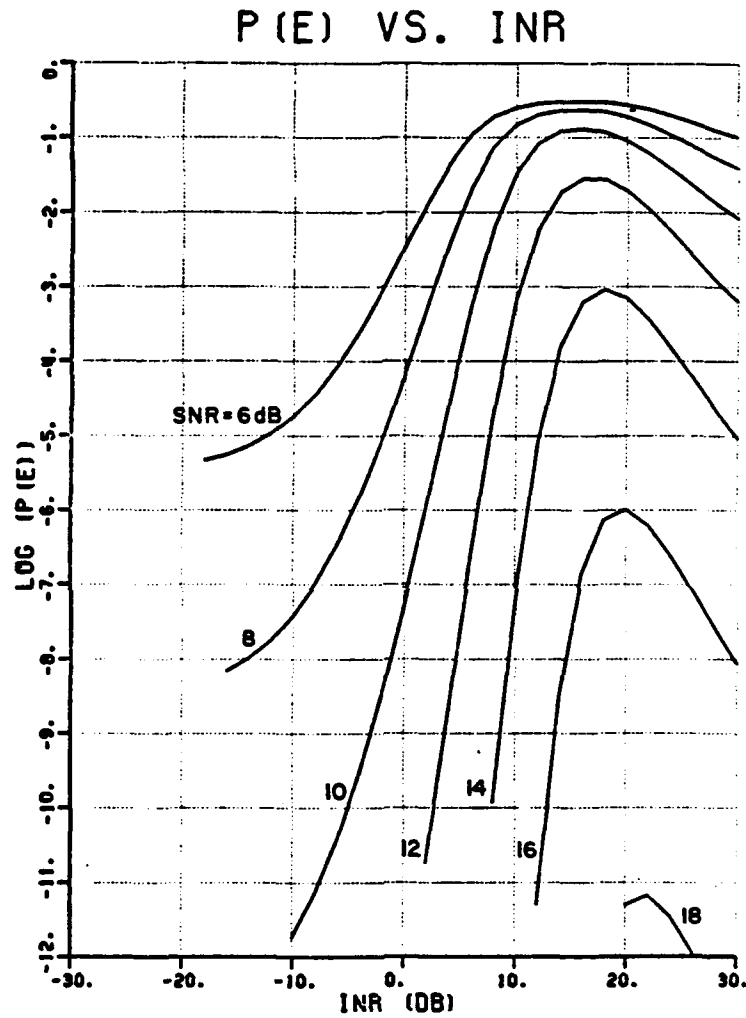


Figure 5.23. DPSK $P(e)$ vs. INR for 3-element array ($\theta_i=10^\circ$, $k=10$, $\Delta\omega T=\pi/2$).

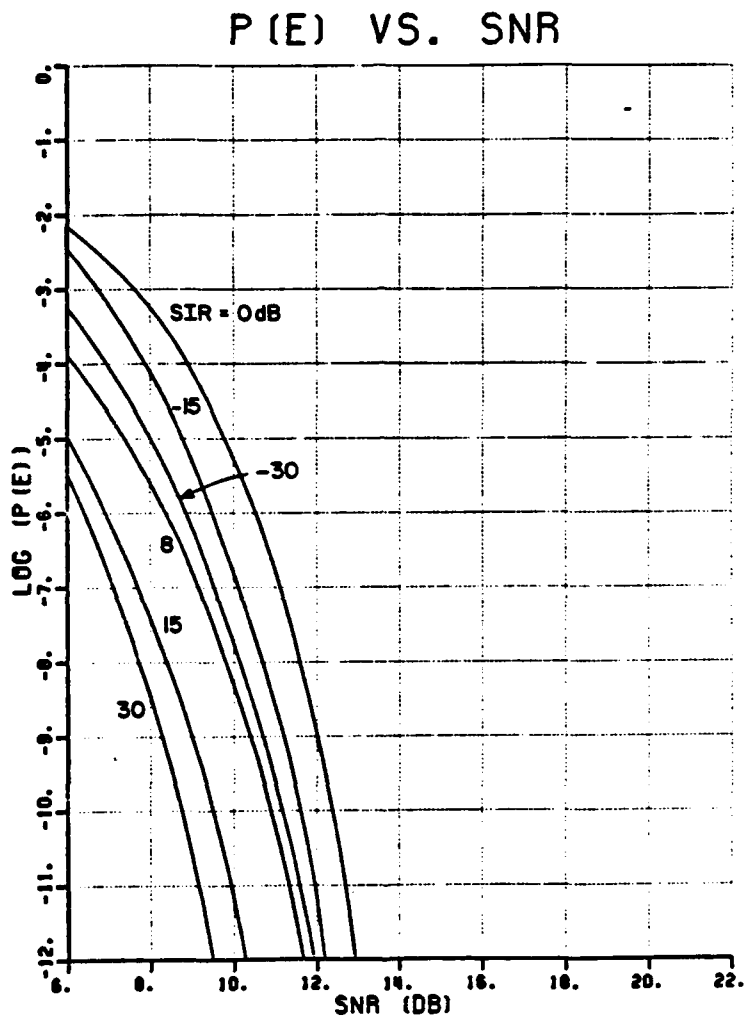


Figure 5.24. DPSK $P(e)$ vs. SNR for 3-element array ($\theta_i=10^\circ$, $k=10$, $\Delta\omega T=2\pi$).

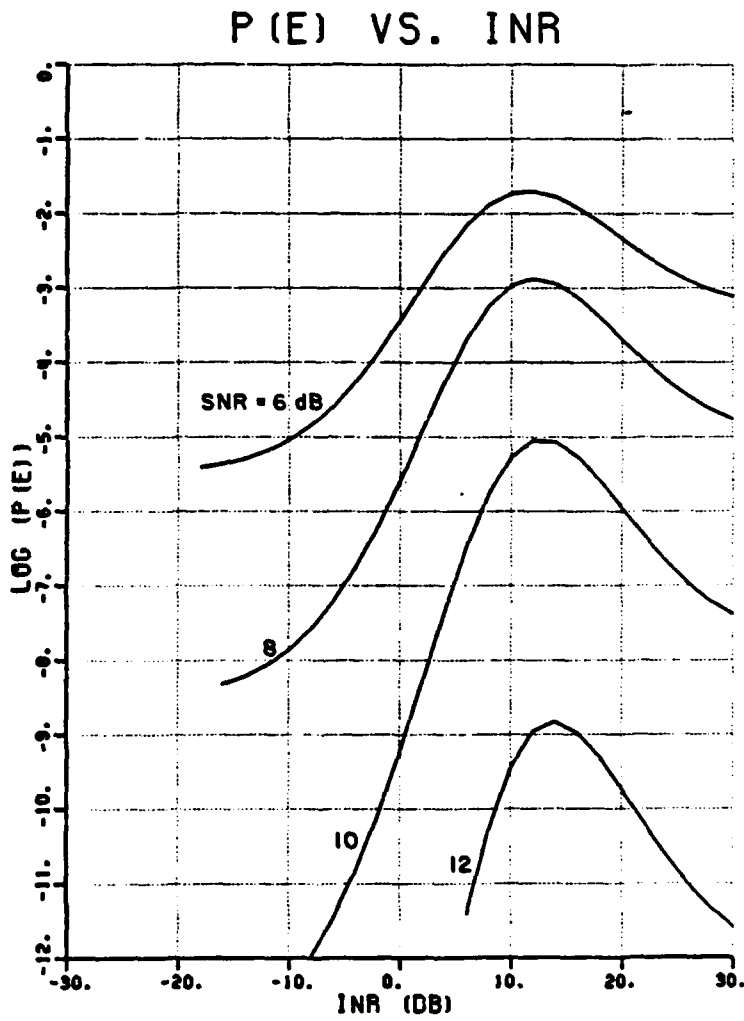


Figure 5.25. DPSK $P(e)$ vs. INR for 3-element array ($\theta_i=10^\circ$, $k=10$, $\Delta\omega T=2\pi$).

CHAPTER VI

PERFORMANCE OF AN FSK COMMUNICATION SYSTEM WITH CW INTERFERENCE

A. INTRODUCTION

In this chapter we examine the performance of a noncoherent binary frequency shift keyed (FSK) communication system that uses an LMS adaptive array to suppress CW interference. Figure 6.1 shows a typical binary FSK waveform. "1" and "0" bits are each represented by a burst of energy at one of two signalling frequencies (ω_1 and ω_0 respectively).

Figure 6.2 shows a simple non-coherent FSK detector. In this detector, the received signal is passed through two bandpass filters (BPFs), each of which is tuned to one of the signalling frequencies. The output of each filter is envelope detected. The envelope detector outputs are sampled at the end of each bit interval and bit decisions are made based upon a comparison of these samples.

Hudson [6] proposed a method of generating an FSK reference signal for the LMS array. This method requires that the transmitted bit stream be encoded into a Markov symbol stream prior to transmission. The reference generation circuit uses the known Markov transition probabilities of the symbol stream to make symbol predictions. This circuit uses the symbol predictions to generate a reference signal for

the array that is partially correlated with the desired signal. The feasibility of this system was experimentally verified in [7].

In this chapter, as in the previous chapters, we assume that a reference signal is available to the array which is a perfect replica of the desired signal. Although the reference generation method discussed above does not generate a perfect reference signal (due to symbol prediction errors) the assumption of a perfect reference signal makes the array weight calculations more tractable.

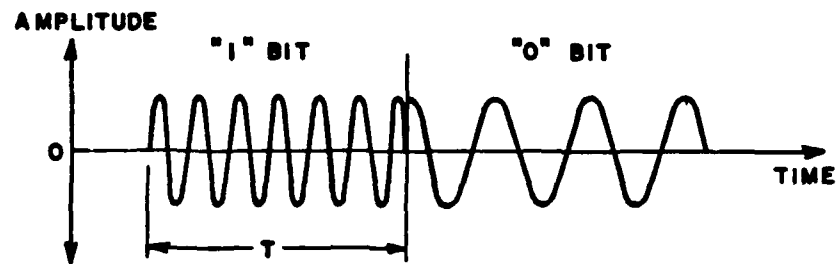


Figure 6.1. A typical FSK waveform.

B. ARRAY PERFORMANCE

In this section we use the results from Chapter II to derive the signal power levels at the output of the LMS array for the case of an FSK desired signal. We first describe the real form of the desired signal and calculate its ACF. We then use this real ACF to calculate the complex ACF (which we will need in the array calculations).

The desired signal during the n^{th} bit interval is given by,

$$d(t) = A_d \cos(\omega_0 t + \psi_0), \quad (6.1)$$

during "0" bits and

$$d(t) = A_d \cos(\omega_1 t + \psi_1), \quad (6.2)$$

during "1" bits where

A_d = the desired signal amplitude,

ω_0 = the "0" signalling frequency,

ω_1 = the "1" signalling frequency,

ψ_0 = the phase angle of the carrier during "0" symbols,

ψ_1 = the phase angle of the carrier during "1" symbols.

We assume that ψ_0 and ψ_1 are independent and identically distributed, each $\sim U[0, 2\pi]$, and that T is the symbol duration. The FSK signal described above might be generated by switching between two free-running oscillators, one tuned to each of the signalling frequencies.

We assume that the incoming symbol stream is symmetric (i.e. "0"s and "1"s are equally likely) and that each symbol is statistically independent of all others. Thus each symbol represents one bit of information.

We assume that the interference is a CW signal that is exactly aligned in frequency (but not necessarily in phase) with one of the desired signal symbols. If we arbitrarily choose ω_0 as the interference frequency, we have

$$\tilde{i}(t) = A_i \exp(\omega_0 t + \psi_i) \quad (6.3)$$

where A_i is the interference amplitude and ψ_i is the interference phase angle which is $\sim U[0, 2\pi]$ and independent of both ψ_0 and ψ_1 .

We now calculate the autocorrelation function of the desired and interfering signals. The analytic ACF for the interference is given by (3.4). For the desired signal we first determine the ACF for the real signal $d(t)$ and then calculate $\tilde{R}_d(\tau)$ using the relationship [15],

$$\tilde{R}_d(\tau) = 2[R_d(\tau) + j\hat{R}_d(\tau)], \quad (6.4)$$

where $\tilde{R}_d(\tau)$ is the ACF of $\tilde{d}(t)$, $R_d(\tau)$ is the ACF of $d(t)$, and the carat denotes the Hilbert transform.

The ACF of the desired signal as described above was calculated by Bennet and Rice [25] for the case of an infinitely long symbol stream under the conditions,

$$\omega_0 T \neq \pi K,$$

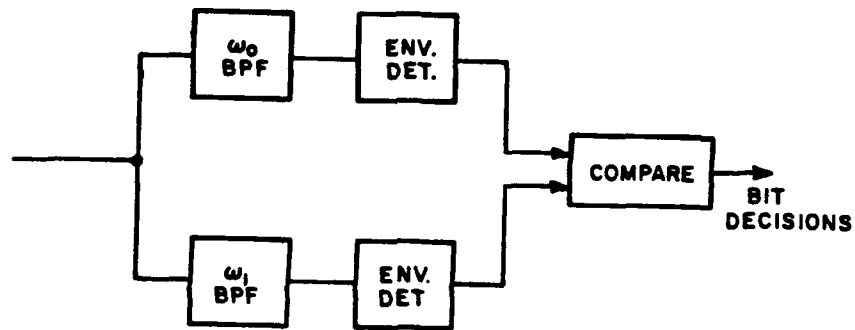


Figure 6.2. FSK detector.

$$\omega_1 T \neq \pi M,$$

and,

$$\omega_0 T + \omega_1 T \neq \pi N,$$

where T is the symbol duration and K , M , and N are arbitrary integers. These conditions are not particularly restrictive for real systems since the instability of real oscillators insures that the inequalities are satisfied.*

Under the above-listed conditions the ACF for the real signal $d(t)$ is given by [25],

* We assume that no special effort is made at the transmitter to synchronize the bit intervals with the carriers.

$$R_d(\tau) = \frac{A_d^2}{8} \frac{(T - |\tau|)}{T} (\cos\omega_0\tau + \cos\omega_1\tau) + \frac{A_d^2}{8} (\cos\omega_0\tau + \cos\omega_1\tau) \quad (6.5)$$

for $|\tau| < T$. This result can also be obtained by calculating the ACF of two on-off-keyed (OOK) waveforms, one with carrier frequency ω_0 and the other at frequency ω_1 . Addition of these two ACFs yields Equation (6.5).

Substitution of $R_d(\tau)$ from (6.5) into (6.4) yields, R_d^{\sim} ,

$$\begin{aligned} R_d^{\sim} &= 2 \frac{A_d^2}{4} \left(1 - \frac{|\tau|}{2T}\right) [(\cos\omega_0\tau + \cos\omega_1\tau) + j(\sin\omega_0\tau + \sin\omega_1\tau)] \\ &= \frac{A_d^2}{2} \left(1 - \frac{|\tau|}{2T}\right) [e^{j\omega_0\tau} + e^{j\omega_1\tau}] \end{aligned} \quad (6.6)$$

The desired signal covariance matrix is calculated by substitution of (6.6) into (2.20). Before writing the expression for ϕ_d we make some simplifying assumptions similar to those that we made in previous chapters for the PSK systems. First, we assume that the interelement propagation delay is much shorter than the symbol duration, (i.e. $T_d \ll T$). We also assume that the signalling frequencies are close enough so that the interelement phase shift for the desired signal is essentially independent of the transmitted symbol (i.e., $\omega_0 T_d \approx \omega_1 T_d = \phi_d$).

These simplifying assumptions allow us to approximate the desired signal ACF by

$$R_d^{\sim}(\tau) \approx A_d^2 e^{j\omega\tau} \quad (6.7)$$

Under the above assumptions the desired signal covariance matrix becomes,

$$\phi_d \approx A_d^2 \begin{bmatrix} 1 & e^{-j\phi_d} & e^{-2j\phi_d} \\ e^{j\phi_d} & 1 & e^{-j\phi_d} \\ e^{2j\phi_d} & e^{j\phi_d} & 1 \end{bmatrix}. \quad (6.8)$$

The simplifications used to obtain the approximation (6.8) do not seriously affect the array performance calculations. Although these simplifications essentially cause us to neglect the desired signal bandwidth, it is shown in [15] that the array behavior is not strongly dependent on the desired signal bandwidth (for the bandwidths of interest here). These simplifications allow us to calculate the array performance without specifying the carrier frequencies or the symbol rate.

The covariance matrices for the interference and the noise signals are identical to those given by (3.7) and (3.8) for BPSK with $\omega_i = \omega_0$. The total covariance matrix ϕ , is determined by summing ϕ_d , ϕ_i , and ϕ_n . The array weights and output power levels are calculated using Equations (2.5) and (2.28) through (2.34).

C. FSK DETECTOR PERFORMANCE WITH CW INTERFERENCE AND AWGN

In this section we determine the probability of error for the FSK detector of Figure 6.2 when the desired signal is corrupted by both white Gaussian noise and CW interference. A similar problem is addressed

in [26] and the results of this analysis are summarized here.

We assume that the composite signal at the detector input is given by

$$s(t) = \sqrt{2P_d} \cos(\omega_k t + \gamma_k) + \sqrt{2P_i} \cos(\omega_0 t + \gamma_i) + n(t) \quad (6.9)$$

where $\kappa = 0$ or 1 depending on the transmitted symbol, γ_k is the phase of the desired signal at the detector input, γ_i is the interference phase (where it is assumed that γ_1, γ_0 and γ_i are i.i.d $\sim U[0, 2\pi]$), and $n(t)$ is a white Gaussian noise signal with two-sided PSD $n/2$.

We assume that the detector BPFs are ideal, each with bandwidths $1/T$. Therefore the desired and interfering signals will nearly reach their steady state values at the end of the symbol interval. We assume that the passbands of the two filters are not overlapping and we neglect any intersymbol interference or crosstalk. The noise produces (independent) zero-mean Gaussian random processes with variance n/T at the output of each of the BPFs.

At each BPF output we either have Gaussian thermal noise alone or the sum of a CW signal and the Gaussian noise signal. The probability density function of the amplitude of the filter output has a Rayleigh distribution in the former case or a Rician [27] distribution in the latter case. We denote the output of the "0" and "1" envelope detectors at the end of the given symbol interval by Z_0 and Z_1 respectively.

We first assume that a "0" symbol is transmitted. In this case the "0" filter has the sum of two sinusoids (the desired signal and the interference) plus the thermal noise at its input. The "1" filter sees

only the noise signal at its input. We denote by γ the phase difference between the two sinusoids in the "0" filter (i.e., $\gamma = \gamma_0 - \gamma_i$). The (Rician) PDFs of the amplitudes of the filter outputs conditioned on γ are then given by,

$$f(Z_0|\gamma, "0") = \frac{Z_0}{(n/T)} I_0 \frac{A_{00}Z_0}{(n/T)} \exp\left(-\frac{Z_0^2 + A_{00}^2}{2n/T}\right), \quad (6.10)$$

for the "0" filter and,

$$f(Z_1|\gamma, "0") = \frac{Z_1}{(n/T)} I_0 \frac{A_{10}Z_1}{(n/T)} \exp\left(-\frac{Z_1^2 + A_{10}^2}{2n/T}\right), \quad (6.11)$$

for the "1" filter, where I_0 is the modified Bessel function of the first kind of order zero and A_{ij} is the amplitude of the sinusoidal signal at the input to the i filter when symbol j is transmitted.

Therefore, A_{00} and A_{10} are given by,

$$A_{00} = \sqrt{2P_d + 4\sqrt{P_d P_i} \cos\gamma + 2P_i}, \quad (6.12)$$

and,

$$A_{10} = 0. \quad (6.13)$$

Since no sinusoidal signal is present at the input of the "1" filter when a "0" is transmitted (i.e. since $A_{10} = 0$) then the Rician distribution given in (6.11) is actually a Rayleigh distribution [27],

$$f(Z_1 | \gamma, "0") = \frac{Z_1}{(n/T)} \exp \left[-\frac{Z_1^2}{2(n/T)} \right] \quad (6.14)$$

We now assume that a "1" symbol is transmitted. In this case, each filter has both a CW signal and a Gaussian noise signal at its input. The (Rician) PDFs for the amplitudes of the filter outputs are given by,

$$f(Z_0 | \gamma, "0") = \frac{Z_0}{(n/T)} I_0 \left(\frac{A_{01} Z_0}{(n/T)} \right) \exp \left(-\frac{Z_0^2 + A_{01}^2}{2(n/T)} \right), \quad (6.15)$$

for the zero filter and,

$$f(Z_1 | \gamma, "1") = \frac{Z_1}{(n/T)} I_0 \left(\frac{A_{11} Z_1}{(n/T)} \right) \exp \left(-\frac{Z_1^2 + A_{11}^2}{2(n/T)} \right), \quad (6.16)$$

where,

$$A_{01} = \sqrt{2P_i}, \quad (6.17)$$

and,

$$A_{11} = \sqrt{2P_d}. \quad (6.18)$$

For equally likely symbols, the probability of a symbol error conditioned on γ is given by,

$$\frac{1}{2} P[Z_1 > Z_0 | \gamma, "0" \text{ sent}] + \frac{1}{2} P[Z_0 > Z_1 | \gamma, "1" \text{ sent}] \quad (6.19)$$

These probabilities can be directly evaluated [26] to give us the following expression for the conditional symbol error probability,

$$\begin{aligned}
P(e|\gamma) = & \frac{1}{2} \left[Q \left(\frac{A_{10}}{\sqrt{2n/T}}, \frac{A_{00}}{\sqrt{2n/T}} \right) \right. \\
& - \frac{1}{2} I_0 \left(\frac{A_{10}A_{00}}{2n/T} \right) \exp \left(-\frac{1}{2} \left(\frac{A_{10}^2 + A_{00}^2}{2n/T} \right) \right) \\
& + Q \left(\frac{A_{11}}{\sqrt{2n/T}}, \frac{A_{01}}{\sqrt{2n/T}} \right) \\
& \left. - \frac{1}{2} I_0 \left(\frac{A_{11}A_{01}}{2n/T} \right) \exp \left(-\frac{1}{2} \left(\frac{A_{11}^2 + A_{01}^2}{2n/T} \right) \right) \right] \quad (6.20)
\end{aligned}$$

where $Q(a,b)$ is Marcum's Q-function [24]. Since $A_{10}=0$ we can use the relationships,

$$Q(0,b) = e^{-(b/2)^2}, \quad (6.21)$$

and,

$$I_0(0) = 1 \quad (6.22)$$

to simplify (6.20). The resulting expression for error probability conditioned on γ is,

$$\begin{aligned}
P(e|\gamma) = & \frac{1}{2} \left[\frac{1}{2} \exp \left(-\frac{1}{2} \frac{A_{00}^2}{2n/T} \right) + Q \left(\frac{A_{01}}{\sqrt{2n/T}}, \frac{A_{11}}{\sqrt{2n/T}} \right) \right. \\
& \left. - \frac{1}{2} I_0 \left(\frac{A_{01}A_{11}}{2n/T} \right) \exp \left(-\frac{1}{2} \left(\frac{A_{01}^2 + A_{11}^2}{2n/T} \right) \right) \right] \quad (6.23)
\end{aligned}$$

We integrate $P(e|\gamma)$ over the (uniformly distributed) phase angle γ to obtain the symbol error probability,

$$P(e) = \frac{1}{4\pi} \int_0^{2\pi} \left[\frac{1}{2} \exp\left(-\frac{1}{2} \frac{A_{00}^2}{\sqrt{2n/T}}\right) + Q\left(\frac{A_{01}}{\sqrt{2n/T}}, \frac{A_{11}}{\sqrt{2n/T}}\right) - \frac{1}{2} I_0\left(\frac{A_{01}A_{11}}{\sqrt{2n/T}}\right) \exp\left(-\frac{1}{2} \left(\frac{A_{01}^2 + A_{11}^2}{2n/T}\right)\right) \right] d\gamma. \quad (6.24)$$

This is the general expression for the symbol error probability for the FSK detector with a single CW interferer exactly on one of the signalling frequencies.

We note that if $P_i = 0$ then $A_{01} = 0$ and $A_{00} = A_{11} = 2\sqrt{P_d}$. In this case we can use (6.21) and (6.22) to further simplify (6.24). In this case $P(e)$ becomes,

$$P(e) = \frac{1}{2} e^{-\frac{1}{2} (E_d)/n} \quad (6.25)$$

which is the well known result for non-coherent FSK with AWGN but no interference [7].

The general expression for $P(e)$ given by (6.22) was evaluated numerically to determine the detector performance. Figures 6.3 and 6.4 show the results from calculations of $P(e)$ for several SNR and INR values. Simpson's rule was used to evaluate the integral in (6.22) where the iterative method described in [24] was used to evaluate Marcum's Q function. Either a polynomial or an asymptotic approximation was used to estimate I_0 . We note that the performance of the binary FSK detector with CW interference is worse than that of either of the binary PSK detectors discussed in chapters III and V.

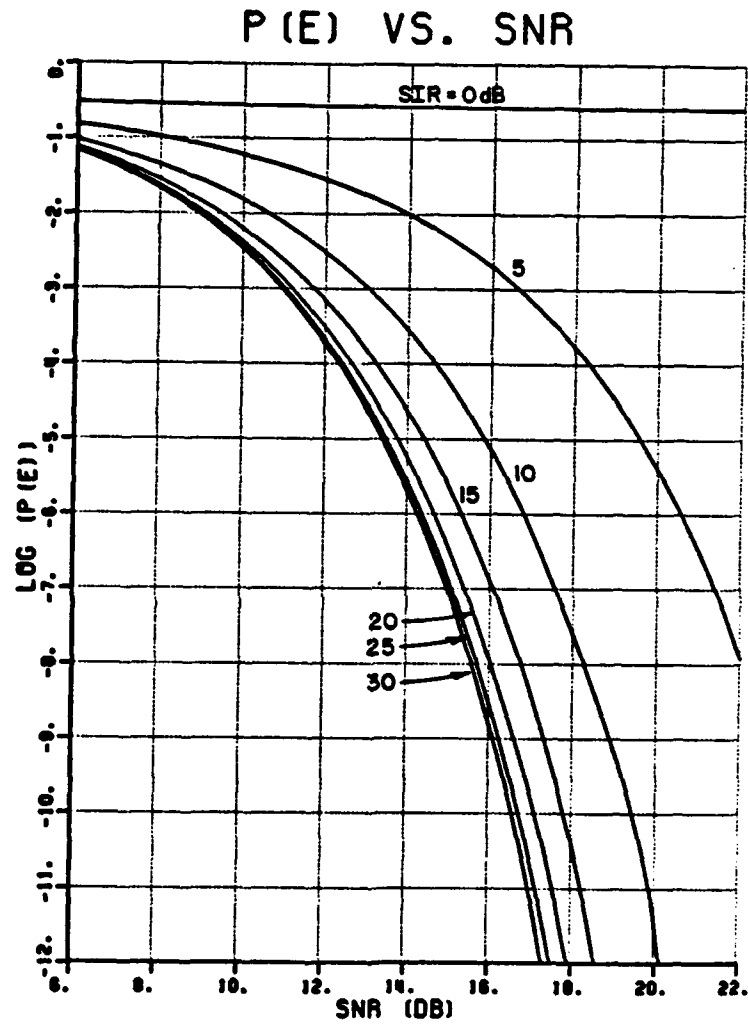


Figure 6.3. Performance of ideal FSK detector with CW interference.

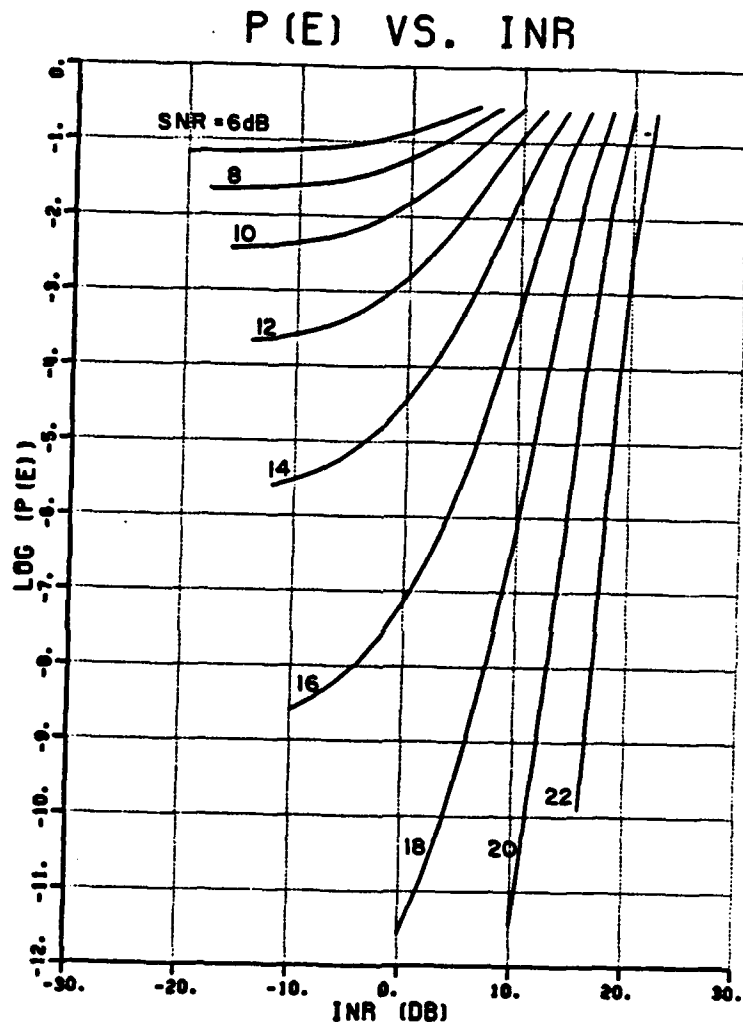


Figure 6.4. Performance of ideal FSK detector with CW interference.

D. PERFORMANCE OF THE COMBINED LMS ARRAY/FSK DETECTOR

In this section we calculate the bit-error-probability for the FSK system that includes the LMS array. As noted at the end of section B of this chapter, the covariance matrix for FSK signalling given by (6.8) is identical to that of BPSK (after the simplifying assumptions were made in both cases). Therefore, the adaptive array calculations for the FSK and BPSK cases are the same. Thus to calculate the system performance we need only to calculate $P(e)$ for the FSK detector when the array output signals appear at the detector input.

Figures 6.5 through 6.10 show the system performance for θ_j values of 10, 20 and 80°. The array bandwidth factor k is set equal to 5 in each of the cases shown. Qualitatively, the FSK curves are very similar to those calculated for the other modulation methods. The FSK error probabilities are slightly worse than either of the binary PSK cases and roughly equal to those to QPSK (for the same θ_j and k values). Actually FSK is slightly better than QPSK in regions near the "humps" in the $P(e)$ vs. INR curves, but worse in the other regions. Results for FSK cases with $k=10$ were also calculated but are not presented here since they display no unexpected characteristics.

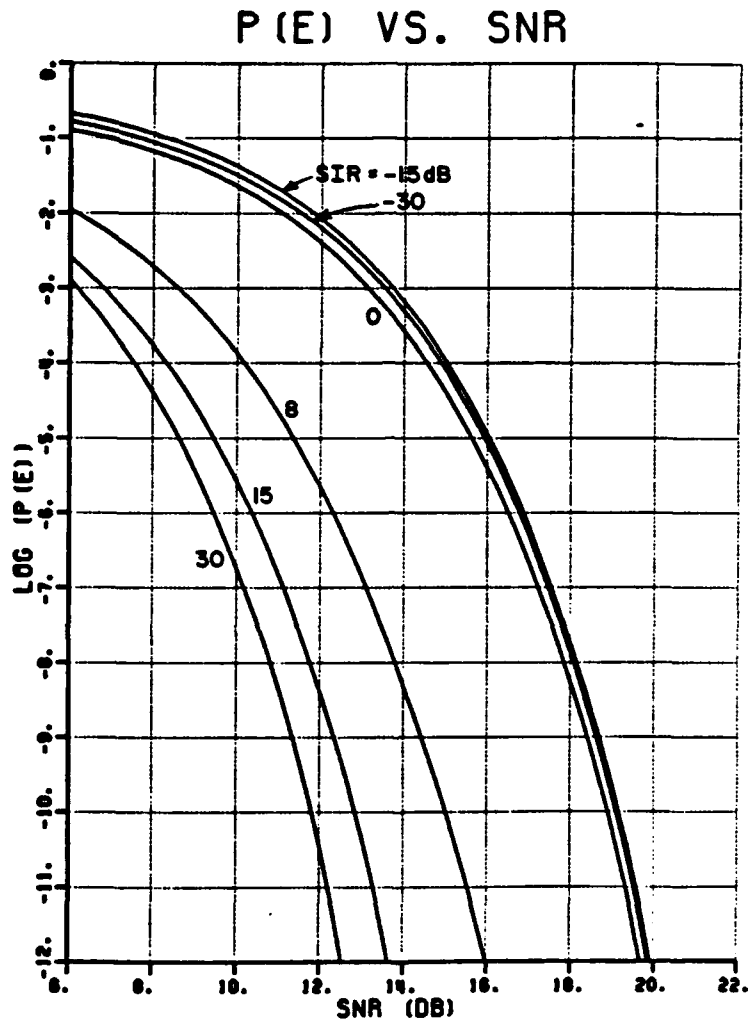


Figure 6.5. FSK P(e) vs. SNR for 3-element array ($\theta_i=10^\circ$, $k=5$).

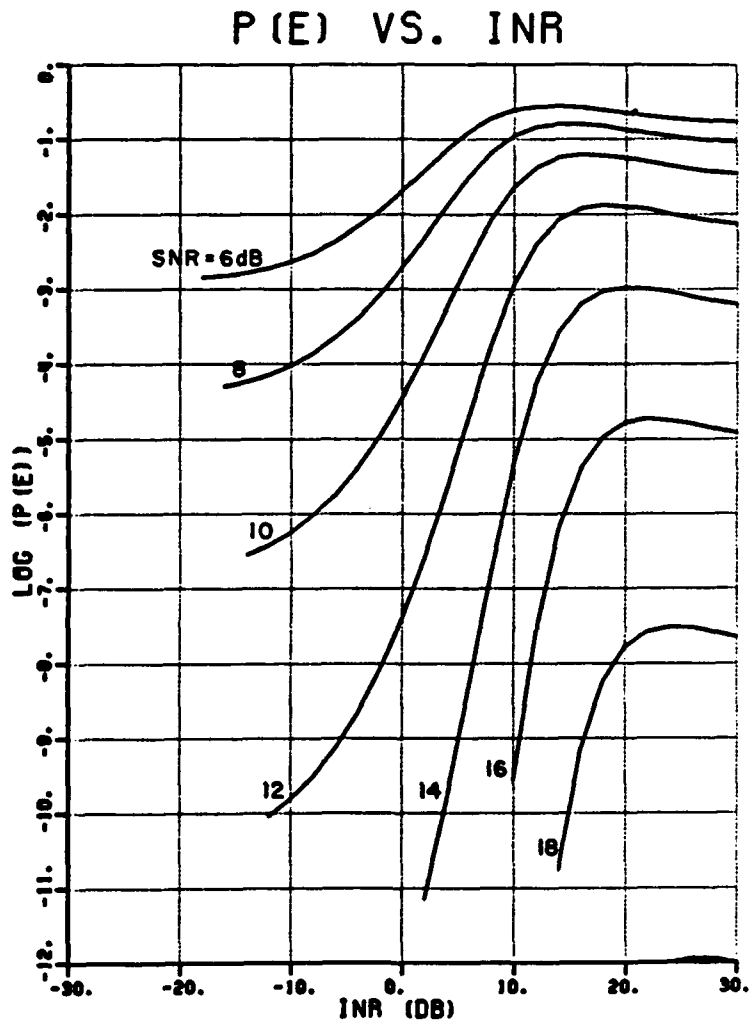


Figure 6.6. FSK $P(e)$ vs. INR for 3-element array ($\theta_i=10^\circ$, $k=5$).

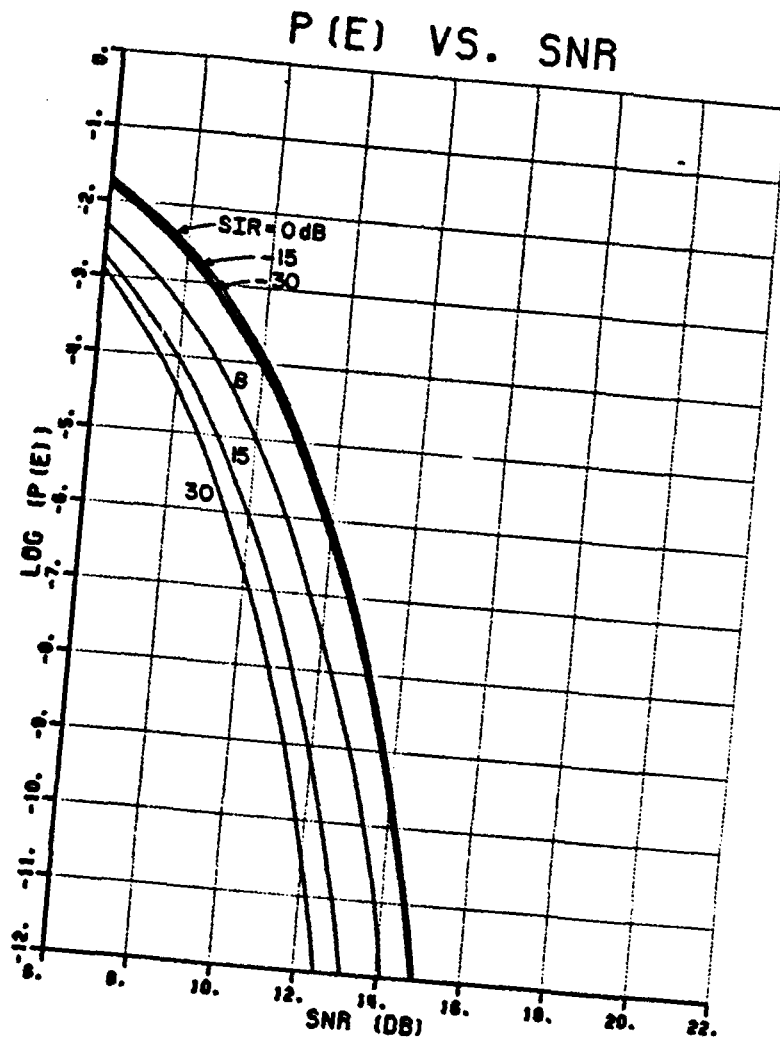


Figure 6.7. FSK $P(e)$ vs. SNR for 3-element array ($\theta_1=20^\circ$, $k=5$).

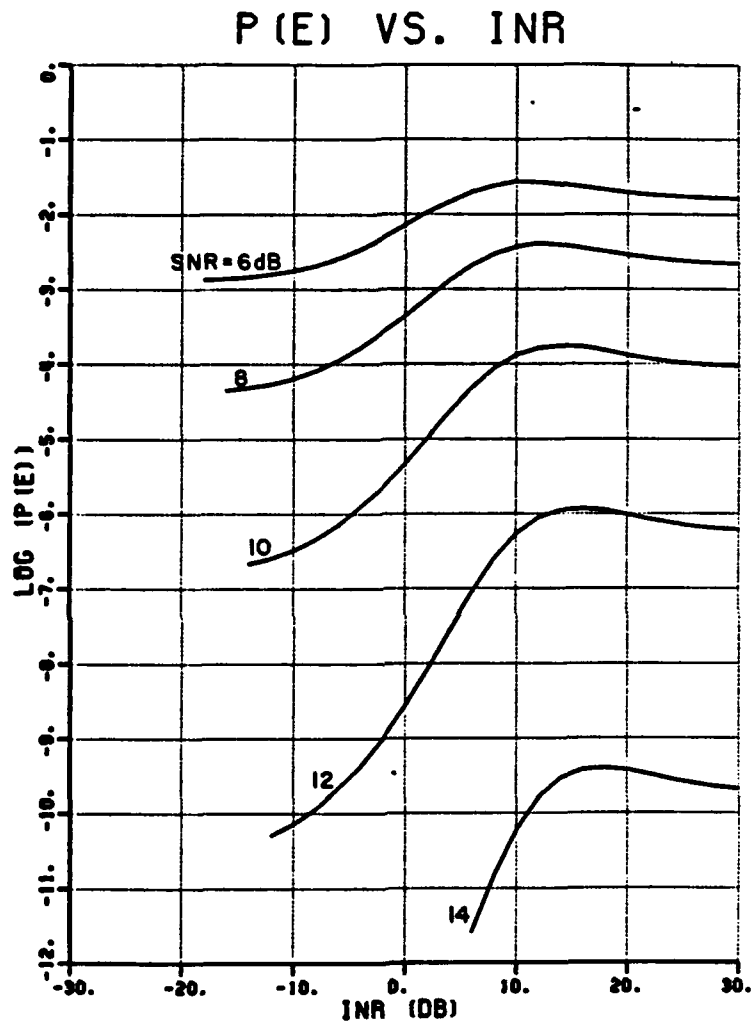


Figure 6.8. FSK $P(e)$ vs. INR for 3-element array ($\theta_i=20^\circ$, $k=5$).

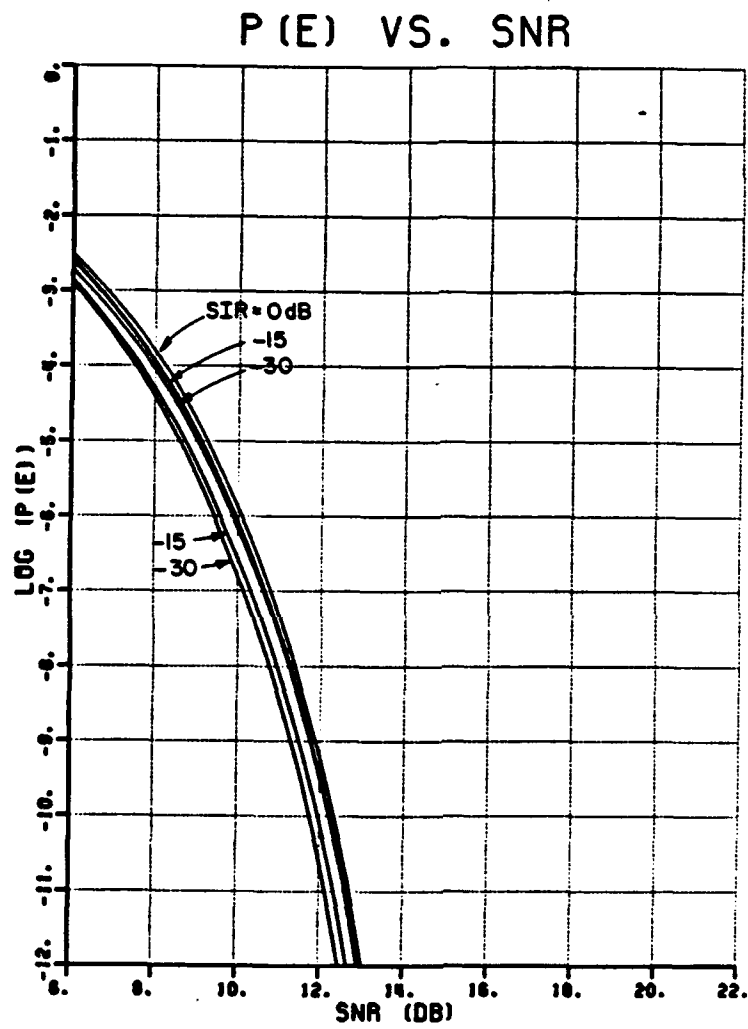


Figure 6.9. FSK $P(e)$ vs. SNR for 3-element array ($\theta_1=80^\circ$, $k=5$).

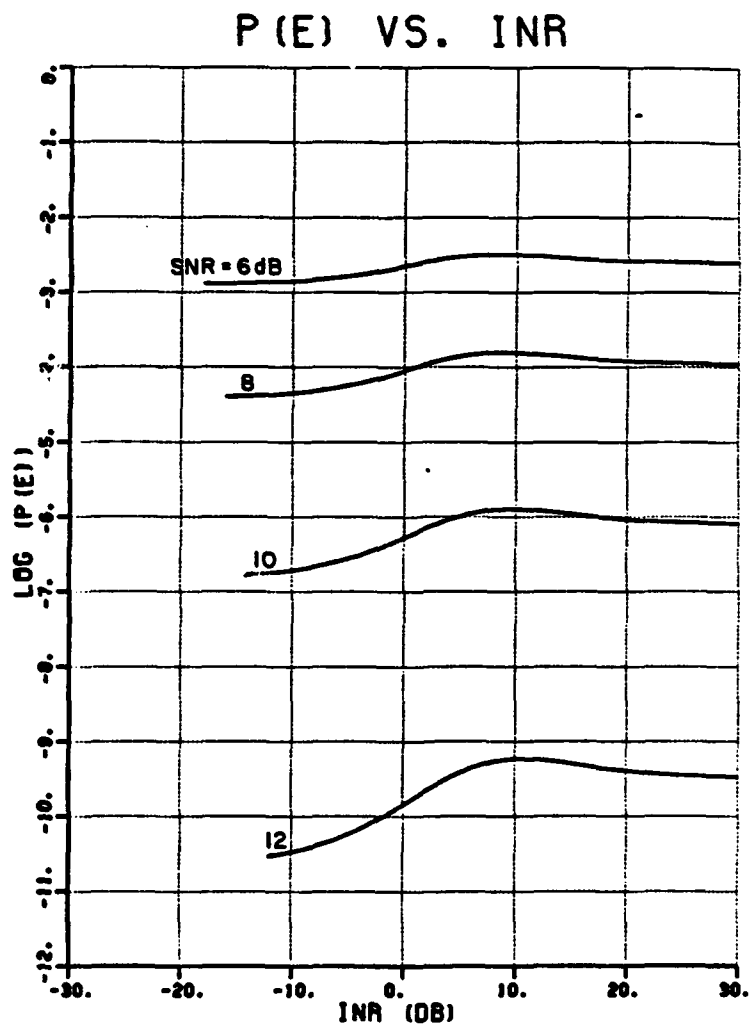


Figure 6.10. FSK $P(e)$ vs. INR for 3-element array ($\theta_j=90^\circ$, $k=5$).

CHAPTER VII

PERFORMANCE OF A NARROWBAND ADAPTIVE ARRAY WITH BPSK SIGNALLING AND CW INTERFERENCE

A. INTRODUCTION

Chapters III through VI examined the performance of several communication systems that included LMS arrays. We found that $P(e)$ for these systems increases as the array bandwidth increases. In this chapter we more closely examine the effects of bandwidth on system performance.

In the previous chapters we found that the system performance was similar for BPSK, QPSK, DPSK, and FSK desired signal modulation. Therefore, in this and the following chapters, we limit our discussion to the BPSK system with the understanding that similar qualitative performance would be achieved for each of the other modulation methods.

In Chapters III, IV, and V we used correlator-type PSK detectors. The $P(e)$ calculations that we made assumed that the detector input bandwidth was wide enough so that the desired signal was passed with negligibly small distortion. Therefore, this model did not allow us to calculate $P(e)$ for values of k less than approximately 5.

In this chapter we describe modified BPSK signalling and detector models that allow us to calculate $P(e)$ for k values as small as $1/2$. These models are based upon the Nyquist pulse shaping criterion [16,28].

This criterion states that, with appropriate transmit and receive filtering, we can communicate over a bandlimited channel with no intersymbol interference (ISI). Using this Nyquist criterion we can limit the transmitted signal bandwidth to $(1/T)$ Hz. Furthermore, for a fixed input SNR, the bandlimited BPSK system can achieve a $P(e)$ value equal to that of standard (infinite bandwidth) BPSK. Several practical aspects of narrowband signalling are discussed in [29].

In the next section we examine the performance of the narrowband BPSK system without an adaptive array. In section C we calculate the system performance when the adaptive array is added to reject CW interference. In Section C we also examine the effects of the array input bandwidth on this performance.

B. BPSK SIGNALLING OVER A NARROWBAND CHANNEL

In this section we describe a narrowband BPSK communication system. In this system the transmitted signal bandwidth is limited to $(1/T)$ Hz. This bandwidth corresponds to a bandwidth factor k (as defined in the previous chapters), of $1/2$. At the receiver, a matched filter processes the waveform. The output of this filter is periodically sampled and symbol decisions are made based upon the signs of the output samples. By judicious choice of the transmit and receive filters we can eliminate ISI by insuring that the receiver response to each symbol is zero at the sampling instants corresponding to all other symbols.

Figure 7.1 shows the narrowband BPSK system model. The transmitted baseband signal $f(t)$ is passed through the transmit filter which has a transfer function,

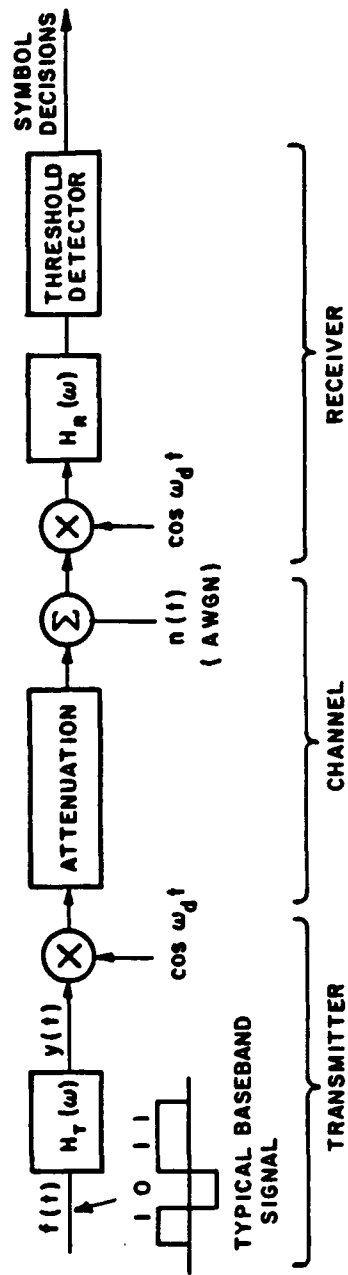


Figure 7.1. Narrowband BPSK communication system.

$$H_T(\omega) = P_{(\pi/T)}(\omega) \left[\frac{1}{\text{sinc}(\frac{\omega T}{2})} \right] \quad (7.1)$$

where,

$$P_{(\pi/T)}(\omega) = \begin{cases} 1 & ; \quad -\pi/T \leq \omega \leq \pi/T \\ 0 & ; \quad |\omega| > \pi/T \end{cases} \quad (7.2)$$

To understand how this filter works we examine its response to a single input pulse. Figure 7.2(a) shows a simple input pulse $f(t) = p_{T/2}(\omega)$. Figure 7.2(b) shows the filter transfer function $H_T(\omega)$. The filter output (in the time domain) is given by,

$$g(t) = f(t) * h_T(t) \quad (7.3)$$

where $h_T(t)$ is the transmit filter impulse response and $*$ denotes convolution. Application of the convolution theorem of Fourier analysis yields,

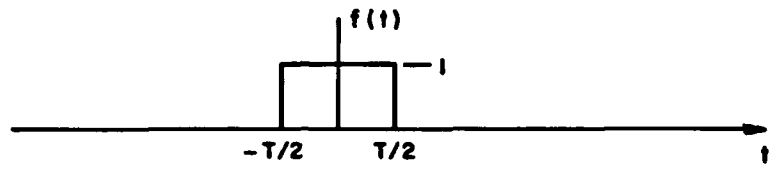
$$G(\omega) = F(\omega)H_T(\omega) \quad (7.4)$$

where $G(\omega)$ and $F(\omega)$ are the Fourier transforms of $g(t)$ and $f(t)$ respectively. We calculate $F(\omega)$ using a standard Fourier transform pair,

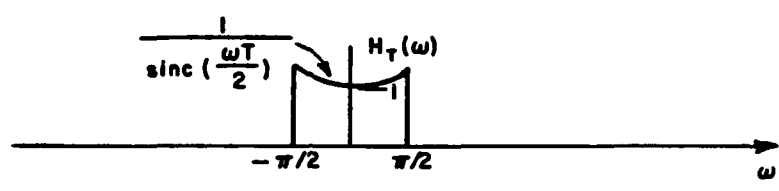
$$F(\omega) = T \text{ sinc}(\omega T/2). \quad (7.5)$$

We evaluate $G(\omega)$ from (7.1), (7.4) and (7.5),

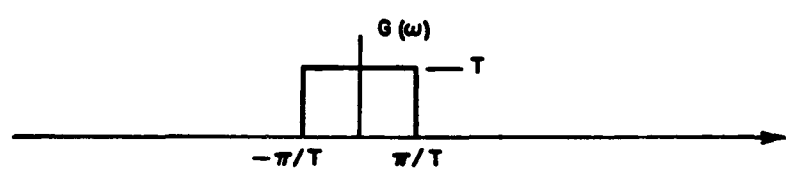
$$G(\omega) = T p_{(\pi/T)}(\omega). \quad (7.6)$$



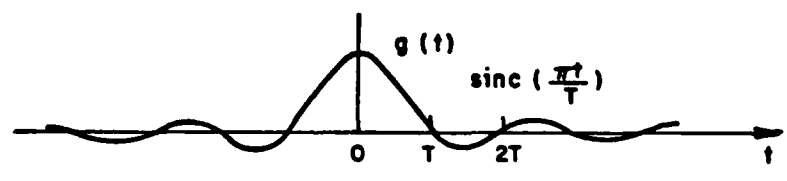
(a) Baseband pulse prior to filtering



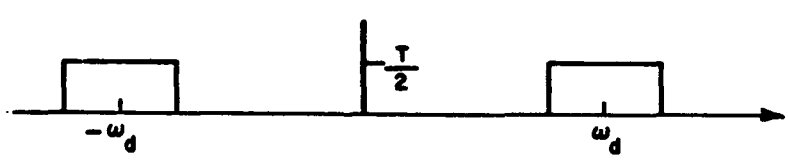
(b) Transmit filter transfer function



(c) Fourier transform of filtered pulse



(d) Filtered baseband pulse



(e) Fourier transform of carrier modulated by a single filtered pulse

Figure 7.2. Transmitter processing of baseband pulse.

Figure 7.2(c) shows $G(\omega)$. Application of another standard Fourier transform pair yields,

$$g(t) = \text{sinc}(\pi t/T). \quad (7.7)$$

This waveform is shown in Figure 7.2(d).

As we have just shown, the transmit filter converts the rectangular baseband digital pulses into a series of sinc pulses. Note that the transmitted symbols are separated by T seconds and $\text{sinc}(\pi t/T)=0$ for $t=nT$ ($n=1, 2, 3, \dots$). Therefore, the single symbol represented by $f(t)$ will produce no ISI for any preceding or following symbols.

$g(t)$ is multiplied by a carrier, $\cos(\omega_d t)$, prior to transmission. The transmitted signal is therefore given by,

$$g(t)\cos(\omega_d t) = \text{sinc}(\pi t/T)\cos(\omega_d t). \quad (7.8)$$

Figure 7.2(e) shows the Fourier transform of the transmitted signal.

As the signal propagates through the channel, it is attenuated and corrupted by an AWGN process $n(t)$ with two-sided PSD $N_0/2$. Later we consider the effects of interference added as the signal propagates through the channel.

At the receiver the signal is given by

$$r(t) = A_d \text{sinc}\left(\frac{\pi t}{T}\right)\cos(\omega_d t) + n(t) \quad (7.9)$$

where we have neglected the propagation delay. This signal is multiplied by $\cos(\omega_d t)$ and the resulting signal is passed through the receive filter which is an ideal low pass filter with cutoff frequency π/T radians ($1/2T$ Hz). This filter removes the double frequency term

and limits the thermal noise power. The signal at the receive filter input is given by

$$r(t)\cos(\omega_d t) = \frac{A_d}{2} \text{sinc}\left(\frac{\pi t}{T}\right)[1 + \cos(2\omega_d t)] + n(t)\cos(\omega_d t) \quad (7.10)$$

The output from this filter consists of a desired signal term X_d and a noise term X_n . From (7.10) we see that

$$X_d = \frac{A_d}{2} \text{sinc}\left(\frac{\pi t}{T}\right) \quad (7.11)$$

since the receive filter eliminates the double frequency term.

The noise signal at the input to the filter $n(t)\cos(\omega_d t)$ has (two-sided) PSD $N_0/4$ or equivalently, a single sided PSD of $N_0/2$. Since the receive filter has a bandwidth of $1/2T$ Hz X_n is a zero-mean Gaussian random variable with variance $(N_0/2)(1/2T) = N_0/4T$.

We note that X_d reaches its maximum value at $t=0$. The detector output is sampled at $t=0$ to detect the symbol represented by $f(t)$. The receiver output is sampled at points where $t=nT$ ($n=1, 2, 3, \dots$) to detect the symbols that follow. Figure 7.3 shows the filter output (without the noise signal) for the transmitted symbol sequence 1011. From this figure we see that, unlike the conventional BPSK waveform, the narrowband BPSK signal does not have a constant envelope. The varying amplitude of the envelope for narrowband BPSK requires that the transmitter must have a peak-to-average power ratio greater than unity.

The receiver makes symbol decisions based upon the sign of the receive filter output at the sampling instants. Positive output samples

produce "1" decisions and negative output samples produce "0" decisions. The symbol error probability is given by

$$P(e) = \frac{1}{2} P(X_d + X_n < 0 | "1" \text{ sent}) + \frac{1}{2} P(X_d + X_n > 0 | "0" \text{ sent}) \quad (7.12)$$

From the symmetry of signal space we can show that the two conditional probabilities in this expression are equal. Therefore the expression for $P(e)$ becomes,

$$\begin{aligned} P(e) &= \frac{1}{2} P(X_d + X_n < 0 | "1" \text{ sent}) \\ &= P(X_n < \frac{-A_d}{2}) \end{aligned} \quad (7.13)$$

where X_n is a zero-mean Gaussian random variable with variance $N_0/4$.

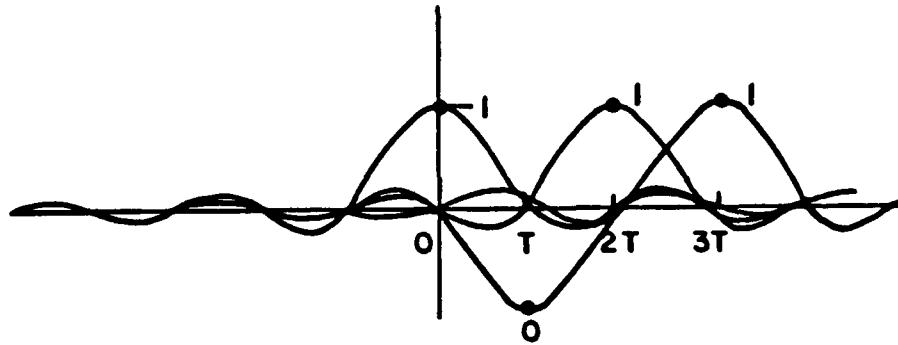
Therefore

$$P(e) = \text{erfc} \left(\sqrt{\frac{A_d^2 T}{N_0}} \right). \quad (7.14)$$

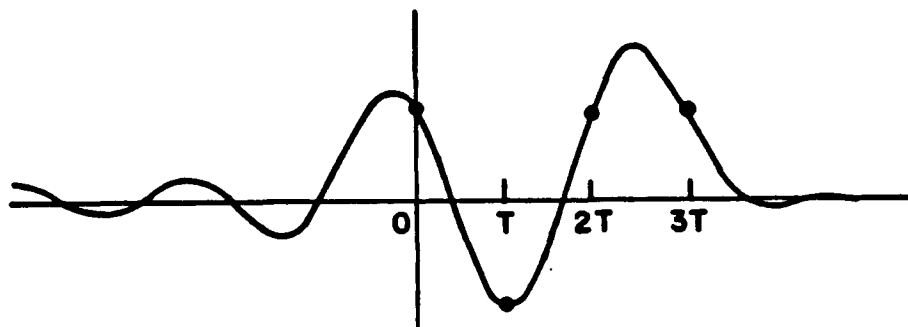
E_b , the energy-per-bit in the desired signal component of $r(t)$, is given by $A_d^2 T/2$ (this is easily shown by application of Parseval's theorem to the desired signal component in Equation (7.10)). Therefore, Equation (7.14) can be rewritten,

$$P(e) = \text{erfc} \left(\sqrt{\frac{2E_b}{N_0}} \right). \quad (7.15)$$

This expression for $P(e)$ is the same as the well known result for ideal detection of an unfiltered (and thus infinite bandwidth) BPSK signal in the presence of AWGN. Equation (7.15) implies that, with a bandlimited



(a) Individual waveforms representing the sequence 1011



(b) Composite waveform for the sequence 1011

Figure 7.3. Baseband signal for simple binary sequence.

system, we can achieve performance equal to that of an infinite bandwidth standard BPSK system.

The results presented above were derived under the assumption that AWGN is the only corrupting signal at the receiver input. We now calculate the system performance when $r(t)$ also includes a random-phase CW interfering signal with amplitude A_i . We assume that the interference is at a frequency where it is not rejected by the receive filter. In [18] Rosenbaum shows that, in this case, $P(e)$ is given by,

$$P(e) = \frac{1}{2\pi} \int_0^{\pi} \operatorname{erfc} \left\{ \sqrt{\frac{2E_d}{N_0}} + \sqrt{\frac{2E_i}{N_0}} \cos(\gamma_{rel}) \right\} d\gamma_{rel} \quad (7.16)$$

where E_i and γ_{rel} (which can be considered a dummy variable of integration) are as defined in Chapter III. The derivation of this equation is similar to that used to obtain Equation (3.44) in Chapter III.

We note that Equation (7.15) is almost identical to Equation (3.44), our general expression for $P(e)$ for BPSK. The only difference is the factor of $\operatorname{sinc}(\omega T/2)$ in the interference term Equation (3.44). This term is caused by the frequency response of the integrator in the integrate-and-dump detector used in Chapter III. The frequency response of the detector that we use in this chapter is constant over the detector passband.

The preceding analysis suggests that we can transmit $(1/T)$ bits per second over an RF channel with a bandwidth $(1/T)$ Hz with the same performance as we would have with standard BPSK. However, to achieve

these results, we must be able to realize the transmit and receive filters in the narrowband model. The noncausal nature of the impulse response of these filters is evidence that the filters are not realizable.

Good approximations to ideal Nyquist pulse shaping filters do exist. Most notably, members of the raised-cosine family of filters [16] provide performance equal to that achieved with the ideal low-pass transmit and receive filters used our narrowband model. Actually, the ideal low-pass filter is one member of the family of raised-cosine filters. All raised-cosine filters have the same equivalent noise bandwidth as the ideal filters and produce the same $P(e)$ with no ISI. These filters have a passband between 0% and 100% larger than the ideal low-pass filters assumed our model. Approximations for many of these raised-cosine filters can be realized [30]. Reference [16] provides a thorough analysis of system performance with non-ideal filters (without interference).

C. BPSK SYSTEM PERFORMANCE WITH AN LMS ARRAY AND CW INTERFERENCE

Figure 7.4 shows a block diagram of a narrowband receiving system that includes an LMS adaptive array. We assume that the transmitter and channel are the same as those shown in Figure 7.1. We also assume that, as in previous chapters, the desired and interfering signals arrive from angles θ_d and θ_i respectively (measured from the broadside direction). The BPFs at the element inputs are assumed to be ideal with bandwidth $k(2/T)$.

In order to calculate the adaptive array performance we must calculate the ACF of the desired signal $\tilde{d}(t)$. $\tilde{d}(t)$, the analytic desired signal during the n^{th} symbol interval, is given by,

$$\tilde{d}(t) = b_n A_d \text{sinc}(\pi t/T) \exp(j\omega_d t) \quad (n-1)T < t < nT \quad (7.17)$$

where $b_n = +1$ if the n^{th} bit is a 1 and $b_n = -1$ if the n^{th} bit is a 0.

Figure 7.5 shows $S_d^{\sim}(\omega)$, the PSD of $\tilde{d}(t)$. $R_d^{\sim}(\tau)$, the ACF of $\tilde{d}(t)$, the inverse Fourier transform of $S_d^{\sim}(\omega)$. $R_d^{\sim}(\tau)$ is given by,

$$R_d^{\sim}(\tau) = A_d^2 \text{sinc}\left(\frac{\pi\tau}{T}\right) \exp(j\omega_d \tau) \quad (7.18)$$

We can use Equations (2.20) and (7.18) to calculate the desired signal covariance matrix. If we make our usual simplifying assumption that $T_d \ll T$, then $R_d^{\sim}(\tau)$ is approximated by,

$$R_d^{\sim}(\tau) \approx A_d^2 \exp(j\omega_d \tau) \quad (7.19)$$

With this approximation the desired signal covariance matrix is the same as that which we used for each of the previously examined modulation methods (see for example Equation (3.9)).

The interference and noise models are the same as in Chapter III. Therefore, since the desired signal, interference and noise covariance matrices are the same as in Chapter III, the adaptive array calculations for the narrowband model are identical to those for the wideband model of Chapter III.

As discussed in the previous section if the interference is at a frequency which falls within the receive filter bandwidth, then $P(e)$

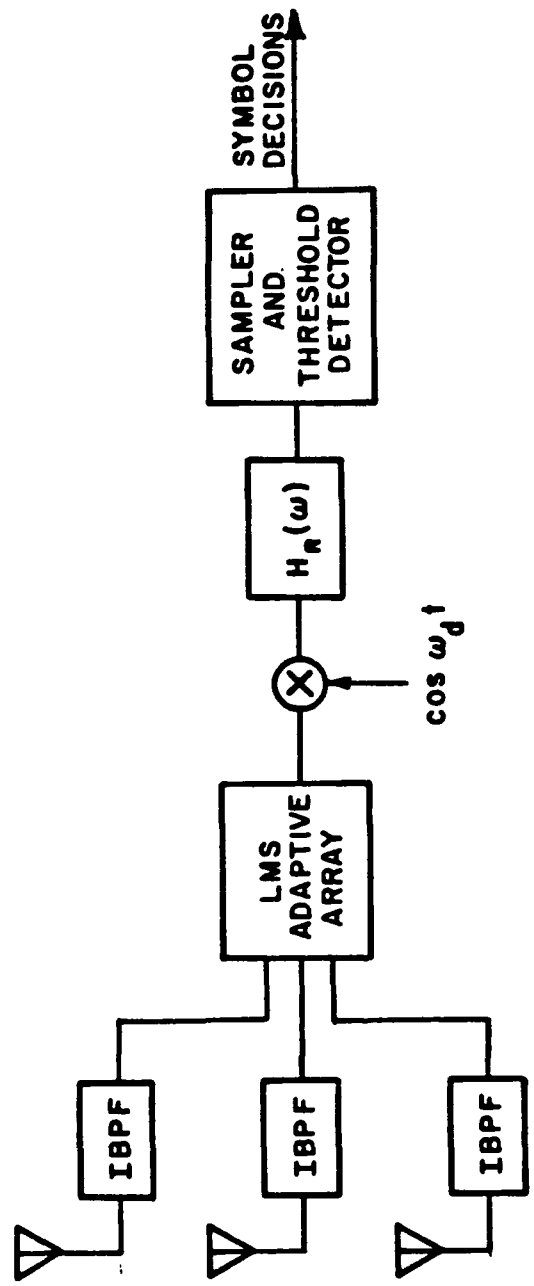


Figure 7.4. Narrowband BPSK receiver using an adaptive array.

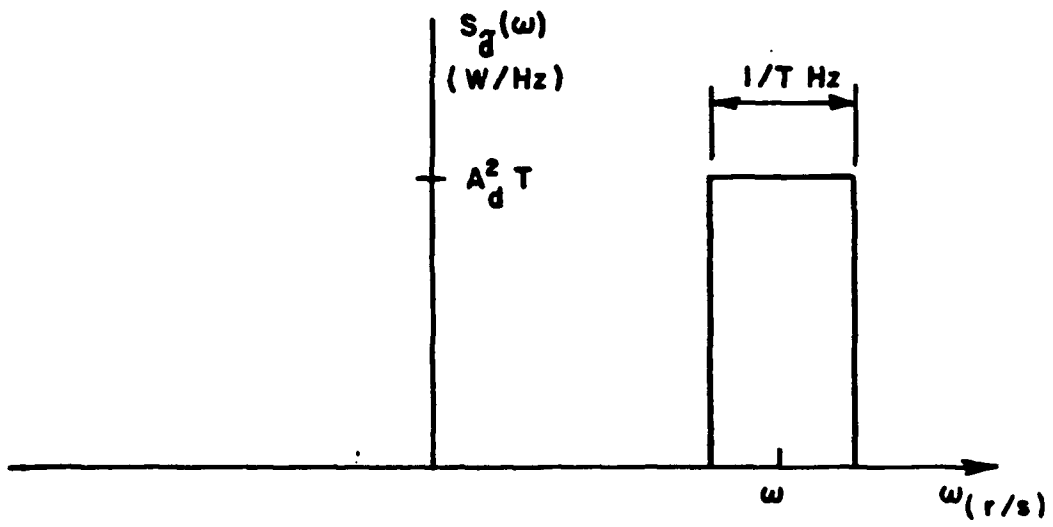


Figure 7.5. Desired signal PSD.

will be given by (7.16). As previously noted, this expression is the same as Equation (3.44) with $\Delta\omega T$ set equal to zero. Although the signal and receiver structures assumed in Chapter III and the present chapter differ significantly, the expressions that describe the performance of both the array and detector are nearly identical for the two cases. In fact, for $\Delta\omega T=0$, the mathematical formulations for the wideband and narrowband models are identical. However, the range of k values over which each of the models is appropriate is not the same. The wideband model of Chapter III is only valid for k values greater than approximately 5. For the narrowband model we can make k as small as $1/2$. For k values greater than 5, the narrowband and wideband systems (with $\Delta\omega T=0$) perform identically.

Figures 7.6 through 7.11 show the (narrowband) system performance for $k=1/2$. For this k value, there are no humps in the $P(e)$ vs. INR curves. Therefore we might be tempted to state that the bandwidth corresponding to $k=1/2$ is optimum. However, upon a careful comparison of Figures 7.6, 3.9, and 3.15, we see that $P(e)$ for $k=1/2$ is actually higher than it is for $k=5$ or $k=10$ at the left hand sides of the curves. Thus we make the unexpected observation that, for low INR values, the system performance improves as the noise power at the array input increases.

For easy comparison, curves showing the performance of both the wideband ($k=10$) and narrowband ($k=1/2$) systems are plotted in Figure 7.12. This figure shows $P(e)$ vs. INR curves for $\theta_i=10$ degrees and an SNR of 12 dB. For INR values above approximately 10 dB the narrowband

system performs better than the wideband system. However, for INR values below 10 dB the wideband system performs better.

There is a simple explanation for this behavior. As the INR increases, the array begins to null the interference when the interference and noise powers at the array input are approximately equal. Therefore the null begins to form at a lower INR value when $k=1/2$ than it does when $k=10$. Consider the cases shown in Figure 7.12 for an INR value of 5 dB. Figures 7.13(a) and (b) show the adapted antenna patterns for $k=10$ and $k=1/2$ respectively. For $k=10$, the array has not formed a null in the interference direction and the desired signal is very close to a pattern maximum. When $k=1/2$, a null is formed on the interference. Furthermore, since the desired and interfering signals are spatially close, the array no longer keeps the desired signal near a pattern maximum. Therefore, the SNR at the array output is lower with $k=1/2$ than with $k=10$ for the case shown. The increase in $P(e)$ due to the SNR reduction with $k=1/2$ is greater than that which occurs due to the residual interference power at the array output with $k=10$.

Figure 7.14 shows the system performance of $\text{SNR}=12$ dB, $\theta_i=10^\circ$, and k values of $1/2$, 1 , and 2 . The curves shown in this figure show that there is no k value that is optimal for all INR values. The curve for $k=1$ lies significantly below that for $k=1/2$ for INR values below approximately 12 dB. For larger INR values the $P(e)$ for $k=1$ is only very slightly greater than that for $k=1/2$. For $k=2$ we see even better performance below 12 dB but a hump is beginning to form in the curve

P (E) VS. SNR

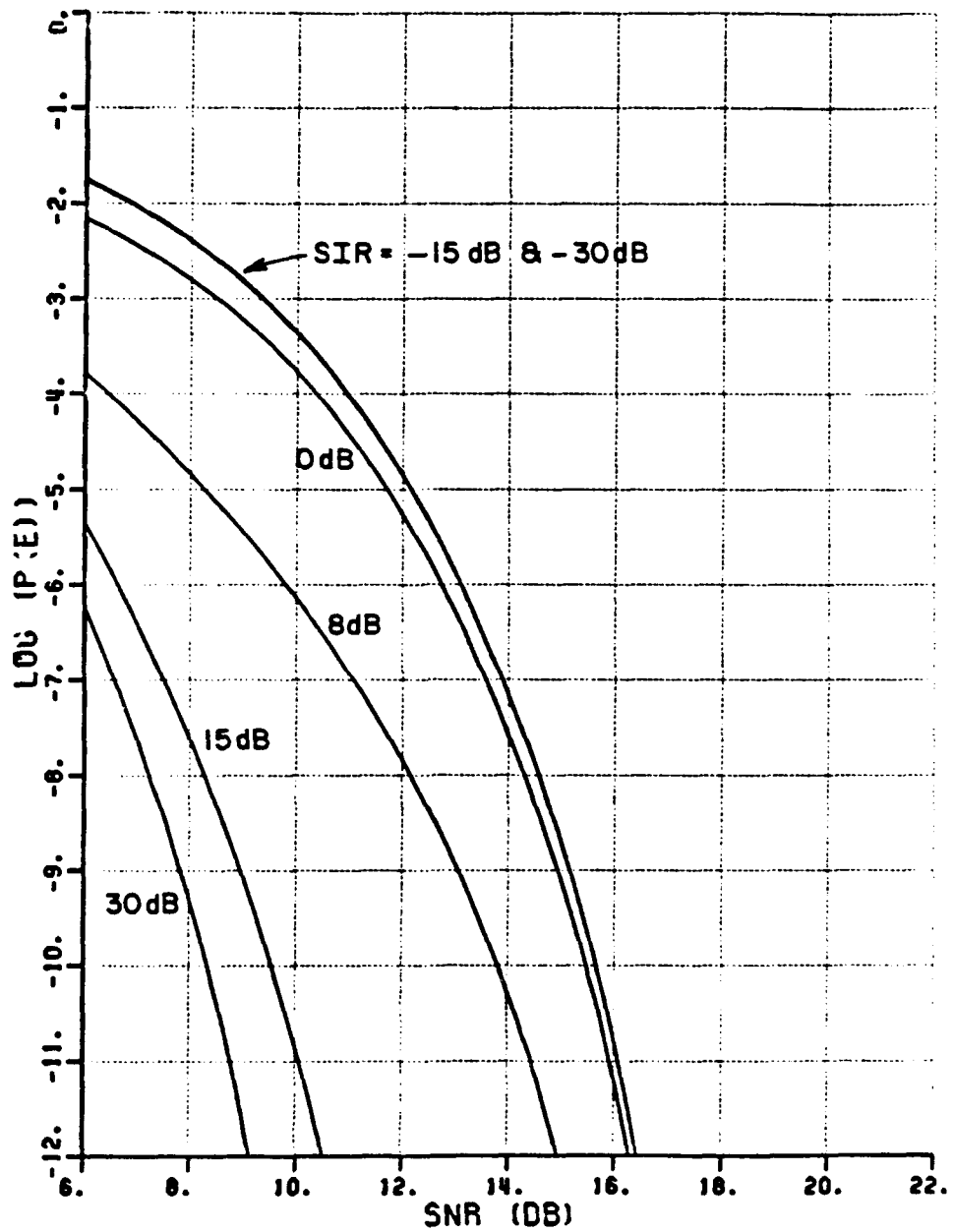


Figure 7.6. $P(e)$ vs. SNR for 3-element narrowband array ($\theta_d=0^\circ$, $\theta_i=10^\circ$, $k=1/2$).

P (E) VS. INR

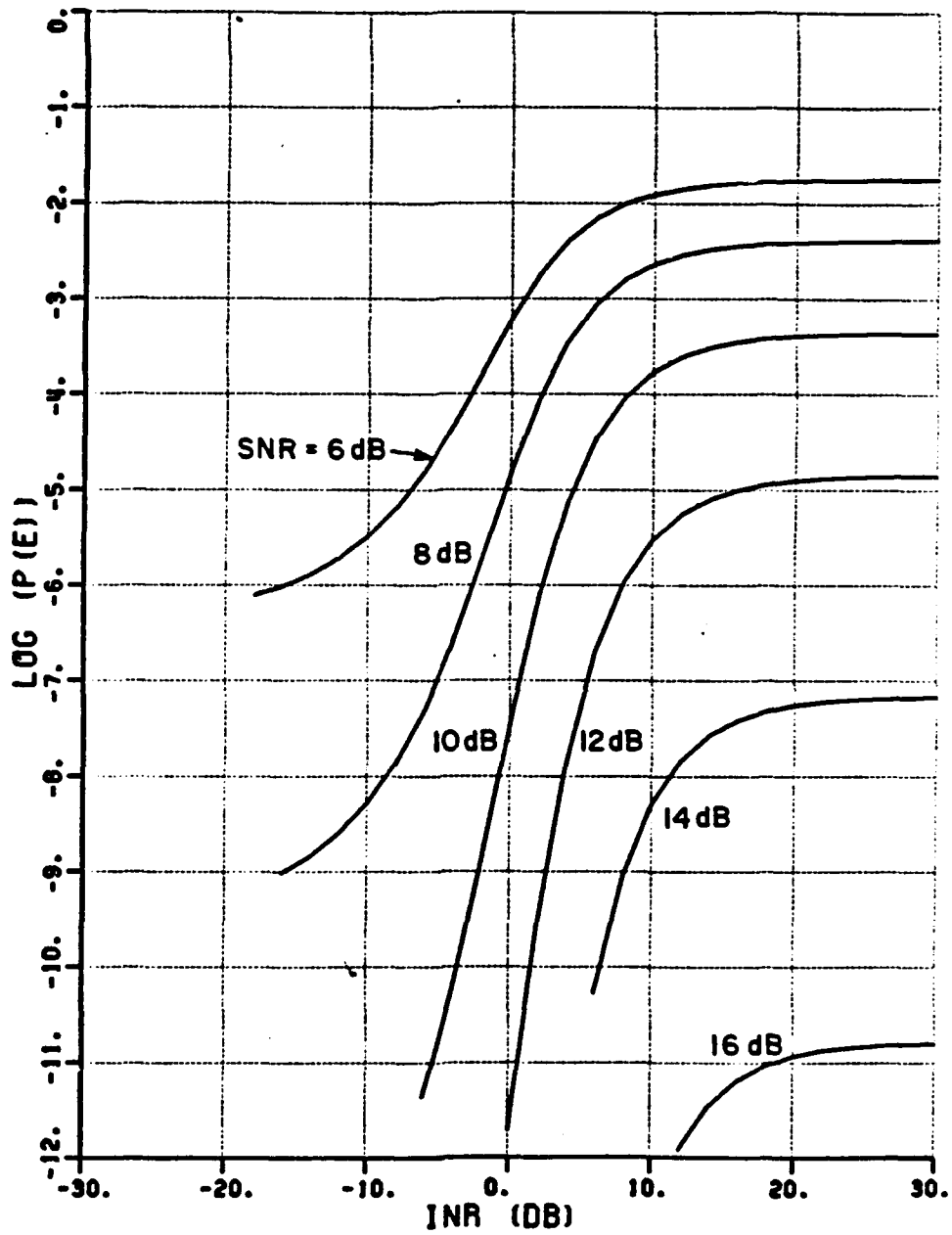


Figure 7.7. $P(e)$ vs. INR for 3-element narrowband array ($\theta_d=0^\circ$, $\theta_i=10^\circ$, $k=1/2$).

P (E) VS. SNR

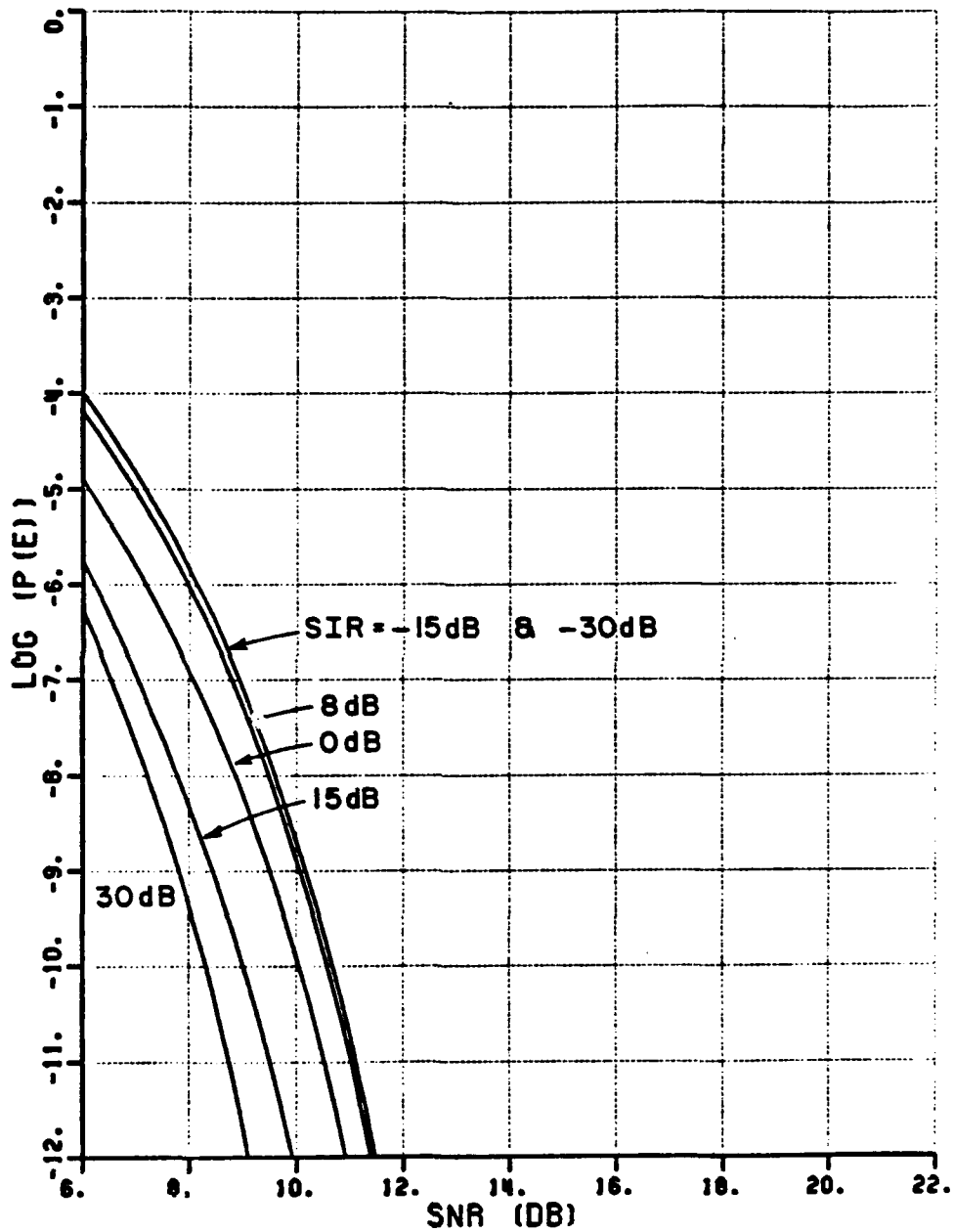


Figure 7.8. $P(e)$ vs. SNR for 3-element narrowband array ($\theta_d=0^\circ$, $\theta_i=20^\circ$, $k=1/2$).

P (E) VS. INR

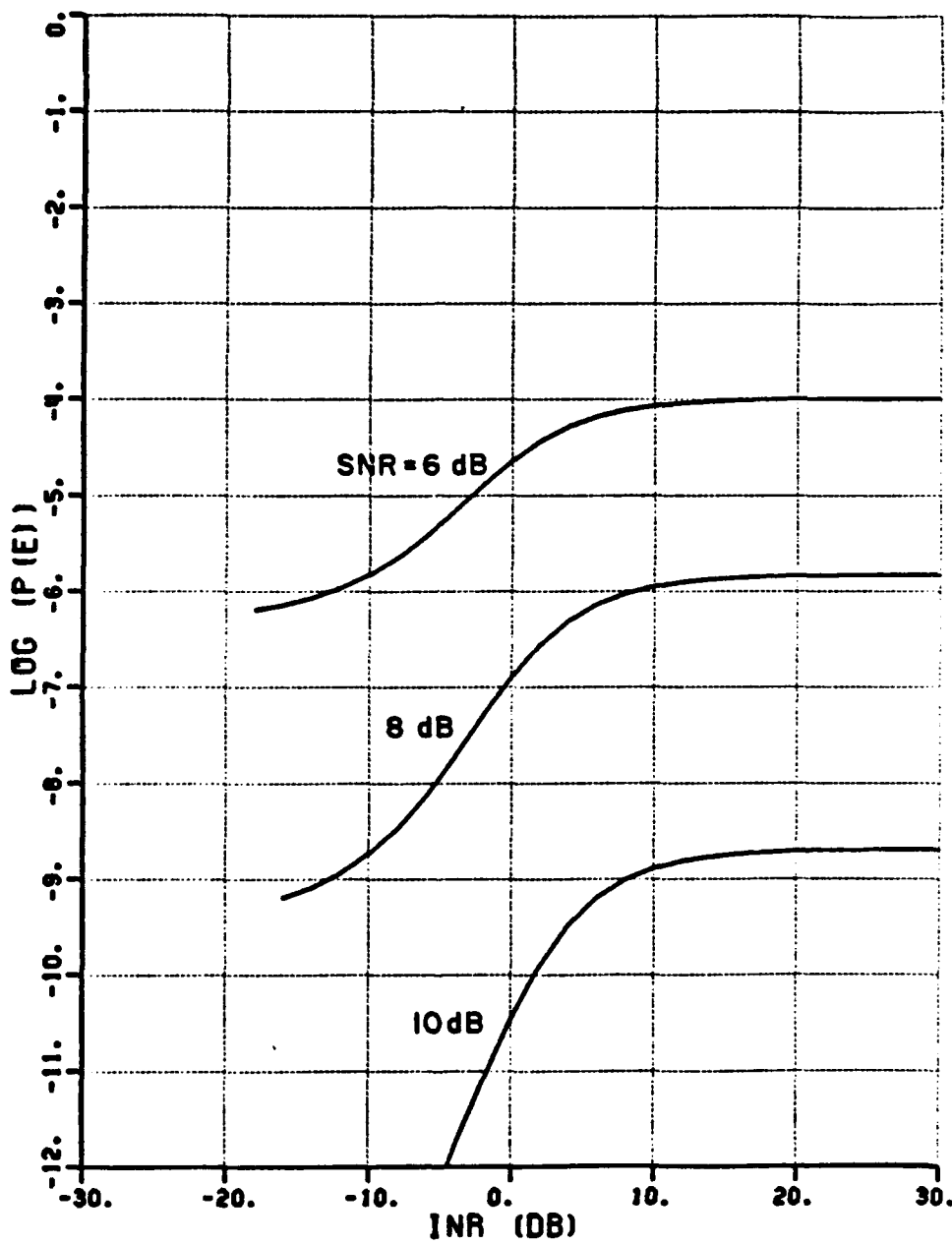


Figure 7.9. P(e) vs. INR for 3-element narrowband array ($\theta_d=0^\circ$, $\theta_i=20^\circ$, $k=1/2$).

P (E) VS. SNR

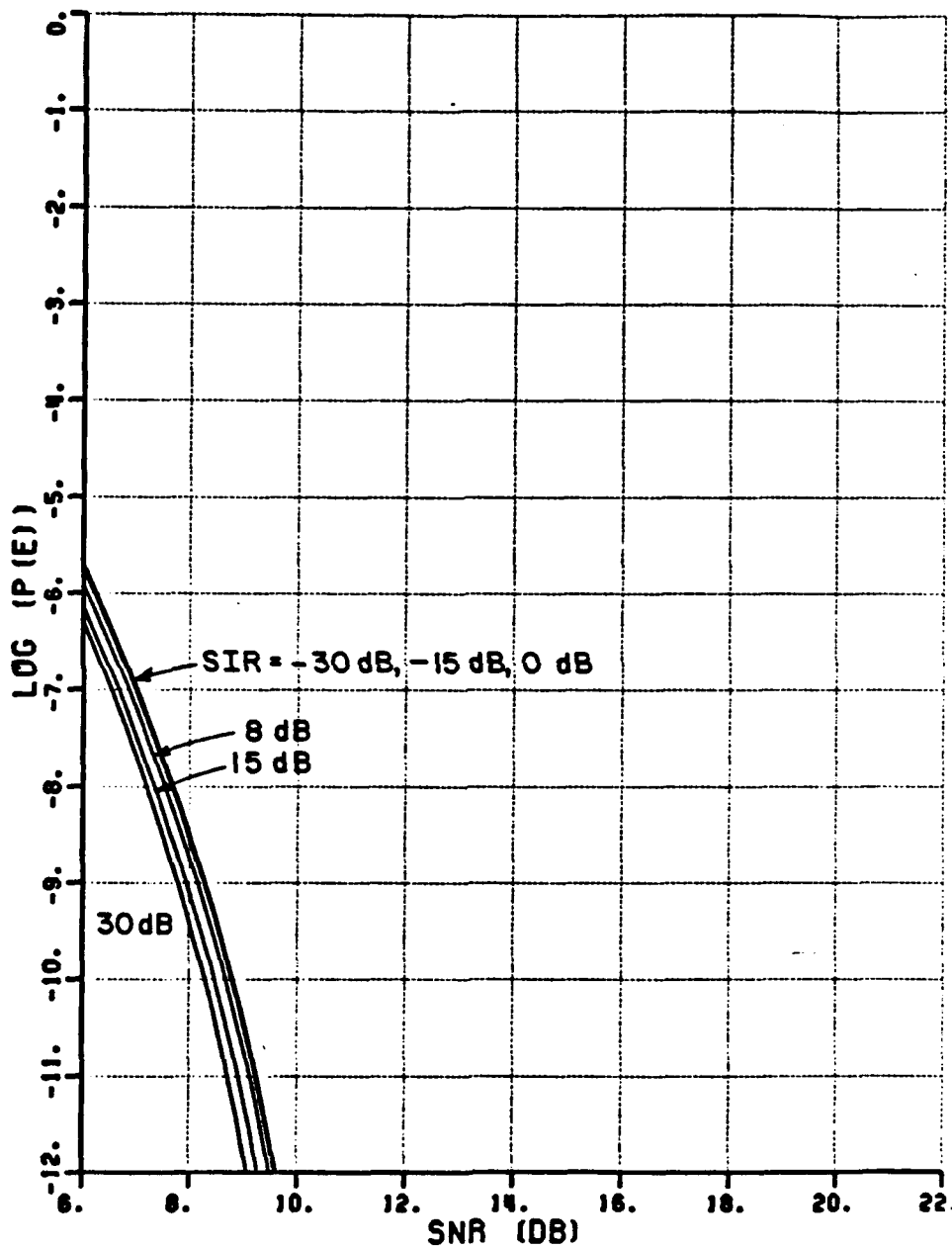


Figure 7.10. $P(e)$ vs. SNR for 3-element narrowband array ($\theta_d=0^\circ$, $\theta_i=80^\circ$, $k=1/2$).

P (E) VS. INR

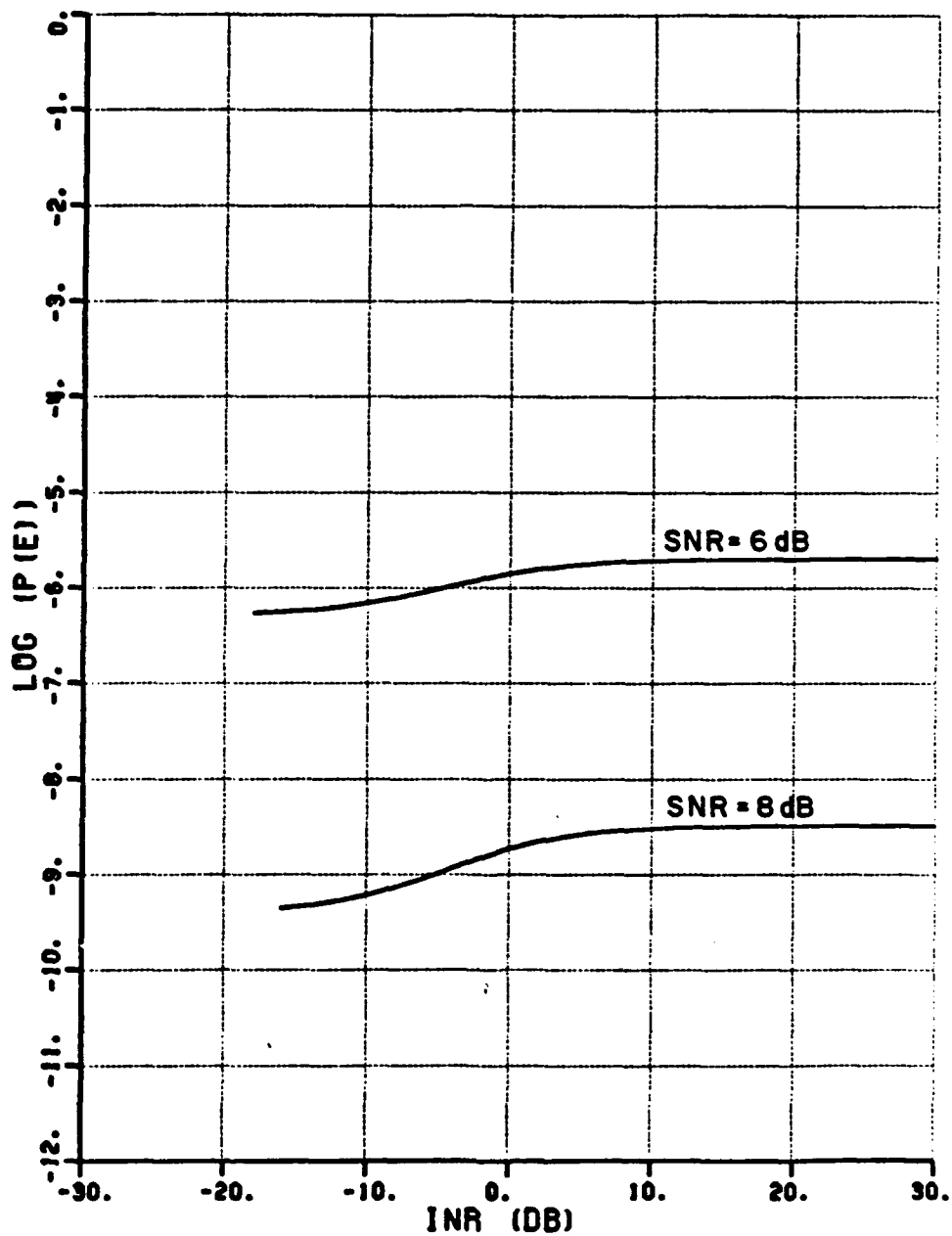


Figure 7.11. $P(e)$ vs. INR for 3-element narrowband array ($\theta_d=0^\circ$, $\theta_i=80^\circ$, $k=1/2$).

P (E) VS. INR

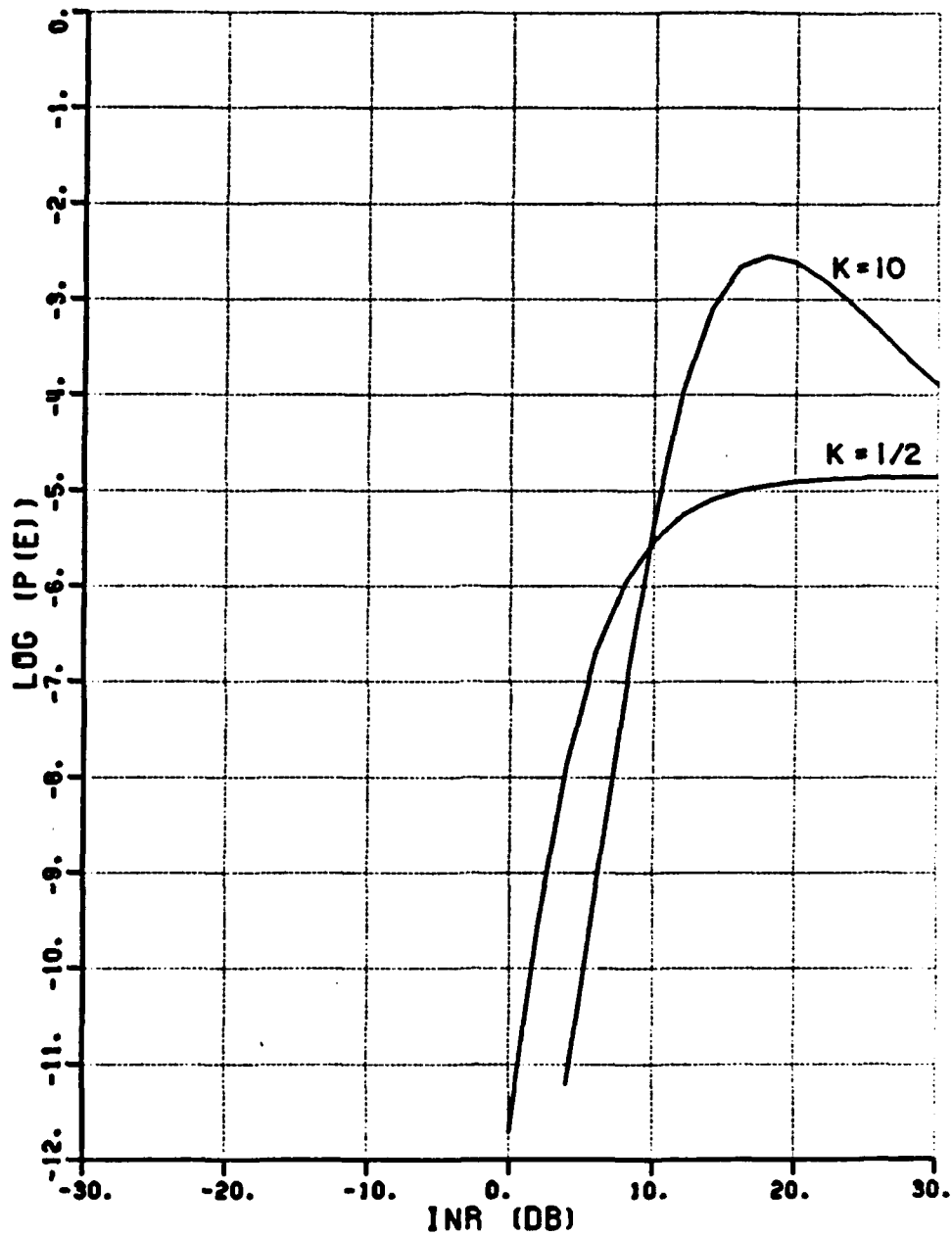
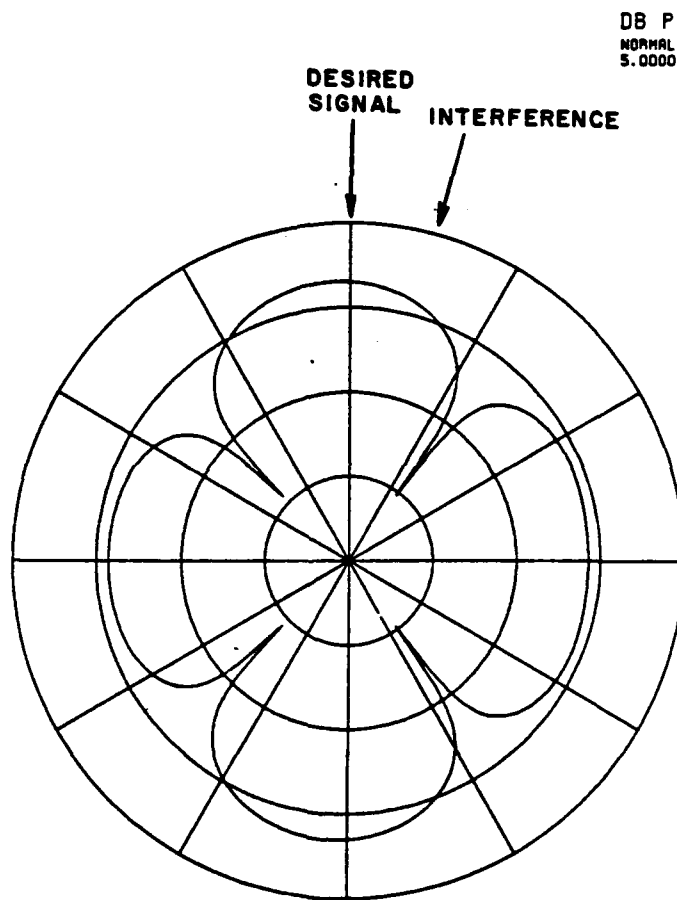


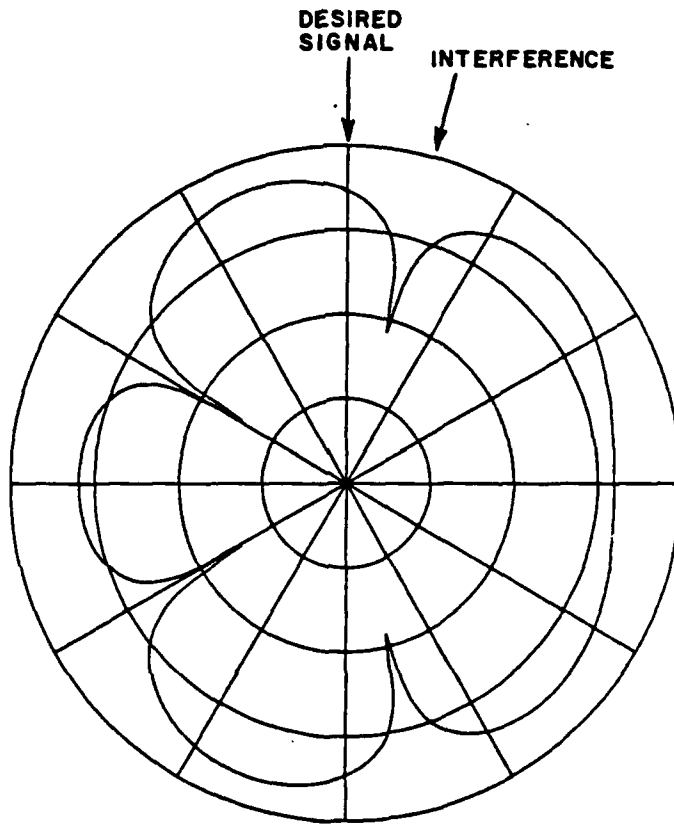
Figure 7.12. P(e) vs. INR for SNR=12 dB for two different k values ($\theta_d=0^\circ$, $\theta_i=10^\circ$).



(a) $k = 10$

Figure 7.13. Adapted antenna patterns for two k values. SNR=12 dB, $\theta_d=0^\circ$, $\theta_i=10^\circ$.

DB PLOT
NORMALIZED TO
5.0000 DB



(b) $k = 1/2$

Figure 7.13. Continued.

performance below 12 dB but a hump is beginning to form in the curve above 12 dB. $P(e)$ vs. INR curves were plotted for several other values of SNR and θ_i and similar results were observed. In each case the hump in the curve appears for k values greater than about 2.

In previous chapters we examined the performance of the various systems when the interference was at a frequency where the detector performance was not degraded (but where the interference was within the array input BPF passbands). For the narrowband system, if $|\Delta\omega|$ is greater than π/T , the interference will be completely rejected by the detector. The performance for this case will be the same as we found for the wideband system when the interference frequency was at a null in the detector frequency response. Therefore, the results shown in Figures 3.20 and 3.21 depict the performance of both the wideband and narrowband BPSK systems when the interference is at a frequency where the detector is not affected.

In this chapter we have examined the performance of a bandlimited BPSK system with an adaptive array. We found that the humps in the $P(e)$ vs. INR curves are only seen for k values greater than approximately 2. We found the best performance for k values between 1/2 and 2. Since the performance for k values between 1 and 2 is never much worse than that for $k = 1/2$ (and sometimes better) we conclude that there is little reason to expend greater cost or effort to reduce k below 2.

P (E) VS. INR

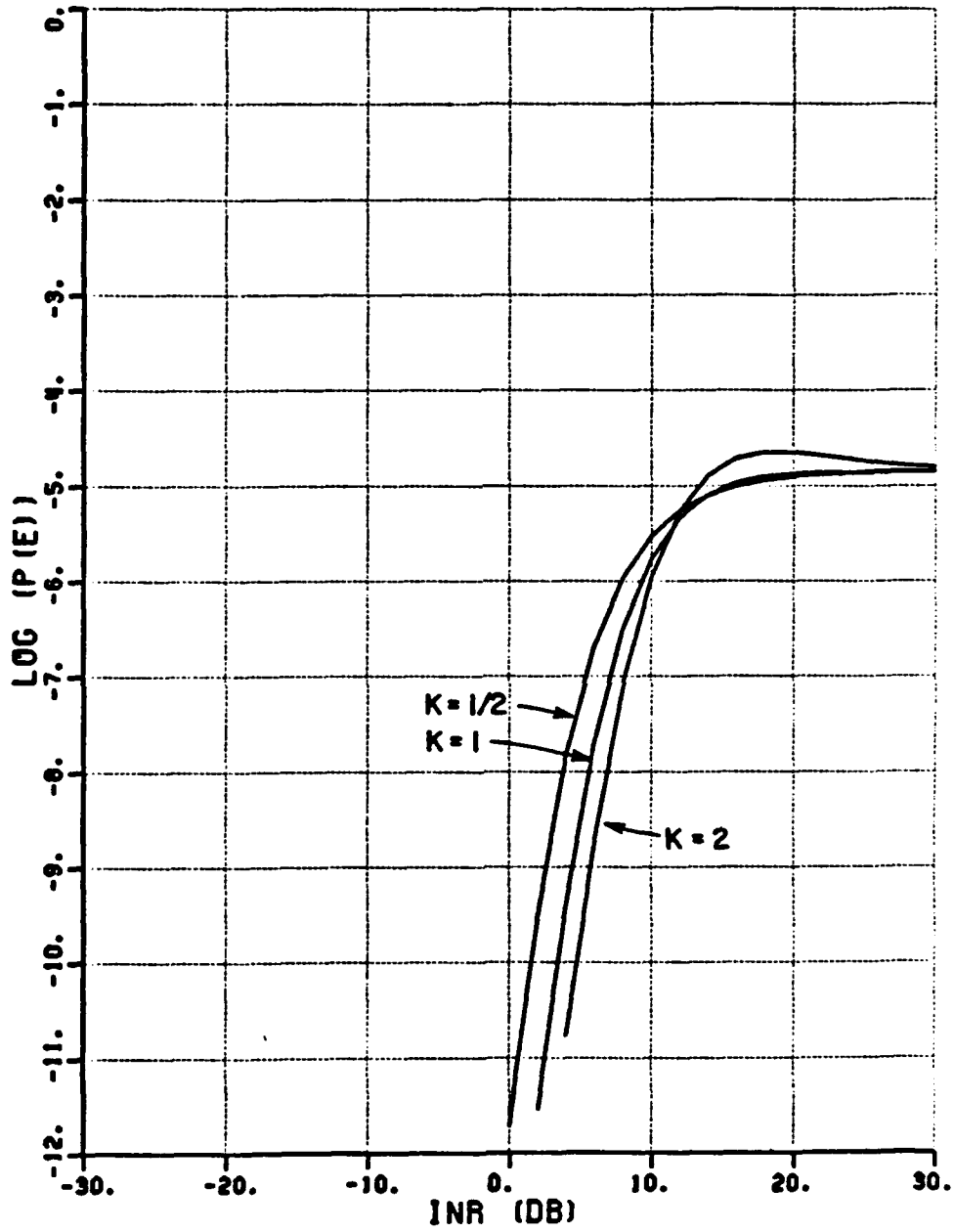


Figure 7.14. $P(e)$ vs. INR for three k values. SNR=12 dB, $\theta_d=0^\circ$, $\theta_i=10^\circ$.

CHAPTER VIII

PROTECTION OF A BPSK SYSTEM FROM WIDEBAND INTERFERENCE

A. INTRODUCTION

In the previous chapters we considered the performance of digital communication systems in the presence of CW interference. In this chapter we determine the protection that the adaptive array can offer to a communication system with bandlimited AWGN interference. We calculate the performance of the narrowband BPSK system described in Chapter VII as a function of the signal powers, arrival angles, and the interference and array input bandwidths.

We also examine the performance of a modified LMS array with noise interference. This modified array uses tapped delay line transversal filters to implement the element weights. These filters allow the array to steer nulls that are much wider in bandwidth than those possible with conventional LMS array.* We shall find that the modified array often provides performance better than the conventional array for AWGN interference.

Section B describes the desired signal and interference models. Section C describes the results of performance calculations and discusses the effects of the various system parameters. Section D summarizes the results and compares these results with those of previous chapters.

*By conventional we mean the LMS array with a single complex weight behind each element.

B. SYSTEM MODEL

In this chapter we again use the BPSK modulation method described in the previous chapter. The same desired signal and noise models are used; however, we assume that the interfering signal at each element input is a zero-mean Gaussian random process with power $(P_i)_{in}$. The PSD of this interference is shown in Figure 8.1. The center frequency is ω_i and the bandwidth of the interference is $\Delta\omega_i'$ where the prime indicates that we are considering the signals at the input to the element BPFs.

We assume for simplicity that $\omega_i = \omega_d$ as this assumption has little bearing on the derived results. We shall show that varying ω_i slightly about ω_d has little effect on the array performance. Varying ω_i about

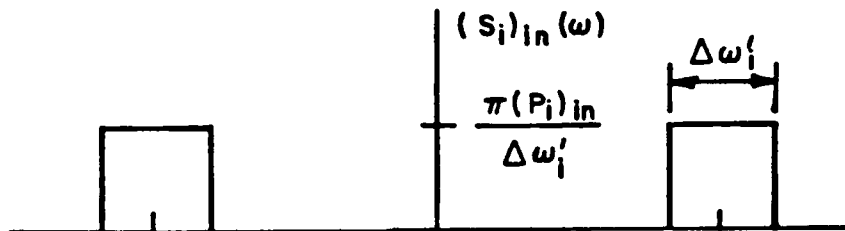


Figure 8.1. Interference PSD at element BPF inputs.

ω_d will never hurt the detector performance since the detector is simply a multiplier (where the array output is multiplied by $\cos(\omega_d t)$) followed by an ideal low-pass filter. In fact when ω_i differs greatly from ω_d then the detector filter may completely reject the interference.

We define the relative bandwidth of the interference as,

$$B_i' = (\Delta\omega_i')/\omega_i . \quad (8.1)$$

Similarly, we define the desired signal relative bandwidth by,

$$B_d = (\Delta\omega_d)/\omega_d , \quad (8.2)$$

where $\Delta\omega_d$ is the bandwidth of the desired signal and ω_d is its center frequency. The relative bandwidth of each input BPF is

$$B_{in} = 2kB_d , \quad (8.3)$$

where k is the bandwidth factor as described in the previous chapters.

If B_i' is larger than B_{in} then the input BPFs will reject some of the interfering signal. Therefore the relative bandwidth of the interference at the BPF output is

$$B_i = \text{MIN}(B_{in}, B_i') \quad (8.4)$$

where $\text{MIN}(A,B)$ denotes the smaller of the two quantities A and B . Note that we could not write B_i in this simple form without the assumption that $\omega_i = \omega_d$. The bandwidth of the interference at the BPF outputs is given by $\Delta\omega_i$, where

$$\Delta\omega_i = \omega_i B_i . \quad (8.5)$$

The power in the interference at each BPF output is

$$\sigma_i^2 = (P_i)_{in} \text{MIN}(B_{in}/B_i', 1). \quad (8.6)$$

The ACF of $\tilde{i}(T)$ is given by

$$R_i^{\sim}(\tau) = \sigma_i^2 \text{sinc}(\Delta\omega_i\tau/2)\exp(j\omega_i\tau). \quad (8.7)$$

Substitution of $\Delta\omega_i$ from (8.5) into (8.7) yields,

$$R_i^{\sim}(\tau) = \sigma_i^2 \text{sinc} [(0.5)B_i\omega_i\tau] \exp(j\omega_i\tau). \quad (8.8)$$

From Equations (2.14) and (2.16) we see that $\phi_i = \omega_i T_i$; therefore, we have

$$R_i^{\sim}(\tau) = \sigma_i^2 \text{sinc} [(0.5)B_i(\phi_i/T_i)\tau] \exp [j(\phi_i/T_i)\tau]. \quad (8.9)$$

Now we can substitute this expression for $R_i^{\sim}(\tau)$ into (2.21) to determine the interference covariance matrix ϕ_i . With this substitution ϕ_i becomes

$$\phi_i = \sigma_i^2 \begin{bmatrix} 1 & \text{sinc}[\frac{1}{2}B_i\phi_i]e^{-j\phi_i} & \text{sinc}[-B_i\phi_i]e^{-j2\phi_i} \\ \text{sinc}[\frac{1}{2}B_i\phi_i]e^{j\phi_i} & 1 & \text{sinc}[-\frac{1}{2}B_i\phi_i]e^{-j\phi_i} \\ \text{sinc}[B_i\phi_i]e^{j2\phi_i} & \text{sinc}[\frac{1}{2}B_i\phi_i]e^{j\phi_i} & 1 \end{bmatrix} \quad (8.10)$$

From this expression we can justify our previous assertion that the array performance is not very sensitive to slight variations in ω_i

about ω_d . The terms in the interference covariance matrix represent Equation (8.9) evaluated at $t = \pm nT_i$ where $n=0, 1, \text{ or } 2$. The only variable in (8.9) that is dependent on ω_i is the argument of the exponent of $\exp[j(\phi_i/T_i)t]$.*

Using (2.16) we can expand the exponential terms in (8.10) to obtain,

$$\exp[\pm jn\phi_i] = \exp[\pm jn(\omega_i/\omega_d)\pi\sin\theta_i] . \quad (8.11)$$

From this expression we see that small fluctuations in ω_i about ω_d produce small fluctuations in the interelement phase shift. This is the same effect that is observed when θ_i varies slightly. Since a change in θ_i of a few degrees does not dramatically change the array performance we can assert that a small change in ω_i will not either. This assertion was verified by performance calculations in which ω_d , ω_i , B_d and B_i were chosen independently. Very slight variations in performance were noted as the ratio (ω_d/ω_i) was varied from approximately 0.9 to 1.1.

We assume that ϕ_d and ϕ_n are the same as in Chapter VII. The array weights can be calculated, as usual, using (2.9), (2.25) and (2.5).

Both the desired signal and interference are modified by the array. However, we presently show that the array adds very little distortion to the desired signal while it changes the spectrum of the interference considerably. The array acts as a transversal filter when processing the signals at its input. Such a filter is shown in Figure 8.2. The delay

*Note that the product $B_i\phi_i$ in the argument of the sinc function is independent of ω_i . This is easily shown from (8.1), (8.4) and (2.16).

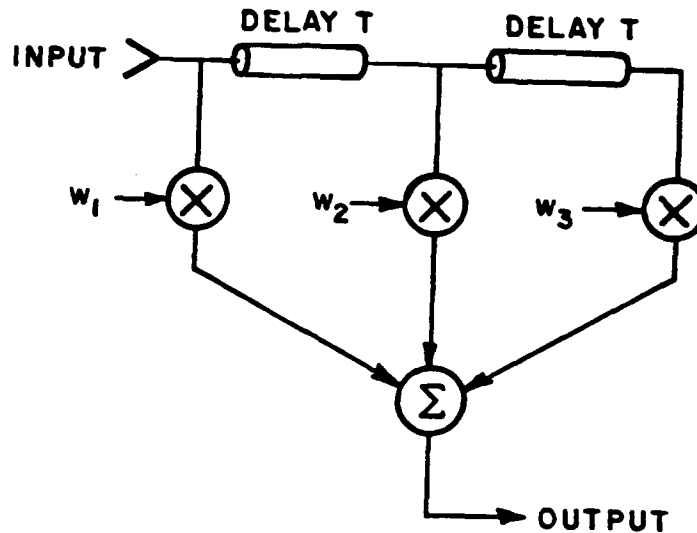


Figure 8.2. Transversal filter with two delay elements and three weights.

between filter taps, which is labeled T in this figure, is the interelement time delay. The transfer function of the filter for a three-element array is given by,

$$H(\omega) = w_1 + w_2 \exp(-j\omega T) + w_3 \exp(-j\omega 2T). \quad (8.12)$$

If $\theta_d \neq \theta_i$ the interelement time delays are different for the desired and interfering signals. Therefore these two signals are processed by different transfer functions. In general, the LMS weights produce a transfer function for the desired signal that is very close to the ideal all pass filter (i.e. $H(\omega)$ has a constant magnitude and linear phase shift over the frequency range of interest). The LMS weights typically produce a transfer function for the interference which has nulls at frequencies where the interference PSD is large.

As an example of the spectral filtering properties of the 3-element array, the equivalent filter transfer functions were calculated for a specific case. Figures 8.3 and 8.4 show the desired signal and interference transfer functions when $\theta_d=0^\circ$, $\theta_i=10^\circ$, SNR=12 dB, INR=20 dB, $B_d=0.1$, and $B_i=0.1$. From these figures we see that the array has a negligible effect on the desired signal while it significantly modifies the interference signal spectrum.

The power P_d of the desired signal at the array output is given by Equation (2.32) where $\tilde{R}_d(\tau)$ is given by (7.17). The desired signal at the array output is processed by the detector which consists of a multiplier (where the signal is multiplied by $\cos(\omega_d t)$) and an ideal low-pass filter which rejects all but the baseband signal components. A power loss of one half occurs during both the multiplication and filtering processes so the desired signal power at the detector output is $P_d/4$. Therefore the desired signal at the detector output at the n^{th} bit sampling instant is given by

$$X_d(n) = b_n \sqrt{(P_d/2)} \text{sinc}[(\pi/T)(t-nT)] \quad (8.13)$$

where $b_n=1$ if the n^{th} bit is a "1" and $b_n=-1$ if the n^{th} bit is a "0".

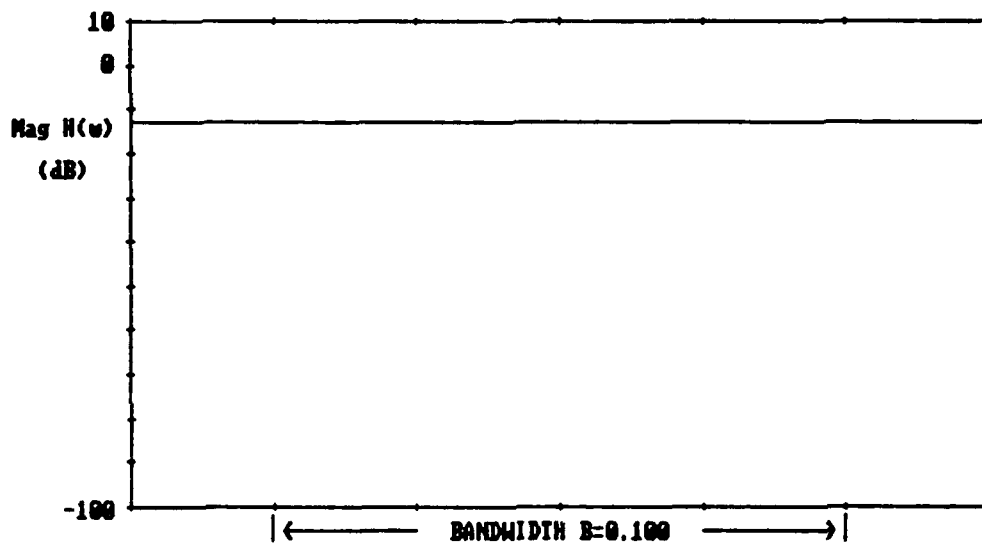
The noise signal at the array output has a two-sided PSD of $n/2$ where $n/2$ is given by Equation (3.14). At the multiplier output this signal has a two-sided PSD of $n/4$ (at baseband) or equivalently, a one-sided PSD of $n/2$. The detector low pass filter has a bandwidth of $1/2T$. Therefore, the noise produces a Gaussian random variable (GRV) $X_n(n)$ at the filter output at the n^{th} sampling instant with variance,

$$\begin{aligned}\text{Var}[X_n(n)] &= (n/2)(1/2T) \\ &= n/(4T).\end{aligned}\tag{8.14}$$

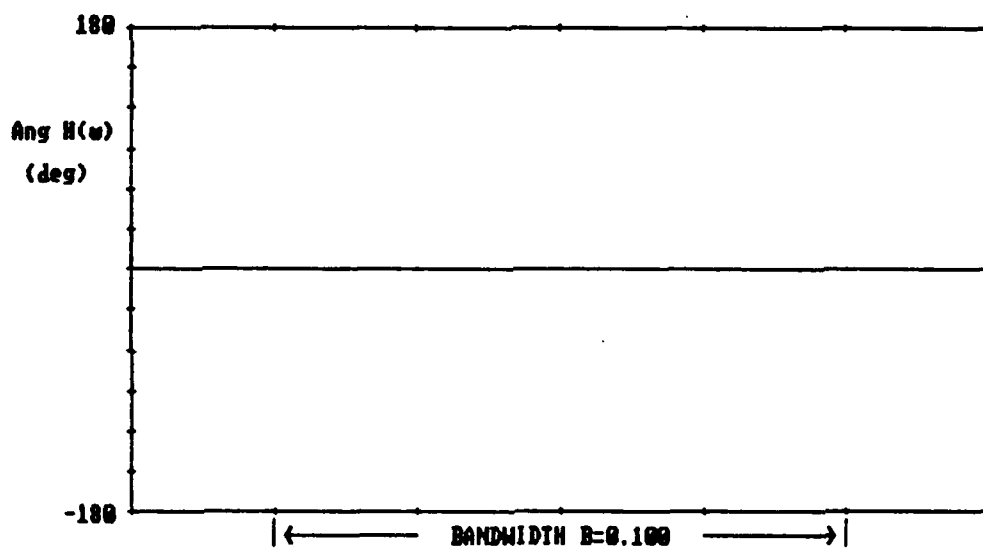
Calculation of the interference power at the detector input is not as straightforward as calculation of the noise power is even though the interference signal, like the noise signal, is a Gaussian random process. Since the thermal noise signals are statistically independent white noise processes, their weighted sum at the array output is also a white noise process. However, the interference signals are correlated from element to element; therefore, the spectrum of the interference signal at the array output will be modified by the interference transfer function of the array as shown in Figure 8.3.

Since all of the processing done to the signals is linear, the random variable produced by the interference signal at the detector output is Gaussian. Since only the interference in the frequency band bounded by $\omega_d \pm \Delta\omega_d/2$ affects the detector we need only to calculate the array output power of the interference signal in this band to calculate the detector performance. We denote this power by $(P_i)_{\text{det}}$. Calculation of the actual PSD of the interference signal at the array output is not necessary.

To calculate the output interference power $(P_i)_{\text{det}}$ we use (2.33) with $R_i(t)$ set equal to the ACF of the portion of the interference signal at the array input that is in the frequency band of interest. This ACF is given by,



(a) Amplitude response at θ_d



(b) Phase response at θ_d

Figure 8.3. Frequency response of LMS array in the desired signal direction ($\theta_d=0^\circ$, $\theta_i=10^\circ$, SNR = 12 dB, INR = 20 dB, $k = 1/2$, $B_d = B_i = 0.1$).

$$\begin{aligned}
(R_i^{\sim})_{\text{det}}(\tau) &= [\sigma_i^2 \text{MIN}[1, (B_d/B_i)]] \\
&\quad \text{sinc}[(1/2)\text{MIN}(B_d, B_i)\omega_i\tau] \exp(j\omega_i\tau)
\end{aligned} \tag{8.15}$$

Substitution of $(R_i^{\sim})_{\text{det}}$ for R_i^{\sim} in (2.33) yields $(P_i)_{\text{det}}$ at the array output. When this signal is applied to the detector, the multiplication and filtering processes reduce the interference power by a factor of four (just as it did for the desired and noise signals). Therefore the interference produces a GRV at the detector output at the n^{th} sampling instant with variance,

$$\text{Var}[X_i(n)] = (P_i)_{\text{det}}/4 . \tag{8.16}$$

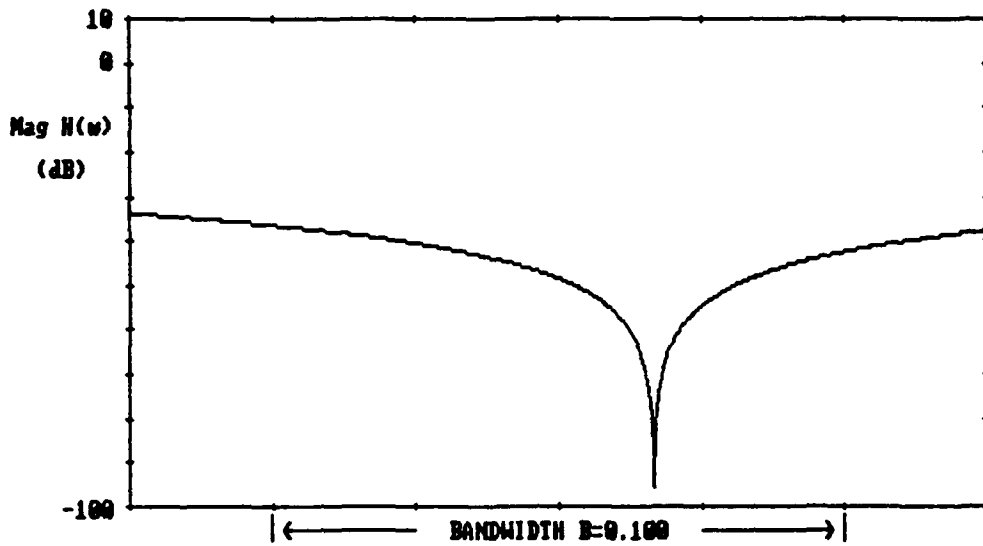
The probability of an error for the n^{th} bit is,

$$\begin{aligned}
P(e) &= 0.4P[X_i(n) + X_n(n) < -\sqrt{(P_d/2)} \mid \text{"1" sent}] \\
&\quad + 0.5P[X_i(n) + X_n(n) > \sqrt{(P_d/2)} \mid \text{"0" sent}]
\end{aligned} \tag{8.17}$$

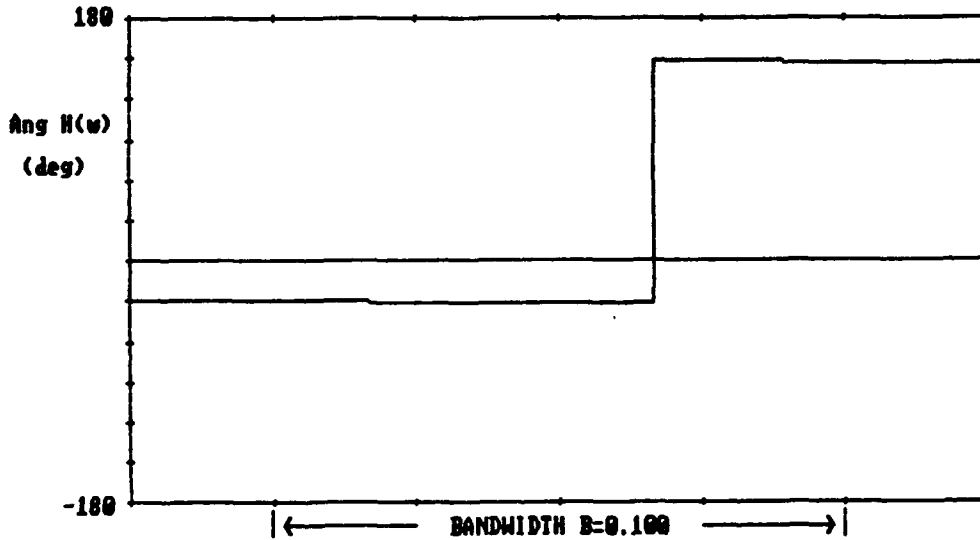
The two probabilities in this expression are equal. Therefore $P(e)$ can be written

$$P(e) = P[X_i(n) + X_n(n) > \sqrt{(P_d/2)} \mid \text{"0" sent}]. \tag{8.18}$$

Since $X_i(n)$ and $X_n(n)$ are independent GRVs with variance $(P_i)_{\text{det}}/4$ and $n/4T$ respectively, their sum is a GRV with variance $(P_i)_{\text{det}}/4 + n/4T$. Therefore $P(e)$ is given by



(a) Amplitude response at θ_i



(b) Phase response at θ_i

Figure 8.4. Frequency response of LMS array in the interference signal direction ($\theta_d=0^\circ$, $\theta_i=10^\circ$, $\text{SNR} = 12 \text{ dB}$, $\text{INR} = 20 \text{ dB}$, $k = 1/2$, $B_d = B_i = 0.1$).

$$P(e) = \text{erfc}[\sqrt{(P_d/2)} / \sqrt{(P_i)_{\text{det}}/4 + n/4T}]. \quad (8.19)$$

Multiplication of the numerator and denominator in the argument of the error function by $\sqrt{4T}$ yields,

$$P(e) = \text{erfc}[\sqrt{2E_b/(E_i+n)}] \quad (8.20)$$

where $E_b = P_d T$ and $E_i = (P_i)_{\text{det}} T$.

Since both the interference and noise signal produce independent zero-mean GRVs at the detector output, $P(e)$ is dependent only upon the SINR at the detector input where we make the definition,

$$\text{SINR}_{\text{det}} = E_d/(E_i+n). \quad (8.21)$$

With this definition (8.19) becomes,

$$P(e) = \text{erfc}[\sqrt{2 \text{SINR}_{\text{det}}}] . \quad (8.22)$$

Note that if $E_i=0$ then $P(e) = \text{erfc}[\sqrt{(2E_d/n)}]$ the familiar result for BPSK with AWGN.

C. RESULTS OF PERFORMANCE CALCULATIONS

The derivations of the previous section can be used to calculate the performance of the BPSK system with a 3-element LMS array and noise interference. In this section the results of such calculations are presented for several signal scenarios.

Figure 8.5 shows the results from typical performance calculations. This plot shows $P(e)$ as a function of SNR for several noise bandwidths

for $\theta_d=0^\circ$, $\theta_i=10^\circ$, and $k=1/2$. In each case the signal to interference power ratio (SIR) is -30 dB. The lowest curve in this plot corresponds to the case where the relative bandwidth, $B_i' = 0$. The other curves correspond to B_i' values of 0.01, 0.025, 0.05 and 0.075. From these curves we see that the array offers less protection as the interference bandwidth increases.

$P(e)$ was calculated as a function of SNR for several different values of θ_i and SIR. Figure 8.6 shows a compilation of the results which allows easy comparison. The scale of each of the small plots in Figure 8.6 is the same as that of Figure 8.5. From these figures we see that the system has the most difficulty in suppressing strong broadband interference when the desired signal and interfering signals are spatially close. The effects of a large interference bandwidth are most detrimental at very low SIR values (i.e. when the interference is significantly stronger than the desired signal at the array input). For an SIR value of 0 dB, the system performance with broadband interference (for $B_i' < 0.075$) is not significantly worse than it is with $B_i' = 0$.

In general, the resolution properties of a linear array are dependent upon the signal arrival angles. A linear array can steer a null with infinite bandwidth in the broadside direction*. However, it becomes more difficult to achieve a broadband null as the interference arrival angle varies from the broadside to the endfire direction.

* For example, a 3-element linear array with a weight vector $W=[-1,2,-1]^T$ has a null in the broadside direction for all frequencies.

P (E) VS. SNR

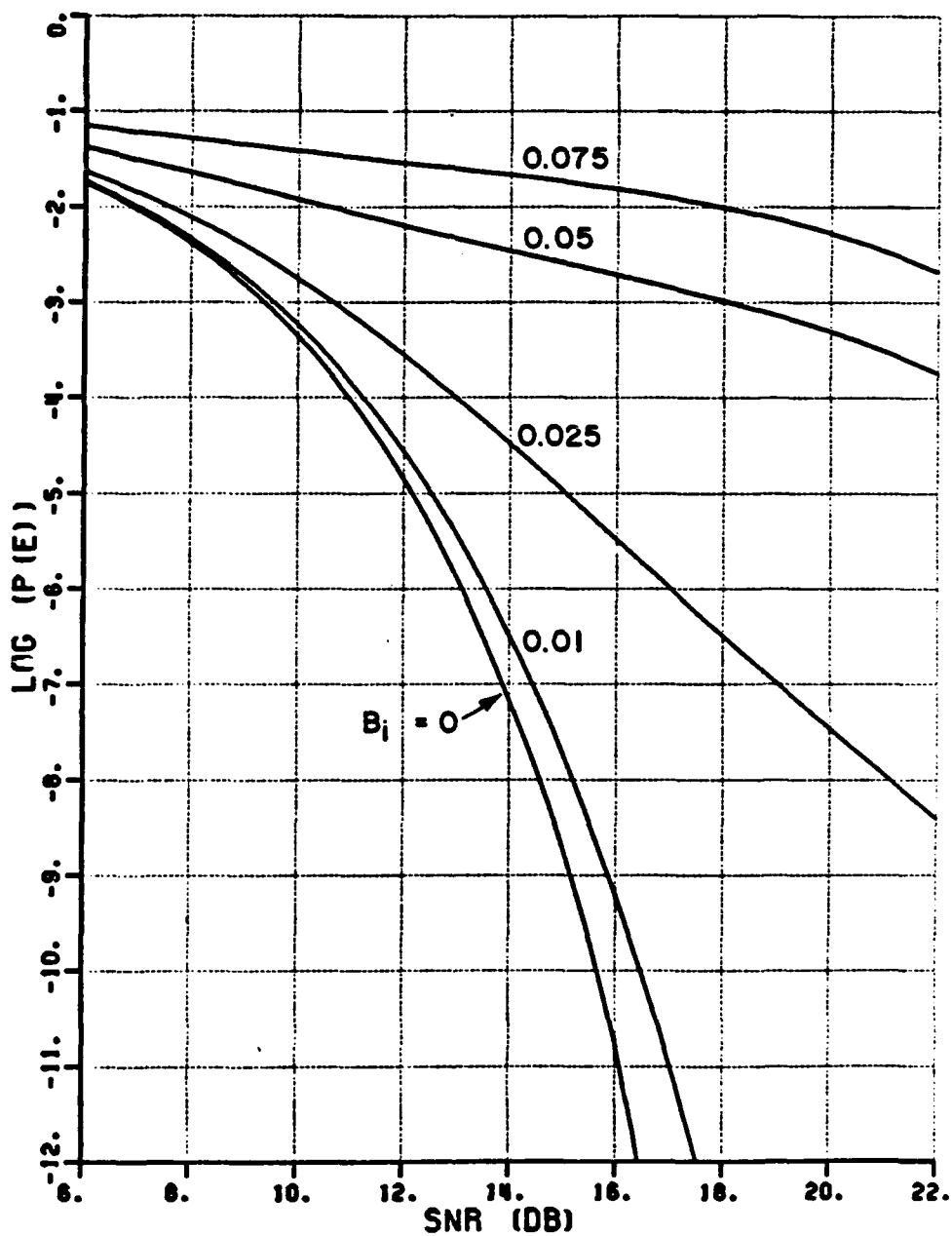


Figure 8.5. Three-element array performance with noise interference ($\theta_d=0^\circ$, $\theta_i=10^\circ$, $k = 1/2$, $B_d = 0.1$).

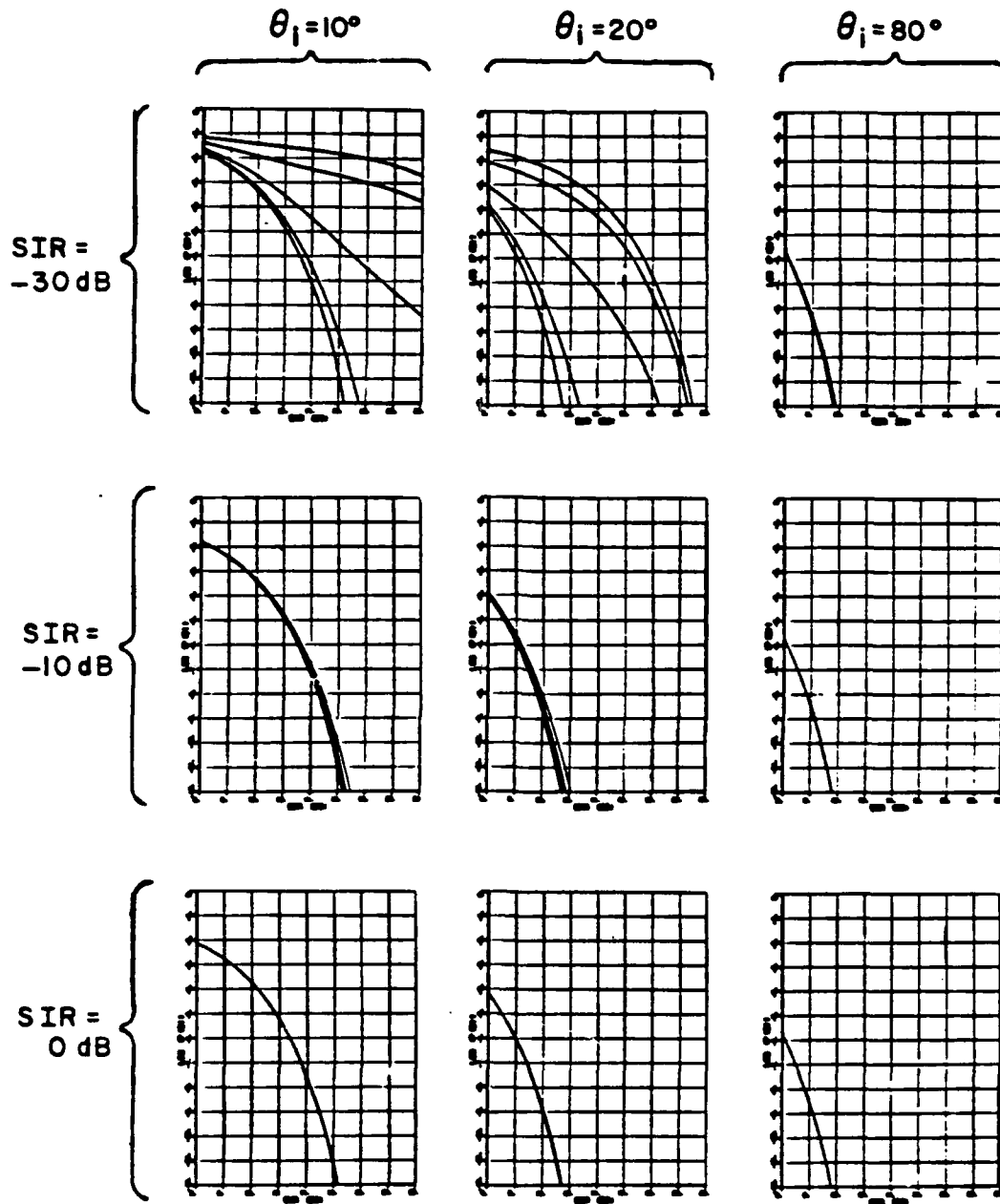


Figure 8.6. Performance of a 3-element array with noise interference for various SIR values ($\rho_d=0^\circ$, $k=1/2$, $B_d=0.1$). B_i values and scales are the same as those of Figure 8.5.

In order to determine the effects of arrival angle of a broadband interference signal, we examine several cases for which the desired and interfering signals are separated by 20° . A mosaic of the resulting $P(e)$ vs. SNR plots for these cases is shown in Figure 8.7. This figure shows the system performance for two combinations of arrival angles and three SIR values. The left-hand curves in Figure 8.7 show the performance when $\theta_i=0^\circ$ and $\theta_d = 20^\circ$. When $\theta_i=0^\circ$ the array steers a wideband null in the interference direction and good performance is noted at all SIR levels.

The right-hand plots in Figure 8.7 show the performance when $\theta_i=90^\circ$ and $\theta_d=70^\circ$. In these cases the array has significant difficulty nulling the interference, especially for the broadband interference. Although the performance appears poor in these latter cases it is important to note that $P(e)$ with no adaptive array would be nearly 0.5 for each of the cases considered.

From the results presented above, we see that the interference is most effective when it is relatively strong and broadband. In each of the cases that we have examined so far $k = 1/2$ and $B_i' < B_d$. We next compare the performance for four different cases including some cases where $B_i' > B_d$ and/or $k > 1/2$. The cases to be examined are:

- (A) $B_d = 0.1, 0 < B_i' < 0.075, k = 1/2$
- (B) $B_d = 0.01, 0 < B_i' < 0.075, k = 1/2$
- (C) $B_d = 0.1, 0 < B_i' < 0.075, k = 10$
- (D) $B_d = 0.01, 0 < B_i' < 0.075, k = 10$

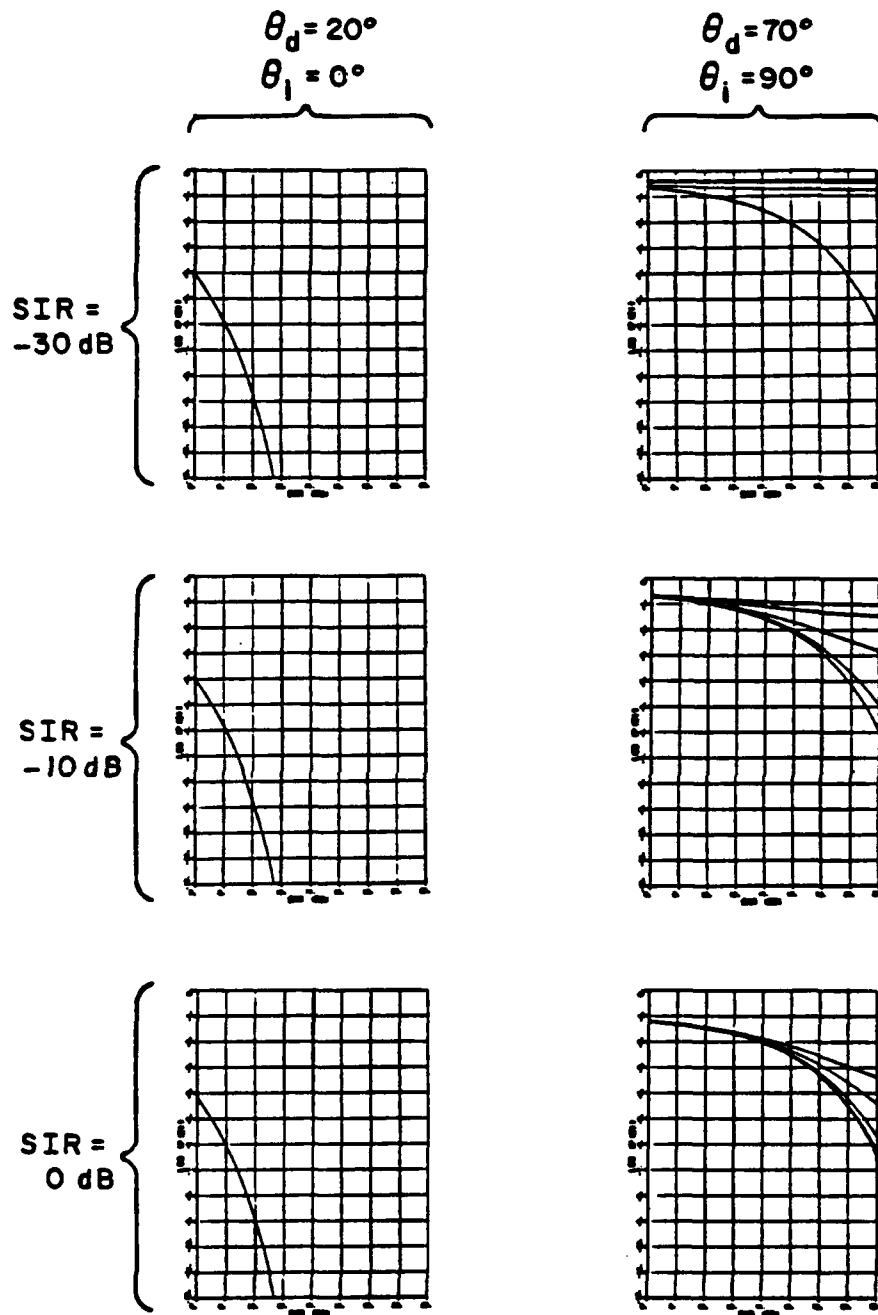


Figure 8.7. Performance of a 3-element array with noise interference for various SIR values ($\theta_d=90^\circ$, $k=1/2$, $B_d=0.1$). B_i values and scales are the same as those of Figure 8.5.

In each case $\theta_d=0^\circ$, $\theta_i=10^\circ$ and $\text{SNR} = 12 \text{ dB}$. Case (A) is the case considered previous in this chapter (see Figure 8.6). Case (B) is similar except that the desired signal bandwidth is reduced by a factor of 10. The array bandwidth is also reduced by this factor since $k = 1/2$ in both cases (A) and (B). In case (B) some of the interference signal is blocked by the array input BPFs when B_i' is greater than 0.01. k is equal to 10 for cases (C) and (D). The other variables are the same as in cases (A) and (B) respectively.

Figure 8.8 shows the results for case (A). For this case the interference is passed by both the input BPFs and the detector filter. From Figure 8.8 we see that the interference bandwidth has little effect on the system performance for INR values below about 15 dB. For large INR values the system performance quickly degrades as the interference bandwidth increases. These are exactly the observations that we made for this case after examination of Figure 8.6.

Figure 8.9 shows the results for case (B). The upper two curves in this figure show the performance when $B_i'=0$ and $B_i'=0.01$. For these cases $B_i' < B_d$ and the performance is the same as it was in case (A) for these B_i' values. For the other three cases shown in this figure $B_i' > B_d$. In these cases the array input BPFs reject some of the interference and the performance monotonically increases as B_i' increases. Therefore, for the narrowband array, a fixed-power interference signal is most disrupting when its bandwidth is equal to the array bandwidth.

P (E) VS. INR

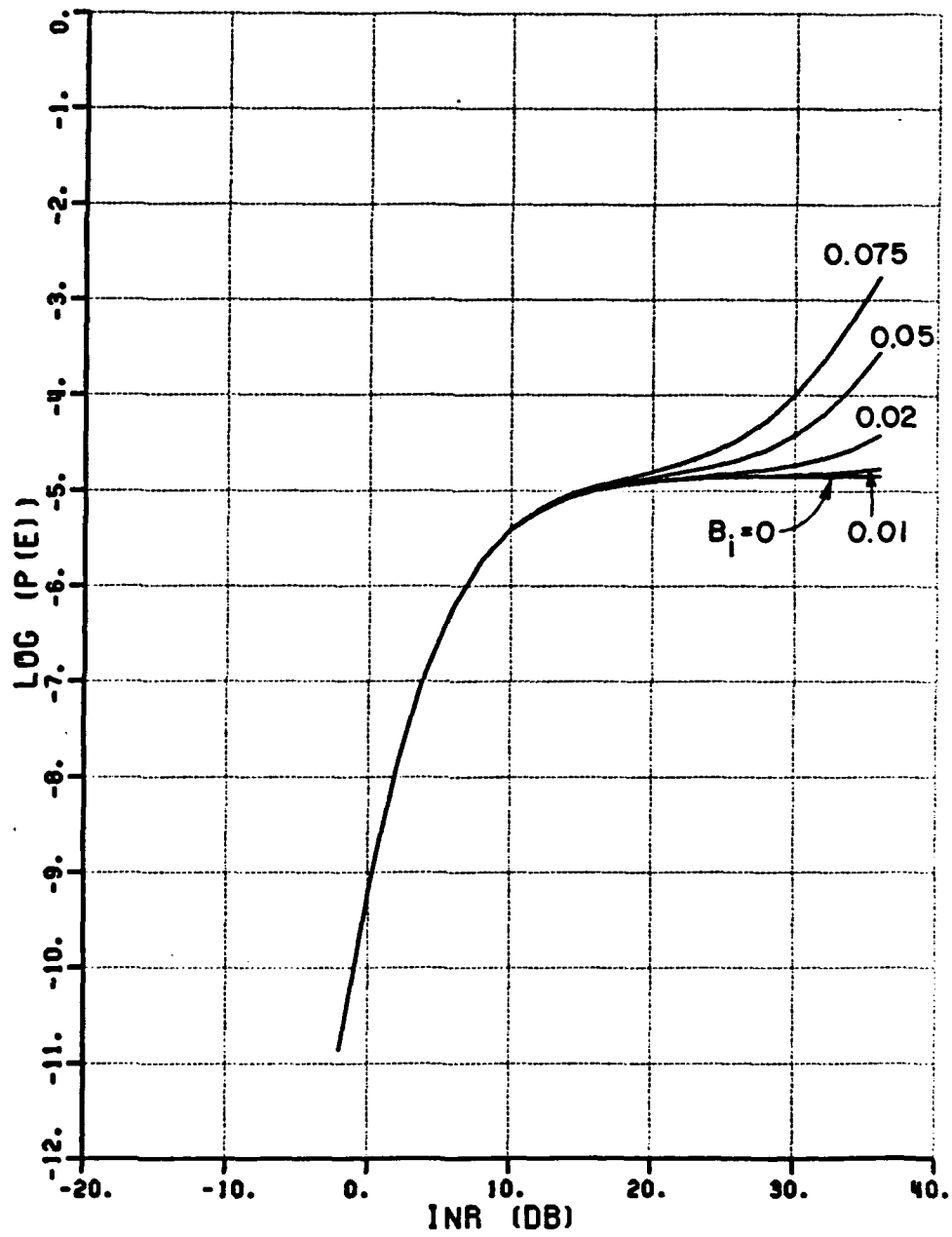


Figure 8.8. 3-element array performance - Case (A).

P (E) VS. INR

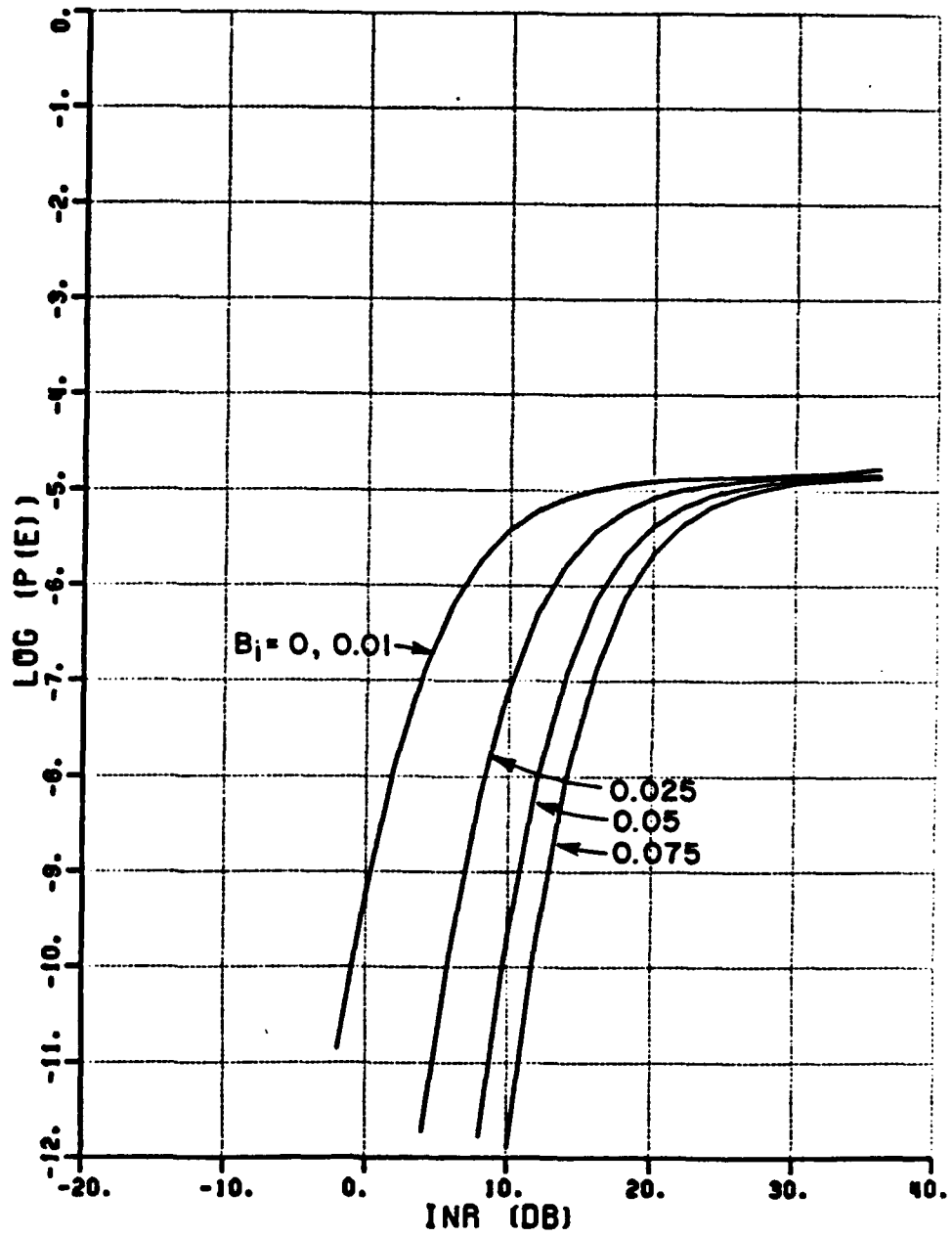


Figure 8.9. 3-element array performance - case (B).

Figure 8.10 shows the results for case (C). As in case (A), the interference in this case is passed by both the input BPFs and the detector filter. We see from Figure 8.10 that the performance becomes bandwidth dependent for INR values above approximately 25 dB. At high INR values the curves quickly diverge indicating poor performance with strong wideband interference. The only difference between the cases shown in Figures 8.8 and 8.10 is the difference in the value of k . Examination of these figures indicates the increase in k from $1/2$ to 10 produces two effects. First, for the case when $k=10$, the characteristic hump appears in the $P(e)$ vs. INR curves. The appearance of this hump is not surprising since we have seen it for each of the other modulation/interference combinations that we have examined so far. The second important difference to be noted when comparing Figures 8.8 and 8.10 is the different INR value at which the curves begin to diverge. This value is approximately 15 dB for the case when $k=1/2$ and 25 dB when $k=10^*$.

Figure 8.11 shows the results of the calculations for case (D). In this case the interference is passed by the input BPFs but is partially blocked by the detector filter for $B_i' > 0.01$. For the cases shown in the upper two curves, the interference falls entirely within the passband both the input and detector filters. The performance shown in these two curves is identical to that shown in the corresponding curves

* Note that the noise power at each element input is 13 dB larger for case (C) than it was for case (A). Therefore, the curves begin to diverge at approximately the same value of P_i/P_n at the array input for the two cases.

P (E) VS. INR

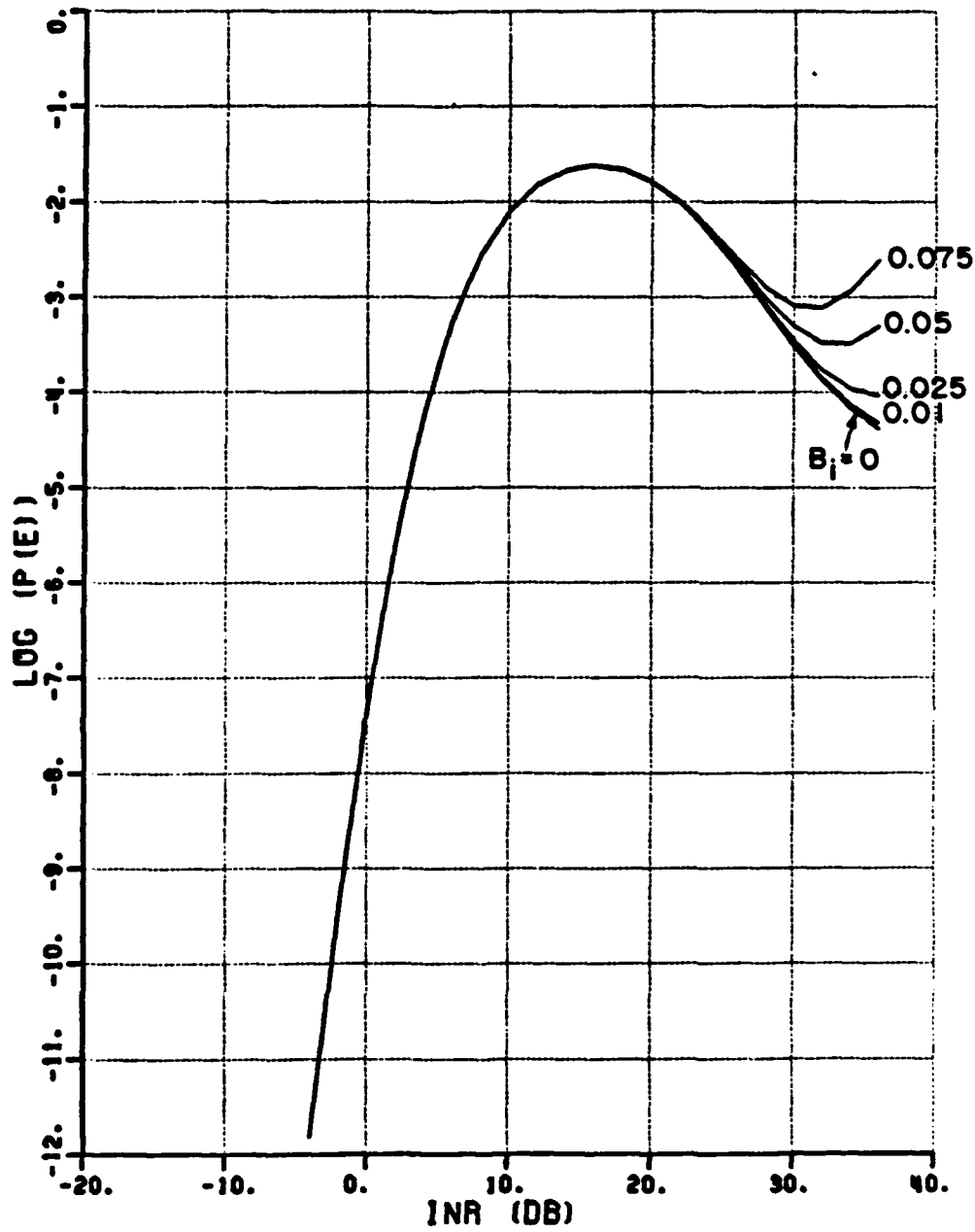


Figure 8.10. 3-element array performance - case (C).

P (E) VS. INR

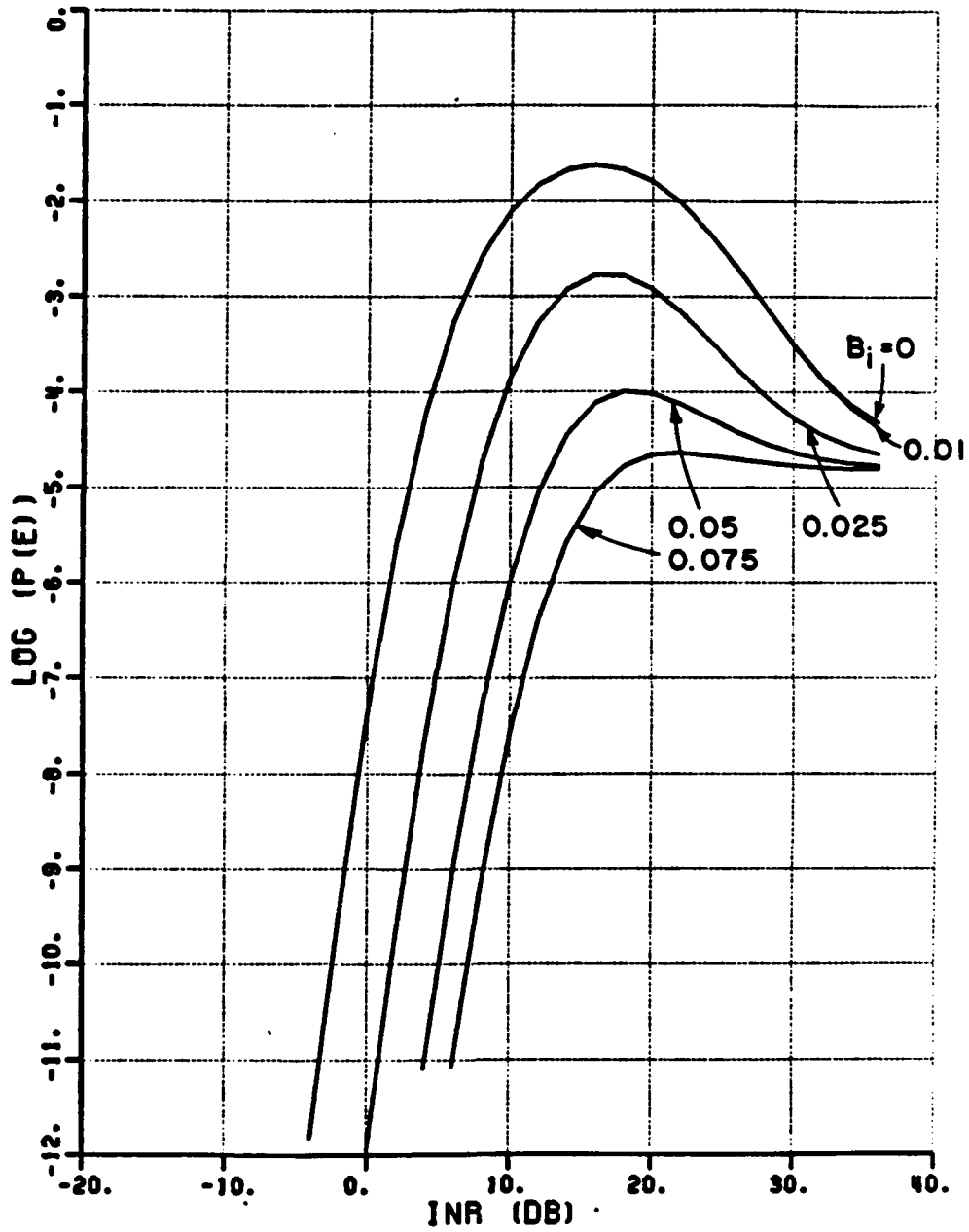


Figure 8.11. 3-element array performance - case (D).

in Figure 8.10. However, for the larger values of interference bandwidth, a significant portion of the interference is rejected by the detector filter. For these cases, the performance with a fixed-power jammer monotonically improves as the bandwidth increases.

In each of the cases discussed above the system performance became worse as the interference bandwidth increased until the point was reached where the interference and desired signal bandwidths were equal. This behavior was noted for each of the array input bandwidths examined. We found that the performance was best for small k values. Therefore, for best performance, the desired signal bandwidth and the array input bandwidths should each be as small as possible. Similarly, from a different point of view, the most effective jamming strategy is to spread the interference power over as wide a bandwidth as possible while keeping the bandwidth less than or equal to the desired signal bandwidth.

It is interesting to compare the results obtained in this chapter for zero-bandwidth noise interference with those presented in the previous chapter for CW interference. We might at first expect these two cases to produce identical results since the adaptive array calculations are identical in the two cases. However, the equations from which $P(e)$ is calculated for each case are significantly different. When the results are compared for the two cases we note that significantly poorer performance is obtained for the zero-bandwidth Gaussian noise case. In the CW interference case we assume that we have a sinusoidal interference signal with a fixed amplitude and random

phase. In the noise case we assume that we have a Gaussian random process for which we know the variance. Figure 8.12 shows a typical member of the ensemble of noise waveforms under the assumption that the bandwidth is not zero but is very small*.

For maximum effectiveness with a fixed average power, a narrowband jammer will be more effective if the CW output signal is modulated with a Gaussian random process so as to produce an output waveform similar to that shown in Figure 8.12. If such a signal is to be truly Gaussian, the transmitter must be capable of transmitting at peak power levels which greatly exceed the average power level. Whether or not a particular transmitter can do this depends on its hardware design. If the maximum and peak power capabilities of a particular narrowband transmitter are equal then the transmitter might as well send a CW signal of constant amplitude so that the maximum power level is always being transmitted.

D. PERFORMANCE OF A TAPPED DELAY LINE LMS ARRAY WITH WIDEBAND INTERFERENCE

In this section we examine the performance of a modified LMS array with broadband Gaussian interference. This array has transversal filters (i.e., tapped delay lines) behind each element instead of a

* If we were to assume that the Gaussian process truly has zero bandwidth then the interference would be a constant amplitude CW signal. Our Gaussian assumption would therefore apply to the statistics of the ensemble of possible interference waveforms and not the time statistics of one ensemble member. Therefore the zero-bandwidth Gaussian interference process is not ergodic.

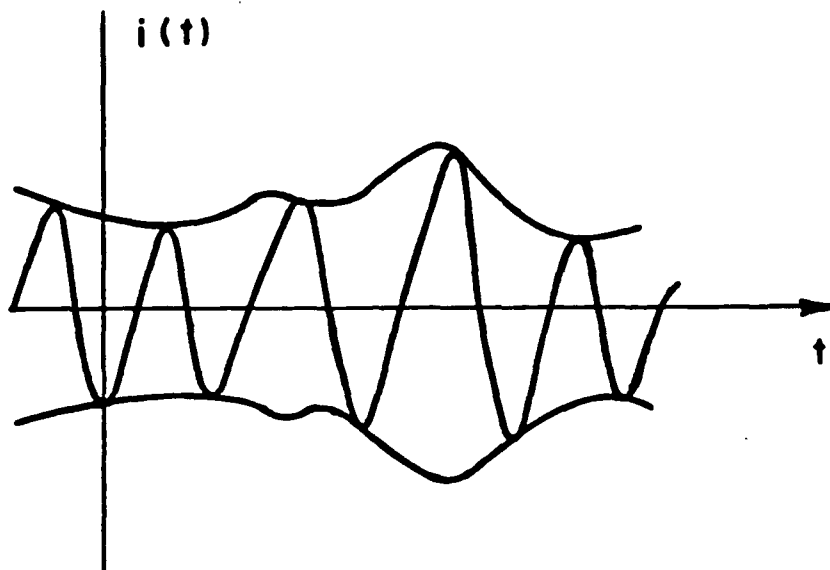


Figure 8.12. Sample interference waveform with $B_j \approx 0$.

single complex weight. The use of tapped delay lines as the weighting elements in the LMS array was first suggested by Widrow [1]. Compton and Rodgers studied the performance of several different structures of tapped delay line (TDL) LMS arrays in [31]. We first present a short description of the TDL array and why it is effective against wideband interference. We then present the results from performance calculations which illustrate the performance improvement offered by this type of processing.

We first examine why TDL adaptive array processing is more effective than conventional LMS processing. We consider a 2-element array as an example. A 2-element array has a transfer function for the interference of,

$$H_i(\omega) = w_1 + w_2 \exp[-j\omega_i T_i] \quad (8.23)$$

where w_1 and w_2 are the element weights and T_i is the interelement time delay given by (2.14). If the array is to steer a null on the interference $H_i(\omega)$ should be zero. Thus, for a null, we require,

$$w_1 = -w_2 \exp[-j\omega_i T_i] . \quad (8.24)$$

Since w_1 and w_2 are simply complex numbers, (8.24) can only be satisfied at a single frequency ω_i . Thus, with appropriate weights, the 2-element array can completely cancel a CW interfering signal. However, complete cancellation is impossible for broadband interference since the element weights are frequency independent.

Now let us examine the transfer function of the 2-tap TDL filter shown in Figure 8.13. The transfer function of this filter is,

$$H(\omega) = w_1 + w_2 \exp[-j\omega T] , \quad (8.25)$$

where T is the time delay produced by the delay line. If we use such a filter to implement each of the element weights in an adaptive array we might expect to improve the performance against broadband interference. This improvement is to be expected since the TDL element weights are not frequency independent. Therefore the TDL filters can (approximately) compensate for the frequency dependence of the complex exponential term in (8.24).

Compton [32] studied the optimum delay line length and number of taps for suppression of a single wideband jammer. The results of this study indicated that the length of the delay line is not particularly

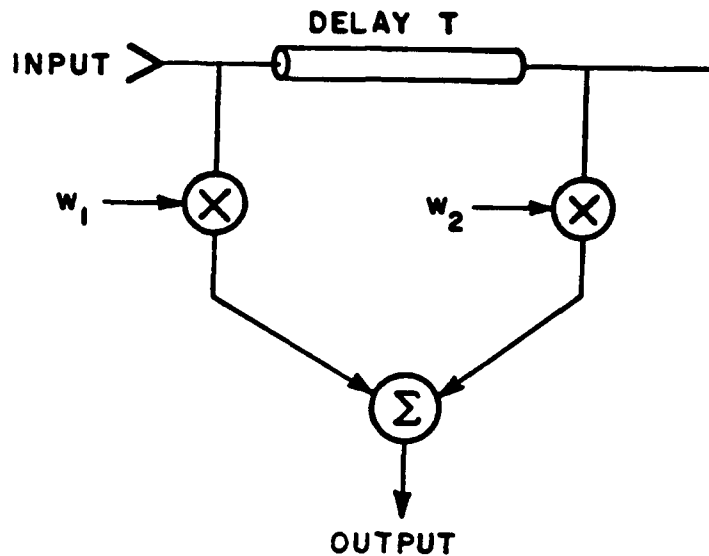


Figure 8.13. 2-tap transversal filter.

critical as long as it is shorter than approximately one wavelength. In a real array, extremely short delay lines should be avoided since they may require a very large dynamic range for the weights. Compton also shows that a single wideband noise jammer can effectively be suppressed with just two taps per delay line.

We now consider the 3-element TDL LMS array shown in Figure 8.14. The signal received by each array element is processed by a 2-tap TDL with complex weights and a quarter wavelength delay between taps. The weighted signals are summed to produce the array output. Conventional LMS feedback loops are used to drive each element weight. The signals at the tap outputs are given by,

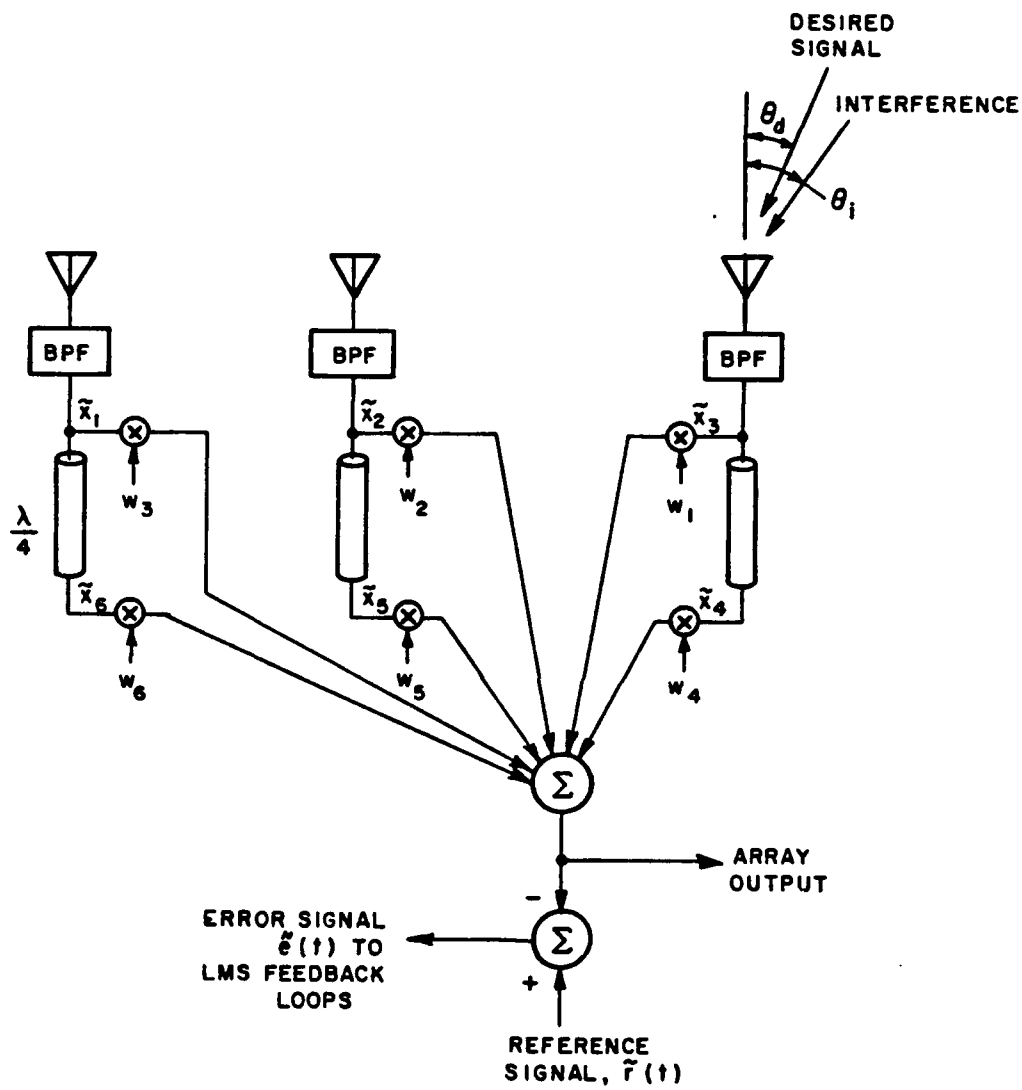


Figure 8.14. 3-element tapped delay line LMS array.

$$\tilde{x}_1(t) = \tilde{d}(t) + \tilde{i}(t) + \tilde{n}_1(t) \quad (8.26)$$

$$\tilde{x}_2(t) = \tilde{d}(t-T_d) + \tilde{i}(t-T_i) + \tilde{n}_2(t) \quad (8.27)$$

$$\tilde{x}_3(t) = \tilde{d}(t-2T_d) + \tilde{i}(t-2T_i) + \tilde{n}_3(t) \quad (8.28)$$

$$\tilde{x}_4(t) = \tilde{x}_1(t-T) \quad (8.29)$$

$$\tilde{x}_5(t) = \tilde{x}_2(t-T) \quad (8.30)$$

$$\tilde{x}_6(t) = \tilde{x}_3(t-T) \quad (8.31)$$

where T_d and T_i are the interelement time delays for the desired signal and interference. The desired signal covariance matrix is given by,

$$\Phi_d = \begin{bmatrix} \tilde{R}_d(0) & \tilde{R}_d(-T_d) & \tilde{R}_d(-2T_d) & \tilde{R}_d(-T) & \tilde{R}_d(-T_d-T) & \tilde{R}_d(-2T_d-T) \\ \tilde{R}_d(T_d) & \tilde{R}_d(0) & \tilde{R}_d(-T_d) & \tilde{R}_d(T_d-T) & \tilde{R}_d(-T) & \tilde{R}_d(-T_d-T) \\ \tilde{R}_d(2T_d) & \tilde{R}_d(T_d) & \tilde{R}_d(0) & \tilde{R}_d(2T_d-T) & \tilde{R}_d(T_d-T) & \tilde{R}_d(-T) \\ \tilde{R}_d(T) & \tilde{R}_d(-T_d+T) & \tilde{R}_d(-2T_d+T) & \tilde{R}_d(0) & \tilde{R}_d(-T_d) & \tilde{R}_d(-2T_d) \\ \tilde{R}_d(T_d+T) & \tilde{R}_d(T) & \tilde{R}_d(-T_d+T) & \tilde{R}_d(T_d) & \tilde{R}_d(0) & \tilde{R}_d(-T_d) \\ \tilde{R}_d(2T_d+T) & \tilde{R}_d(T_d+T) & \tilde{R}_d(T) & \tilde{R}_d(2T_d) & \tilde{R}_d(T_d) & \tilde{R}_d(0) \end{bmatrix} \quad (8.32)$$

Similarly,

$$\Phi_i = \begin{bmatrix} \tilde{R}_i(0) & \tilde{R}_i(-T_i) & \tilde{R}_i(-2T_i) & \tilde{R}_i(-T) & \tilde{R}_i(-T_i-T) & \tilde{R}_i(-2T_i-T) \\ \tilde{R}_i(T_i) & \tilde{R}_i(0) & \tilde{R}_i(-T_i) & \tilde{R}_i(T_i-T) & \tilde{R}_i(-T) & \tilde{R}_i(-T_i-T) \\ \tilde{R}_i(2T_i) & \tilde{R}_i(T_i) & \tilde{R}_i(0) & \tilde{R}_i(2T_i-T) & \tilde{R}_i(T_i-T) & \tilde{R}_i(-T) \\ \tilde{R}_i(T) & \tilde{R}_i(-T_i+T) & \tilde{R}_i(-2T_i+T) & \tilde{R}_i(0) & \tilde{R}_i(-T_i) & \tilde{R}_i(-2T_i) \\ \tilde{R}_i(T_i+T) & \tilde{R}_i(T) & \tilde{R}_i(-T_i+T) & \tilde{R}_i(T_i) & \tilde{R}_i(0) & \tilde{R}_i(-T_i) \\ \tilde{R}_i(2T_i+T) & \tilde{R}_i(T_i+T) & \tilde{R}_i(T) & \tilde{R}_i(2T_i) & \tilde{R}_i(T_i) & \tilde{R}_i(0) \end{bmatrix} \quad (8.33)$$

and the noise covariance matrix is given by,

$$\Phi_i = \begin{bmatrix} \tilde{R}_n(0) & 0 & 0 & \tilde{R}_n(-T) & 0 & 0 \\ 0 & \tilde{R}_n(0) & 0 & 0 & \tilde{R}_n(-T) & 0 \\ 0 & 0 & \tilde{R}_n(0) & 0 & 0 & \tilde{R}_n(-T) \\ \tilde{R}_n(T) & 0 & 0 & \tilde{R}_n(0) & 0 & 0 \\ 0 & \tilde{R}_n(t) & 0 & 0 & \tilde{R}_n(0) & 0 \\ 0 & 0 & \tilde{R}_n(T) & 0 & 0 & \tilde{R}_n(0) \end{bmatrix} \quad (8.34)$$

where we denote the noise ACF at each element by $\tilde{R}_n(\tau)$.

We assume the same desired and interference signal models used previously in this chapter. We also assume that the element BPFs have the same bandwidth as the desired signal (i.e. the bandwidth factor $k=0.5$). Furthermore, for simplicity, we shall only consider the case where the interference bandwidth is less than or equal to that of the desired signal.

The calculations of the noise covariance matrix are somewhat more complicated in this case than for the previous cases that we considered. In each of these previous cases the noise covariance matrix was diagonal (i.e., $\Phi_n = \sigma^2 I$). In these cases, to calculate the covariance matrix, we only needed to know the total noise power (σ^2) at each element input and not its PSD or ACF. In the present case we must also include the non-zero off-diagonal terms in the noise covariance matrix.

We assume that white Gaussian noise is present at the input to each element input. The ideal BPFs at the element inputs limit the noise spectrum to a rectangular passband as shown in Figure 8.14. We assume that the total noise passed by each filter has power σ^2 . Therefore, the noise complex ACF is given by,

$$R_n(\tau) = \sigma^2 \text{sinc}(\Delta\omega_i \tau / 2) \exp(j\omega_d \tau). \quad (8.35)$$

We assume that the array reference signal is of the form,

$$\tilde{r}(t) = \tilde{d}(t) / \sqrt{(P_d)_{in}} \quad (8.36)$$

where $(P_d)_{in}$ is the desired signal power at each element input. The reference correlation vector S is then given by,

$$S = \begin{bmatrix} \tilde{R}_d(0) \\ \tilde{R}_d(T_d) \\ \tilde{R}_d(2T_d) \\ \tilde{R}_d(T) \\ \tilde{R}_d(T_d+T) \\ \tilde{R}_d(2T_d+T) \end{bmatrix} \quad (8.37)$$

From the equations given above we can calculate the array performance. The array weights are calculated first using

$$W = [\phi_d + \phi_i + \phi_n]^{-1} S. \quad (8.38)$$

The power levels of the desired signal, interference, and the thermal noise at the array output are then calculated using (2.32) through (2.34).

In Chapter II we defined the SINR at the array output as

$$\text{SINR} = \frac{P_d}{P_i + P_n}. \quad (8.39)$$

Earlier in this chapter we found that $P(e)$ of the ideal detector was dependent only upon the SINR at the detector input where we defined SINR_{det} as

$$\text{SINR}_{\text{det}} = \frac{E_d}{(E_i)_{\text{det}} + n} \quad (8.40)$$

where $E_d = P_d T$, $E_i = (P_i)_{\text{det}} T$ and n is the one-sided real noise PSD at the detector input. We defined $(P_i)_{\text{det}}$ as the power in the portion of

the interference signal that lies within the band of frequencies for which the detector is sensitive. Since, in the present case, we assume that the interference bandwidth is less than or equal to the desired signal bandwidth then $(P_i)_{\text{det}} = P_i$. Thus (8.40) becomes

$$\text{SINR}_{\text{det}} = \frac{P_d T}{P_i T + n} \quad (8.41)$$

or equivalently

$$\text{SINR}_{\text{det}} = \frac{P_d}{P_i + n/T} \quad (8.42)$$

Since we assumed that the bandwidth of the BPFs at the element inputs is $1/T$ then n/T is the noise power P_n at the detector input (i.e., the array output). Therefore

$$\text{SINR}_{\text{det}} = \frac{P_d}{P_i + P_n} \quad (8.43)$$

A comparison of (8.39) and (8.43) indicates that SINR_{det} , upon which $P(e)$ is a simple function of, is equal to the SINR at the array output, i.e.,

$$\text{SINR}_{\text{det}} = \text{SINR} \quad (8.44)$$

Using this expression in (8.22) we have

$$P(e) = \text{erfc}[(2)(\text{SINR})] \quad (8.45)$$

Thus $P(e)$ for the case at hand can be simply calculated from the SINR at the array output.

We now use the derivations described above to calculate the performance of the TDL LMS array with BPSK signalling and broadband noise interference. As an example we consider one of the cases for which we found particularly poor performance with the standard LMS array. We examine the system performance when the input signal scenario is identical to that for the case shown in Figure 8.5. For this case $\theta_d=0^\circ$, $\theta_j=10^\circ$, SIR = -30 dB, and $B_j = 0, 0.01, 0.025, 0.05, \text{ and } 0.075$. The results for the TDL LMS array are shown in Figure 8.15.

A comparison of Figures 8.5 and 8.15 indicates that adding the TDL processing to the LMS array greatly improves performance. In fact, the performance for all of the non-zero B_j values for the TDL array is as good as the $B_j=0$ case. Therefore, the TDL array has completely eliminated the performance degradation caused by non-zero bandwidth of the single jammer. This performance improvement was noted for a wide variety of input signal scenarios.

Rules for designing TDL LMS arrays did not exist until recently [23] and several aspects of their performance are yet to be studied. For example, the performance of the TDL LMS array in the presence of multiple broadband jammers has yet to be examined in detail. However, the results presented here indicate it appears that continued study of the TDL LMS array would be worthwhile.

P (E) VS. SNR

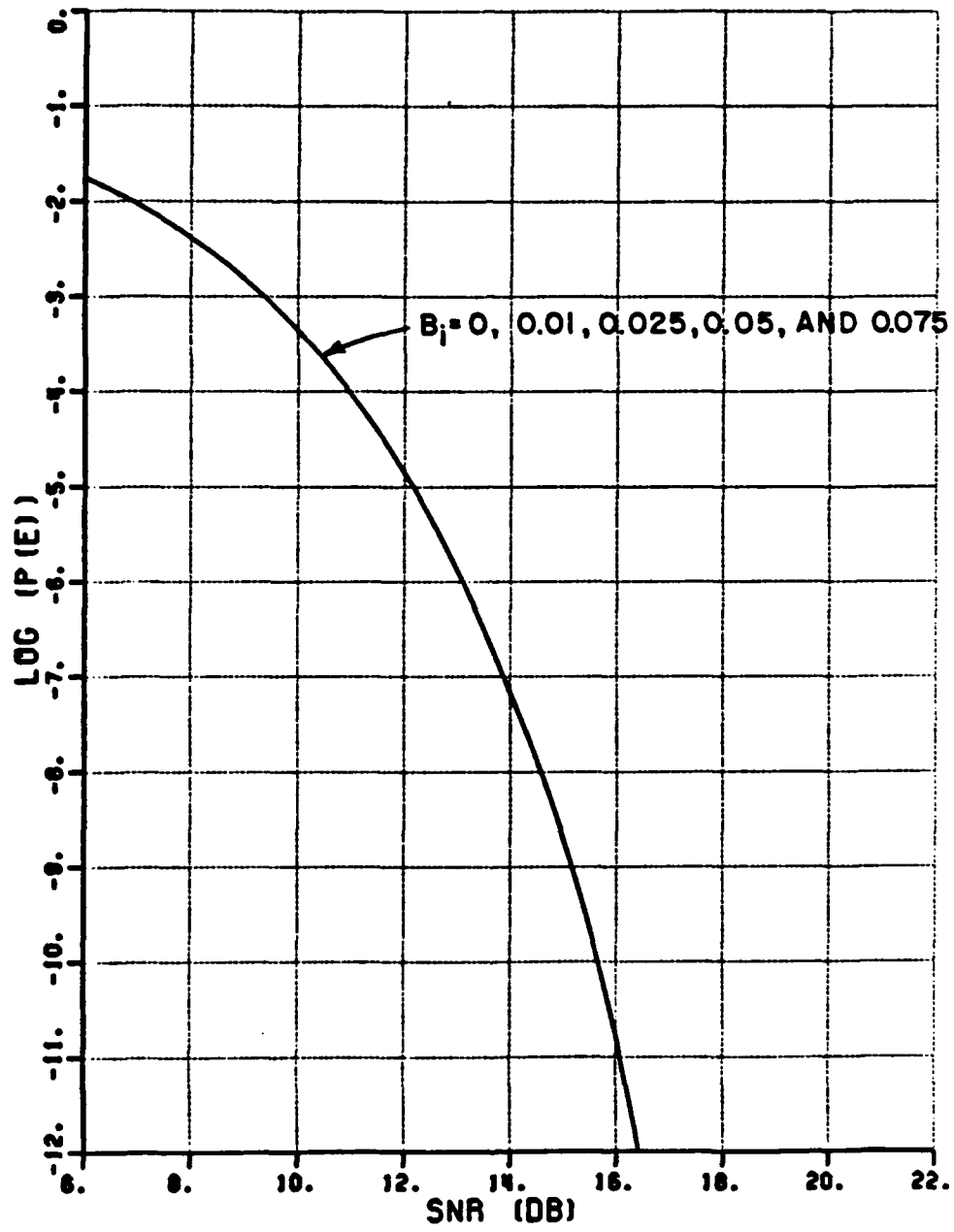


Figure 8.15. Performance of the 3-element TDL LMS array for the same cases shown in Figure 8.5.

CHAPTER IX

SUMMARY AND CONCLUSIONS

In this dissertation we have examined the performance of several communication systems that use LMS adaptive arrays for interference suppression. $P(e)$ at the detector output was used as the measure of system performance.

We have found that the LMS array improves the communication system performance in many cases. We first examined the performance of BPSK, QPSK, DPSK and FSK systems with CW interference. We showed that, qualitatively, the performances of these systems were quite similar. We found that the variations in performance noted among the different systems with the same input signals were generally consistent with the well known relative performance levels of their respective modulation methods. We found that no particular modulation technique provided unusually good or poor performance. For this reason we used BPSK modulation in the latter chapters with the understanding that similar qualitative performance would be observed with any of the other modulation methods.

We found that the system performance is dependent upon several factors. The performance is best when there is a large spatial separation between the desired and interfering signals. The performance generally becomes worse as the array input bandwidth increases beyond the desired signal bandwidth. We defined k as the ratio of the array

input bandwidth to the reciprocal of the symbol rate. For k values greater than approximately 2, humps appear in the $P(e)$ vs. INR curves. The height of these humps becomes larger as k increases. The peaks of the humps occur at INR values where the interference power is approximately equal to the thermal noise power at the array input.

In order to determine the optimum system bandwidth, we described a minimal bandwidth BPSK system that allows the BPSK signal to occupy a bandwidth corresponding to $k=1/2$. We examined the performance of the narrowband system for k values between $1/2$ and 10 . In general we found the best performance for small k values. However, for weak interference, we found that the very narrowband (i.e., $k = 1/2$) system performed slightly worse than systems with $k=1$ or $k=2$. We found that the array, with $k=1/2$, successfully nulls the weak interference; but the constraints imposed on the pattern by the null also produce a slight decrease in the desired signal power at the array output. The net effect of the null, in this case, is to reduce the output SNR and $P(e)$. However, the differences in performance noted for k values between $1/2$ and 2 are small.

We calculated the performance of the narrowband BPSK system for the case where the interfering signal is a Gaussian noise signal with non-zero bandwidth. We found that, for a fixed interference power, $P(e)$ increases as the interference bandwidth increases until the interference and desired signal bandwidths are equal. Therefore, the interference is most effective when its bandwidth is the same as the desired signal. We found that wideband interference was especially disruptive when the

input interference power is 10 dB or more larger than the desired signal power. We found that wideband interference is most effective when it arrives from a direction near endfire since the interelement time delay is largest in this direction. We suggested that a nonlinear element geometry would eliminate this susceptibility to endfire broadband interference.

We next calculated the effects of noise interference on a tapped delay line (TDL) LMS array. In this array transversal filters are used to implement the element weights. We found that the TDL LMS array was not sensitive to the interference bandwidth for any of the signal levels and bandwidths that we examined. The primary disadvantage of the TDL LMS array is the added hardware complexity.

In summary we found that the LMS array can offer a significant degree of interference protection to digital communication systems. The system performance is not unusually dependent on the modulation method. For best results we found that the desired signal and array input bandwidths should each be as small as possible. We also found that the system performance is best when the desired signal and interference were well separated spatially. We showed that wideband interference is more effective than CW interference but that tapped delay line processing greatly reduces the system susceptibility to wideband interference.

REFERENCES

- [1] Applebaum, S.P., "Adaptive Arrays," Syracuse University Research Corporation Report SPL TR 66-1, August 1966.
- [2] Widrow, B., Mantey, P.E. Griffiths, L.J., and Goode, B.B., "Adaptive Antenna Systems," Proc. IEEE, 55, 12, December 1967, pp. 2143.
- [3] Compton, R.T., Jr., "An Adaptive Array in a Spread Spectrum Communication System," Proc. IEEE, 66, 3, March 1978, pp. 289.
- [4] Winters, J.H., "Spread Spectrum in a Four-phase Communication System Employing Adaptive Arrays," IEEE Trans. COM-30, May 1982, p. 929.
- [5] Compton, R.T., Jr., Huff, R.J., Swarner, W.G., and Ksienski, A.A., "Adaptive Arrays for Communication Systems: An Overview of Research at The Ohio State University," IEEE Trans. AP-24, September 1976, p. 599.
- [6] Hudson, E.C., "Use of An Adaptive Array in a Frequency-Shift Keyed Communication System," Report 712684-1, The Ohio State University ElectroScience Laboratory, Columbus, Ohio, August 1980.
- [7] Ganz, M.W., "On the Performance of an Adaptive Array in a Frequency-Shift Keyed Communication System," M.Sc. thesis, Department of Electrical Engineering, The Ohio State University, Columbus, Ohio, 1982.
- [8] Gupta, I.J. and Ksienski, A.A., "Prediction of Adaptive Array Performance," IEEE Trans. Aerosp. Electron. Sys., Vol. AES-19, May 1983, pp. 380-388.
- [9] Gupta, I.J., "Effect of Jammer Power on the Performance of Adaptive Arrays," IEEE Trans. Antennas and Propagation, Vol. AP-32, September 1984, pp. 933-938.
- [10] Compton, R.J., Jr., "On Eigenvalues, SINR, and Element Patterns in Adaptive Arrays," IEEE Trans. Antennas and Propagation, Vol. AP-32, June 1984, pp. 643-647.
- [11] Gupta, I.J. and Ksienski, A.A., "Dependence of Adaptive Array Performance on Conventional Array Design," IEEE Trans. Antennas and Propagation, Vol. AP-30, pp. 549-553.

- [12] Al-Ruwais, A.S. and Compton, R.T., Jr., "Adaptive Array Behavior with Sinusoidal Envelope Modulated Interference," IEEE Trans. Aerosp. Electron. Syste, Vol. AES-19, September 1983, pp. 677-687.
- [13] Al-Ruwais, A.S. and Compton, R.T., Jr., "Adaptive Array Behavior with Periodic Envelope Modulated Interference," IEEE Trans. Aerosp. Electron. Sys., November 1985, pp. 757-766.
- [14] Acar, L. and Compton, R.T., Jr., "The Performance of an LMS Adaptive Array with Frequency Hopped Signals," IEEE Trans. Aerosp. Electron. Sys., May 1985, pp. 360-371.
- [15] Compton, R.T., Jr., Adaptive Arrays - Concepts and Performance, Englewood Cliffs, N.J., Prentice-Hall, 1986.
- [16] Ziemer, R.E. and Peterson, R.L., Digital Communications and Spread Spectrum Systems, New York, MacMillan, 1985.
- [17] Scire, F.J., "A Probability Density Function for the Modulo Y Values of the Sum of Two Statistically Independent Processes," Proc. IEEE, 56, 2, February 1968, pp. 204-205.
- [18] Rosenbaum, A.S., "PSK Error Performance with Gaussian Noise and Interference," Bell Syst. Tech. Journal, Vol. 48, February 1969, pp. 413-442.
- [19] Prabhu, V.K., "Error Rate Considerations for Coherent Phase-Shift Keyed Systems with Co-Channel Interference," Bell Syst. Tech. Journal, Vol. 48, March 1969, pp. 743-767.
- [20] Van Trees, H.L., Detection, Estimation, and Modulation Theory - Part I, New York, John Wiley & Sons, 1968.
- [21] Papoulis, A., The Fourier Integral and its Applications, New York, McGraw-Hill, 1962.
- [22] Ziemer, R.E. and Tranter, W.H., Principles of Communications, Boston, Houghton Mifflin, 1976, Chapter 5.
- [23] Park, J.H., Jr., "On Binary DPSK Detection," IEEE Trans. Communications, Vol. COM-26, April 1978, pp. 484-486.
- [24] Parl, S., "A New Method of Calculating the Generalized Q Function," IEEE Trans. Inform. Theory, Vol. IT-26, January 1980, pp. 121-124.
- [25] Bennett, W.R. and Rice, S.O., "Spectral Density and Autocorrelation Functions Associated with Binary Frequency-Shiftkeying," Bell System Tech. Journal, Sptember 1963, pp. 2355-2385.

- [26] Wang, L., "Error Probability of a Binary Noncoherent FSK System in the Presence of Two CW Tone Interferers," IEEE Trans. on Communications, Vol. COM-22, pp. 1948-1949.
- [27] Whalen, A.D., Detection of Signals in Noise, New York, Academic Press, 1971, p. 105.
- [28] Lucky, R.W., Salz, J., and Weldon, E.J., Principles of Data Communications, New York, McGraw-Hill, 1968, Chapters 4, 5 and 7.
- [29] Bayless, J.W., Collins, A.C., and Pederson, R.D., "The Specification of Bandlimited Digital Radio Systems," IEEE Trans. Communications, Vol. COM-27, December 1979, pp. 1763-1770.
- [30] Feher, K., Digital Communications: Microwave Applications, Englewood Cliffs, NJ, Prentice-Hall, 1981, Chapter 3.
- [31] Rodgers, W.E. and Compton, R.T., Jr., "Adaptive Array Bandwidth with Tapped Delay-line Processing," IEEE Trans., Vol. AES-15, January 1979, p. 21.
- [32] Compton, R.T., Jr., "The Bandwidth Performance of a Two-Element Adaptive Array with Tapped Delay-line Processing," Report 717253-3, The Ohio State University ElectroScience Laboratory, Columbus, Ohio, prepared under Contract N00019-85-C-0119 for Naval Air Systems Command.